UVSOR ACTIVITY REPORT 2012

Upgrade project
"UVSOR-III"

BL4U
Scanning Transmission
X-ray Microscopy

**UVSOR Facility
Institute for Molecular Science
National Institutes of Natural Sciences**

Preface

This Activity Report covers the research activities carried out at the UVSOR facility in FY2012 (April 2011-March 2012).

The UVSOR facility began operation in 1983, making this year, 2013, the 30th year since its launch. Over these 30 years, various new technologies have been developed in the generation and utilization of synchrotron radiation, and we have eagerly adopted these new technologies, to improve and upgrade the equipment. As a result, even today, the facility is one of the highest performing low-energy synchrotron radiation facilities in the world. In 2003, we made the first major upgrade to the storage ring and started to call it UVSOR-II. In FY2012, we made the second major upgrade. The commissioning was successful. Now we have started to call the machine UVSOR-III. It has small emittance around 15 nm-rad and six undulators. It is operated fully in the top-up mode. A new STXM beam-line, BL4U, was also successfully commissioned, which will be opened for users from June 2013.

UVSOR-III has eight straight sections. Two of them are used for the RF system and for the beam injection. The six of them are now occupied by the undulators. In future, our efforts will go into improving the performance of the light source and upgrading the existing undulators and beam-lines. As its first step, the upgrade of the BL5U is under preparation. The reconstruction work will be done in March 2013.

In March, 2012, Mr. Eiken Nakamura moved to Synchrotron Radiation Research Center at Nagoya University to join construction of a new synchrotron radiation facility, Aichi synchrotron research center. He had been working for about 30 years as an engineer in the facility from the very beginning of its construction. We are grateful for his works devoted for the facility and the users for many years and wish his success in the new facility.

We look forward to more exciting achievements in FY2012 at UVSOR-III. We welcome the opportunity to assist researchers worldwide in utilizing our facility as a prominent international hub for synchrotron radiation research.
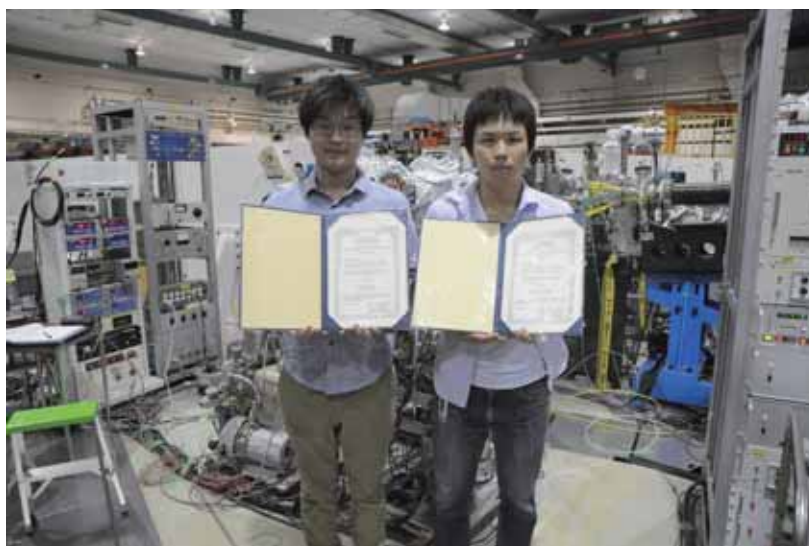
April, 2013

Masahiro Katoh
Director of UVSOR

2012 Annual Meeting Award of the Particle Accelerator Society of Japan Given to Mr. Yohei Hida, Mr. Takahiro Niwa and Dr. Yoshitaka Taira

Mr. Yohei Hida, Mr. Takahiro Niwa received the 2012 Annual Meeting Award of the Particle Accelerator Society of Japan for their poster presentations, and Dr. Yoshitaka Taira for his oral presentation. All these three were from Nagoya University and worked in the accelerator group of UVSOR as research assistants. Their presentations were based on the research works at UVSOR. Mr. Hida presented the successful commissioning of the pulsed sextupole magnet for the beam injection. Mr. Niwa presented the successful development of a pulse width measurement system for the polarized electron gun. Dr. Taira presented results from the application of the ultra-short gamma-ray pulses based on Laser-Compton scattering. Congratulations!

Young Scientist Award of the Physical Society of Japan Given to Dr. Yoshitaka Taira

Dr. Yoshitaka Taira received the Young Scientist Award of the Physical Society of Japan, for his PhD work at UVSOR, Generation and Application of Ultra-short Gamma-ray Pulses based on 90 degree Laser-Compton Scattering. He was from Nagoya University and worked in the accelerator group of UVSOR for three years. After finishing his PhD work, he started working in The National Institute of Advanced Industrial Science and Technology (AIST). Congratulations, Dr. Taira!

UVSOR Organization

IMS OHMINE, Iwao (Director General)
IMS KOSUGI, Nobuhiro (Deputy Director General)

UVSOR Facility: KATOH, Masahiro (Director)

Users in IMS

UVSOR Users Association

UVSOR Steering Commitee

Accelerator Physics: KATOH, Masahiro (Prof.)

Photophysics: KIMURA, Shin-ichi (Assoc. Prof.)

Photochemistry: SHIGEMASA, Eiji (Assoc. Prof.)

UVSOR Staff

Director

KATOH, Masahiro	Professor	mkatoh@ims.ac.jp	

Light Source Division (Accelerator Physics)

KATOH, Masahiro	Professor	mkatoh@ims.ac.jp	
ADACHI, Masahiro	Assistant Professor		(until Mar. 2013)
OHIGASHI, Takuji	Assistant Professor	ohigashi@ims.ac.jp	
KONOMI, Taro	Assistant Professor	konomi@ims.ac.jp	
ITO, Atsushi	Visiting Professor		
YAMAZAKI, Jun-ichiro	Unit Chief Engineer	yamazaki@ims.ac.jp	
HAYASHI, Kenji	Engineer	h-kenji@ims.ac.jp	
TANAKA, Seiichi	Post-Doctoral Fellow		(until Oct. 2012)
ARAI, Hidemi	Post-Doctoral Fellow		(until Mar. 2013)
TOKUSHI, Tetsuzyo	Supporting Engineer	tetsuzyo@ims.ac.jp	
INAGAKI, Yuichi	Supporting Engineer	yinagaki@ims.ac.jp	(since Dec. 2012)

Beamline Division (Photophysics)

KIMURA, Shin-ichi	Associate Professor	kimura@ims.ac.jp	
MATSUNAMI, Masaharu	Assistant Professor	matunami@ims.ac.jp	
HASUMOTO, Masami	Unit Chief Engineer	hasumoto@ims.ac.jp	
SAKAI, Masahiro	Engineer	sakai@ims.ac.jp	
IIZUKA, Takuya	Post-Doctoral Fellow		(until Jul. 2012)
Koswattage Kaveenga Rasika	Visiting Researcher	rasika@ims.ac.jp	(since Aug. 2012)

Beamline Division (Photochemistry)

SHIGEMASA, Eiji	Associate Professor	sigemasa@ims.ac.jp	
IWAYAMA, Hiroshi	Assistant Professor	iwayama@ims.ac.jp	
HORIGOME, Toshio	Facility Chief Engineer	horigome@ims.ac.jp	
KONDO, Naonori	Engineer	nkondo@ims.ac.jp	
ISHIKAWA, Lisa	Post-Doctoral Fellow		(until Nov. 2012)

Secretary

HAGIWARA, Hisayo   hagiwara@ims.ac.jp
KAWAI, Shigeko   kawai@ims.ac.jp

UVSOR Steering Committee

KATOH, Masahiro	UVSOR, IMS	Chair
KIMURA, Shin-ichi	UVSOR, IMS	
SHIGEMASA, Eiji	UVSOR, IMS	
ITO, Atsushi	Tokai Univ. (Visiting. Prof., IMS)	
YOKOYAMA, Toshihiko	IMS	
OHSHIMA,Yasuhiro	IMS	
TADA, Mizuki	IMS	(until Mar. 2013)
FUJI, Takao	IMS	
AKIYAMA, Syuji	IMS	(since Apr. 2013)
KINOSHITA, Toyohiko	JASRI	
KOBAYASHI, Yukinori	KEK-PF	
KONDOH, Hiroshi	Keio Univ.	
SHIMADA, Kenya	Hiroshima Univ.	
HARADA, Yoshihisa	Univ. of Tokyo	
NAKAGAWA, Kazumichi	Kobe Univ.	
SODA, Kazuo	Nagoya Univ.	

UVSOR Users Association

SODA, Kazuo	Chair, Nagoya Univ.
URISU, Tsuneo	Nagoya Univ.
TANAKA, Shin-ichiro	Osaka Univ.
KERA, Satoshi	Chiba Univ.
ITO, Takahiro	Nagoya Univ.
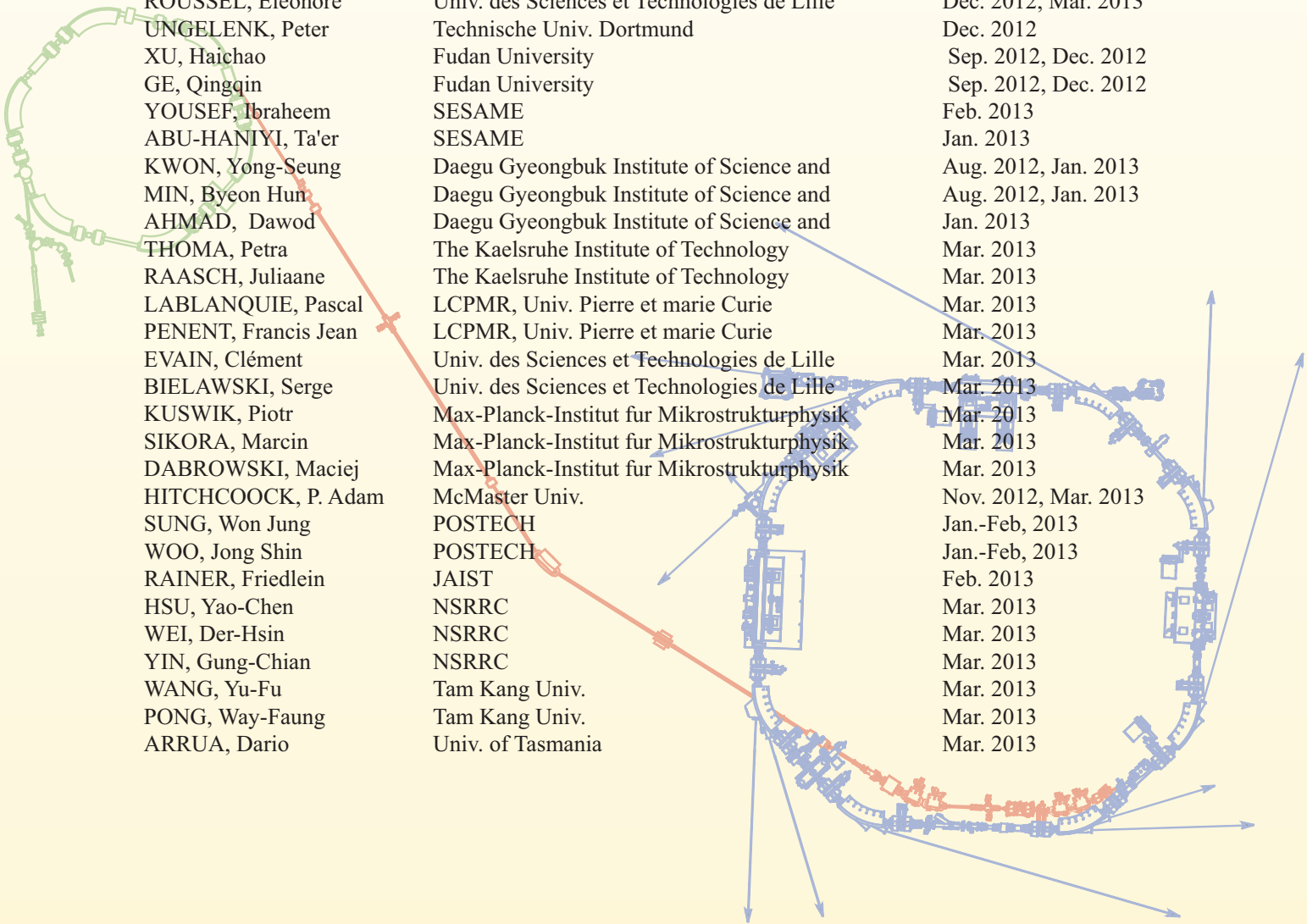
Graduate Students

HAJIRI, Tetsuya	Nagoya Univ.	(until Mar. 2013)
NIWA, Ryosuke	Nagoya Univ.	(until Sep. 2012)
UEMATSU, Yohei	Nagoya Univ.	(until Sep. 2012)
HIDA, Yohei	Nagoya Univ.	(until Sep. 2012)
NIWA, Takahiro	Nagoya Univ.	(until Sep. 2012)
SHIMURA, Yusuke	Nagoya Univ.	(until Sep. 2012)
HIRATE, Satoshi	Nagoya Univ.	(until Sep. 2012)
KAJIURA, Yohei	Nagoya Univ.	(since Nov. 2012)
KATO, Masaki	Nagoya Univ.	(since Nov. 2012)
KANEKO, Masaki	Nagoya Univ.	(since Nov. 2012)
KAWAKAMI, Ryo	Nagoya Univ.	(since Nov. 2012)
MOMIYAMA, Haruya	Nagoya Univ.	(since Nov. 2012)
SEKITA, Sou	Nagoya Univ.	(since Nov. 2012)

Visiting Scientists

ZHANG, Guobin	NSRL, Univ. of Science & Technology of China	Jun. 2012
KHAN, Shaukat	Technische Univ. Dortmund	Sep. 2012
KOH, Yoonyoung	Yonsei Univ.	Oct. 2012
JUNG, Wonsig	Yonsei Univ.	Oct. 2012
CHO, Soo Hyun	Yonsei Univ.	Oct. 2012
SZWAJ, Christophe	Univ. des Sciences et Technologies de Lille	Dec. 2012
ROUSSEL, Eleonore	Univ. des Sciences et Technologies de Lille	Dec. 2012, Mar. 2013
UNGELENK, Peter	Technische Univ. Dortmund	Dec. 2012
XU, Haichao	Fudan University	Sep. 2012, Dec. 2012
GE, Qingqin	Fudan University	Sep. 2012, Dec. 2012
YOUSEF, Ibraheem	SESAME	Feb. 2013
ABU-HANIYI, Ta'er	SESAME	Jan. 2013
KWON, Yong-Seung	Daegu Gyeongbuk Institute of Science and	Aug. 2012, Jan. 2013
MIN, Byeon Hun	Daegu Gyeongbuk Institute of Science and	Aug. 2012, Jan. 2013
AHMAD, Dawod	Daegu Gyeongbuk Institute of Science and	Jan. 2013
THOMA, Petra	The Kaelsruhe Institute of Technology	Mar. 2013
RAASCH, Juliaane	The Kaelsruhe Institute of Technology	Mar. 2013
LABLANQUIE, Pascal	LCPMR, Univ. Pierre et marie Curie	Mar. 2013
PENENT, Francis Jean	LCPMR, Univ. Pierre et marie Curie	Mar. 2013
EVAIN, Clément	Univ. des Sciences et Technologies de Lille	Mar. 2013
BIELAWSKI, Serge	Univ. des Sciences et Technologies de Lille	Mar. 2013
KUSWIK, Piotr	Max-Planck-Institut fur Mikrostrukturphysik	Mar. 2013
SIKORA, Marcin	Max-Planck-Institut fur Mikrostrukturphysik	Mar. 2013
DABROWSKI, Maciej	Max-Planck-Institut fur Mikrostrukturphysik	Mar. 2013
HITCHCOOCK, P. Adam	McMaster Univ.	Nov. 2012, Mar. 2013
SUNG, Won Jung	POSTECH	Jan.-Feb, 2013
WOO, Jong Shin	POSTECH	Jan.-Feb, 2013
RAINER, Friedlein	JAIST	Feb. 2013
HSU, Yao-Chen	NSRRC	Mar. 2013
WEI, Der-Hsin	NSRRC	Mar. 2013
YIN, Gung-Chian	NSRRC	Mar. 2013
WANG, Yu-Fu	Tam Kang Univ.	Mar. 2013
PONG, Way-Faung	Tam Kang Univ.	Mar. 2013
ARRUA, Dario	Univ. of Tasmania	Mar. 2013

Light Source in 2012

1. Status of UVSOR Accelerators

In spring 2012, we made a major upgrade in which all the bending magnets were replaced with combined function ones. An in-vacuum undulator and a pulse sextupole magnet for a novel injection scheme were also installed. The reconstruction works was finished until the middle of June, which was delayed by an accident on the injection septum magnet during the baking.

The storage ring has eight straight sections. After this upgrade, the ring of about 50m circumference has six undulators. Other two straight sections were used for the RF system and the injection septum. Thus, there is no space reserved for undulators. After this upgrade, we have started to call the machine UVSOR-III.
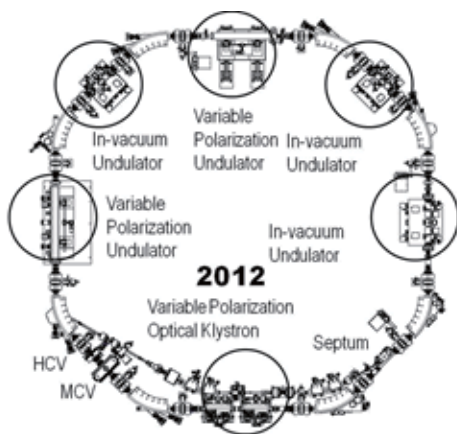
Fig. 1. Undulators in UVSOR-III.

Fig. 2. New In-vacuum Undulator for BL4U STXM Beamline.

We started the commissioning of the UVSOR-III in the middle of June. It took two weeks to succeed in the beam storage, which was unusually long. We found that the injection efficiency strongly depends on the machine parameters such as betatron tunes. The reason of this is still under investigation. Until the end of July, we had operated the storage ring with high beam current for vacuum conditioning. Finally, we started the users operation from the beginning of August. However, during the users beam time, we observed sudden beam losses by a few milliamperes or a few tens of milliampere. Although its frequency is getting lower, we still observe them. Presumably this may due to the dust trapping phenomena. During this shut down, we broke the vacuum system and left them for a few weeks. This might cause this.

In the fiscal year 2012, we operated UVSOR-III from June to March, for 32 weeks for users, although we operate for 36 weeks usually. This shorter operation period was due to the long shutdown for the upgrade program. We operated the machine for 30 weeks in the multi-bunch top-up mode, in which the beam current was kept at 300 mA, and 2 weeks in the single-bunch/multi-bunch hybrid mode, in which the machine is operated in single-bunch top-up mode during daytime and in the multi-bunch top-up mode during nighttime. The monthly statistics of the operation time and the integrated beam current are shown in Fig. 1.
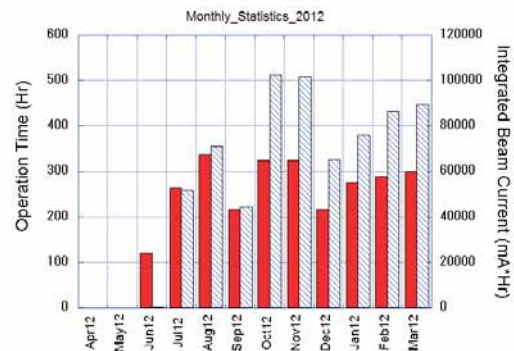

Fig. 3. Monthly statistics in FY2012.

The weekly operation schedule is as follows. On Monday, from 9 am to 9 pm, the machine is operated for machine studies. On Tuesday and Wednesday, from 9am to 9pm, the machine is operated for users. From Thursday 9am to Friday 9pm, the machine is operated for 36 hours continuously for users. Thus, the beam time for users in a week is 60 hours. Usually, we have a few weeks dedicated for machine study, however, in 2012, we did not have them to keep the beam time for users.

In this fiscal year, we had a few troubles on the

injector, malfunctions of switching modules of the klystron pulse modulator and a trouble of the high voltage cable. Fortunately, in all cases the beam time for users could be secured by extending the operation time in the same weeks.

2. Improvements and Developments

Beam Injection with Pulse Quadrupole Magnets

A novel injection scheme using a pulsed sextupole magnets was tested. During the shutdown, a vacuum duct for an injection kicker magnet was replaced to be compatible with the sextupole magnet. The magnet was designed by a graduate student from Nagoya University and the construction and the field measurement was finished until the end of March.

For the test operation, the kicker magnet was replaced with the sextupole magnet, temporally. We succeeded in injecting the beam during the first machine study time. After a few times of the machine studies, the injection efficiency was around 20 %, which should be improved in near future [1].

Turn-by-turn Beam Position Monitor System

We designed and constructed a turn by turn beam position monitor (BPM) system, which is very useful for the commissioning of the storage ring [2]. Since such a system is not necessary in the daily operation, we developed a conventional system. The signals from the pick-up electrodes of the BPM's were sent to a digital oscilloscope through a signal switching system constructed by a co-axial relays remotely controlled. It was proved that the system was quit powerful during the commissioning. We could get useful information, such as the betatron tunes, the energy mismatching between the beam transport line and the storage ring and so on, before the beam storage.

Design Study on the Reconstruction of BL5U Polarization Variable Undulator

The undulator for BL5U was designed and constructed in 1996 to provides polarization variable synchrotron radiation to the BL5U beam-line and also to work for the resonator free electron laser as an optical klystron. Since a new optical klystron has been constructed and installed last year at the straight section #1, we have decided to remodel this undulator to a normal undulator with higher brightness. Currently the undulator has three magnet arrays on each pole to produce helical and horizontal linear polarized light. We are going to change this magnetic configuration to the APPLE-II one with a shorter period length, 60 mm as utlizing the present mechanical frame. The remodeling will be carried out in March 2014 together with an upgrade of the beam-line.

[1] Y. Hida *et al.,* in this report.
[2] K. Hayashi *et. al.,* in this report.

Masahiro KATOH (UVSOR Facility)

UVSOR Accelerator Complex
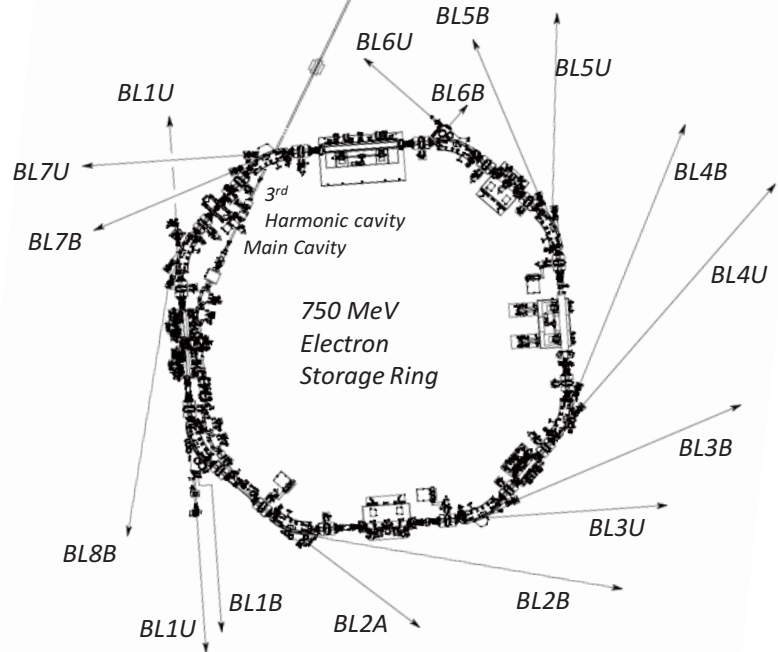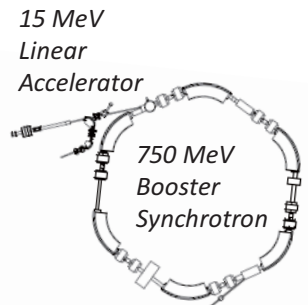
Injection Linear Accelerator

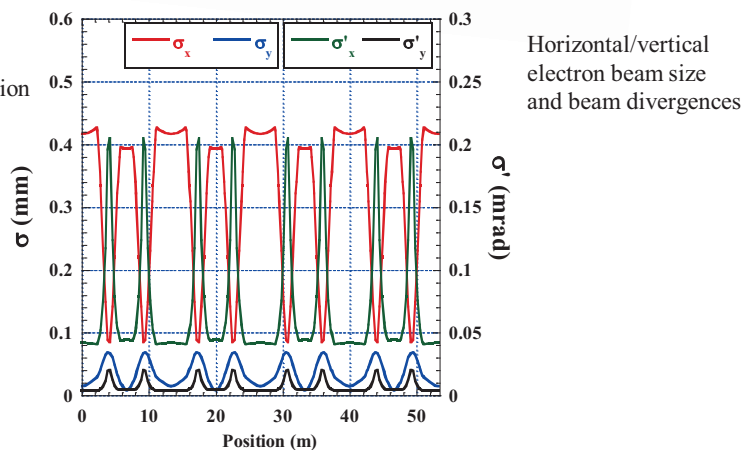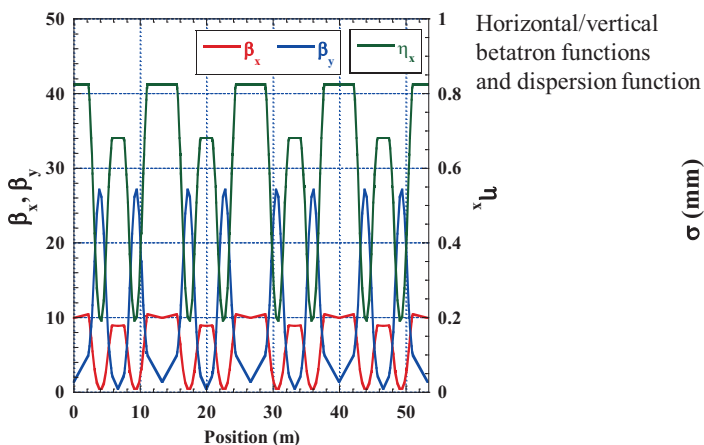|	
Energy	15 MeV
Length	2.5 m
Frequency	2856 MHz
Accelerating RF Field	$2\pi/3$ Traveling Wave
Klystron Power	1.8 MW
Energy Spread	~1.6 MeV
Repetition Rate	2.6 Hz

UVSOR-III Storage-Ring

Energy	750 MeV
Injection Energy	750 MeV
Maximum Storage Current	500 mA (multi bunch)
	100 mA (single bunch)
Normal operation current	300 mA (multi bunch)
(Top-up mode)	50 mA (single bunch)
Natural Emittance	17.5 nm-rad
Circumference	53.2 m
RF Frequency	90.1 MHz
Harmonic Number	16
Bending Radius	2.2 m
Lattice	Extended DBA × 4
Straight Section	(4 m × 4)+(1.5 m × 4)
RF Voltage	120 kV
Betatron Tune	
Horizontal	3.75
Vertical	3.20
Momentum Compaction	0.030
Natural Chromaticity	
Horizontal	-8.1
Vertical	-7.3
Energy Spread	5.26×10^{-4}
Coupling Ratio	1%
Natural Bunch Length	128 ps

Booster Synchrotron

Energy	750 MeV
Injection	15 MeV
Frequency	32 mA (uniform filling)
Circumference	26.6 m
RF Frequency	90.1 MHz
Harmonic Number	8
Bending Radius	1.8m
Lattice	FODO × 8
Betatron Tune	
Horizontal	2.25
Vertical	1.25
Momentum Compaction	0.138
Repetition Rate	1 Hz (750 MeV)

15 MeV
Linear
Accelerator

750 MeV
Booster
Synchrotron

BL5B
BL6U
BL1U
BL6B
BL5U
BL7U
BL4B
3rd Harmonic cavity
Main Cavity
BL7B
BL4U
750 MeV
Electron
Storage Ring
BL3B
BL8B
BL3U
BL1U
BL1B
BL2B
BL2A

Electron Beam Optics of UVSOR-III Storage Ring

Horizontal/vertical betatron functions and dispersion function

Horizontal/vertical electron beam size and beam divergences
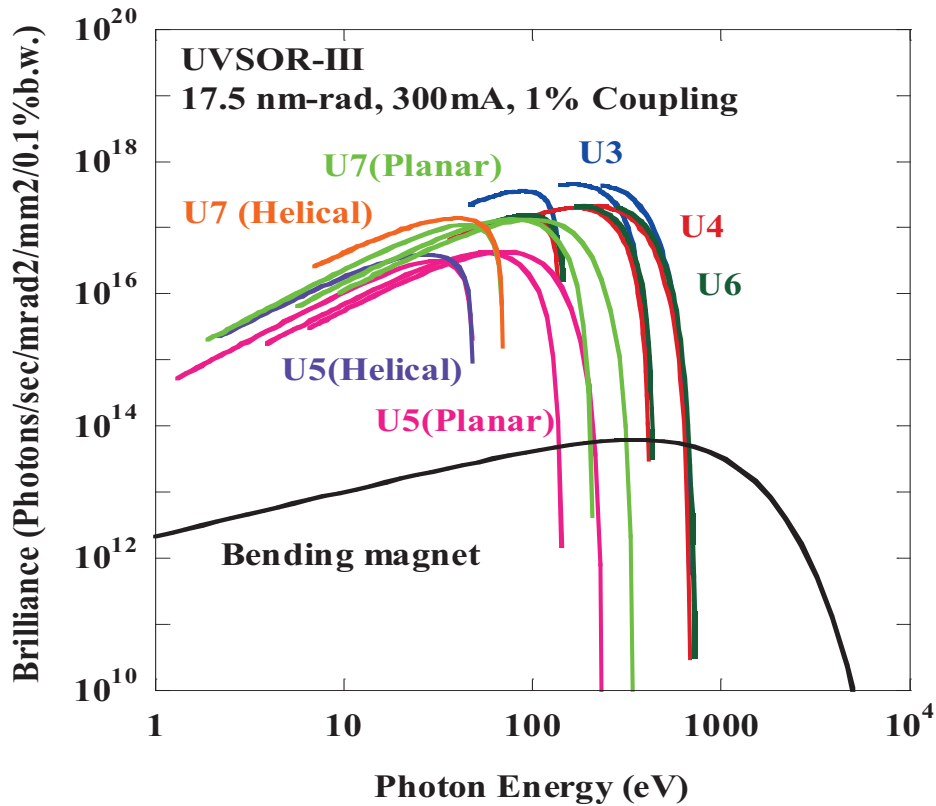
Insertion Device

Brilliance of radiation from the insertion devices (U3, U4, U5, U6 and U7) and a bending magnet of UVSOR-III

U3 In-vacuum Undulator

Number of Periods	50
Period length	38 mm
Pole Length	1.9 m
Pole Gap	15-40 mm
Deflection Parameter	2.0-0.24

U4 In-vacuum Undulator

Number of Periods	50
Period length	38 mm
Pole Length	0.99 m
Pole Gap	13-40 mm
Deflection Parameter	2.4-0.19

U5 Helical Undulator/ Optical Klystron

Number of Periods	21 / 9+9 (Opt. Kly.)
Period length	110 mm
Pole Length	2.35 m
Pole Gap	30-150 mm
Deflection Parameter	4.6-0.07 (Helical)
	8.5-0.15 (Linear)

U6 In-vacuum Undulator

Number of Periods	26
Period length	36 mm
Pole Length	0.94 m
Pole Gap	13-40 mm
Deflection Parameter	1.78 - 0.19

U7 Apple-II

Variable Polarization Undulator

Number of Periods	40
Period length	76 mm
Pole Length	3.04 m
Pole Gap	24-200 mm
Deflection Parameter	5.4 (Max. Horizontal)
	3.6 (Max. Vertical)
	3.0 (Max. Helical)

Bending Magnets

Bending Radius	2.2 m
Critical Energy	425 eV

Beamlines in 2012

It has been widely recognized that the UVSOR facility is one of the highest brilliance light sources in the extreme-ultraviolet region among synchrotron radiation facilities with electron energy less than 1 GeV, after the successful accomplishment of the upgrade project on the storage ring (UVSOR-II project). As described in the previous section, further improvement on the emittance was scheduled in 2012, by replacing all of the bending magnets with newly designed combined-function magnets. This UVSOR-III project has been successfully completed, and the emittance was reduced from 27 to 17 nm-rad.

Eight bending magnets and five insertion devices are now available for utilizing synchrotron radiation at UVSOR. There has been a total of twenty operational beamlines in 2012, which are classified into two categories. Nine of them are the so-called "Open beamlines", which are open to scientists of universities and research institutes belonging to the government, public organizations, private enterprises and those of foreign countries. The rest of the three beamlines are the "In-house beamlines", and are dedicated to the use of research groups within IMS.

We have one soft X-ray station equipped with a double-crystal monochromator, seven extreme ultraviolet and soft X-ray stations with a grazing incidence monochromator, three vacuum ultraviolet stations with a normal incidence monochromator, one infrared (IR) station equipped with Fourier-Transform interferometers, as shown in the appended table (next page) for all available beamlines at UVSOR in 2012.

"Development and Application of Light Source Technology Based on Electron Storage Ring and Laser" proposed by the UVSOR machine group was accepted in 2008, as a research program in "Quantum Beam Technology Project" conducted by MEXT/JST. In connection, the straight section U1 is now used for generating coherent THz and VUV radiation, where two beamlines have been constructed.

BL4U has been newly constructed in 2012. The installation of the beamline components including a scanning transmission soft X-ray microscope (STXM) has been started during the shutdown term before the summer of 2012, and the commissioning of BL4U has been initiated in the autumn of the same year. The first STXM data has been successfully obtained in December 2012. BL4U will open to users in June 2013, immediately after the shutdown term. BL2B, which has long been utilized as an in-house beamline, will be reorganized as an open

beamline in 2013.

A supplementary budget for upgrading the UVSOR facility has been approved in the winter of 2012. The supplementary budget includes the cost for the upgrade of the undulator U5, and for the construction of a new soft X-ray beamline at BL5U and a spin-resolved photoemission experimental setup. As a new undulator for BL5U, an Apple-II type with the period length of 60 mm, whose total length is about 2.5 m, is chosen. The spectral region from 20 eV to 200 eV will be covered with the first and higher harmonic radiation. Concerning the monochromator at BL5U, a variable-included-angle Monk-Gillieson mounting with an entrance slit-less configuration, which is the same as those installed at BL4U and BL6U, has been selected. The spin-resolved photoemission setup will be equipped with a high-resolution hemispherical electron energy analyzer with a highly efficient Mott detector. In pursuit of realizing photoemission experiments with very high spatial resolution, a specially designed post-focusing mirror system is planned to be introduced, where a small beam spot at the sample position (less than 10 μm in diameter) will be achieved. The practical construction of the beamline is scheduled to begin in the spring of 2014 and the beamline commissioning will follow. BL5U will be open to users in the autumn of the same year.

In order to promote beamline upgrades and developments of new experimental techniques by users, a new research proposal category named, the "long-term project proposal", has been introduced in 2012. The available period of this proposal category is three years. Two proposals, one on BL3B and the other on BL2B, have been accepted. Further discussion toward formulating a basic plan on the beamline construction with users, will be continued.

All users are required to refer to the beamline manuals and the UVSOR guidebook (the latest revision in PDF format uploaded on the UVSOR web site in June 2010), on the occasion of conducting the actual experimental procedures. Those wishing to use the open and in-house beamlines are recommended to contact the beamline master (see next page), respectively. For updated information of UVSOR, http://www.uvsor.ims.ac.jp.

Eiji SHIGEMASA (UVSOR Facility)

Beamlines at UVSOR

Beamline	Monochromator / Spectrometer	Energy Range	Targets	Techniques	Contact
BL1U	Free electron laser	1.6 - 13.9 eV			M. Katoh mkatoh@ims.ac.jp
BL1B	Martin-Puplett FT-FIR	0.5 - 30 meV	Solid	Reflection Absorption	S. Kimura kimura@ims.ac.jp
BL2A	Double crystal	585 eV - 4 keV	Solid	Reflection Absorption	N. Kondo nkondo@ims.ac.jp
BL2B*	18-m spherical grating (Dragon)	24 - 205 eV	Gas	Photoionization Photodissociation	H. Katayanagi kata@ims.ac.jp
BL3U*	Varied-line-spacing plane grating (Monk-Gillieson)	60 - 800 eV	Gas Liquid Solid	Absorption Photoemission Photon-emission	N. Kosugi kosugi@ims.ac.jp
BL3B	2.5-m off-plane Eagle	1.7 - 30 eV	Solid	Reflection Absorption	M. Hasumoto hasumoto@ims.ac.jp
BL4U	Varied-line-spacing plane grating (Monk-Gillieson)	130 - 700 eV	Gas Liquid Solid	Absorption (Microscopy)	T. Ohigashi ohigashi@ims.ac.jp
BL4B	Varied-line-spacing plane grating (Monk-Gillieson)	25 eV - 1 keV	Gas Solid	Photoionization Photodissociation Photoemission	E. Shigemasa sigemasa@ims.ac.jp
BL5U	Spherical grating (SGM-TRAIN†)	5 - 250 eV	Solid	Photoemission	M. Sakai sakai@ims.ac.jp
BL5B	Plane grating	6 - 600 eV	Solid	Calibration Absorption	M. Hasumoto hasumoto@ims.ac.jp
BL6U*	Variable-included-angle varied-line-spacing plane grating	30 - 500 eV	Gas Solid	Photoionization Photodissociation Photoemission	E. Shigemasa sigemasa@ims.ac.jp
BL6B	Michelson FT-IR	3 meV - 2.5 eV	Solid	Reflection Absorption	S. Kimura kimura@ims.ac.jp
BL7U	10-m normal incidence (modified Wadsworth)	6 - 40 eV	Solid	Photoemission	M. Matsunami matunami@ims.ac.jp
BL7B	3-m normal incidence	1.2 - 25 eV	Solid	Reflection Absorption	M. Hasumoto hasumoto@ims.ac.jp
BL8B	Plane grating	1.9 - 150 eV	Solid	Photoemission	S. Kimura kimura@ims.ac.jp

Yellow columns represent undulator beamlines.
* In-house beamline.
† Spherical grating monochromator with translating and rotating assembly including normal incidence mount.

BL1U

Free Electron Laser

The free electron laser (FEL) at UVSOR-II is being moved to a dedicated long straight section (S1). The FEL is equipped with a variably polarized optical klystron of 3 m in length and an optical cavity of 13.3 m in length. By using various multilayer mirrors for the cavity, the FEL can provide coherent light in a wide wavelength range from 800 nm to 199 nm. The pulse duration is typically several tens of picoseconds. The repetition rate is approximately 11 MHz. The average output power depends on the wavelength but its typical value is several hundred milliwatts. Output power higher than 1 W was recorded at 230 nm and 570 nm. The FEL can be operated in top-up injection mode. Users can use the FEL for several hours with quasi-constant output power. The laser pulses are naturally synchronized with the synchrotron radiation pulses that are provided at other synchrotron radiation beamlines. The laser beam can be transported to the beamlines using a mirror system for pump and probe experiments if requested.
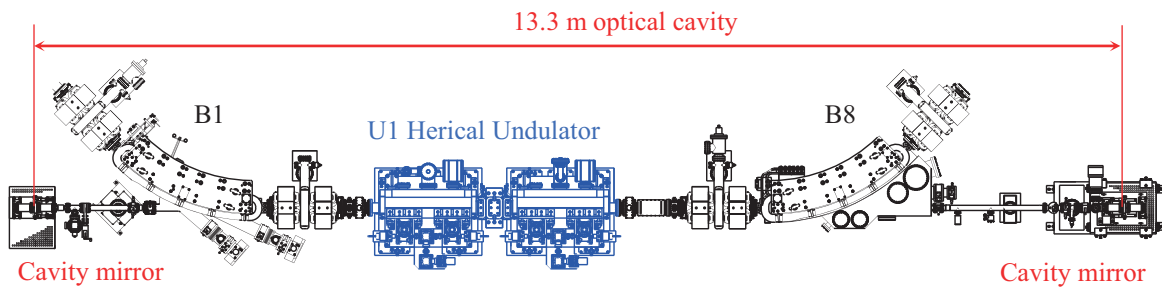
Fig. 1. Schematic of the 13.3 m-long optical cavity.
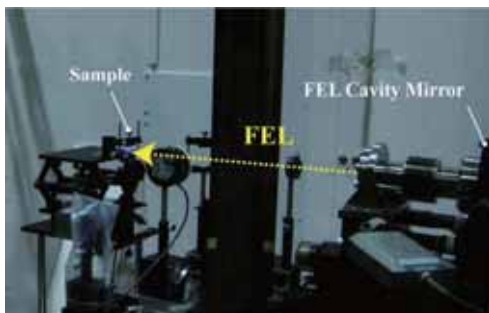
Fig. 2. Left and right circularly polarized FEL being delivered to B4 for an application experiment.
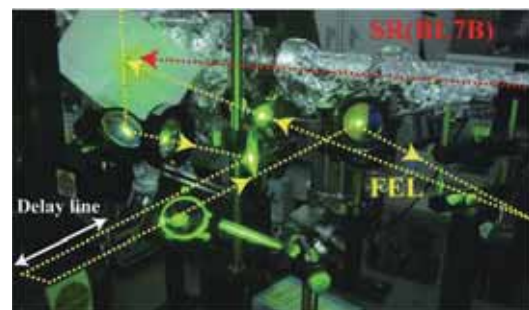
Fig. 3. The FEL is delivered to BL7B. The FEL is irradiated on a target simultaneously with the SR .

FEL Specifications

Wavelength	199-800 nm
Spectral band width	$\sim 10^{-4}$
Polarization	Circular/linear
Pulse rate	11.26 MHz
Max. average power	~ 1 W
Cavity type	Fabry-Perot
Cavity length	13.3 m
Cavity mirror	HfO_2, Ta_2O_5, Al_2O_3 multilayer

BL1B

Terahertz Spectroscopy Using Coherent Synchrotron Radiation

Coherent synchrotron radiation (CSR) is a powerful light source in the terahertz (THz) region. This beamline has been constructed for basic studies on the properties of THz-CSR. However, it can be also used for measurements of reflectivity and transmission spectra of solids using conventional synchrotron radiation.

The emitted THz light is collected by a three-dimensional magic mirror (3D-MM, M0) of the same type as those already successfully installed at BL43IR in SPring-8 and BL6B in UVSOR-III. The 3D-MM was installed in bending-magnet chamber #1 and is controlled by a 5-axis pulse motor stage (x, z translation; θ_x, θ_y, θ_z rotation). The acceptance angle was set at 17.5-34 degrees (total 288 mrad) in the horizontal direction. The vertical angle was set at ±40 mrad to collect the widely expanded THz-CSR.

The beamline is equipped with a Martin-Puplett type interferometer (JASCO FARIS-1) to cover the THz spectral region from 4 to 240 cm^{-1} ($h\nu$ = 500 μeV-30 meV). There is a reflection/absorption spectroscopy (RAS) end-station for large samples (~ several mm). At the RAS end-station, a liquid-helium-flow type cryostat with a minimum temperature of 4 K is installed.
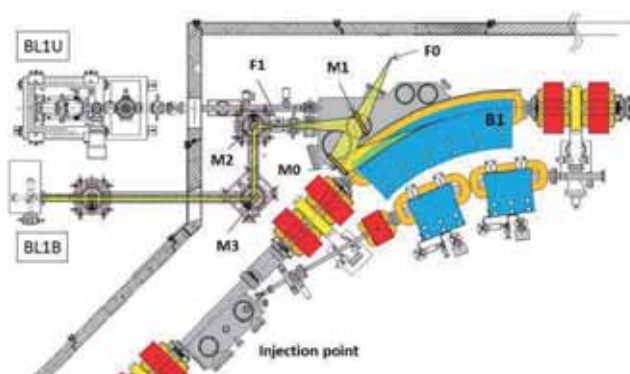
Fig. 1. Schematic top view of the beam extraction part of the THz-CSR beamline, BL1B. The three-dimensional magic mirror (3D-MM, M0) and a plane mirror (M1) are located in the bending-magnet chamber. A parabolic mirror (M2) is installed to form a parallel beam. The straight section (BL1U) is used for coherent harmonic generation (CHG) in the VUV region.
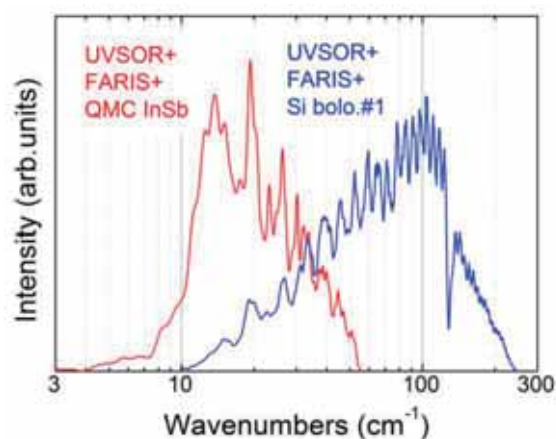
Fig. 2. Obtained intensity spectra with the combination of a light source (UVSOR), interferometer (FARIS-1), and detectors (Si bolometer and InSb hot-electron bolometer).

Beamline Specifications

Interferometer	Martin-Puplett (JASCO FARIS-1)
Wavenumber range (Energy range)	4-240 cm^{-1} (500 μeV-30 meV)
Resolution in cm^{-1}	0.25 cm^{-1}
Experiments	Reflection/transmission spectroscopy
Miscellaneous	Users can use their experimental system in this beamline.

BL2A

Soft X-Ray Beamline for Photoabsorption Spectroscopy

   BL2A, which was moved its previous location as BL1A in 2011, is a soft X-ray beamline for photoabsorption spectroscopy.   The beamline is equipped with a focusing premirror and a double-crystal monochromator [1]. The monochromator serves soft X-rays in the energy region from 585 to 4000 eV using several types of single crystals, such as β-Al_2O_3, beryl, KTP ($KTiOPO_4$), quartz, InSb, and Ge. The throughput spectra measured using a Si photodiode (AXUV-100, IRD Inc.) are shown in Fig. 1. The typical energy resolution (E / ΔE) of the monochromator is approximately 1500 for beryl and InSb. There are no experimental setups that are specific to this beamline, except for a small vacuum chamber equipped with an electron multiplier (EM) detector. Photoabsorption spectra for powdery samples are usually measured in total electron yield mode, with the use of the EM detector.

[1] Hiraya *et al.*, Rev. Sci. Instrum. **63** (1992) 1264.
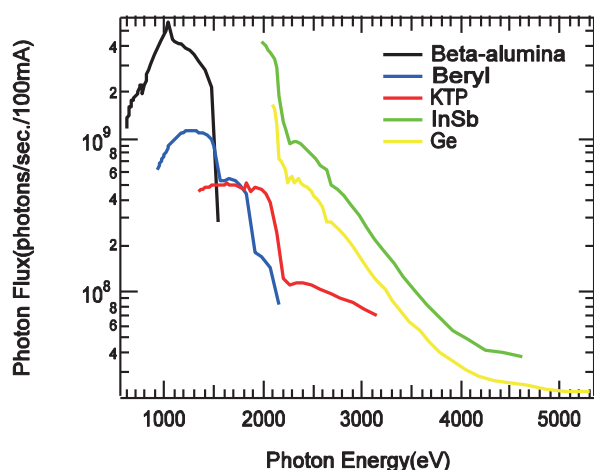
Fig. 1. Throughput spectra of the double-crystal monochromator at BL2A.

Fig. 2. Side view of BL2A.

Beamline Specifications

Monochromator	Double crystal monochromator
Monochromator crystals: (2d value, energy range)	β-Al_2O_3 (22.53 Å, 585–1609 eV), beryl (15.965 Å, 826–2271 eV), KTP (10.95 Å, 1205–3310 eV), quartz (8.512 Å, 1550–4000 eV), InSb (7.481 Å, 1764–4000 eV), Ge (6.532 Å, 2094–4000 eV)
Resolution	$E/\Delta E$ = 1500 for beryl and InSb
Experiments	Photoabsorption spectroscopy

BL2B

Beamline for Gas Phase Photoionization and Reaction Dynamics

This beamline has been developed to study ionization, excitation, and decay dynamics involving inner-valence electrons, $2p$ electrons of the third row atoms, and 4d electrons of the lanthanides. The monochromator is a spherical grating Dragon type with 18-m focal length. High throughput (1×10^{10} photons s^{-1}) and high resolution ($E/\Delta E$ = 2000 - 8000) are achieved simultaneously under the condition of the ring current of 100 mA [1]. The optical system consists of two pre-focusing mirrors, an entrance slit, three spherical gratings (G1 - G3), two folding mirrors, a movable exit slit, and a refocusing mirror [2]. The monochromator is designed to cover the energy range of 23–205 eV with the three gratings: G1 (2400 lines mm^{-1}, R = 18 m) at 80–205 eV; G2 (1200 lines mm^{-1}, R = 18 m) at 40–100 eV; G3 (2400 lines mm^{-1}, R = 9.25 m) at 23–50 eV. The percentage of the second-order light contamination at $h\nu$ = 45.6 eV is 23% for G2 or 7% for G3.

We have been measuring the yield curves of various fullerene ions [3]. Geometrical structures and electronic properties of fullerenes have attracted widespread attention because of their novel structures, novel reactivity, and novel catalytic behaviors as typical nanometer-size materials. However, spectroscopic information was very limited in the extreme UV region, owing to difficulties in acquiring sufficient sample amounts. This situation has rapidly changed since the start of this century, because the techniques related to syntheses, isolation, and purification have advanced so rapidly that an appreciable amount of fullerenes can now be readily obtained.

[1] M. Ono, H. Yoshida, H. Hattori and K. Mitsuke, Nucl. Instrum. Meth. Phys. Res. A **467-468** (2001) 577.
[2] H. Yoshida and K. Mitsuke, J. Synchrotron Radiation **5** (1998) 774.
[3] J. Kou, T. Mori, Y. Kubozono and K. Mitsuke, Phys. Chem. Chem. Phys. **7** (2005) 119.
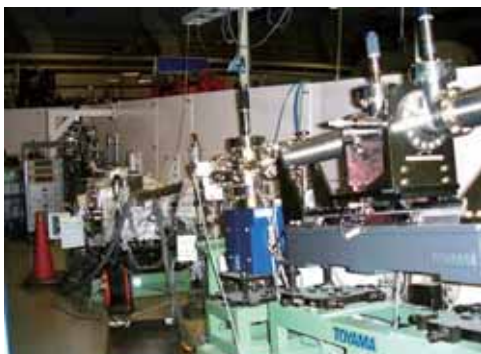
Fig. 1. 18 m spherical grating monochromator at BL2B.

Fig. 2. End station of BL2B for gas phase spectroscopy of refractory materials.

Beamline Specifications

Monochromator	18 m spherical grating Dragon-type
Wavelength Range	6-55 nm; 24-205 eV
Resolution	2000–8000 depending on the gratings
Experiments	Mass spectrom.; photoelectron spectrosc.; momentum imaging spectrosc.; e$^-$-ion coincidence spectrosc.; fullerene beam source

BL3U

Varied-Line-Spacing Plane Grating Monochromator for Molecular Soft X-Ray Spectroscopy

The beamline BL3U is equipped with an in-vacuum undulator composed of 50 periods of 3.8 cm period length. The emitted photons are monochromatized by the varied-line-spacing plane grating monochromator (VLS-PGM) designed for various spectroscopic investigations in the soft X-ray range including soft X-ray emission studies. Three holographically ruled laminar profile plane gratings are designed to cover the photon energy range from 60 to 800 eV. The beamline has two endstations, namely, XES setup and multi-purpose setup. The XES setup is used for soft X-ray emission spectroscopy. The beam is horizontally focused onto the sample position by a plane-elliptical mirror, M2X. In the multi-purpose setup, the beam is focused by the toroidal mirror M2. Between the sample position and M2, the differential pumping is placed.
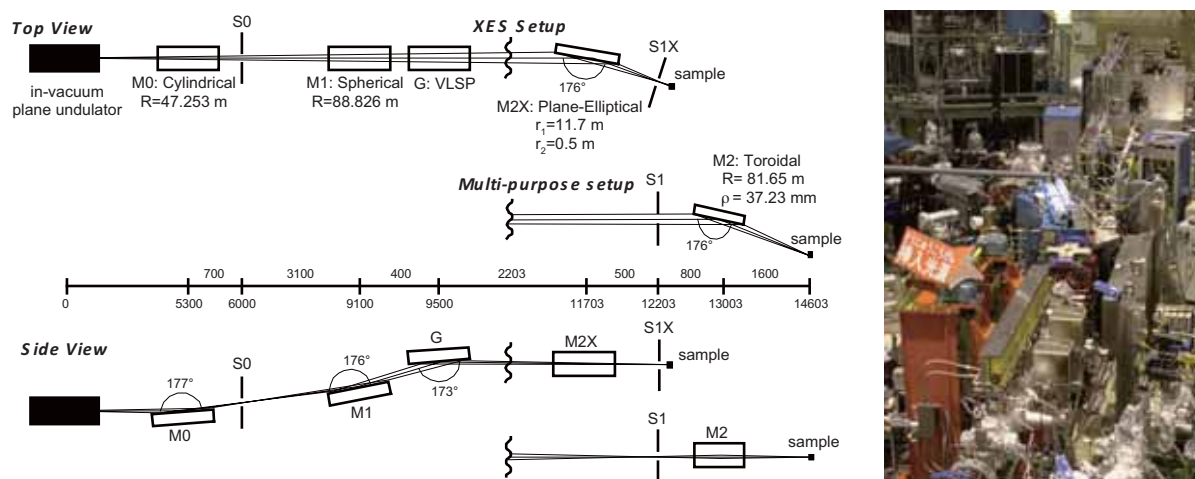
Fig. 1. Schematic layout (left) and the photography (right) of the BL3U. The distances along the beam from the center of the in-vacuum plane undulator are shown in millimeters. S1X and M2X can be replaced with the other exit slit S1 so that experiments can be carried out at either the XES or the multipurpose endstation. In the XES setup, the sample is placed 5–10 mm downstream of S1X.

Beamline Specifications

Monochromator	Varied-line-spacing plane grating monochromator
Energy Range	60-800 eV
Resolution	$E / \Delta E > 10\ 000$
Experiments	Soft X-ray spectroscopy (XPS, XES, XAS)
Beam Size (XES Endstation)	Gaussian shape Vertical 5-20 μm; Horizontal 41 μm (FWHM)

BL3B (HOTRLU)

VIS-VUV Photoluminescence and Reflection/Absorption Spectroscopy

BL3B has been constructed to study photoluminescence (PL) in the visible (VIS) to vacuum ultraviolet (VUV) region. This beamline consists of a 2.5 m off-plane Eagle type normal-incidence monochromator, which covers the VUV, UV, and VIS regions, i.e., the energy (wavelength) region of 1.7-31 eV (40-730 nm), with three spherical gratings having constant grooving densities of 1200, 600, and 300 l/mm optimized at the photon energies of ~20, ~16, and ~6 eV, respectively. The schematic side view and top view layouts are shown in Figs. 1(a) and 1(b), respectively. The FWHM of the beam spot at the sample position is 0.25 mm (V) × 0.75 mm (H). Low energy pass filters (LiF, quartz, WG32, OG53) can be inserted automatically to maintain the optical purity in the G3 (300 l/mm) grating region (1.7~11.8 eV). Figure 2 shows the throughput spectra (photon numbers at a beam current of 300 mA) for each grating with entrance and exit slit openings of 0.1 mm (resolving power E / ΔE of ~2000 (G3, ~6.8 eV)). Since both slits can be opened up to 0.5 mm, a monochromatized photon flux of 10^{10} photons/s or higher is available for PL measurements in the whole energy region.

The end station is equipped with a liquid-helium-flow type cryostat for sample cooling and two detectors; one of which is a photomultiplier with sodium salicylate and the other a Si photodiode for reflection/absorption measurement. For the PL measurements in the wide energy region from VIS to VUV, two PL monochromators, comprising not only a conventional VIS monochromator but also a VUV monochromator with a CCD detector, are installed at the end station.
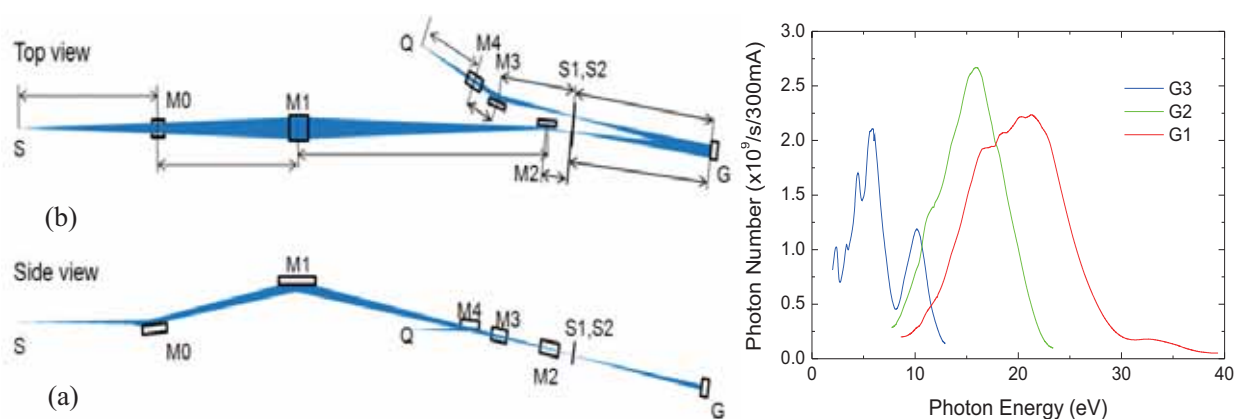
Fig. 1. Schematic layout of the BL3B (a) side view and (b) top view.

Fig. 2. Throughput spectra for each grating (G1:1200 l/mm, G2:600 l/mm and G3:300 l/mm) with S1 = S2 = 0.1 mm.

Beamline Specifications

Monochromator	-2.5 m normal-incidence monochromator
Energy range	1.7-31 eV (40~730 nm)
Resolution ($\Delta h\nu/ h\nu$)	≥ 12000 (at ~ 6.9 eV, 0.02 mm slits, G1 (1200 l/mm)
Experiments	Photoluminescence, reflection, and absorption spectroscopy, mainly for solids

BL4U

Scanning Transmission X-ray Microscopy in the Soft X-ray Region

In the soft x-ray region, there are several absorption edges of light elements and transition metals. The near edge X-ray absorption fine structure (NEXAFS) brings detailed information about the chemical state of target elements. A scanning transmission X-ray microscope (STXM) in the soft X-ray region is a kind of extended technique of the NEXAFS with high spatial resolution. The STXM has a capability of several additional options, for example, in-situ observations, 3-dimensional observation by computed tomography and ptychography, by utilizing the characteristics of the X-rays. The STXM can be applied to several sciences, such as polymer science, material science, cell biology, environmental science, and so on.

This beamline equips an in-vacuum undulator, a varied-line-spacing plane grating monochromator and a fixed exit slit. The soft X-ray energy range from 130 to 700 eV with the resolving power (E/ΔE) of 6,000 (as of March 2013) is available. The aperture size of the fixed exit slit determines not only the resolving power but also the size of a microprobe. A Fresnel zone plate is used as a focusing optical device through an order select aperture and its focal spot size of ~30 nm (as of March 2013) is available at minimum. An image is acquired by detecting intensities of the transmitted X-rays by a photomultiplier tube with scintillator with scanning a sample 2-dimensionally. By changing the energy of the incident beam, each 2-dimensional NEXAFS image is stacked. A main chamber of STXM is separated from the beamline optics by a silicon nitride membrane of 100-nm thickness; therefore, sample folders can be handled in vacuum or in helium.
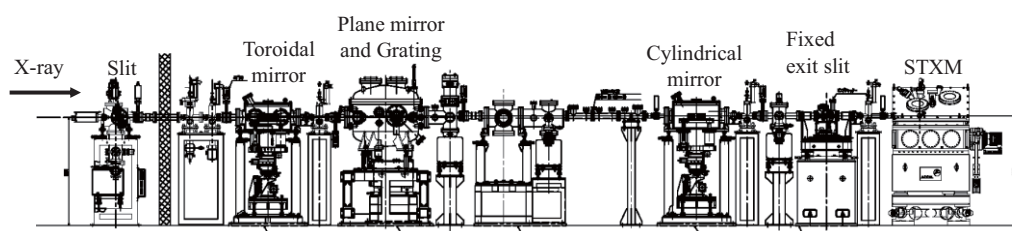
Fig. 1. Schematic image of the STXM beamline, BL4U.
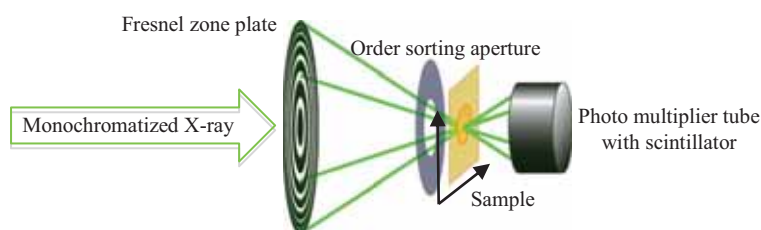
Fig. 2. Schematic image of the STXM.

Beamline Specifications

Energy range (E)	130 -700 eV
Resolving power (E/ΔE)	~6000
Focusing optical element	Fresnel zone plate
Spatial resolution	~30 nm
Experiments	2-dimensinal absorption spectroscopy
Measurement environment	standard sample folder in vacuum or in helium, specially designed sample cell in ambient condition

BL4B

Varied-Line-Spacing Plane Grating Monochromator for Molecular Soft X-Ray Spectroscopy

The beamline BL4B equipped with a varied-line-spacing plane grating monochromator (VLS-PGM) was constructed for various spectroscopic investigations in a gas phase and/or on solids in the soft X-ray range. Three holographically ruled laminar profile plane gratings with SiO_2 substrates are designed to cover the photon energy range from 25 to 800 eV. The gratings with groove densities of 100, 267, and 800 l/mm cover the spectral ranges of 25–100, 60–300, and 200-1000 eV, respectively, and are interchangeable without breaking the vacuum. Fig. 1 shows the absolute photon flux for each grating measured using a Si photodiode (IRD Inc.), with the entrance- and exit-slit openings set at 50 and 50 μm, respectively. The maximum resolving power ($E/\Delta E$) achieved for each grating exceeds 5000.
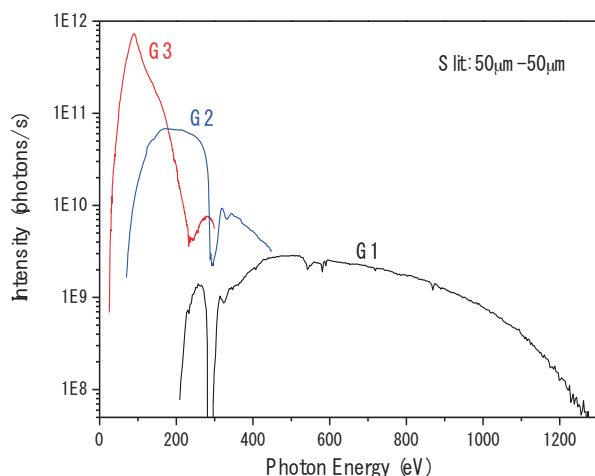
Fig. 1. Throughput from the VLS-PGM monochromator on BL4B.

Fig. 2. Photo of BL4B.

Beamline Specifications

Monochromator	Varied-line-spacing Plane Grating Monochromator
Energy range	25-1000 eV
Resolution	$E / \Delta E$ > 5000 (at maximum)
Experiments	Soft X-ray spectroscopy (mainly, angle-resolved photoion spectroscopy for gaseous targets and photoelectron spectroscopy for gaseous and solid targets)

BL5U

Photoemission Spectroscopy of Solids and Surfaces

This beamline is designed for high-resolution angle-resolved photoemission study of solids and surfaces with horizontal-linearly and circularly (CW, CCW) polarized synchrotron radiation from a helical undulator. The beamline consists of a Spherical Grating Monochromator with a Translational and Rotational Assembly Including a Normal incidence mount (SGM-TRAIN) and a high-resolution angle-resolved photoemission spectrometer.

The SGM-TRAIN is an improved version of a constant-length SGM that aims at realizing the following points: (1) covering the wide energy range of 5–250 eV, (2) high energy resolving power, (3) use of linearly and circularly polarized undulator light, (4) reduction of higher-order light, and (5) two driving modes (rotation and translation of gratings) by computer control. The second-order light is well suppressed using laminar profile gratings and combinations of mirrors and gratings.
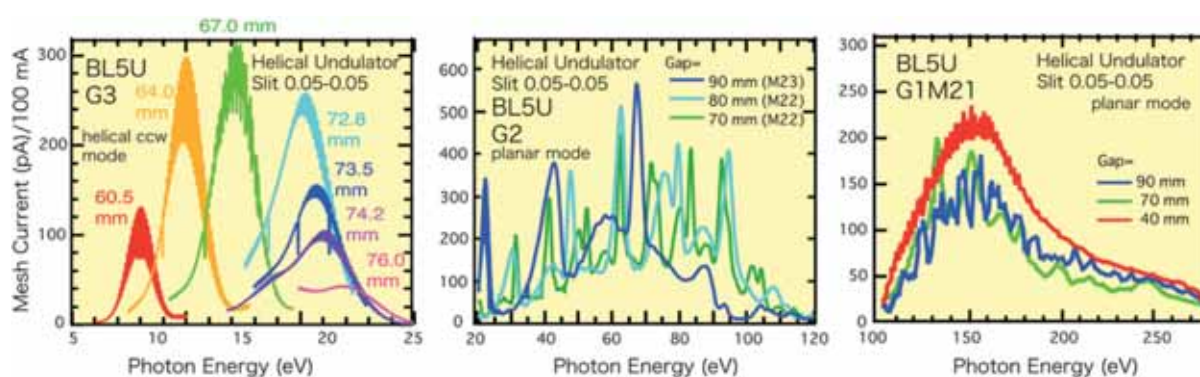
Fig. 1. Throughput spectra from the SGM-TRAIN monochromator at BL5U.

Beamline Specifications

Monochromator	SGM-TRAIN
Energy Range	5-250 eV
Resolution	$h\nu / \Delta E > 2{,}000$ for < 40 μm slits
Experiment	ARPES, AIPES, XAS
Flux	$<10^{11}$ photons/s for <40 μm slits (in the sample position)
Main Instruments	Hemispherical photoelectron analyzer (MBS-Toyama 'Peter' A-1), LEED of reverse type (OMICRON), Liq-He flow cryostat (5-400 K)
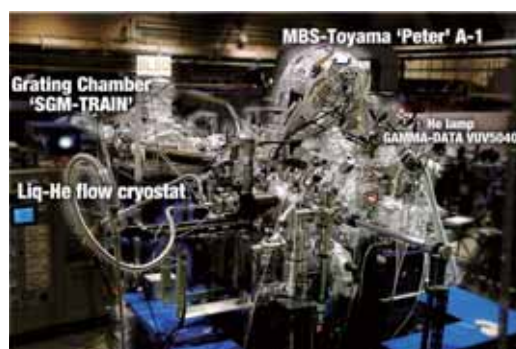
Fig. 2. High-resolution angle-resolved photoemission apparatus at BL5U.

BL5B

Calibration Apparatus for Optical Elements and Detectors

BL5B has been constructed to perform calibration measurements for optical elements and detectors. This beamline is composed of a plane grating monochromator (PGM) and three endstations in tandem. The most upstream station is used for the calibration measurements of optical elements, the middle one for optical measurements for solids, and the last for photo-stimulated desorption experiments. The experimental chamber at the most downstream station is sometimes changed to a chamber for photoemission spectroscopy. The calibration chamber shown in Fig. 2 is equipped with a goniometer for the characterization of optical elements, which has six degrees of freedom, X-Y translation of a sample, and interchanging of samples and filters. These are driven by pulse motors in vacuum. Because the polarization of synchrotron radiation is essential for such measurements, the rotation axis can be made in either the horizontal or vertical direction (s- or p-polarization).
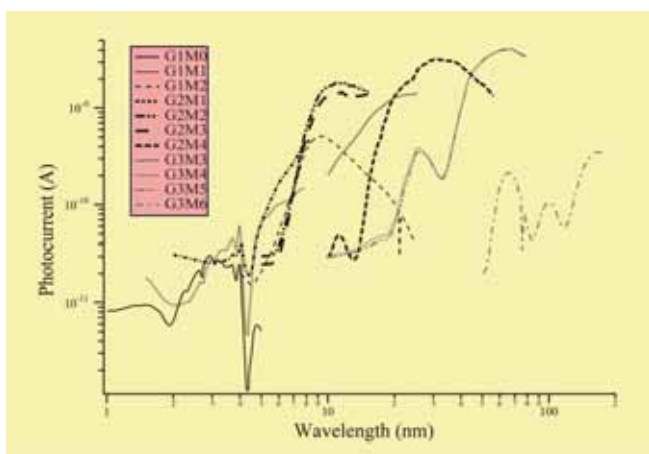
Fig. 1. Throughput spectra for possible combinations of gratings and mirrors at BL5B measured by a gold mesh.
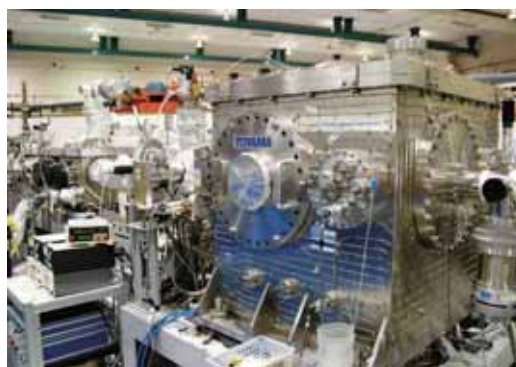
Fig. 2. A side view of the experimental chamber for calibration measurements.

Beamline Specifications

Monochromator	Plane Grating Monochromator
Energy range	6-600 eV (2-200 nm)
Resolution	$E / \Delta E \sim 500$
Experiments	Calibration of optical elements, absorption of solids, photo-stimulated desorption from rare-gas solids

BL6U

Variable-Included-Angle VLS-PGM for Molecular Soft X-Ray Spectroscopy

The beamline BL6U equipped with a variable-included-angle Monk-Gillieson mounting monochromator with a varied-line-spacing plane grating was constructed for various spectroscopic investigations requiring high-brilliance soft X-rays in a gas phase and/or on solids. Through a combination of undulator radiation and sophisticated monochromator design (entrance slit-less configuration and variable-included-angle mechanism), using a single grating, the monochromator can cover the photon energy ranging from 30 to 500 eV, with resolving power of greater than 10000 and photon flux of more than 10^{10} photons/s. Figure 1 shows an example of the monochromator throughput spectra measured using a Si photodiode, with the exit-slit opening set at 30 μm, which corresponds to the theoretical resolving power of 10000 at 80 eV.
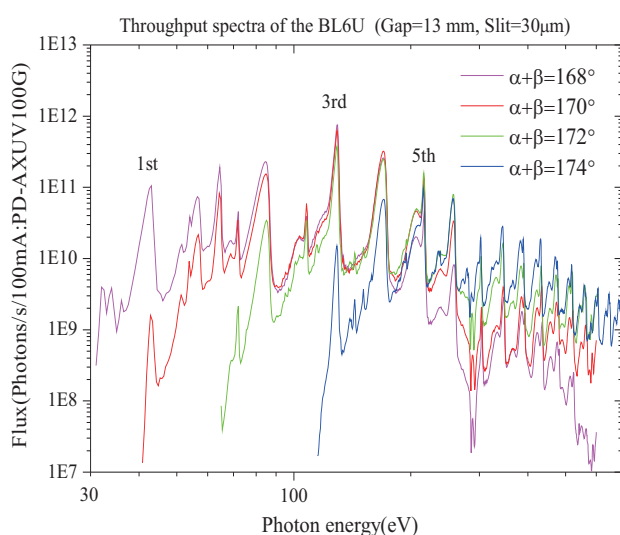
Fig. 1. Throughput spectra of the BL6U monochromator at various included angles.

Fig. 2. Photo of BL6U.

Beamline Specifications

Monochromator	Variable-included-angle Varied-line-spacing Plane Grating Monochromator
Energy range	40-500 eV
Resolution	$E / \Delta E > 10000$ (at maximum)
Experiments	High-resolution soft X-ray spectroscopy (mainly photoelectron spectroscopy for gaseous and solid targets)

BL6B

Infrared and Terahertz Spectroscopy of Solids

Synchrotron radiation (SR) has good performance (high brilliance and high flux) not only in the VUV and soft X-ray (SX) regions but also in the infrared (IR) and THz regions. BL6B covers the IR and THz regions. The previous beamline, BL6A1, which was constructed in 1985, was the pioneer in IRSR research. The beamline was deactivated at the end of FY2003 and a new IR/THz beamline, BL6B (IR), was constructed in FY2004. The front-end part including bending duct #6 was replaced with a new part having a higher acceptance angle (215 (H) $\times$ 80 (V) mrad^2) using a magic mirror, as shown in Fig. 1 [1].

The beamline is equipped with a Michelson type (Bruker Vertex70v) interferometer to cover a wide spectral region from 30 to 20,000 cm^{-1} ($h\nu$ = 4 meV-2.5 eV), as shown in Fig. 2. There are two end-stations; one for reflection/absorption spectroscopy (RAS) of large samples (up to several mm) and the other for IR/THz microscopy (transmission microscopy: TM) of tiny samples (up to several tens of μm). At the RAS end-station, a liquid-helium-flow type cryostat with a minimum temperature of 10 K is installed. At the TM end-station, pressure- and temperature-dependent THz spectroscopy can be performed. A superconducting magnet with a maximum field of 6 T can be installed by the exchange with the TM end-station.

[1] S. Kimura, E. Nakamura, T. Nishi, Y. Sakurai, K. Hayashi, J. Yamazaki, M. Katoh, "Infrared and terahertz spectromicroscopy beam line BL6B(IR) at UVSOR-II," Infrared Phys. Tech. **49** (2006) 147.
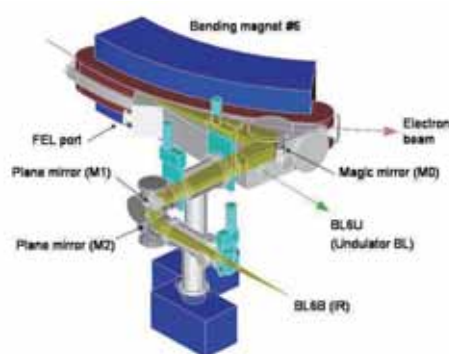
Fig. 1. Design of the optics and front end of BL6B.
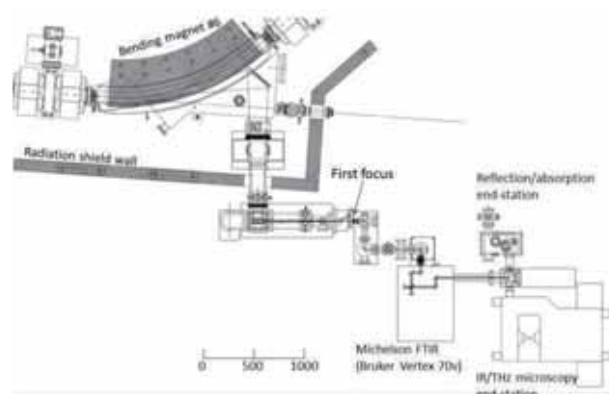
Fig. 2. Schematic top view of BL6B.

Beamline Specifications

Interferometer	Michelson (Bruker Vertex70v)
Wavenumber Range (Energy range)	30-20,000 cm^{-1} (4 meV-2.5 eV)
Resolution in cm^{-1}	0.1cm^{-1}
Experiments	Reflectivity and transmission Microspectroscopy Magneto-optics
Miscellaneous	Users can use their experimental system in this beamline.

BL7U (SAMRAI)

Angle-Resolved Photoemission of Solids in the VUV Region

Beamline 7U, named the Symmetry- And Momentum-Resolved electronic structure Analysis Instrument (SAMRAI) for functional materials, was constructed to provide a photon flux with high energy resolution and high flux mainly for high-resolution angle-resolved photoemission spectroscopy of solids [1]. An APPLE-II-type variable-polarization undulator is installed as the light source. The undulator can produce intense VUV light with horizontal/vertical linear and right/left circular polarization. The undulator light is monochromatized by a modified Wadsworth type monochromator with three gratings (10 m radius; 1200, 2400, and 3600 lines/mm optimized at $h\nu = 10, 20$, and 33 eV). The energy resolution of the light ($h\nu / \Delta h\nu$) is more than 10^4 with a photon flux of 10^{11}-10^{12} ph/s or higher on samples in the entire energy region.

The beamline has a photoemission end-station equipped with a 200 mm-radius hemispherical photoelectron analyzer (MB Scientific AB, A-l analyzer) with a wide-angle electron lens and a liquid-helium-cooled cryostat with 6-axis pulse motor control (AVC Co., Ltd., i-GONIO). The main function of the beamline is to determine the three-dimensional Fermi surface and electronic structure of solids at low temperatures and their temperature dependence in order to reveal the origin of their physical properties.

[1] S. Kimura, T. Ito, M. Sakai, E. Nakamura, N. Kondo, K. Hayashi, T. Horigome, M. Hosaka, M. Katoh, T. Goto, T. Ejima, K. Soda, "SAMRAI: A variably polarized angle-resolved photoemission beamline in the VUV region at UVSOR-II," Rev. Sci. Instrum. **81** (2010) 053104.
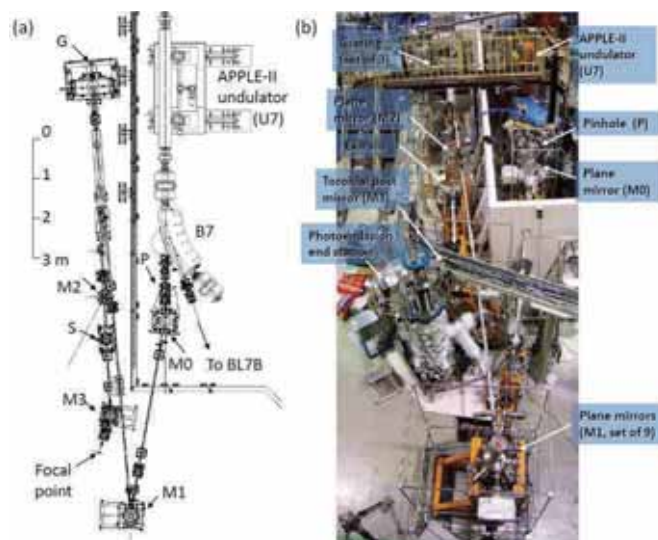
Fig. 1. Layout (a) and photograph (b) of the SAMRAI beamline consisting of an APPLE-II type undulator (U7), a modified Wadsworth type monochromator (M0-S), and a high-resolution photoemission analyzer at the focal point. The monochromator has five major optical components: two plane mirrors (M0 and M1) with water cooling, one set of three spherical gratings (G), an exit slit (S), and one toroidal refocusing mirror (M3). The spherical gratings have a radius of 10 m and are located 22 m from the center of the undulator. There is no entrance slit. S is located 6.47 m from G. A second branch for a VUV microscope end-station is planned to be constructed after the plane mirror (M2) located between G and S.

Beamline Specifications

Light source	APPLE-II type undulator ($\lambda_u = 76$ mm, $N = 36$) vertical/horizontal linear, right/left circular
Monochromator	10 m normal-incidence monochromator (modified Wadsworth type)
Photon energy range	6~40 eV ($\lambda = 30$~200 nm)
Resolution ($h\nu/\Delta h\nu$)	1×10^4-5×10^4
Photon flux on sample	$\geq 10^{12}$-10^{11} ph/s (depending on $h\nu$)
Beam size on sample	200 (H) $\times$ 50 (V) μm^2
Experiments	Angle-resolved photoemission of solids (MB Scientific A-1 analyzer, acceptance angle: $\pm$ 18 deg)

BL7B

3 m Normal-Incidence Monochromator for Solid-State Spectroscopy

BL7B has been constructed to provide sufficiently high resolution for conventional solid-state spectroscopy, sufficient intensity for luminescence measurements, wide wavelength coverage for Kramers–Kronig analyses, and minimum deformation to the polarization characteristic of incident synchrotron radiation. This beamline consists of a 3-m normal incidence monochromator, which covers the vacuum ultraviolet, ultraviolet, visible, and infrared, i.e., the wavelength region of 40–1000 nm, with three gratings (1200, 600, and 300 l/mm). Two interchangeable refocusing mirrors provide two different focusing positions. For the mirror with the longer focal length, an LiF or a MgF_2 window valve can be installed between the end valve of the beamline and the focusing position. Fig.1 shows the absolute photon intensity for each grating with the entrance and exit slit openings of 0.5 mm. A silicon photodiode (AXUV-100, IRD Inc.) was utilized to measure the photon intensity and the absolute photon flux was estimated, taking the quantum efficiency of the photodiode into account.
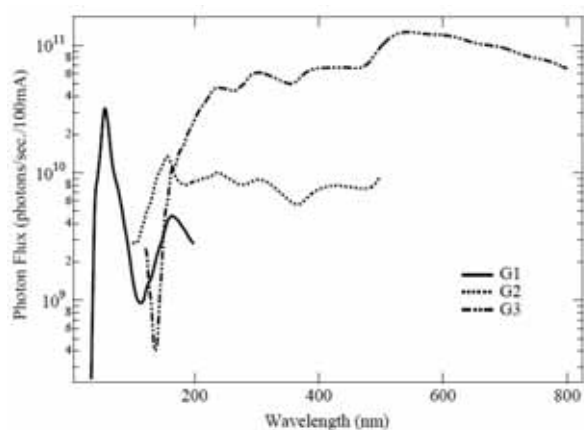
Fig. 1. Throughput spectra of BL7B measured using a silicon photodiode.

Fig. 2. Photo of BL7B.

Beamline Specifications

Monochromator	3 m Normal-Incidence Monochromator
Wavelength Range	50-1000 nm (1.2-25 eV)
Resolution	$E / \Delta E$ = 4000-8000 for 0.01 mm slits
Experiments	Absorption, reflection, and fluorescence spectroscopy, mainly for solids

BL8B

Angle-Resolved Ultraviolet Photoelectron Spectrometer for Solids

BL8B is a beamline for the angle-resolved ultraviolet photoemission spectroscopy (ARUPS) system, which is designed to measure various organic solids such as molecular crystals, organic semiconductors, and conducting polymers. This beamline consists of a plane-grating monochromator (PGM), a sample preparation chamber with a fast-entry load-lock chamber, a measurement chamber (base pressure 1×10^{-10} Torr), a cleaning chamber (base pressure 1×10^{-10} Torr), and a sample evaporation chamber (base pressure 3×10^{-10} Torr). The cleaning chamber is equipped with a back-view LEED/AUGER, an ion gun for Ar^+ sputtering, and an infrared heating unit. The PGM consists of premirrors, a plane grating, focusing mirror, and a post-mirror, with an exit slit. It covers the wide range from 2 to 130 eV with two exchanging gratings (G1: 1200 l/mm, G2: 450 l/mm) and five cylindrical mirrors. The toroidal mirror focuses the divergent radiation onto the sample in the measurement chamber. The spot size of the zeroth-order visible light at the sample surface is approximately 1×1 mm^2. Figure 1 shows the throughput spectra of PGM (slit = 100 μm). The energy resolution at a slit width of 100 μm was found to be $E/\Delta E = 1000$ in the wavelength range from 2 to 130 eV. A hemispherical electron energy analyzer of 75 mm mean radius with an angular resolution less than 2° can be rotated around the vertical and horizontal axes. The sample mounted on a manipulator (temperature range 14–320 K) can also be rotated around two axes.
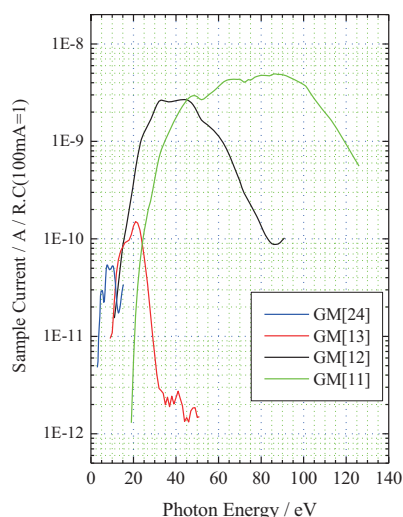
Fig. 1. Throughput spectra of plane-grating monochromator at BL8B (slit = 100 μm).

Fig. 2. A photo of BL8B.

Beamline Specifications

Monochromator	Plane-grating monochromator
Wavelength Range	9-600 nm
Resolution	$E / \Delta E = 1000$
Experiments	Angle-resolved ultraviolet photoemission spectroscopy

Development of Pulse Duration Measurement System for Coherent Harmonic Generation Experiments

H. Zen[1], M. Adachi[2,3], S. Tanaka[2] and M. Katoh[2,3]

[1]Institute of Advanced Energy, Kyoto University, Gokasho, Uji, Kyoto 611-0011, Japan
[2]UVSOR Facility, Institute for Molecular Science, Okazaki 444-8585, Japan
[3]The Graduate University for Advanced Studies (SOKENDAI), Okazaki 444-8585, Japan

The Coherent Harmonic Generation (CHG) from relativistic electron beam through the interaction with high power laser is promising way to generate short pulse EUV coherent radiation [1]. However, saturation limits the number of photon in a pulse [2]. In conventional laser, Chirped Pulse Amplification (CPA) technique is commonly used to avoid damage or saturation and to obtain high power laser beam. We proposed utilization of CPA to CHG technique to overcome the saturation problem [3].

We are planning to make proof of principle experiment at the wavelength of 266 nm which corresponds to the 3rd harmonics of Ti-sapphire laser. For the experiment, we need a pulse duration measurement system and an UV pulse compressor.

In this fiscal year, we have designed and developed the pulse duration measurement system. We selected an optical cross correlation as the way to measure the UV pulse duration, since 150-fs Ti-sapphire laser is available in UVSOR for the pump beam of cross correlation. Figure 1 shows the schematic diagram of pulse duration measurement system. Fundamental of Ti-sapphire laser (800 nm) and 266-nm radiation from CHG is focused together to BBO crystal which is optimized for Difference Frequency Generation (DFG). Then, 400-nm radiation is generated from DFG crystal when the fundamental and CHG radiation enter to the crystal at the same time. By measuring the dependence of the 400-nm radiation intensity on the time delay between the two pulses, we can measure the temporal profile of UV light. Figure 2 shows the photo of the developed pulse duration measurement system.

To check the properties of developed system, we generated UV laser beam from 800-nm laser beam (150 fs-FWHM) and 3rd harmonic generation crystals. Figure 3 shows the result of cross correlation measurement of the UV laser beam. The measured pulse duration was 0.8 ps in FWHM. This value is much longer than the expected pulse duration of UV laser beam (around 150 fs). Since we used DFG crystal of 2-mm thickness in this experiment to obtain larger signal, group velocity mismatch of 800-nm and 266-nm light in the crystal causes 0.75-ps slip of those pulses. Therefore, the measured result (0.8 ps, FWHM) indicates the temporal resolution of the developed system. This value is acceptable for the proof of principle experiment, because we will generate 10-100 ps UV radiation and compress it to

1 ps or shorter. Moreover, we are now planning to install thinner crystal (1 mm, 0.5 mm) to obtain better temporal resolution.
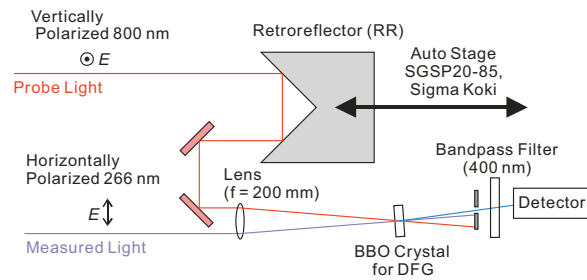

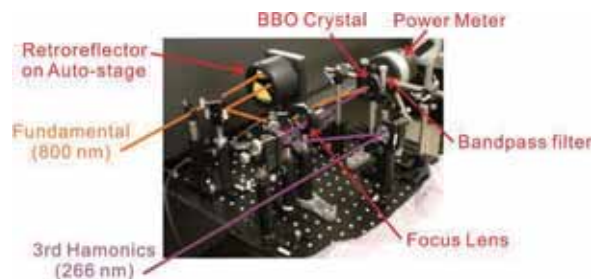Fig. 1. Schematic drawing of pulse duration measurement system.

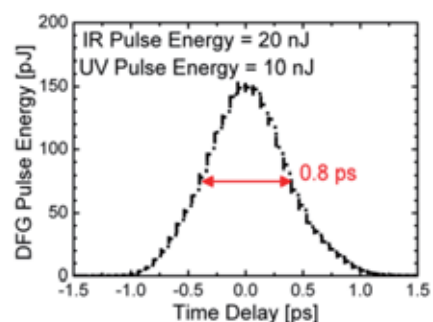Fig. 2. Photo of the developed pulse duration measurement system.

Fig. 3. Result of cross correlation measurement.

[1] R. Prazeres *et al.*, Nucl. Inst. Meth. A **304** (1991)72.
[2] T. Tanikawa *et al.*, Appl. Phys. Exp. **3** (2010) 2702.
[3] H. Zen *et al.*, Proc. of FEL2011 (2012) 366.

Development of an Electron Beam Bunch Length Measurement System for the Transmission-type Polarized Electron Source

N. Yamamoto [1], T. Niwa [2], T. Inagaki [2], M. Hosaka [1], A. Mano [1], Y. Takashima [2,1],
T. Konomi [3], M. Adachi [3], M. Katoh [3,1], K. Sakaue [4] and T. Takatomi [5]

[1] *Nagoya University Synchrotron Radiation Research Center, Nagoya, Aichi, 464-8603*
[2] *Graduate School of Engineering, Nagoya University, Nagoya, Aichi, 464-8603*
[3] *UVSOR Facility, Institute for Molecular Science (IMS), Okazaki, Aichi, 444-8585*
[4] *Research Institute for Science and Engineering, Waseda University (RISE), Tokyo, 169-8555*
[5] *High Energy Accelerator Research Organization (KEK), Ibaraki, 305-0801*

Spin polarized electron sources are expected as electron sources for next high energy accelerators, such as the International Linear Accelerator (ILC). In the development of the transmission-type spin polarized electron sources, the electron spin polarization of ~90 % and he high beam brightness of $\sim 2 \times 10^7$ A.cm^{-2}.sr^{-1} were already achieved at Nagoya University [1, 2].

For the next step of the development, the time response of the transmission-type photocathode has to be characterized. Then we designed and manufactured an electron beam bunch length measurement system using a radio frequency (rf) deflecting cavity [3].

The system consisted of a laser injection system using a mode-locked Ti:Sapphire laser, an rf deflecting cavity and a beam profile monitor. The system was modified for 20-keV electron beams, which corresponds to the Lorentz factor β of 0.272. At low energy, the difference between velocities of rf waves and electron beams is important for designing the cavity structure. Concerning beam dynamics, stretching of bunch length due to space charge effect is also non - negligible.

Parameters of the deflecting cavity are shown in Table 1. The deflecting cavity is made of Oxygen-Free Copper and has one cell rectangular structure with six frequency tuners. Electron beams are deflected by magnetic field of TM120 mode in deflecting cavity. The resonance frequency is 2612.9 MHz that is 29 times of beam reputations (90.1 MHz). The longitudinal length was chosen to be 46.81 mm with consideration for beam deflecting efficiency. The deflecting efficiency is maximized when the longitudinal length is equal to the product of the rf half-wavelength and the Lorentz factor β.

Most of cavity designs are made by analytical calculation from Maxwell equations and a 3-D simulation cord ANSYS HFSS are also used for designs of rf input and monitor ports.

The fabrication and assembling of the cavity was made at Equipment Development Center of IMS and Mechanical Engineering Center of KEK. After them, a set of rf measurements was performed with an Agilent N5230A Network Analyzer. The frequency tuning range is 2.9 MHz from 2611.2 to 2614.1 MHz. The loaded and unloaded quality factors are 10,155 and 20,565 respectively and in good agreement with the calculation (only just 4% below). The gradient of magnetic field along with longitudinal direction was also measured by the bead-pull method and confirmed by the HFSS simulation.

The deflecting cavity and beam profile monitor were installed in the downstream of the polarized electron gun at UVSOR. The operation test by using 20-keV CW beams was done and it is demonstrated that the performances of the cavity are enough to deflect the 20-keV beams.

We are preparing the picosecond laser injection system for generation of pulsed electron beams. By using this system consisting of grating dispersion compensators and an 30m photonic crystal fiber, the laser pulse duration can be changed in the range of a few to several tens picoseconds.

In near future, the systematic measurements of the temporal response of electron sources are scheduled and the results will be feed backed for the photocathode developments to realize fast temporal response, highly brightness and highly spin polarized simultaneously.

Table 1. Parameters of the RF cavity

Size	
Width	121.01 mm
Height	129.98 mm
Longitudinal length	46.81 mm
Resonance mode	TM120
Resonance frequency	2612.9 MHz
Quality factor (Loaded)	10,155
Quality factor(Unloaded)	20,565
Input coupling factor	1.02
Magnetic field at 1 W	1.57 G (Max.)

[1] N. Yamamoto, T. Nakanishi *et al*., J. Appl. Phys. **103** (2008) 064905.
[2] X.G. Jin, N. Yamamoto *et al*., Appl. Phys. Ex. **1** (2008) 045002.
[3] T. Niwa, N. Yamamoto *et al*., Proc. of the 9th Annual Meeting of PASJ, pp. (2012) 1100.

Pulsed Sextupole Injection in UVSOR-III

Y. Hida[1], H. Zen[2], T. Konomi[3,4], N. Yamamoto[5], M. Adachi[3,4], M. Hosaka[5], K. Hayashi[3],
J. Yamazaki[3], Y. Takashima[1] and M. Katoh[3,4]

[1]*Graduate School of Engineering, Nagoya University, Nagoya, Aichi, 464-8603, Japan*
[2]*Institute of Advanced Energy, Kyoto University, Gokasho, Uji, Kyoto 611-0011, Japan*
[3]*UVSOR Facility, Institute for Molecular Science, Okazaki 444-8585, Japan*
[4]*The Graduate University for Advanced Studies (SOKENDAI), Okazaki 444-8585, Japan*
[5]*Nagoya University Synchrotron Radiation Research Center, Nagoya, Aichi, 464-8603, Japan*

Since 2010, the top-up injection of electron beam to storage ring has been started to keep the beam current almost constant during user experiments in UVSOR [1]. For the electron beam injection, we essentially require kicking the electron beam in horizontal direction and the kick induces betatron oscillation of electron beam. This oscillation disturbs user experiments and causes undesired spikes in measured data. To prevent this effect, beamline users are required to stop their measurement for ten seconds during the injection and for five seconds after the injection.

A new injection scheme called as pulsed multipole injection has been developed in KEK [2, 3]. We decided to introduce this scheme with pulsed sextupole magnet (PSM) to UVSOR to increase the efficiency of user experiments. Based on the numerical experiments, the PSM has been designed as Fig. 1 and fabricated as Fig. 2(a). The magnet was made of 0.2-mm-thick laminated silicon steel sheets to reduce eddy current effects. The coil is formed by a one-turn cupper bar with a diameter of 5 mm. Figure 2(b) shows the photo of PSM after installation to the UVSOR-III storage ring. The main specification of the designed PSM and its power supplies are summarized in Table 1.

Fig. 2. Photo of the manufactured sextupole magnet (a). Photo of the sextupole magnet after installation to the storage ring (b).

Table 1.   Specification of the sextupole magnet.

Sextupole Magnet	
Core Length	240 mm
Vertical Gap	45 mm
Horizontal Gap	136 mm
Inductance	2.15 μH
Power Supply	
Peak Excitation Current	2200 A
Pulse Width	1.3 μs

We have performed test experiments of electron beam injection with PSM. After optimization of horizontal and vertical tune of the UVSOR-III storage ring, we achieved maximum injection efficiency of 23% and electron beam injection up to 300 mA in multi-bunch filling (12 bunches in 16 RF buckets). We have already observed the drastic suppression of horizontal electron beam movement with PSM injection.

For further improvement of injection efficiency, the maximum excitation current will be increased and place of PSM will be moved.

Fig. 1. Geometry of designed sextupole magnet and magnetic flux lines calculated by Poisson.

[1] H. Zen *et al.*, Proc. of IPAC10 (2010) 2576.
[2] K. Harada *et al.*, Phys. Rev. ST Accel. Beams **10** (2007) 123501.
[3] H. Takagi *et al.*, Phys. Rev. ST Accel. Beams **13** (2010) 020705.

III-1. ACCELERATORS AND LIGHT SOURCES

Light Source

Saturation of the Laser-Induced Narrowband Coherent Synchrotron Radiation Process

M. Hosaka[1], N. Yamamoto[1], Y. Takashima[1,2], C. Szwaj[3], M. Le Parquier[3], C. Evain[3],
S. Bielawski[3], M. Adachi[4], H. Zen[4], T. Tanikawa[4], S. Kimura[4], M. Katoh[4], M. Shimada[5]
and T. Takahashi[6]

[1]*Nagoya University Synchrotron Radiation Research Center, Nagoya 464-8603, Japan*
[2]*Graduate School of Engineering, Nagoya University, Nagoya 464-8603, Japan*
[3]*Universit´e des Sciences et Technologies de Lille, F-59655 Villeneuve d'Ascq Cedex, France*
[4]*UVSOR, Institute for Molecular Science, Myodaiji-cho, Okazaki 444-8585, Japan*
[5]*High Energy Accelerator Research Organization, KEK, Tsukuba, 305-0801, Japan*
[6]*Research Reactor Institute, Kyoto University, 590-0494, Japan*

In a bending magnet, a relativistic electron bunch can radiate narrowband terahertz coherent synchrotron radiation when its longitudinal distribution is sinusoidally modulated. We have already demonstrated this by creating the modulation using interaction between an electron beam and a laser pulse containing a sinusoidal amplitude modulation. We have also demonstrated that the emitted power increases with the beam current and the laser power and the scaling is quadratic. However, when the laser power is arbitrarily increased, a departure to this quadratic increase with laser power is also expected, eventually leading to a decrease of emitted power with laser.

In order to observe the saturation phenomenon in the long pulse regime, we used higher energy pulses (by means of a new amplifier), and realized a pulse-shaper able to provide modulated pulses with adjustable duration and modulation period. The experiment is performed with an electron energy of 600 MeV and a laser pulse modulation period of 2.38 ps (i.e., a terahertz emission spectroscopic wavenumber of 14 cm-1), near the maximum efficiency of the system. In the present conditions, departures from quadratic scaling are typically observed, as is shown in Fig. 1. Near maximum laser pulse duration available from the pulse shaper (191 ps FWHM), only a slight (though noticeable) departure from quadratic scaling is observed [Fig. 1 (b)]. However, when the laser pulses are further compressed [down to 28.5 ps FWHM in Fig. 1(c)], a strong saturation effect is observed, leading to the appearance of a maximum.

In order to analyze the process in detail, we use the theoretical approach introduced in the framework of laser-induced CSR. We have calculated an integrated form factor of the CSR as a function of modulation energy. We have also estimated the modulated energy as a function of laser energy and pulse duration. The calculated result is compared with the experimental one. Although not shown here, the theoretical values of the integrated form factor is consistent with the experiment [2]. Future extensions of this work concern studies of the consequences of this saturation
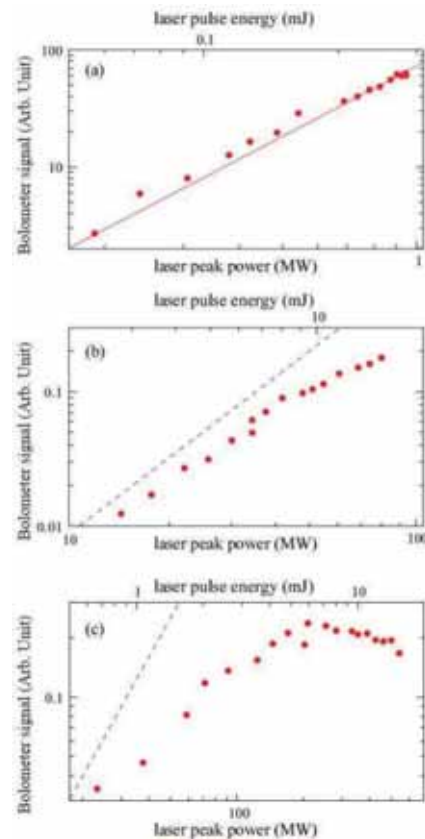

Fig. 1. Typical scalings of terahertz signal versus laser power, for three power ranges. (a): reference quasi-quadratic behavior that was already observed at low power, with a 2 mJ amplifier and 300 ps long pulses.

effect in various situations. This may be important in order to compare the ultimate limits due to saturation effects (in particular in THz pulse energy and peak power) due to the saturation effect, in the cases of slicing, and modulated pulse based strategies.

[1] S. Bielawski, *et al.,* Nature Physics **4** (2008) 390.
[2] M. Hosaka *et al.,* Phys. Rev. ST Accel Beams **16** (2013) 020701.

Light Source

Design and Performance Test of a Buncher Magnet for a New Optical Klystron at UVSOR-III

Y. Uematsu[1], M. Hosaka[2], S. Sekita[1], Y. Asano[1], N. Yamamoto[2]
Y. Takashima[1,2], M. Adachi[3], H. Zen[3], S. Tanaka[3], T. Konomi[3] and M. Katoh[3]
[1]*Graduate School of Engineering, Nagoya University, Nagoya 464-8603, Japan*
[2]*Nagoya University Synchrotron Radiation Research Center, Nagoya 464-8603, Japan*
[3]*UVSOR, Institute for Molecular Science, Myodaiji-cho, Okazaki 444-8585, Japan*

New coherent sources using a relativistic electron beam are being developed at UVSOR-III storage ring. An optical klystron consists of two undualtors separated by a buncher magnet plays an important role for the sources, especially for the coherent harmonic generation. We adapted apple-II type undulators made of permanent magnets and an electromagnet buncher magnet with 3 poles for the optical klystron. The buncher was designed under the conditions that it should be sufficiently compact to be installed in a limited space between the two undulators (the length along the propagation direction of the electron beam should be less than 400 mm) and the magnetic field is sufficient strong: $R56 > 70$ μm, with vanishing first and second field integrals. Taking into account the cost, we have adapted indirect cooling for the coils and therefore the maximum current density is limited around 4 A/mm. The numerical magnetic field calculation was performed with Radia code [1] and optimization of the magnetic field was carried out. Figure 1 shows 3-D drawings of the buncher created by Radia. The shape of the field poles is specially designed in order to increase magnetic field around the electron beam path. After the designed work, the buncher was fabricated. Magnetic field of the constructed buncher was measured and the result is very consistent with the simulation calculation using Radia [3]. The bucher was installed between the two undulators already installed at UVSOR-III 1S. It can be said that then construction of the optical klystron was finally completed.

The performance test of the buncher was carried by observing spontaneous radiation from the optical
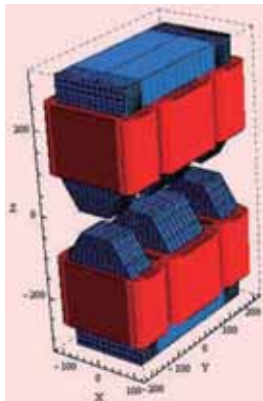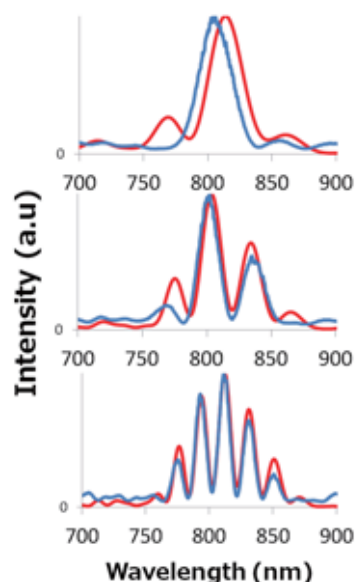

Fig. 1. 3-d drawing of the designed bucher.

Fig. 2. Measured (blue) and calculated (red) spectra of spontaneous radiation from optical klystron.

klystron. Since the spontaneous spectrum as a result of interference between two undulators, is sensitive to the buncher magnetic field, we can characterize the buncher by analyzing the spontaneous spectra. The experiment was made with the electron energy of 600 MeV and the fundamental wavelength of the undulators of 800 nm. Figure 2 shows examples of measured spectra changing excitation current of the buncher. Calculated spectra using spectra [3] are also plotted in the figure. The agreement between measured and calculated spectra reveals that the performance of the bucher is as designed.

Soon we are going to make an experiment on coherent harmonic generation using the optical klystron.

[1] O. Chubar, P. Elleaume, J. Chavanne, J. Synchrotron Rad. **5** (1998) 481.
[2] Y. Uematsu, Master's Thesis, Nagoya University (2013).
[3] T. Tanaka and H. Kitamura, J. Synchrotron Radiant. **8** (2001) 1221.

III-1. ACCELERATORS AND LIGHT SOURCES

Combined-Function Bending Magnets for UVSOR-III

K. Hayashi, M. Adachi, T. Konomi, J. Yamazaki and M. Katoh

UVSOR Facility, Institute for Molecular Science, Okazaki 444-8585, Japan

In the first major upgrade, from UVSOR to UVSOR-II, in 2003, most of the storage ring magnets were replaced, but the bending (dipole) magnets were left untouched for later upgrade. In the next major upgrade, to UVSOR-III, in 2012, all eight bending magnets were replaced with newly designed combined-function ones to reduce emittance from 27 to 17 nm-rad.

The parameters of the new and old bending magnets are listed in Table 1. The quadrupole component of the magnetic field is achieved by adjusting the cross-sectional shape of the pole. The sextupole component is generated by adjusting the longitudinal end-shape of the pole. The mass of the new magnets was reduced, but a sufficient good-field region (<0.1%) of ±3 cm was retained.

Table 1. Design parameters of bending magnets.

	New	Old
Bending radius (m)	2.2	2.2
Bending angle	45°	45°
K1 (m^{-1}) (quadrupole)	−1.2	0
K2 (m^{-2}) (sextupole)	−2.43 (×2)	0
Good field region (cm)	±3	±5
Pole width (cm)	14	18
Gap at center (cm)	5.5	4.8
Mass (metric ton)	3.3	4.3
Material	SUY1	S10C

The pole shape is shown in Figs. 1 and 2. To generate the quadrupole defocusing magnetic field as well as the dipole magnetic field, the pole face is taper-shaped. The sextupole magnetic field component is achieved by shaping the end section of the bending magnets like a paraboloid so that the effective magnetic-field length varies according to the horizontal orbit position of the electrons.
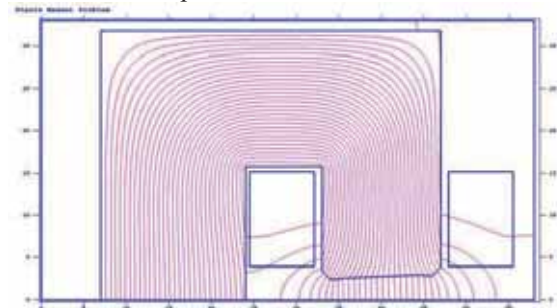
Fig. 1. Cross-sectional view of combined-function bending magnets (upper half is shown).
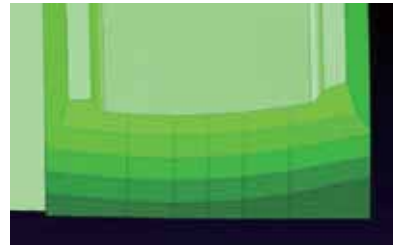
Fig. 2. End-shape of the new bending magnet.

The shape details were investigated by using the 2D calculation code Poisson for cross-sectional shape and the 3D calculation code Opera for longitudinal end-shape. The magnets (Fig. 3) were made by NEC TOKIN Corporation, Japan.

Fig. 3. A new bending magnet (lower half is shown).

The measured magnetic field-strength distribution is shown in Fig. 4. For unknown reasons the quadrupole field strength, which is represented by the gradient of the graph, is about 3% smaller than the design value. The good field region was about ±3 cm. The effective magnetic length was within 1 mm of the design value, 1.728 m.
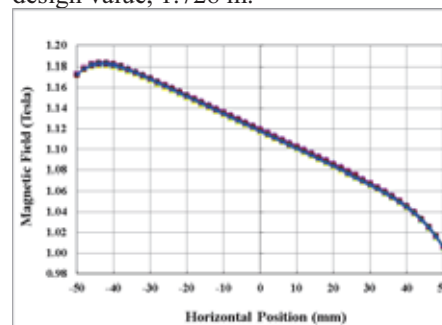

Fig. 4. Horizontal distribution of magnetic field.

The new bending magnets were installed in the UVSOR storage ring in April 2012 and have been operational since August.

We are very grateful to Dr. Y. Shoji of New SUBARU for his kind collaboration.

Turn-By-Turn BPM for UVSOR-III

K. Hayashi[1], T. Toyoda[2], M. Adachi[1], T. Konomi[1], J. Yamazaki[1] and M. Katoh[1]

[1]*UVSOR Facility, Institute for Molecular Science, Okazaki 444-8585, Japan*

[2]*Instrument Development Center, Institute for Molecular Science, Okazaki 444-8585, Japan*

A major upgrade of the electron storage ring at the UVSOR facility started in April 2012. To help in the commissioning procedure we have developed a turn-by-turn Beam Position Monitor (BPM) system, which consists of a signal-switching circuit, a digital oscilloscope, and software [1].

The UVSOR-III storage ring has 24 BPMs, each of which consists of four button electrodes (Fig. 1). We use a commercial signal-processing system (Bergoz Co.) for regular operation.
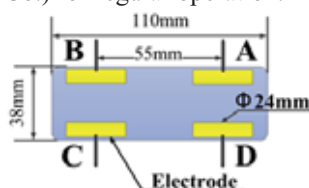
Fig. 1. Layout of BPM electrodes.

At commissioning— especially before the success of the beam storage is confirmed—we need to find out such things as the number of turns the beam has made and where the beam has been lost. Most of these things can be determined by using a turn-by-turn BPM system, but such a system is not necessary for daily operation. We therefore decided to construct a turn-by-turn BPM system, as follows:

•The system was constructed as cheaply and simply as possible.

•We used an existing digital oscilloscope for waveform observation and recording.

•We used existing RF cables that were normally used to connect the BPM heads and the Bergoz signal processing system.

•We set up the oscilloscope in the ring and controlled it via a LAN.

•We developed a signal-switching box that could be controlled via the LAN.

Fig. 2 is a block diagram of the system.

Fig. 2. Block diagram of the BPM system.

The signal-switching box is shown in Fig. 3. Because the BPM signal is a weak (tens of mVs to sub-mV) high-speed pulse (a 100-ps bunch length corresponds to a frequency region of several GHz), we use coaxial switches (Teledyne Coax Switches) to switch signals at low attenuation.

We use a digital oscilloscope (5-GHz sampling frequency, 1-GHz analog signal band) to record four signals from one BPM head; the heads are selected one by one. The data are analyzed off-line.

Fig. 3. BPM switching box.

We control the coaxial switches with an "mbed" microcontroller (NXP Semiconductors), which can be controlled remotely through the LAN. The control application for the BPM system was constructed in HTML (and CSS), which implements a JavaScript library that can handle I/O ports. When we access the mbed from the web browser, the mbed responds as an HTTP server and a control application is displayed in the web browser.

An example of the injection beam trajectory is shown in Fig. 4. By using this system, we have been able to determine not only the orbit but also the betatron tune. At commissioning, the system was very powerful in achieving beam storage.
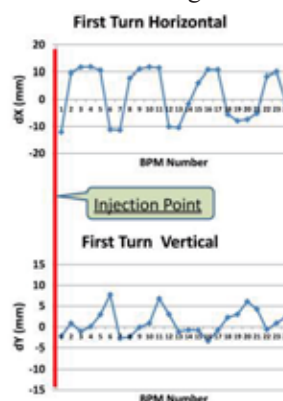

Fig. 4. Example of an injection orbit.

[1] T. Toyoda, K. Hayashi and M. Katoh, Proc. IBIC2012 (2012) MOPA28.

Commissioning of a Scanning Transmission X-ray Microscopy Beamline

T. Ohigashi[1, 2], H. Arai[1], Y. Inagaki[1], N. Kondo[1], M. Sakai[1], K. Hayashi[1], E. Shigemasa[1, 2],
A. P. Hitchcock[3], N. Kosugi[1, 4] and M. Katoh[1, 2]

[1]*UVSOR Facility, Institute for Molecular Science, Okazaki 444-8585, Japan*
[2]*The Graduate University for Advanced Studies (SOKENDAI), Okazaki 444-8585, Japan*
[3]*Brockhouse Institute of Materials Research, McMaster University, Hamilton, ON L8S 4M1, Canada*
[4]*Department of Photo-Molecular Science, Institute for Molecular Science, Okazaki 444-8585, Japan*

Construction of a scanning transmission X-ray microscopy (STXM) beamline, BL4U, was started in April 2012 as part of the UVSOR-III upgrade project [1]. This beamline covers the X-ray energy range from 100 to 700 eV. The STXM end station is used to measure near edge X-ray absorption fine structure (NEXAFS) spectra to analyze chemical states of specific elements, especially light elements, with high spatial resolution. To achieve satisfactory performance of the STXM, we need high intensity, high photon energy resolution, and high stability of the beam position as well as fine coordination of the light source, the monochromator and the STXM. We have been developing interface software and a control system for the complete beamline.

BL4U is equipped with an in-vacuum undulator and a variable included angle Monk-Gillieson mounting monochromator using a varied-line-spacing plane grating. During monochromator commissioning, the X-ray energy range from 270 to 640 eV was calibrated. Then, the 9th harmonic peak of the undulator was synchronized with the X-ray energy of the monochromator by changing the gap width from 13 to 40 mm. The energy resolution (E/ΔE) of the monochromator was evaluated from the absorption spectrum of the K absorption edge of nitrogen gas. The nitrogen gas was introduced into the STXM chamber (~1 mbar) and the transmitted x-rays were measured with a photo multiplier tube. The absorption spectrum measured with exit slits of 30 x 30 µm is shown in Fig. 1. From this spectrum, the resolving power was estimated to be ~6,000. On the other hand, the intensity of X-rays around the carbon K absorption edge from 283 to 300 eV, was very low because of carbon contamination on the mirrors. We expect this problem will be solved by cleaning the mirror chambers and recoating the mirrors.

As a test sample, printer toner particles were studied at the oxygen K edge. Toner particles were embedded in resin and a thin specimen was prepared with an ultra-microtome. A stack of 78 X-ray transmission images was acquired from 522 to 564 eV. The exit slit was set to 30 x 30 µm and the dwell time was 3 msec for each pixel. A spectrum of each component of the specimen, matrix and resin, is extracted from the each specific part of the image stack. By fitting these spectral data of the matrix, the resin and the wax, to the image stack, chemical distributions of the components are clearly distinguished as shown in Fig. 2. These analyses are performed by using aXis2000 [2].

The commissioning of the beamline is almost finished. The STXM system is now ready for user operation. Currently, different kinds of measurement methods and sample cells for in-situ observation are under development for various upcoming applications.
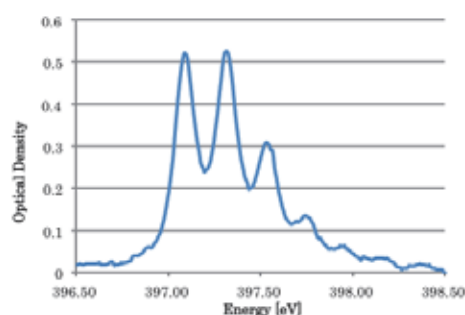

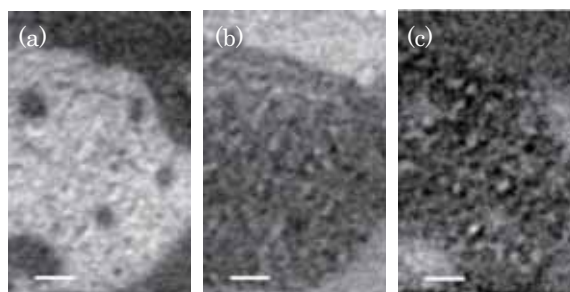Fig. 1. 1s-π* absorption spectrum of nitrogen gas.

Fig. 2. Chemical maps of three components in a printer tonner sample, (a) matrix, (b) resin and (c) wax. Higher concentrations of each component are brighter. Scale bars are 1 µm.

[1] T. Ohigashi, T. Araki, E. Nakamura, N. Kondo, E. Shigemasa, N. Kosugi and M. Kato, UVSOR Activity Report **39** (2012) 42.
[2] http://unicorn.mcmaster.ca/aXis2000.html

Ⅲ-2. INSTRUMENTAL DEVELOPMENTS

Reflectance Measurements of Black Coatings for Stray Light Rejection Used in Bepi Colombo Mission

K. Uji[1], K. Yoshioka[2], G. Murakami[2] and I. Yoshikawa[1]

[1]*Department of Earth and Planetary Science, Graduate School of Science,*
The University of Tokyo, Tokyo113-0033, Japan
[2]*Institute of Space and Astronautical Science, Sagamihara 252-5210, Japan*

We study the tenuous atmosphere of Mercury through the spectroscopic observations. To date, some species (e.g., H, He, O, Na, Mg, K and Ca) have been identified in the Mercury's atmosphere. As these species have many resonance scattering lines in the extreme ultraviolet (EUV) region, spectroscopic observations will enable us deduce the source process, current environment, and evolution of the Mercury's atmosphere.

We are now developing an ultraviolet spectrometer; PHEBUS (Probing of Hermean Exosphere by Ultraviolet Spectroscopy) which is a part of the BepiColombo mission. From the orbit around Mercury, PHEBUS will observe the atmosphere in the EUV and FUV (far ultraviolet) region. In this mission, the signals from the targets are so faint that the stray light must be kept as low as possible. The black coatings techniques are commonly used in various space telescopes and optical instruments in order to reject the stray light in the instrument.

In this experiment, we measure the reflectivities of two types of black coatings in EUV range. As these black coatings have low reflectivities (less than 1 %), the intense light is needed for the accurate measurement.

We install Indium filters on the entrance of the beam line in order to eliminate the multi-order lines. At first, we investigate the purity of the 83.4 nm line through indium filters. We judge the purity from consistency between the wavelength characteristics of indium filters for continuous lines at UVSOR and those for the particular lines at the EUV facilities of Institute of Space and Astronautical Science (ISAS). The latter is measured for the emission lines of the oxygen gas with the discharged light source. Comparing the transmittances of indium filter measured at UVSOR and at ISAS, we confirm that the pure 83.4 nm light is achieved at UVSOR with the entrance filter.

With the pure 83.4 nm line, we measure the reflectivities of two black coating samples at various incident angles (30, 40, 50, 60, 70 and 80 degrees). One is fabricated by EBINA Co. (hereafter referred to as sample #1) and another is by ACTAR (hereafter referred to as sample #2). These black coatings will be used inside the spectrometer. Sample #1 is also used in the EXCEED spectrometer on board the JAXA's SPRINT-A mission.

The results are shown in Fig. 2 and both samples show low reflectivity. Especially, Sample #1 has lower reflectivity than sample #2 at every incident angles.

As the next step, we plan to measure the reflectivities of these black coatings at various wavelengths.
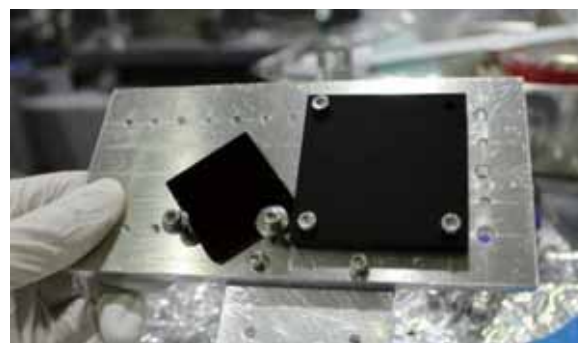

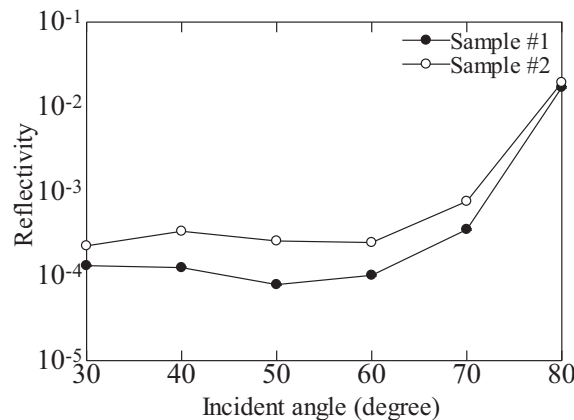Fig. 1. Photo of the black coating samples. Left is fabricated by EBINA and right is by ACTOR.

Fig. 2. The reflectivities of the black coating samples at 83.4 nm. Both samples show low reflectivities.

Performance Test of Infrared Microspectroscopy Using Synchrotron Radiation at UVSOR-III

S. Kimura[1,2], T. Katsumata[3] and J. Koshobu[3]

[1]*UVSOR Facility, Institute for Molecular Science, Okazaki 444-8585, Japan*
[2]*School of Physical Sciences, The Graduate University for Advanced Studies (SOKENDAI), Okazaki 444-8585, Japan*
[3]*IR System Group, JASCO Corporation, Tokyo 192-8537, Japan*

Infrared (IR) synchrotron radiation (SR) has the advantage of higher brilliance and intensity than those of thermal light sources such as the globar (a SiC rod heated to ~1500 K) and the mercury lamp (a discharge lamp with mercury vapor), which utilize the black-body radiation from a heated object [1]. IR microspectroscopy (IR-MS) is currently one of the most common analysis methods for various materials in many fields of science and industry. Commercial IR microspectroscopy instruments, designed for mid-IR spectral range with a thermal IR source, are generally available. However, because of the low brilliance of the thermal light sources, the spatial resolution cannot be the same as the diffraction limit (~ wavelength). With the use of IR-SR, one can further improve the spatial resolution of IR microspectroscopy. Then, we tested that a commercial IR microspectroscopy instrument can be equipped to the IR-SR beamline, BL6B [2] and obtained the performance combined with IR-SR.

A photograph of the IR-MS instrument (FTIR6100+IRT7000, JASCO Corp.) installed at BL6B is shown in Fig. 1. IR-SR was introduced to IR-MS by two plane mirrors through the atmosphere from the free port at the downstream of a CVD-diamond window, which separates a low vacuum area of the Fourier-transform IR interferometer (FTIR) from an ultra-high vacuum area of the front-end part of BL6B.

To demonstrate the performance of IR-SR, IR images of a U. S. Air Force (USAF) test target measured with IR-SR and an internal thermal (globar) source are shown in Fig. 2. The test target, on which a metal pattern is formed on a quartz substrate, was used for the evaluation of spatial resolution. The test target was measured on the focal plane of the IR microscope. By using IR-SR, a clear spatial image was obtained with the instrumental spatial resolution of 5×5 μm^2 in contrast to that of a thermal source, even though the optics in the IR-MS is aligned to the internal source. This implies that the IR-SR is suitable to IR-MS.

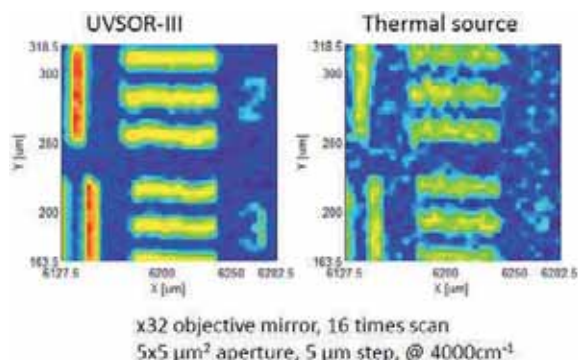The IR-MS instrument will be installed permanently in FY2013.

Fig. 2. Obtained reflectance image of USAF test target at the wavenumber of 4000 cm^{-1} using IR-SRfrom UVSOR-III compared with an internal globarlamp (thermal light source). The objective of the IRmicroscope had a magnification of 32×. The instrumental spatial resolution was set as 5×5 μm^2.

[1] S. Kimura and H. Okamura, J. Phys. Soc. Jpn. **82** (2013) 021004.
[2] S. Kimura, E. Nakamura, T. Nishi, Y. Sakurai, K. Hayashi, J. Yamazaki and M. Katoh, Infrared Phys. Tech. **49** (2006) 147.

Fig. 1. Layout of the IR microspectroscopy (IR-MS) apparatus installed at BL6B. The infrared synchrotron radiation (IR-SR) is introduced to the IR-MS by two plane mirrors through the atmosphere.

Ⅲ-2. INSTRUMENTAL DEVELOPMENTS

Development of the Cold Mirror Coating (Reflective Narrow Band Filter) across 300 mm Diameter for Lyman-Alpha Line (121.6 nm)

N. Narukage[1], R. Ishikawa[2], K. Aoki[2], K. Miyagawa[2],
T. Kobiki[2], R. Kano[2], T. Bando[2] and S. Tsuneta[2]

[1]*Institute of Space and Astronautical Science, Japan Aerospace Exploration Agency,*
3-1-1 Yoshinodai, Chuo-ku, Sagamihara, Kanagawa 252-5210, Japan
[2]*National Astronomical Observatory of Japan, Osawa, Mitaka, Tokyo 181-8588, Japan*

Our team consisting of Japan, US, Spain, France, and Norway is developing a Chromospheric Lyman-Alpha SpectroPolarimeter (CLASP), which is proposed to fly with a NASA sounding rocket in 2015 [1]. CLASP will explore the magnetic fields in the solar atmosphere (the upper chromosphere and transition region) via the Hanle effect in the Lyman-alpha (Lyα) line (121.6 nm) for the first time. This experiment requires precise spectropolarimetric observations with a polarimetric sensitivity of < 0.1% and a wavelength resolution of 0.01 nm.

In order to achieve the polarimetric sensitivity of < 0.1%, the rejection of visible light (VL) from the instrument is indispensable, since the total intensity in the solar VL wavelength range is about 2×10^5 times larger than solar Lyα line. For the VL rejection, we plan to perform the multi-layer "cold mirror coating" on the 300 mm diameter primary mirror of the CLASP. This coating is a reflective narrow band filter with the reflectivity of more than 50 % in the Lyα line, and less than 5 % for VL in average.

Though this coating itself is difficult to adjust the peak wavelength and to enhance the reflectivity, the uniformity of the coating performance across the 300 mm diameter area is also required for the CLASP. If there is a large amount of non-uniformity in the reflectivity, this causes the spurious polarization. So, we performed the development of the uniform coating with Acton Optics and Coatings.

Figure 1 shows the location of the 12 witness samples deployed in the 300 mm diameter area during the coating process. Figure 2 is their reflectivity as a function of wavelength near the Lyα line at AOI = 2 degree measured with UVSOR BL7B. The spatial distributions of the reflectivity at the Lyα line and the peak wavelength are summarized in the left and right panels of Fig. 1, respectively. As a result, the reflectivity of the developed coating is distributed among $60\% \pm 2\%$.

Based on these results, we estimate how much this coating generates the spurious polarization. Figure 3 shows the differences in the pupil maps of the Stokes signals for +Q input between the ideal (uniform) and real coating cases. With these maps, we confirmed that the spurious polarization by this coating is ~ 0.001 %, which is 2 orders smaller than the required polarimetric sensitivity of < 0.1%. Hence, we conclude that the development of the uniform enough coating for the CLASP is successfully completed.
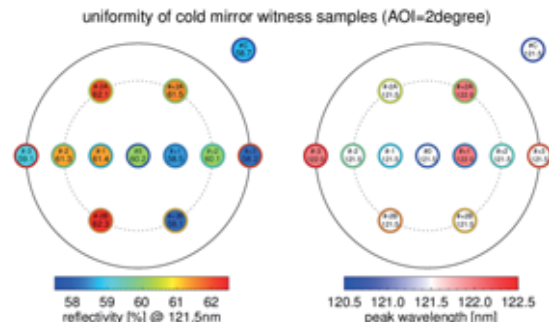

Fig. 1. Location of witness samples during the coating process and the uniformity of the coating performance.
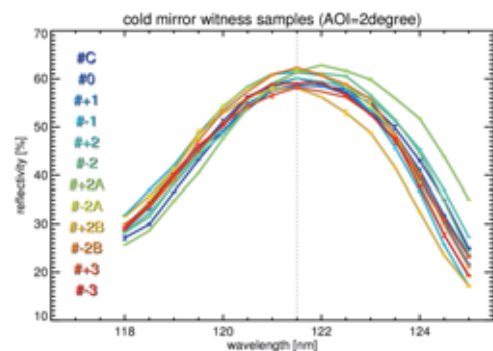

Fig. 2. Measured reflectivity of 12 witness samples as a function of wavelength near the Lyα line.
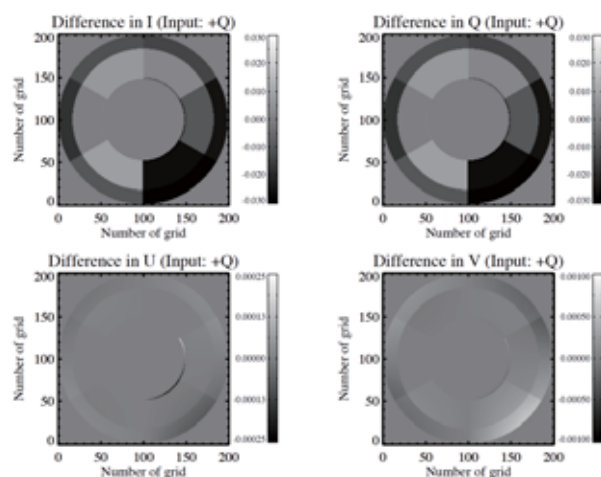

Fig. 3. Difference in Stokes signal pupil map for +Q input between the case for the uniform coating and that for the non-uniform coating.

[1] R. Kano *et al*., SPIE **8443** (2012) 84434F.

Development of the Multi-Layer Coating for the High-Efficiency Reflective Polarizer in Lyman-Alpha Line (121.6 nm)

N. Narukage[1], S. Ishikawa[2], T. Kobiki[2], R. Kano[2], T. Bando[2] and S. Tsuneta[2]

[1]*Institute of Space and Astronautical Science, Japan Aerospace Exploration Agency, 3-1-1 Yoshinodai, Chuo-ku, Sagamihara, Kanagawa 252-5210, Japan*
[2]*National Astronomical Observatory of Japan, Osawa, Mitaka, Tokyo 181-8588, Japan*

Our team consisting of Japan, US, Spain, France, and Norway is developing a Chromospheric Lyman-Alpha SpectroPolarimeter (CLASP), which is proposed to fly with a NASA sounding rocket in 2015 [1]. CLASP will explore the magnetic fields in the solar atmosphere (the upper chromosphere and transition region) via the Hanle effect in the Lyman-alpha (Lyα) line (121.6 nm) for the first time. This experiment requires precise spectropolarimetric observations with a polarimetric sensitivity of < 0.1% and a wavelength resolution of 0.01 nm.

In order to achieve the polarimetric sensitivity of < 0.1%, CLASP requires the high throughput as much as possible for suppressing the photon noise. For this purpose, we plan to apply the high-efficiency reflective polarizer consisting of the Fused Silica substrate and the multi-layer coating of SiO_2 and MgF_2 proposed by Bridou *et al.* [2] as the polarization analyzer of CLASP. This high-efficiency reflective polarizer is theoretically predicted to have a reflectivity of 58.4 % for s-polarized beam, which is about 2.65 times higher than MgF_2 plate of 22 % (This MgF_2 reflectivity was measured at UVSOR BL7B in 2009 [3].).

For the development of the high-efficiency reflective polarizer, we fabricated three polarizers and six witness samples with the multi-layer coating of SiO_2 and MgF_2 performed by Acton Optics and Coatings, and we evaluated their performance with the witness samples at UVSOR BL7B using our measurement system shown in Fig. 1. Our system consists of the beam splitter, beam cleaner and goniometer. The beam splitter made of MgF_2 splits the synchrotron beam into two beams for the measurements and for monitoring the intensity variation of BL7B. This BL7B monitor makes the effect of the intensity fluctuation of the synchrotron beam on the measurements significantly small. The beam cleaner mounted at the Brewster's angle eliminates the p-polarized beam from the beam of BL7B. Then, 100% linear polarized beam can be used for the measurements with the goniometer.

The top and bottom panels in Fig. 2 are the measured reflectivity of 6 witness samples of the high-efficiency reflective polarizer for s- and p-polarized beam, respectively. We note that when we measure R_p and R_s, the goniometer is mounted at the configurations shown in Fig. 1 and rotated 90 degrees from Fig. 1, respectively. Based on our measurements, the polarizers have uniform performance of R_s =

54.7 % and R_p = 0.3 % at their Brewster's angle of 68 degree, which is close to the theoretical value in Bridou *et al.* [2]. We conclude that we have successfully developed the high performance reflective polarizer which has high efficiency and high polarization power ($\equiv$ $(R_s - R_p) / (R_s + R_p)$) of 98.9 %.
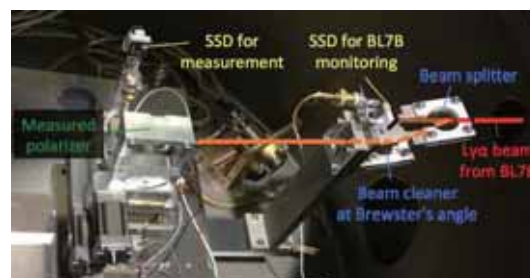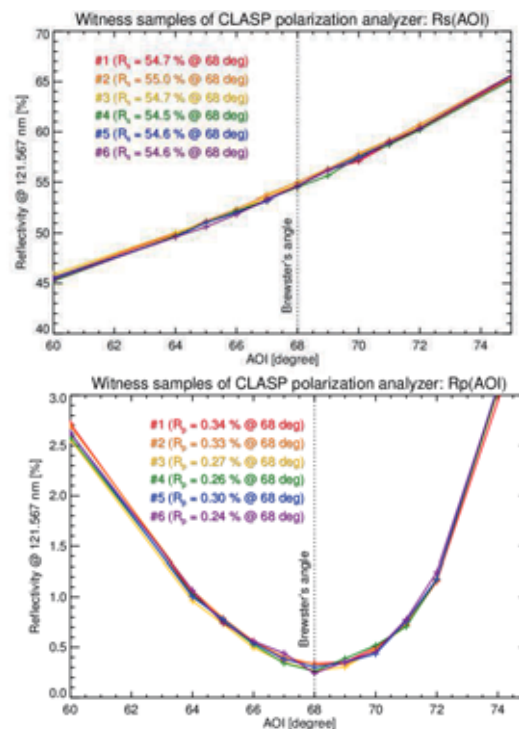

Fig. 1. Our measurement system.

Fig. 2. Measured reflectivity of witness samples for s- (top panel) and p- (bottom panel) polarized beams.

[1] R. Kano *et al.*, SPIE **8443** (2012) 84434F.
[2] F. Bridou *et al.*, Applied Physics A **102** (2011) 641.
[3] H. Watanabe *et al.*, UVSOR Activity Report **37** (2009) 51.

Ⅲ-2. INSTRUMENTAL DEVELOPMENTS

Velocity Map Imaging of Fragment Mixtures from Fullerenes

H. Katayanagi[1,2] and K. Mitsuke[3]

[1]Department of Photo-Molecular Science, Institute for Molecular Science, Okazaki 444-8585, Japan
[2]School of Physical Sciences, The Graduate University for Advanced Studies (SOKENDAI), Okazaki 444-8585, Japan
[3]Faculty of Science, Josai University, Sakado 350-0295, Japan

We have developed a photofragment imaging spectrometer suitable for synchrotron radiation excitation of gaseous molecules of refractory materials such as fullerenes [1, 2]. Using this imaging spectrometer we have measured "yt images" in which fragment masses are shown in t axis and one-dimensional velocity distributions of the fragments are shown in y axis. Translational temperatures (T_{trans}) of the fragments were obtained from the y distributions of the fragments. Values of average kinetic energy release were obtained from T_{trans}.

So far the velocity map images (xy images) have been used to elucidate photodissociation mechanisms of small molecules [3]. Prodhan et al. have expected that velocity map images of fullerene fragments would reveal details of photodissociation mechanism of the fullerenes [4]. Thus we tried to obtain xy images of fragments from the fullerenes in the present study.

The experiments were performed at BL2B in UVSOR. Fullerene powder was loaded in a quartz tube and heated up by an electric heater in vacuum. The fullerene vapor passed through two apertures and reached the ionization region. The fullerene molecular beam thus generated along x axis intersected the monochromatized synchrotron radiation (y axis) at the ionization region. Ions produced there were extracted by a velocity map imaging electrode assembly and projected along z axis on to a position sensitive detector (PSD). Hence the xy images were obtained on the PSD.

Figure 1(a) shows the experimental xy image of parent ions (C_{70}^{2+}) in the molecular beam of C_{70} and 1(b) shows the xy image of a fragment mixture of C_{68}^{2+} - C_{58}^{2+} from C_{70} at the photon energy of 105 eV. Scattering velocity distributions of the fragments are expected to be isotropic [1], so that the fragment images should be circular. However Fig. 1(b) has an oval shape. This shape can be explained as the convolution of the isotropic velocity distribution of the fragments and the anisotropic velocity distribution of the parent molecular beam. These xy images have already been reported in Ref. 2.

Figure 2(a) shows the mixture of C_{58}^{2+} - C_{48}^{2+} fragments produced from C_{60} at the photon energy of 102 eV. The oval shape was observed. Figure 2(b) shows a result of computer simulation for C_{58}^{2+} fragments. In this simulation we assumed that the fragments were emitted isotropically with T_{trans} of 100 K from the anisotropic parent molecular beam of 685 K. Figure 2(b) is similar to 2(a), although 2(a) is a mixture of the fragments. This similarity suggests that the C_{58}^{2+} is the most abundant fragment and that all the fragments have velocity distributions following the Maxwell-Boltzmann distribution. These are in accord with the results in Refs. 1 and 2. However we cannot distinguish singularities of the velocity distributions for production of magic number fragments (C_{50}^{2+} from C_{60} [1] and C_{60}^{2+} from C_{70} [2]) on these xy images, because abundance of these magic number fragments are very small in the mixtures.

We are trying to obtain the xy images of such scarce fragments with improvement of our imaging spectrometer. Observing such xy images will allow us to examine finer details of the production mechanisms of the magic number fragments. This will lead to the understanding of the formation mechanism of the fullerenes.
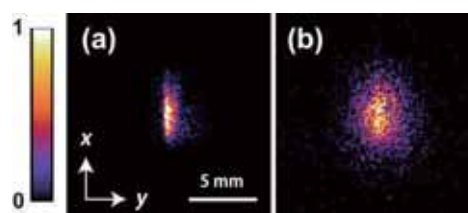

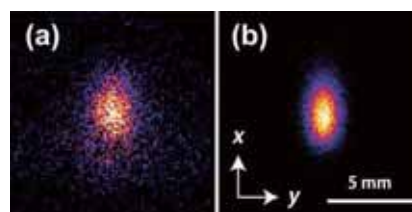Fig. 1. Velocity map (xy) images of (a) parent molecular beam and (b) fragment mixtures from C_{70}.

Fig. 2. Velocity map (xy) images of (a) fragment mixtures from C_{60} and (b) simulated image of C_{58}^{2+} fragments.

[1] H. Katayanagi and K. Mitsuke, J. Chem. Phys. **133** (2010) 081101.
[2] H. Katayanagi and K. Mitsuke, J. Chem. Phys. **135** (2011) 144307.
[3] A. T. J. B. Eppink and D. H. Parker, Rev. Sci. Instrum. **68** (1997) 3477.
[4] Md. S. I. Prodhan *et al.*, Chem. Phys. Lett. **469** (2009) 19.

III-3. MOLECULAR SPECTROSCOPY AND DYNAMICS

Electrochemical Reaction Studied by Soft X-Ray Absorption Spectroscopy
I. Development of Liquid Cell for Electrochemistry

M. Nagasaka[1], H. Yuzawa[1], T. Horigome[1], A. P. Hitchcock[2] and N. Kosugi[1]

[1]*Institute for Molecular Science, Myodaiji, Okazaki 444-8585, Japan*
[2]*Department of Chemistry, McMaster University, Hamilton, ON L8S 4M1, Canada*

To better understanding electrochemistry, it is necessary to investigate the structures of electrolytes including electric double layers at different potentials. The structures of electric double layers were mainly studied by vibrational spectroscopies as reviewed by Ashley and Pons [1], in which the structures of solvent water molecules were determined from the OH stretching mode. It is difficult to investigate the structures of electrolytic solutes in dilute electrolyte solutions. Soft X-ray absorption spectroscopy (XAS) is a powerful tool to study local electronic structure of liquids. The structures of solutes are observed element-selectively even in dilute solutions. Recently, we have developed a liquid cell for the measurement of XAS in transmission mode [2]. In this work, we have developed an in-situ XAS measurement system for studying electrochemical reactions of electrolytes by using the liquid cell with built-in electrodes.

The experiments were performed at BL3U. Figure 1(a) shows schematics of the liquid cell. It consists of four regions I, II, III, and IV, separated by 100 nm-thick Si_3N_4 membranes (NTT AT Co.). Region I is connected to the beam line under vacuum. Regions II and IV are at atmospheric pressure of helium gas. The flow rate of helium gas is controlled by a mass flow controller, and the helium pressure is adjusted by a needle valve set in the gas outlet. The thin liquid layer (region III) is sandwiched between two Si_3N_4 membranes with spacers. Liquid samples are substituted by other samples in combination with a tubing pumping system. The thickness of the liquid layer can be varied from 20 to 2000 nm by changing the He backpressure in regions II and IV [2]. Soft X-rays, which pass through region II and the liquid layer III, are detected by a photodiode (IRD AXUV100) in region IV.

For the investigation of electrochemical reactions, three electrodes are included in the liquid layer III, as shown in Fig. 1(b). The working electrode (WE) is a Au deposited Si_3N_4 membrane, which is one side of the liquid layer III. This membrane is connected with a Au tab for electric conduction. At the opposite side of the Au contact is a teflon™ spacer. The counter electrode (CE) is a Pt mesh. The reference electrode (RE) is a Ag/AgCl electrode with saturated KCl solution, which is isolated from liquid samples by a teflon™ cover. The potential is controlled using a potentiostat (Solartron 1287).

In the present configuration, XAS spectra of electrolytes can be measured at different potentials by using this system. The XAS spectra of solutes in dilute electrolyte solutions are obtained by adjusting the thickness of the liquid layer. We have investigated the change in valence of Fe ions in aqueous iron sulfate solutions by measuring Fe L-edge XAS at different potentials. These results are discussed elsewhere in this volume [3].
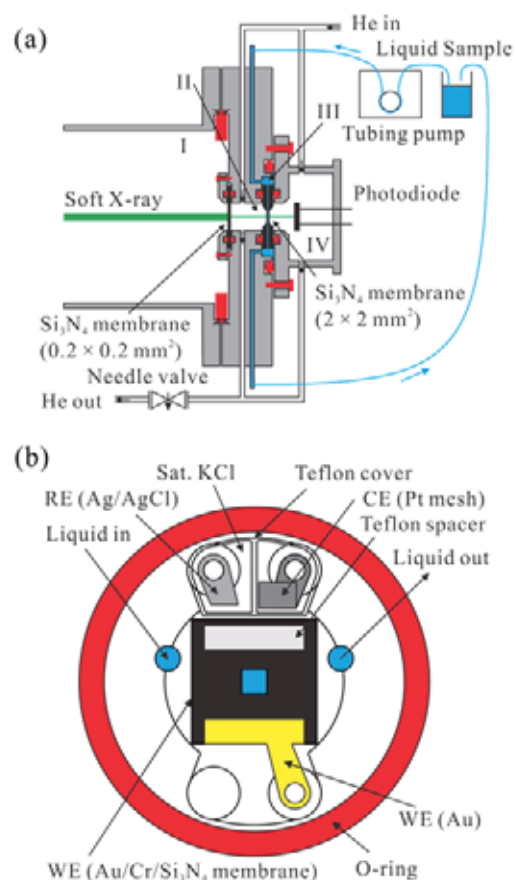

Fig. 1. (a) Schematic of the liquid cell for XAS in transmission mode. (b) Schematics of three electrodes included in the liquid cell.

[1] K. Ashley and S. Pons, Chem. Rev. **88** (1988) 673.
[2] M. Nagasaka *et al.*, J. Electron Spectrosc. Relat. Phenom. **177** (2010) 130.
[3] M. Nagasaka *et al.*, in this volume.

Electrochemical Reaction Studied by Soft X-Ray Absorption Spectroscopy II. Valence Changes of Fe Ions in Aqueous Iron Sulfate Solutions

M. Nagasaka[1], H. Yuzawa[1], T. Horigome[1], A. P. Hitchcock[2] and N. Kosugi[1]

[1]*Institute for Molecular Science, Myodaiji, Okazaki 444-8585, Japan*
[2]*Department of Chemistry, McMaster University, Hamilton, ON L8S 4M1, Canada*

The redox reactions of Fe ions are one of the most common electrochemical systems because of their importance in a variety of fields. Previously, Fe redox reactions were mainly studied by voltammetric methods [1], but it is difficult to measure the change in valence of Fe ions in dilute electrolyte solutions. Soft X-ray absorption spectroscopy (XAS) is a powerful tool to study local electronic structures of liquids. Recently, we have developed a liquid cell for XAS in transmission mode [2]. We have also developed an in-situ system for electrochemistry by using the liquid cell with built-in electrodes [3]. Here we report Fe L-edge XAS results for the change in valence of Fe ions in an aqueous iron sulfate solution induced by variation of the potential at a gold electrode. The experiments were performed at BL3U. The details of the liquid cell are described in this volume [3]. The electrolyte is 0.5 M aqueous iron sulfate at pH = 2.2.

Figure 1 shows the Fe L-edge XAS spectra of an aqueous iron sulfate solution at different potentials. Each XAS spectrum is measured at a constant potential. The XAS L_3 spectra have signals from Fe(II) and Fe(III) ions and show an isosbestic point, indicating only two species are involved. As shown in Fig. 1(a), a nonlinear oxidation of Fe(II) to Fe(III) ions is observed when the potential is increased from 0.0 to 0.9 V. On the other hand, the reduction of Fe(III) to Fe(II) ions varies linearly with the potential when the potential is decreased from 0.9 to -0.4 V, as shown in Fig. 1(b).

Figure 2 shows the fraction of Fe(II) ions from total Fe ions at different potentials, which is determined from the curve fitting procedure of the XAS spectra. The amount of Fe(II) ions decreases by oxidation of Fe(II) to Fe(III) with increasing the potential. Two oxidation processes are revealed. One is a simple oxidation process and the other is a process involving the sulfate ions, which affect electrode kinetic parameters and diffusion coefficients [1]. On the other hand, the formation of Fe(II) from Fe(III) with decreasing the potential is a simple reduction of Fe(III) ions. We will investigate these redox processes by correlating with the XAS results from the cyclic voltammetry at different scanning rates.

[1] A. F. Gil *et al.*, J. Electroanal. Chem. **417** (1996) 129.
[2] M. Nagasaka *et al.*, J. Electron Spectrosc. Relat. Phenom. **177** (2010) 130.
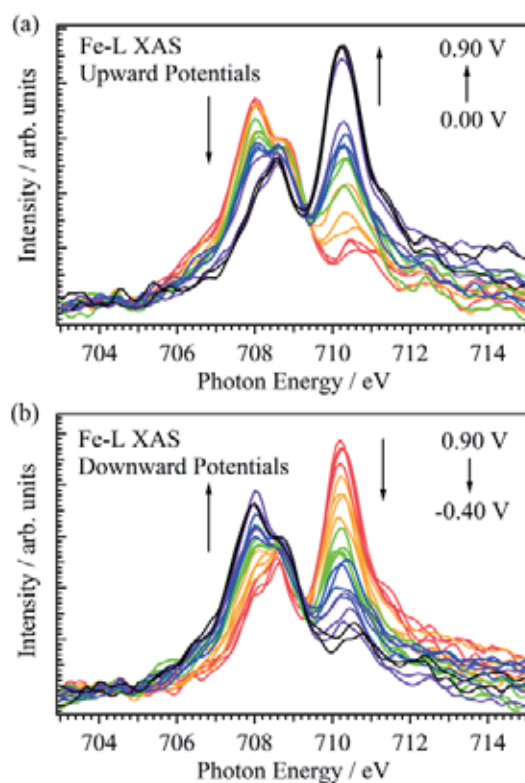[3] M. Nagasaka *et al.*, in this volume.

Fig. 1. Fe L-edge XAS spectra of Fe ions in a 0.5 M aqueous iron sulfate solution at different potentials; (a) increasing from 0.00 to 0.90 V, and (b) decreasing from 0.90 to -0.40 V.
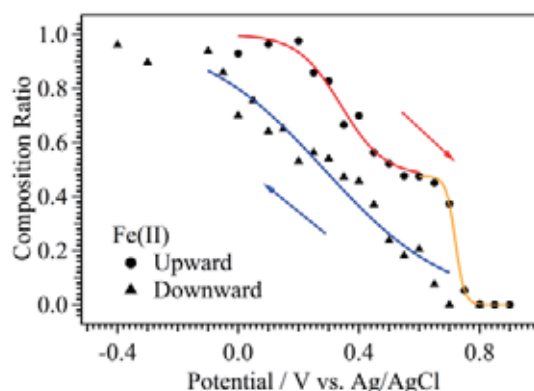

Fig. 2. Fractional composition of Fe(II) ions as a function of potential, obtained from Fe L-edge XAS spectra measured at different potentials.

III-3. MOLECULAR SPECTROSCOPY AND DYNAMICS

In-Situ Observation of Solid-Liquid Heterogeneous Catalytic Reaction by Soft X-ray Absorption Spectroscopy

H. Yuzawa, M. Nagasaka and N. Kosugi

Institute for Molecular Science, Myodaiji, Okazaki 444-8585, Japan

Study of catalytic reaction mechanism is important to obtain some clue to the improvement of activity and selectivity. In-situ observation of the catalytic reaction by spectroscopic approaches such as FT-IR, NMR and XPS, are effective methods to elucidate the reaction mechanism. However, in-situ observation of solid-liquid heterogeneous catalytic reaction is difficult because the photoabsorption of bulk liquids (substrate and/or solvent) hinder the objective change in the spectrum. The spectroscopic observation of this kind of system has been generally carried out by using vapor substrate adsorbed on the catalyst surface instead of liquid substrate [1] although its condition is different from the real one.

We developed a transmission-type liquid cell, which is able to control easily the liquid thin layer, for the soft X-ray XAS [2] and demonstrated that this spectroscopic method was effective to clarify the local structure of various liquid solutions [3]. Thus, in this study, we have extended this method to the in-situ observation of solid-liquid heterogeneous catalytic reaction. As a probe reaction, we have selected hydration of cyanopyrazine on TiO_2 (eq. 1).

$$\text{(structure)} + H_2O \xrightarrow{TiO_2} \text{(structure)} \quad (1)$$
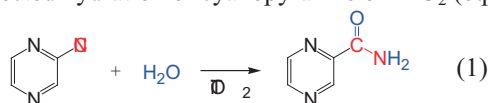
The experiments were carried out in BL3U. Suspension of catalyst was prepared by mixing of cyanopyrazine (3 ml, 0.78 M), ethanol (5 ml), water (35 ml) and TiO_2 (JRC-TIO-4, 0.15 g). Then, the suspension of thin layer (< 1 μm thickness) was sandwiched between two 100 nm-thick Si_3N_4 membranes, and the C K-edge XAS was measured at 323.8−338.5 K. The photon energy was calibrated by the C $1s-3pt_2$ Rydberg peak (297.99 eV) of the CH_4 gas mixture in He [4].

Figure 1a shows the C K-edge XAS spectra of cyanopyrazine, pyrazinamide at 298K and hydration of cyanopyrazine at 331.5 K. Three absorption peaks (285.4, 286.0 and 286.6 eV) are observed in cyanopyrazine (red line) and one absorption peak (285.3 eV) is observed in pyrazinamide (blue line). All these peaks are assigned to the $1s-\pi^*$ excitation. Other absorption peaks could not be observed in the higher photon energy than 287 eV because of overlap with the C K-edge absorption of ethanol. In the spectra of cyanopyrazine hydration (green lines), the intensity of the absorption peak at 285.4 eV decreases slightly, while the other two peaks decrease conspicuously with the reaction time, corresponding to the production of pyrazinamide. Figure 1b shows a

logarithmic plot for the normalized XAS intensity of cyanopyrazine, which is obtained from the factor analysis for Figure 1a (green lines) by using the standard spectra of cyanopyrazine and pyrazinamide. This plot shows linear relationship to the reaction time, indicating that the observed catalytic reaction is the first-order reaction for the concentration of cyanopyrazine and the slope of the line is a reaction rate constant. When the same procedure is applied to the hydration reaction in other temperatures (325.1, 329.8 and 338.5 K), the linear relationship is also obtained. The obtained rate constants show linear relationship in the Arrhenius plot ($E_a = 52.4$ kJ/mol). Thus, this analytical procedure would be reasonable.

Through the above experiments, we can conclude that the transmission soft X-ray XAS approach has a potential for the in-situ observation of the solid-liquid heterogeneous catalysis. In the future, we will improve the system to observe reaction intermediates.
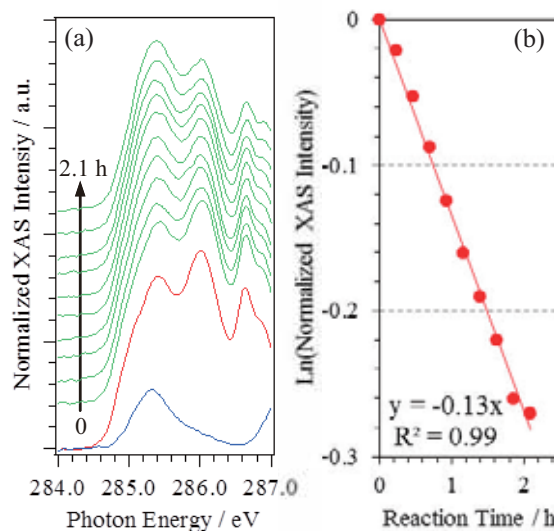

Fig. 1. (a) C K-edge XAS spectra for the cyanopyrazine (0.78 M)−ethanol−water solution (red line), pyrazinamide (0.20 M)−ethanol−water solution (blue line) at 298 K and catalytic hydration of cyanopyrazine on TiO_2 (10 scans (0−2.1 h), green lines) at 331.5 K. (b) A logarithmic plot of the normalized XAS intensity of cyanopyrazine obtained from the factor analysis of green lines in (a).

[1] A. Vimont *et al.*, Chem. Soc. Rev. **39** (2010) 4928.
[2] M. Nagasaka *et al.*, J. Electron Spectrosc. Relat. Phenom. **177** (2010) 130.
[3] For example, M. Nagasaka *et al.*, UVSOR Activity Report **37** (2010) 57.
[4] K. Ueda *et al.*, Chem. Phys. Lett. **236** (1995) 311.

Development of a High-Resolution Magnetic Bottle Electron Spectrometer

M. Sawa[1], Y. Konosu[1], K. Soejima[1], E. Shigemasa[2] and Y. Hikosaka[1]

[1]Department of Environmental Science, Niigata University, Niigata 950-2181, Japan
[2]UVSOR Facility, Institute for Molecular Science, Okazaki 444-8585, Japan

Observing kinetic energy correlation for all the emitted electrons is very useful to understand multiple ionization process of molecules. Such multi-electron coincidence measurements can be achieved with an electron spectrometer using magnetic bottle technique. However, it is difficult for a magnetic bottle electron spectrometer to observe high energy electrons with sufficient energy resolutions, because of their short time-of-flights (TOFs). We have introduced retarding electrodes into our magnetic bottle electron spectrometer, in order to improve energy resolution for high energy electrons.

The electron retarding system consists of an inner drift tube and three metal meshes, as schematically illustrated in Fig. 1. Electrons collected by an inhomogeneous magnetic field in the ionization region are retarded between first and second meshes, when we apply a negative voltage to the second mesh and the inside drift tube. This retardation expands electron TOFs, and higher energy resolution can be achieved.

We have carried out photoelectron-Auger electron coincidence measurements with the electron retarding system to evaluate the kinetic energy resolution and detection efficiency. The results are shown in Fig. 2. Compared to the original energy resolution of $E/\Delta E = 35$ (black dots), the energy resolution is improved up to $E/\Delta E > 200$ by applying retardation voltages. Here, while we cannot observe electrons with lower energies than the retardation voltages, and we has to adjust the retardation voltage to a value lower than the energies of the concerned electrons. The bottom panel of Fig. 2 shows detection efficiencies determined by the ratios between all photoelectron yields and the photoelectron yields measured in coincidence with Auger electron. The detection efficiencies are fairly constant against electron energy, even when the retarding voltage of -180 or -320 V is applied. The detection efficiencies around 50% are reasonable considering the transmission efficiencies of the three meshes and the detection efficiency of the microchannel detector.

We have applied the developed system to the observation of the OCS S2p photoionization and the subsequent Auger decay. Figure 3 displays a two-dimensional map of the coincidence yields between the S2p photoelectron and Auger electrons. The spin-orbit splitting of the S2p^{-1} state is resolved (see the right panel), and the Auger spectrum associated with each core-hole state is derived (the top panel). From these coincidence spectra, the Auger transition probabilities from the two core-hole states can be evaluated.
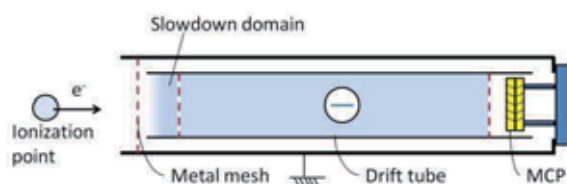

Fig. 1. Schematic of the electron retarding system.
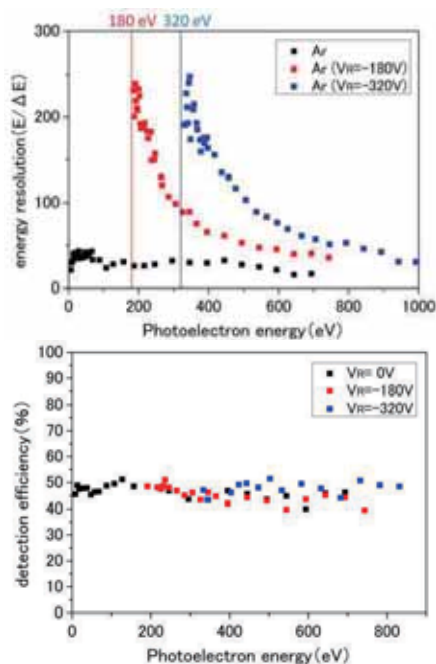

Fig. 2. Energy resolutions (a) and Detection efficiencies (b) observed with/without retarding voltages.
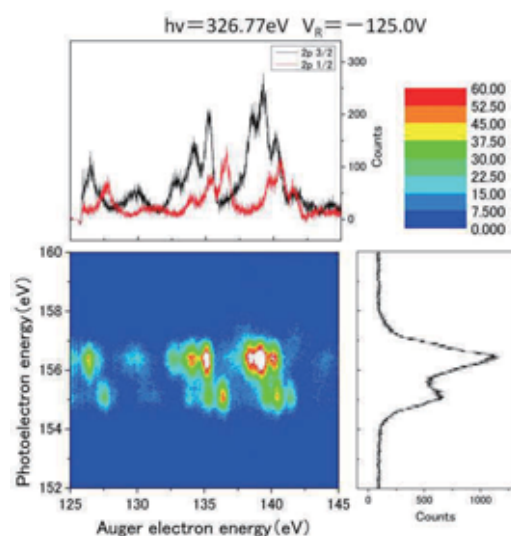

Fig. 3. Energy correlation between OCS S2p photoelectrons and Auger electrons.

Ⅲ-3. MOLECULAR SPECTROSCOPY AND DYNAMICS

Development of a Novel Pulsed Nozzle
for Probing Large Molecules in Vacuum Chamber

T. Tajiri, K. Sakamoto, T. Gejo and K. Honma

Univ. of Hyogo, Koto 3-2-1, Kamigori-cho, Hyogo 678-1205, Japan

The liquid water has been regarded as fundamental material and has been investigated for many years. Particularly interest is the hydrogen network in liquid water, which were investigated by many spectroscopic studies. Since then, many models have been proposed. Recently, in order to investigate the electronic states of liquid water with hydrogen networks, photoelectron spectroscopy and soft x-ray emission spectra have been investigated. To obtain those spectra, liquid phase in vacuum chamber is necessary. Therefore, liquid water beam technique has been employed.

For this liquid phase experiments, we have developed the device that utilizes ultrasonic atomization to produce a dense aerosol microdroplet of water. The ultrasonic atomization technique has been used for generate the microdroplets in mist: The size of liquid droplets was distributed around the micrometer scale. Therefore one can achieve micro droplet of liquid water in vacuum chamber by the injecting them directly.

Last year we have utilized a nozzle with a aperture of 500 μm diameter. Although we have tried to measure photoelectron spectra with this nozzle, low intensity did not allow any significant measurement. This time, we modified the nozzle, in which pulsed valve with high conductance is used.

The experiments were carried out on the bending beamline BL5B at the UVSOR facility in IMS. As figure 1 shows, the experimental set-up consists of three parts: a mist generation part, a transportation part and a nozzle. The microdroplets are generated via ultrasonic atomization. Ultrasonic oscillators (HM2412, Honda Electronics Co., Ltd) operating at 2.4 MHz were installed at the bottom of the water bath. The microdroplet were carried by He and pumped out to obtain a stable stream. A pulsed valve has been placed just before pumping system and the generated microdroplet going into the vacuum chamber. After 10 mm down stream, 10 - 15 eV VUV photons have been radiated to the microdroplets and the excitation UV fluorescence spectra has been measured by photomultiplier tube (R928, HAMAMATSU) installed.

Figure 2 shows the cross section of the pulsed nozzle for microdoloplet. We have modified commercially available General Valve Series 9 with its magnetically activated plunger, which is widely used in the field of atomic and molecular beams. These types produce pulses with a typical width of a few hundreds of microseconds. The 45-mm long, 1.5 mm in diameter plunger was attached to the armature

and operated with a repetition rate in the 1–2 Hz range.

The time profile shows the large molecular are generated relatively slowly after opening the nozzle. Main signal due to mist arises 5 ms after the opening. Since the fluorescence excitation spectra of water clusters strongly depend on its cluster size [1], we can estimate the mean size of droplet in vacuum chamber by these spectra. Simple analysis shows that the size is more than 1000.
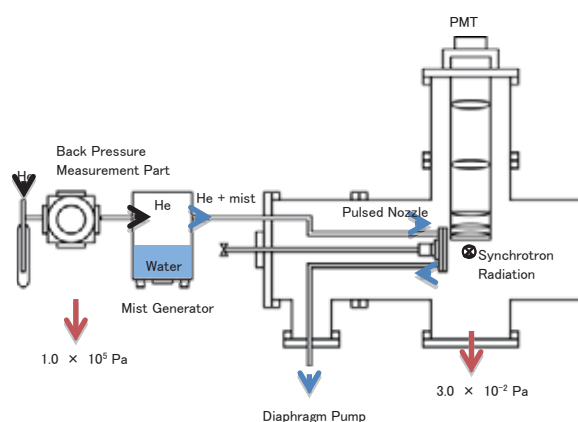

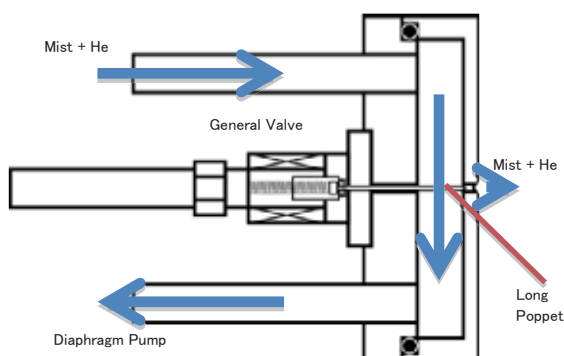Fig. 1. The experimental set-up for the microdroplet generation in vacuum chamber.

Fig. 2. The cross section view of the pulsed nozzle for microdroplet.

[1] M. Ahmed *et al*., J. Phys. Chem. A **98 (**1994) 12530.

Applicability of Database Values of Atomic Mass Absorption Coefficients on Absorption Spectra of L-alanyl-L-alanine Film from 3 to 250 eV

Y. Tanigawa[1], Y. Momoki[1], K. Ishiyama[2], S. Takenaka[2] and K. Nakagawa[1, 2]

[1]Graguate school of Human Development and Environment, Kobe University, Kobe 657-8501, Japan
[2]Faculty of Human Development, Kobe University, Kobe 657-8501, Japan

Absorption spectra of thin films of L-alanyl-L-alanine $C_6H_{12}N_2O_3$ were measured at the photon energy from 3 eV to 250 eV in an attempt to discuss with which energy of radiation is responsible for chemical evolution in space where molecules interact with electromagnetic radiation with wide energy range [1].

Powder of L-alanyl-L-alanine was purchased from SIGMA Pharmacy Company. We prepared thin films of L-alanyl-L-alanine with the vacuum evaporation technique in which heater temperature was set at about 370 K. Collodion films or SiO_2 plates were used as substrate. Prepared thin films were transferred to the measurement system without any contact with air.

Spectral measurement was carried out at the beamlines 5B and 7B. Photon energy region used for measurements were 3.5 to 37 eV at BL7B and 30 to 250 eV at BL5B. Optical density $OD(E)$ was obtained as a function of photon energy E for various samples with different thickness because magnitude of $OD(E)$ around 20 eV was one order larger than that around 90 eV or at higher energies. Here $OD(E)$ was determined to be $OD(E) = \log(I_0(E)/I(E))$, where $I_0(E)$ and $I(E)$ are transmitted light intensity of (substrate) and that of (substrate+sample). Different spectra obtained for different sample were connected. Finally we obtained a smooth spectrum. Similar result was already reported by our group [2].

Translation from $OD(E)$ to absorption cross section $\sigma(E)$ was carried out using following equations;

$$I(E) = I_0(E)e^{-\sigma(E)nl} , \qquad (1)$$

and

$$nSl = N_{HPL} . \qquad (2)$$

Equation (1) is the Lambert-Beer law, where n the number density of sample and l the pass length. The left side of equation (2) shows the total number of L-alanyl-L-alanine molecules in a film of which area is S and the right side shows the total number of L-alanyl-L-alanine molecules in a film analyzed by a high performance liquid chromatography (HPLC).

The first step of our translation from $OD(E)$ to $\sigma(E)$ was carried out around 7 eV for films evaporated on SiO_2 substrate. We cannot use this technique for the films on the collodion substrate because collodion might damage the HPLC system.

Figure 1 shows the absolute values of absorption spectra of L-alanyl-L-alanine film. Vertical axis of the figure was again translated into the optical oscillator strength distribution df/dE determined by the relation [3];

$$\frac{df}{dE}(eV^{-1}) = 1.80 \times \sum_q \chi_q \mu_{aq}(Mb) , \qquad (3)$$

In the equation 3, χ_q is the number of atom q in that molecule and μ_{aq} is the atomic absorption coefficient of atom q in the unit of Mb.

In Fig. 1, the curve A is df/dE spectrum obtained in this work and the curve B shows the calculated result by eq. (3) using the atomic absorption coefficient by Henke et al. [4].

As seen from the figure, curve B can reasonably reproduce the experimental result (curve A). In order to check the applicability in detail of the Henke's atomic absorption coefficient to our L-alanyl-L-alanine data, we extrapolated 250-280 eV part to the region of $E > 280$ eV to obtain the curve C. Making the integration of spectrum from 5 eV to 10000 eV along with the curve C, we obtained value of 62.7 which is very close to 64, the number of 2s and 2p electrons in L-alanyl-L-alanine molecule. Thus we concluded that the Henke's atomic absorption coefficient can reproduce the absorption spectrum within the region from 30eV to 200eV.
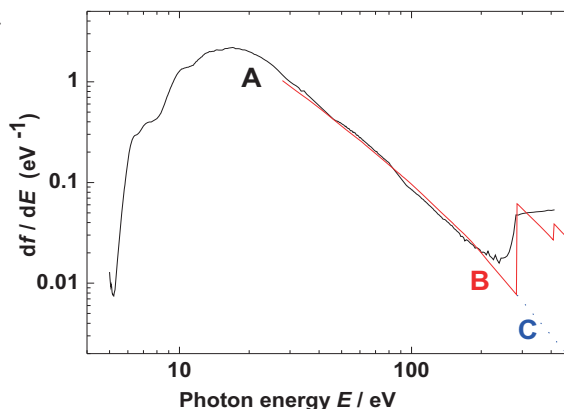

Fig. 1. Absorption spectrum of L-alanyl-l-alanine film. Curve A: Result in this Work. Curve B: Calculated result with Henke [4]. Curve c: See text.

[1]K. Nakagawa, Viva Origino, 37 (2009) 24, in Japanese.
[2] M. Kamohara *et al.,* Rad. Phys. Chem. **77** (2008) 1153.
[3] Y. Hatano, In: Sham, T.K. (Ed.), Chemical Applications of Synchrotron Radiation Part I. World Scientific, Singapore, (2002) 55.
[4] B. L. Henke *et al.,* Atomic Data and Nuclear Data Tables, **54**(1993)181.

Site-Specific Fragmentation Driven by Particular Auger Processes of the C K-Shell Excited *cis*-Hexafluorocyclobutane Molecule

S. Ishikawa[1], K. Okada[1], H. Iwayama[2,3], L. Ishikawa[2] and E. Shigemasa[2,3]

[1]*Department of Chemistry, Hiroshima University, Higashi-Hiroshima 739-8526, Japan*
[2]*UVSOR Facility, Institute for Molecular Science, Okazaki 444-8585, Japan*
[3]*School of Physical Sciences, Graduate University for Advanced Studies (SOKENDAI), Okazaki 444-8585, Japan*

Inner-shell excited states of molecules relax into various molecular cationic states through Auger decays. The resultant cations are in general unstable and dissociate into fragment ions. Information on the correlation between the Auger-final states and the products provides us deeper insight into the fragmentation dynamics of the inner-shell excited molecules. We found in our previous study that after the $C1s^{-1}\sigma_{CC}^*$ and $F1s^{-1}\sigma_{CC}^*$ transitions the *cis*-1,1,2,2,3,4- hexafluorocyclobutane (*cis*-c-$C_4H_2F_6$) molecule dissociates into the fragment ions with C–F bond(s) in higher yield. In this study we have acquired the Auger-electron–photoion coincidence data of the *cis*-c-$C_4H_2F_6$ molecule at the C 1s edge by using a pair of a double toroidal electron analyzer (DTA) and an ion time-of-flight mass spectrometer to obtain information on the Auger processes correlating with such specific fragments.

The experiments have been performed on the soft X-ray beamline BL6U. The experimental setup has been described in a previous paper [1]. Synchrotron radiation was irradiated at right angles to the effusive beam of the gaseous *cis*-c-$C_4H_2F_6$ sample. The electrons traveling through the DTA tube were detected with a position sensitive detector (RoentDek, DLD40). Fragment ions were extracted toward the time-of-flight spectrometer by a pulsed electric field applied just after the Auger electron detection across the ionization region. The coincidence data were obtained as list-mode files, containing a series of a set of the detected electron positions and the ion arrival times. They were acquired in this study at the photon energies of 290.3, 292.8, 297.0 and 327.6 eV.

The resonant Auger spectrum obtained at the photon energy of 297.0 eV has characteristic features that distinguish it from the other spectra acquired in this study. Figure 1a shows the resonant Auger spectrum measured at 297.0 eV and the components coincident with the $CH_{0,1}F^+$, $CH_{0,1}F_2^+$ and $C_2H_{0,1}F_3^+$ fragments. The excitation energy corresponds to the $\sigma_{CC}^* \leftarrow C_{CF2}$ 1s transition of *cis*-c-$C_4H_2F_6$, where C_{CF2} means the carbon of a CF_2 group. The spectra taken at 292.8 eV are also displayed in Fig. 1b for comparison. The intense peak at the final-state energy around 42 eV is distinctive of the 297.0-eV excitation. The coincidence spectra reveal that in this peak the $CH_{0,1}F^+$ and $CH_{0,1}F_2^+$ ions are produced in abundance, whereas the spectra of the fragment ions without a C–F bond give no peak (not shown in Fig. 1). We can conclude that the Auger-final states corresponding to this energy region are responsible for the production of the specific fragment ions. This study clearly demonstrates that the site-specific fragmentation of the C K-shell excited *cis*-c-$C_4H_2F_6$ molecule is strongly correlated with the particular Auger decays.

The experiments at the F K-edge are eagerly in progress and the results will be published in the near future.
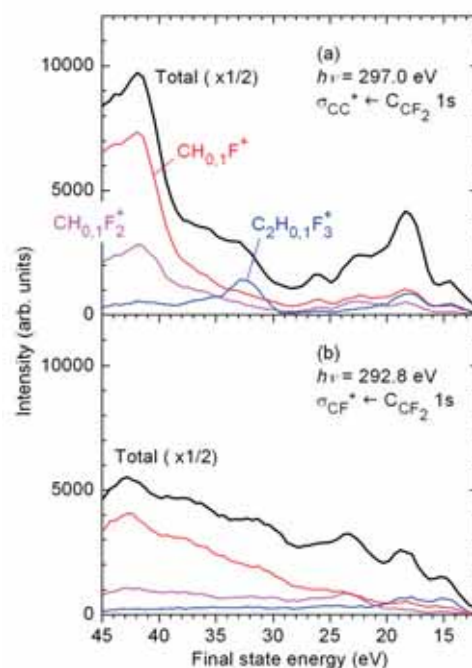

Fig. 1. Resonant Auger spectra coincident with the $CH_{0,1}F^+$, $CH_{0,1}F_2^+$ and $C_2H_{0,1}F_3^+$ fragments acquired at 297.0 eV (panel a) and 292.8 eV (panel b). Total resonant Auger spectra are also plotted as the thicker black lines and are scaled by a half. Abscissa has been obtained as the difference between the photon energy and the electron kinetic energy.

[1] T. Kaneyasu, Y. Hikosaka and E. Shigemasa, J. Electron Spectrosc. Relat. Phenom. **156-158** (2007) 279.

Formation of Metastable Carbon Dioxide Dications Following Core-Hole Creation

Y. Shibata[1], K. Soejima[1], H. Iwayama[2], E. Shigemasa[2] and Y. Hikosaka[1]

[1]*Department of Environmental Science, Niigata University, Niigata 950-2181, Japan*
[2]*UVSOR Facility, Institute for Molecular Science, Okazaki 444-8585, Japan*

The ion yield spectra observed in the inner-shell threshold ranges of carbon dioxide (CO_2) molecules [1] indicate that metastable CO_2^{2+} is favorably produced in the Auger decay of the O 1s core-hole state, compared to the Auger decay of the C1s core-hole state. In this study, we have used an Auger-electron-ion coincidence method to investigate the formation mechanism of the metastable dications following the core-hole creations in CO_2.

The experiment was performed at the undulator beamline BL6U, using an electron-ion coincidence spectrometer [2]. The electrons were analyzed in energy by a double toroidal electron analyzer, while ions were extracted from the interaction region into an ion momentum spectrometer by a pulsed electric field according to the detection of the electron.

Figure 1(a) shows an O 1s Auger spectrum of CO_2, plotted as a function of the kinetic energy and of the binding energy. The Auger spectrum exhibits several band structures corresponding to the formation of different CO_2^{2+} states. Figures 1(b), (c) and (d) represent the spectra of Auger electrons observed in coincidences with metastable CO_2^{2+}, $O^+ + CO^+$ ion pairs and $C^+ + O^+$ ion pairs, respectively. One finds that the formation of metastable CO_2^{2+} is associated with the Auger decay into doubly charged states in the binding energy range of 35-45eV. A calculation implies that the doubly charged states have the electronic configuration of π^{-2} [3].

Figure 2 compares the Auger spectra observed in the decays of the O1s and C1s core-holes, where the red curves are obtained in coincidences with metastable CO_2^{2+}. While the CO_2^{2+} states in the same binding energy range are relevant to the metastable CO_2^{2+} formation following the different core-hole creations, the intensity of the metastable CO_2^{2+} formation is about four times more intense in the O 1s core-hole decay. The favorable production of metastable CO_2^{2+} following the O 1s core-hole creation is qualitatively explained by considering the spatial distribution of the π orbital involved in the decay processes. Since the π valence orbital is mostly localized around the O atom in the CO_2 molecule, the π electron preferentially fills the O 1s core-hole due to a large overlap between the core and valence orbitals. Thus the Auger transition involving the π electrons is favored in the decay of the O 1s core-hole states rather than the C core-hole states, resulting in the favorable formation of metastable CO_2^{2+} states with the configuration of π^{-2} in the decay of the O 1s core-hole states.

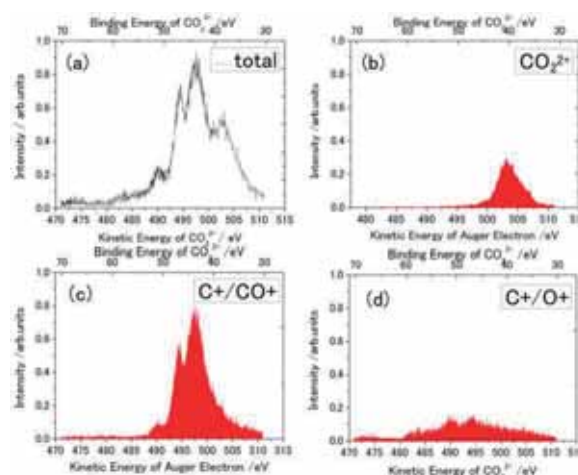Fig. 1. O1s Auger spectrum (a) and Auger spectra obtained in coincidences with (b) metastable CO_2^{2+}, (c) $O^+ + CO^+$ ion pairs and (d) $C^+ + O^+$ ion pairs.
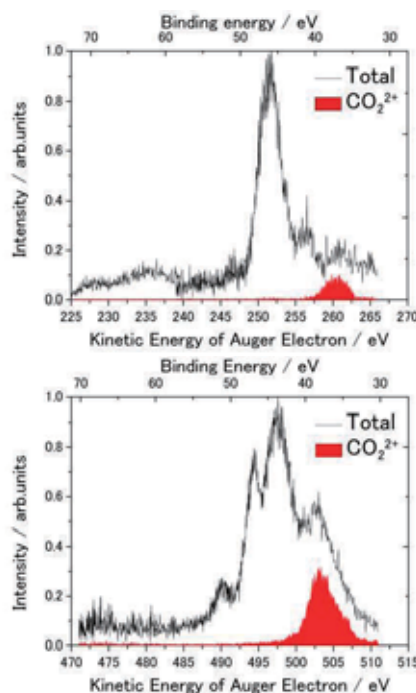

Fig. 2. O1s and C1s Auger spectra (solid lines) and Auger spectra (a) and Auger spectra obtained in coincidences with metastable CO_2^{2+} (red).

[1] G. Ohrwal *et al*., J. Phys. B **35** (2002) 4543.
[2] T. Kaneyasu *et al*., J. Electron Spectrosc. Relat. Phenom. **156-158** (2007) 279.
[3] J. A. Kelber *et al*., J. Chem. Phys. **75** (1981) 652.

High-Resolution Electron Spectroscopy for Ethyl Trifluoroacetate

H. Iwayama[1], F. Penent[2], P. Lablanquie[2] and E. Shigemasa[1]

[1]UVSOR Facility, Institute for Molecular Science, Okazaki 444-8585, Japan
[2]LCPMR, Université Pierre et Marie Curie, 75231 Paris Cedex 05, France

Inner-shell photoionization of light elements is mostly relaxed via an Auger decay process, causing the emission of another electron from an outer-shell. Auger electron spectroscopy (AES) is thus an element-sensitive method with various analytical applications. Since a core hole can be regarded as being strongly localized at a particular atom, it can be expected that the Auger final dicationic state has two valence holes which are also localized near the inner-shell ionized atom. According to this simple atomic picture, the binding energies of the molecular Auger final states would also show chemical shifts. Owing to a hole-hole repulsion, the chemical shift in Auger electron spectra reflects any localization character of the two valence holes.

The interpretation of molecular Auger spectra is complex and the difficulties increase with increasing the number of atoms in a molecule. The Auger spectra become much more complicated in the case where a molecule is composed of several atoms of the same element. While well-defined photoelectron peaks reflecting the chemical shifts can be observed in photoelectron spectra, direct observations of the corresponding chemical shifts in molecular Auger spectra are practically impossible without using a coincidence technique. In order to stabilize the interpretation on the site-specific Auger spectra obtained by such coincidence experiments, however, high-resolution Auger electron spectra as well as theoretical calculations are indispensable. We have carried out high-resolution electron spectroscopic measurements on ethyl trifluoroacetate ($C_4H_5F_3O_2$).

The experiment was performed on the soft X-ray beamline BL6U at UVSOR. The radiation from an undulator was monochromatized by a variable included angle varied line-spacing plane grazing monochromator. The monochromatized radiation was introduced into a cell with sample gases. Kinetic energies of the emitted electrons were measured by a hemispherical electron energy analyzer (MBS-A1) placed at a right angle with respect to the photon beam direction. The direction of the electric vector was set to be parallel to the axis of the electrostatic lens of the analyzer. The kinetic energy resolution of the analyzer was set to 20 meV.

Figure 1(a) and 1(b) show the C 1s photoelectron and Auger electron spectra of $C_4H_5F_3O_2$ at the photon energy of 330 eV, respectively. The chemical shifts are clearly observed in Fig. 1(a). The oxygen and fluorine Auger electron spectra are displayed in Fig. 2 (a) and (b), respectively. It is seen that the populations

of the Auger final states strongly depend on which core electron is ionized. No fine structure is found in every Auger electron spectrum, in spite of the high-resolution.
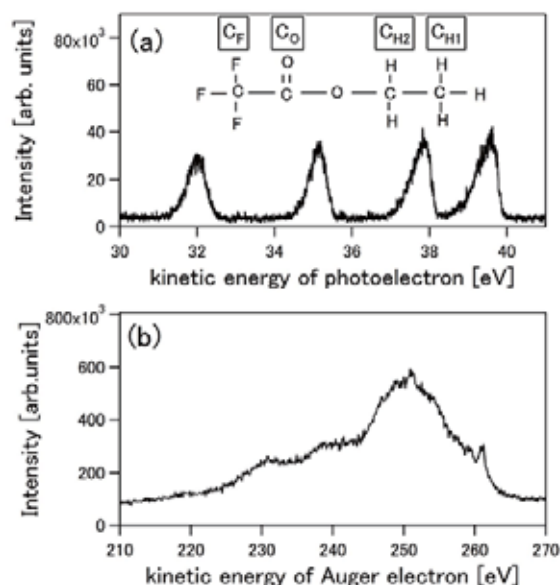

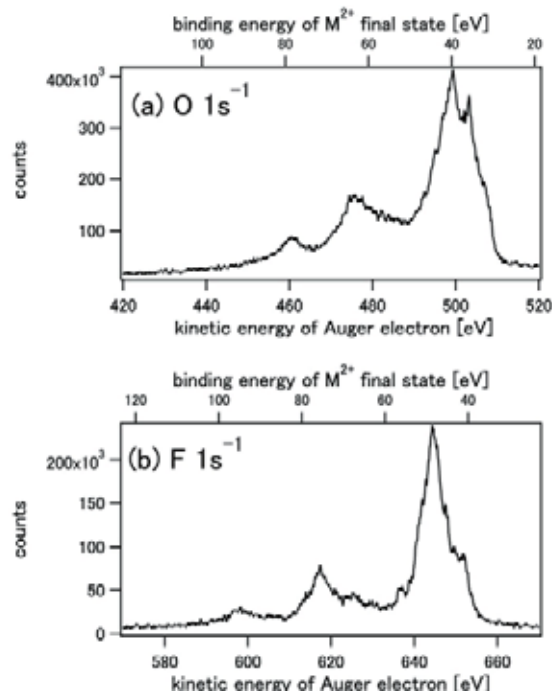Fig. 1. (a) Carbon 1s photoelectron and (b) Auger electron spectra of $C_4H_5F_3O_2$.

Fig. 2. (a) Oxygen and (b) fluorine Auger electron spectra of $C_4H_5F_3O_2$.

Deexcitation Processes after S 2p Photoexcitation of OCS Studied by Angle-Resolved Resonant Auger Electron Spectroscopy

L. Ishikawa, H. Iwayama and E. Shigemasa

UVSOR Facility, Institute for Molecular Science, Okazaki 444-8585, Japan

Soft X-ray absorption spectra of molecules exhibit rich structures in the region below the ionization thresholds, which are due to the excitations of a core electron to unoccupied valence or Rydberg orbitals. The core excited states are predominantly relaxed via Auger electron emission, in the case of the molecules composed of light elements, and subsequently fragmentation follows. Recent works on high-resolution resonant Auger electron spectroscopy have revealed that the nuclear motion of the molecular core-excited states is promoted in competition with the Auger decay.

In the previous work [1], three satellite structures (as labeled 0, 1, and 2 in Fig. 2) between B ($^2\Sigma$) and C ($^2\Sigma$) valence ionized states were observed following the S $2p_{3/2} \to \pi^*$ excitation, and they were assigned to $^4\Pi$, $^2\Pi$, and $^2\Phi$ shake-up-like states on the basis of ab initio theoretical calculations. Here, we revisit this first observation of spin-forbidden shake-up states. Angle-resolved two dimensional (2D) electron spectroscopy has been applied.

The experiments were carried out on the soft X-ray beamline BL6U. The radiation from an undulator was monochromatized by a variable included angle varied line-spacing plane grazing monochromator. For the 2D electron spectroscopy, the monochromator bandwidth was set to $E/\Delta E$ ~1000 at $h\nu$=165eV. Kinetic energies of the emitted electrons were measured by a hemispherical electron energy analyzer (MBS-A1) placed at a right angle relative to the photon beam direction. The direction of the electric vector was set to be either parallel (horizontal direction) or perpendicular (vertical direction) to the axis of the electrostatic lens of the analyzer. The resonant Auger spectra with kinetic energies ranging from 135 to 155 eV were recorded as a function of the photon energy in the S 2p excitation region.

Figure 1 shows the 2D maps of resonant Auger electron spectra following the S 2p excitation of OCS measured in horizontal (left) and vertical (right) directions. The horizontal solid lines in Fig. 1 indicate the resonance peak positions (S $2p_{3/2,1/2} \to \pi^*$ and S $2p_{3/2,1/2} \to \sigma^*$). The diagonal lines in Fig. 1 are due to the valence photoelectrons, while the vertical lines seen in the lower kinetic energy region are owing to the atomic Auger lines. The atomic line widths show clear polarization dependence, which may reflect the anisotropic photoexcitation process. The peak position for the S $2p_{3/2} \to \pi^*$ excitation ($h\nu$=164.4 eV) corresponds to the lowest horizontal line in Fig. 1, where clear island-like structures are detected both in

the horizontal and vertical directions in the kinetic energy region from 146 to 148 eV.

Figure 2 represents the enlargements of the resonant Auger spectra following the S $2p_{3/2} \to \pi^*$ excitation around the satellite region. The structures observed in the horizontal spectrum are good agreement with those in the previous work [1]. However, some differences are seen in the vertical spectrum; the peak position of the $^4\Pi$ state as labelled "0" in the horizontal spectrum differs from that in the vertical spectrum, and a peak at 17.8 eV is seen only in the vertical spectrum. Resonant Auger spectra with much higher resolution may reveal the reason for the discrepancy.
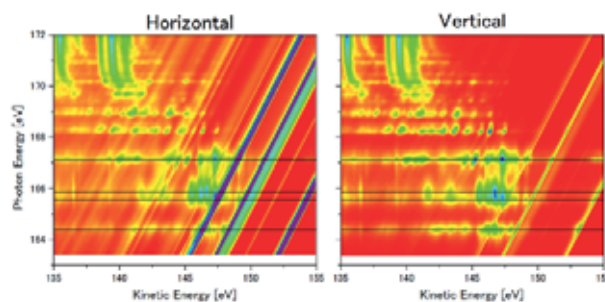

Fig. 1. 2D maps of resonant Auger electron spectra following the S 2p excitations of OCS, obtained at horizontal and vertical directions.
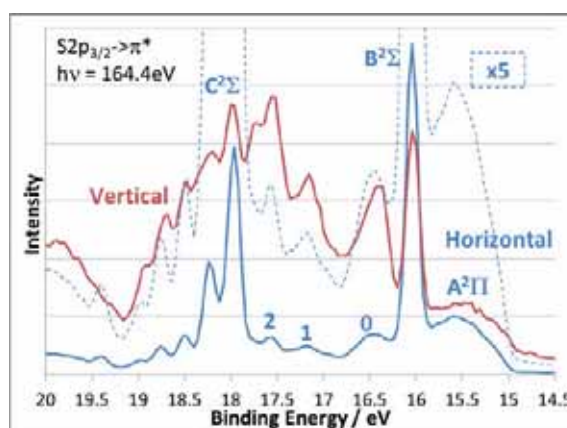

Fig. 2. Participator Auger spectra following the S $2p_{3/2} \to \pi^*$ excitation, measured at horizontal and vertical directions.

[1] S. Masuda, T. Hatsui and N. Kosugi, J. Electron Spectrosc. Rlat. Phenom. **137-140** (2004) 351.

Ⅲ-3. MOLECULAR SPECTROSCOPY AND DYNAMICS

Ultrafast Dynamics in C 1s Core-Excited CF_4 Studied by Two-Dimensional Resonant Auger Spectroscopy

M. N. Piancastelli[1], R. Guillemin[1], M. Simon[1], H. Iwayama[2] and E. Shigemasa[2]

[1]*LCPMR, Université Pierre et Marie Curie, 75231 Paris Cedex 05, France*
[2]*UVSOR Facility, Institute for Molecular Science, Okazaki 444-8585, Japan*

The CF_4 molecule, tetrafluoro methane, has been a benchmark for several spectroscopic studies, due to its high symmetry, same as methane, CH_4. One of the most interesting observations deriving from the comparison between CH_4 and CF_4 is the relative intensity of below-threshold photoabsorption structures around the C 1s ionization threshold associated with transitions to empty molecular orbitals versus Rydberg states. CF_4 is a good candidate to investigate the dynamical properties of core-excited states with an electron in the antibonding lowest-unoccupied molecular orbital (LUMO) in a highly symmetric system.

Here an investigation of ultrafast dissociation following C1s-to-LUMO core excitation in CF_4, with high-resolution resonant Auger spectroscopy, is presented. The main novelty of this work is the use of two-dimensional (2D) maps to record resonant Auger spectra across the resonance as a function of photon energy with a small energy step and then to characterize ultrafast dynamics. This method allows one to follow in great detail the evolution of the resonant enhancement of spectral features corresponding to final ionic states while scanning the energy across the resonance, and to fully exploit the so-called detuning effects.

The experiment was performed on the soft X-ray beamline BL6U at UVSOR. The photon energy resolutions were set to 10000 and 4000 for total-ion yield and 2D map measurements, respectively. Kinetic energies of the emitted electrons were measured by a hemispherical electron energy analyzer (MBS-A1). The direction of the electric vector was set to be parallel to the axis of the electrostatic lens of the analyzer. The kinetic energy resolution of the analyzer was set to 60 meV. The 2D maps were obtained by taking decay spectra at regular photon energy intervals of 100 meV across the resonance.

Figure 1 represents total ion yield curve measured in the C 1s excitation region of CF_4. The double feature with maxima at 297.7 and 298.4 eV is assigned to the Jahn-Teller-split transition to the LUMO (σ^* of t_2 symmetry), followed by the Rydberg series. Figure 2 shows the 2D map after subtraction of the non-resonant contributions, and with on-top two pseudo-absorption curves obtained by the CIS (Constant Ionic State) method, and namely plotting the integrated intensity of the two resonant features, the non-dispersive one related to the fragment and the dispersive one related to the $3t_2$ state, as a function of

photon energy. It is seen that while the intensity of the molecular state closely mimics one of the absorption curve, the non-dispersive feature related to the fragment decreases in relative intensity across the resonance, and disappears in the photon energy region of the Rydberg states. Detailed calculations on the potential curves of the intermediate and final state would be needed to fully clarify this finding.
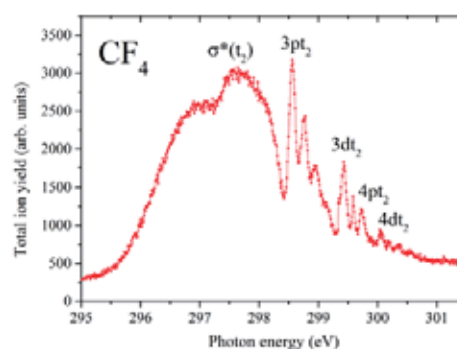

Fig. 1. Total ion yield curve measured in the C 1s excitation region of CF_4.
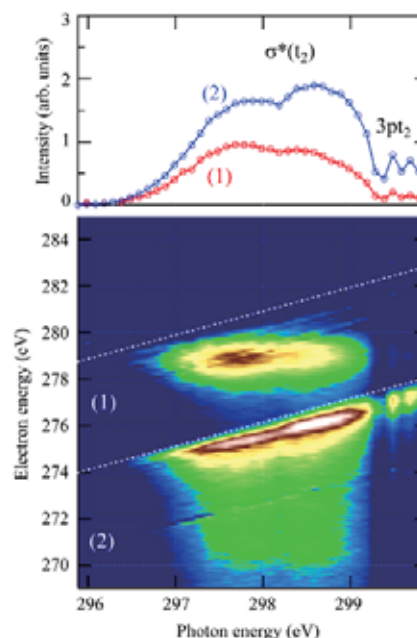

Fig. 2. Top: CIS spectra of the fragment (1) and of the $3t_2$ (2) final states. Bottom: resonant Auger 2-D map showing only the resonant contributions: (1) the non-dispersive state and (2) the $3t_2$ spectral line.

Cl-L$_{23}$VV Normal Auger and Resonant Auger Electron Spectra of CCl$_4$ Molecules

H. Iwayama[1], M. N. Piancastelli[2], R. Guillemin[2], M. Simon[2] and E. Shigemasa[1]

[1]*UVSOR Facility, Institute for Molecular Science, Okazaki 444-8585, Japan*
[2]*LCPMR, Université Pierre et Marie Curie, 75231 Paris Cedex 05, France*

The chlorofluoromethanes have received attention due to their potentially destructive effect on the earth's ozone layer. The inner-shell photoabsorption spectra of the family of tetrahedral molecules CX$_4$ (X=H, F, and Cl) are known to exhibit completely different below-threshold structures, related to transitions to empty molecular orbitals versus Rydberg states. The behaviors of the Rydberg state energies and intensities in these molecules are explained by the cage model, in which the Rydberg states are strongly excluded from CCl$_4$ but not from CF$_4$. CCl$_4$ has been a benchmark for several spectroscopic studies, due to its high symmetry, same as methane, CH$_4$, with four chlorine atoms around the carbon center. CCl$_4$ is one of the good candidates to investigate the dynamical properties of core-excited states with an electron in the antibonding unoccupied molecular orbitals in a highly symmetric system. We have studied the deexcitation processes following the Cl 2p excitations of CCl$_4$ molecules by using Auger electron spectroscopy.

The experiment was performed on the soft X-ray beamline BL6U at UVSOR. The radiation from an undulator was monochromatized by a variable included angle varied line-spacing plane grazing monochromator. The photon bandwidth was set to about 2000 (ΔE ~100 meV). Kinetic energies of the emitted electrons were measured by a hemispherical electron energy analyzer (MBS-A1). The direction of the electric vector was set to be parallel to the axis of the electrostatic lens of the analyzer. The kinetic energy resolution of the analyzer was set to 30 meV.
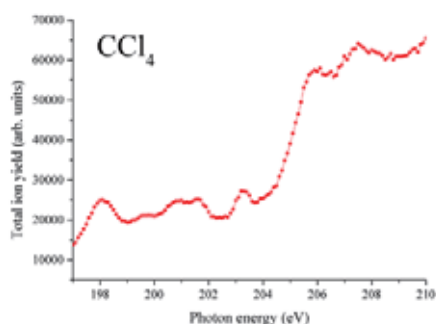

Fig. 1. Total ion yield curve in the Cl 2p excitation region of CCl$_4$.

Figure 1 shows the total-ion yield curve around the Cl 2p excitation region of CCl$_4$. The spectral features in Fig. 1 resemble the prevously measured high-resolution spectrum [1], where the photon bandwidth was about 30 meV. The broad peak around 198 eV is assigned to the excitation of the Cl 2p$_{3/2}$ electron into the lowest unoccupied molecular orbital. The normal Auger electron spectrum and resonant Auger electron spectrum measured on top of this resonance are shown in Fig. 2. The present normal Auger spectrum displays clearer peak structures than that reported in Ref. [2], reflecting much higher resolution. Three peaks near 188 eV in the resonant Auger spectrum correspond to the photoionization of valence electrons. Two relatively sharp peaks around 180 eV seem to be strongly enhanced by the resonance. In order to examine the so-called detuning effect, higher photon energy resolution is required for measuring the resonant Auger spectrum, since its spectral resolution depends on the photon energy resolution. It is planned to record high-resolution resonant Auger spectra across the resonances as a function of photon energy.
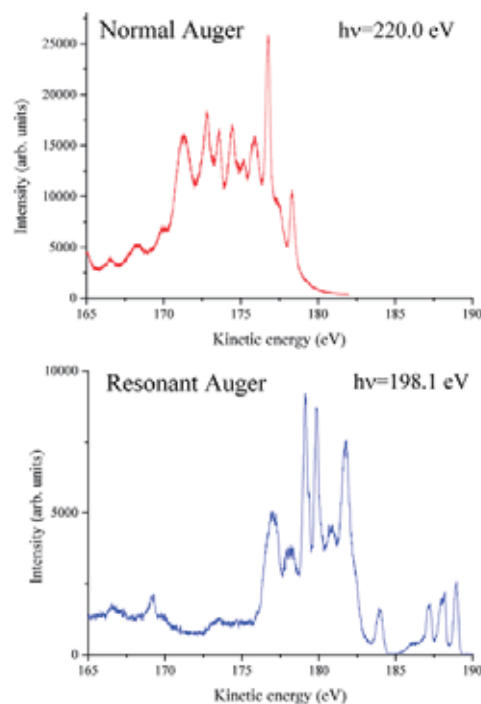

Fig. 2. Cl-L$_{23}$VV normal and resonant Auger spectra of CCl$_4$.

[1] M. de Simone *et al.*, J. Phys. B **35** (2002) 61.
[2] P. G. Fournier *et al.*, Phys. Rev. A **40** (1999) 163.

III-3. MOLECULAR SPECTROSCOPY AND DYNAMICS

Ultrafast Molecular Dissociation of Core-Excited HCl Revisited

P. Lablanquie[1], F. Penent[1], H. Iwayama[2], K. Soejima[3] and E. Shigemasa[2]

[1]LCPMR, Université Pierre et Marie Curie, 75231 Paris Cedex 05, France
[2]UVSOR Facility, Institute for Molecular Science, Okazaki 444-8585, Japan
[3]Department of Enviromental Science, Niigata University, Niigata 950-2181, Japan

Excitation of a core electron to the lowest unoccupied antibonding orbital weakens the molecular bonding and populates generally a dissociative state. Morin and Nenner demonstrated that the $3d \rightarrow \sigma*$ excitation in HBr leads to a fast neutral dissociation which can precede the Auger relaxation; in other words, one can observe 'atomic' 3d hole decays in the Br fragment [1].

In 2012 we showed that the equipment at UVSOR allows one to revisit the HBr fast dissociation with an unprecedented resolution, revealing more detailed atomic Auger peaks. Here we extend our studies and examine ultrafast dissociation following the Cl 2p core excitation in HCl.

The experiments were carried out on the soft X-ray beamline BL6U at UVSOR. The exit slit opening was set to 50 μm, which corresponds to a photon energy resolution ΔE of ~50 meV. The monochromatized radiation was introduced into a gas cell filled with sample gas. Kinetic energies of the emitted electrons were measured by a hemispherical electron energy analyzer (MBS-A1) placed at a right angle relative to the photon beam direction. The axis of the electrostatic lens of the analyzer was set to be parallel to the polarization direction of the incident light. The energy resolution of the analyzer was set to ~12 meV. Under these experimental conditions, the full width at half maximum of the vibrational fine structure for the A state of HCl^+ was measured to be ~65 meV.

Figure 1 (a) gives the resonant Auger spectrum measured on top of the $2p_{3/2} \rightarrow \sigma*$ resonance. Comparison with the off resonance spectrum (b) shows that the molecular X, A and B HCl^+ states are little affected by the resonance, and reveals new peaks which are mainly the Atomic transitions:

$$Cl\,(2p_{3/2})^{-1}\,3s^2 3p^6 \rightarrow Cl^+\,3s^2 3p^4 \quad or \quad Cl^+\,3s 3p^5$$
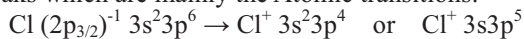
Broad structures at the foot of these peaks correspond to the 'molecular' autoionization during the HCl fast dissociation and amount to ~30% of the decays. The resonant spectrum can thus be used to retrieve the Auger spectrum associated with the decay of a 2p hole in a Cl atom. This is done in Fig. 2: (a) shows the decay of a $2p_{3/2}$ hole, as obtained on the $2p_{3/2} \rightarrow \sigma*$ resonance, while (b) measured on the $2p_{1/2} \rightarrow \sigma*$ resonance gives the decay of a $2p_{1/2}$ hole, with some contribution of the $2p_{3/2}$ hole decay. Comparison with the well-known Auger spectrum for the decay of a 2p hole in Ar in (c) is instructive as one can in this way compare the decay of a 2p hole in atoms with the same $3s^2 3p^6$ valence configuration,

but with different nucleus. One observes a richer satellite structure for Cl (Fig. 2 (a) and (b)) compared to Ar (Fig. 2 (c)), which is probably linked to the difference of the 3d orbital in each case. Calculations are required to test this idea.
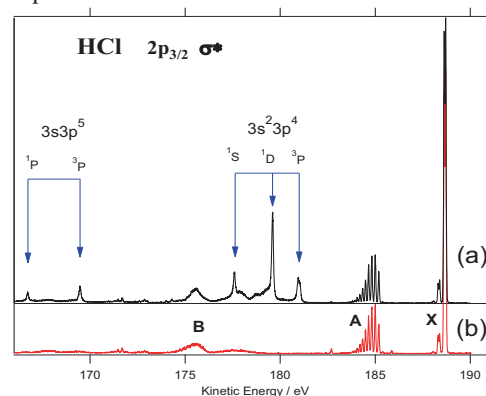

Fig. 1. (a) Resonant Auger spectrum measured on top of the $2p_{3/2} \rightarrow \sigma*$ resonance, compared to a shifted off-resonance spectrum (b). Cl atomic lines are indicated with arrows.
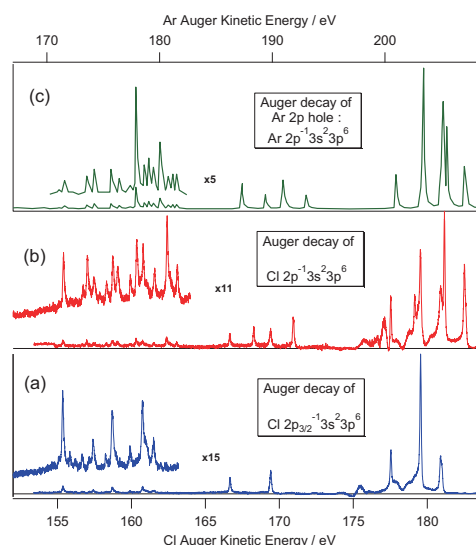

Fig. 2. Resonant Auger decay on $2p \rightarrow \sigma*$ resonances showing the atomic Auger lines for the decay of $2p_{3/2}$ and $2p_{1/2}$ holes in Cl atoms ((a) and (b)), compared to the Auger spectrum for the decay of a 2p hole in Ar (from reference [2]).

[1] P. Morin and I. Nenner, Phys. Rev. Lett. **56** (1986) 1913.
[2] H. Pulkkinen et al., J. Phys. B **29** (1996) 3033.

Dissociation Pathways of Core Excited CF_4 Molecules Studied by an Auger-Electron–Ion Coincidence Method

H. Iwayama, L. Ishikawa and E. Shigemasa

UVSOR Facility, Institute for Molecular Science, Okazaki 444-8585, Japan

When a molecule composed of light elements is irradiated by soft x-rays, an inner-shell electron in the molecule is efficiently promoted into unoccupied molecular orbitals or continua. The core-hole state thus created is quite unstable, and subsequent Auger decay process follows in general. The molecular Auger final state possesses more than one hole in the valence orbitals, which often dissociates into two or more fragments. To understand such molecular photochemistry triggered by the core-hole creation, it is indispensable to correlate the Auger final states with the dissociation pathways. For this purpose, we have developed an Auger-electron-ion coincidence apparatus, which consists of a double toroidal electron analyzer (DTA) [1] and an ion momentum spectrometer. In the present work, we have studied dissociation pathways of core-excited CF_4 molecules around carbon K edge. In particular, we have investigated whether the dissociation processes following the core-to-Rydberg excitation differ from those after the core-to-valence excitation.

The Auger-electron-ion coincidence measurements for core-excited CF_4 molecules were carried out on the undulator beamline BL6U at UVSOR. The radiation from an undulator was monochromatized by a variable included angle varied line-spacing plane grazing monochromator. The electrons ejected at 54.7˚ with respect to the electric vector of the ionization light were analyzed in energy by DTA, while ions were extracted from the interaction region into the momentum spectrometer by a pulsed electric field according to the electron detection. Arrival positions on the detector and time-of-flights of ions were recorded for every event. The pass energy of the DTA was set to 200 eV for observing resonant Auger electrons. The energy resolution was about 1.9 eV. All signals from electron and ion detectors were recorded with an 8ch TDC board. We used photon energies of 298.5 and 299.4 eV, which correspond to C $1s{\rightarrow}\sigma^*(t_2)$ (valence) and $1s{\rightarrow}3pt_2$ (Rydberg) resonances, respectively [2]. The photon bandwidth was set to be 0.03 eV.

Figure 1 shows a resonant-Auger-electron–ion coincidence map obtained at the C $1s{\rightarrow}\sigma^*(t_2)$ resonance excitation. The vertical and horizontal axes of the map correspond to the kinetic energies of Auger electrons and the mass-to-charge ratios of ions, respectively. The one-dimensional spectra displayed in the right and top panels, represent the total events for the Auger electron detection and ion mass-to-charge rations, respectively. Main fragment

ions were $CF_n^+(n{\leq}3)$ and $F_n^+(n{=}1,2)$ ions. We didn't observe CF_4^+ parent ions within the present detection time. In the Auger-electron–ion coincidence map, we found that Auger electrons with high kinetic energy correlate with large fragment ions such as CF_2^+ and CF_3^+, while Auger electrons with low kinetic energy correlate with small fragment ions such as C^+ and F^+. This means that the Auger final states with high binding energy lead to efficient C-F bond breakings. The detailed data analyses are now in progress.
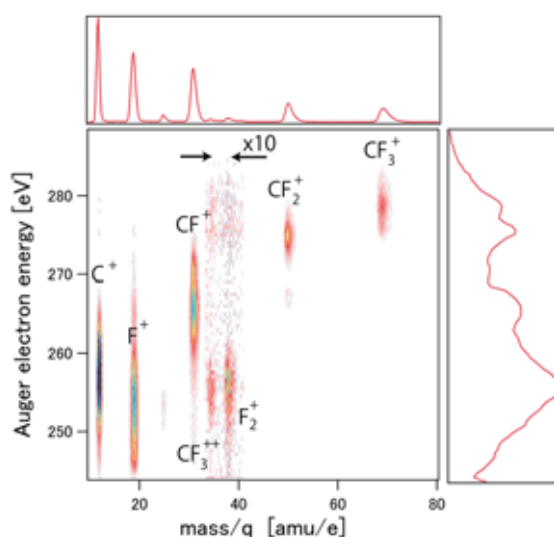

Fig. 1. Two-dimensional map for mass-to-charge ratios of ions in coincidence with resonant Auger electrons, obtained at the C $1s{\rightarrow}\sigma^*(t_2)$ resonance excitation of CF_4. The horizontal axis corresponds to mass-to-charge ratios of ions, and the vertical axis is the kinetic energies of the Auger electrons. The one-dimensional spectra shown at the right and top panels represent the total events for the Auger electron detection and the ion mass-to-charge ratios, respectively.

[1] C. Miron, M. Simon, N. Leclercq and P. Morin, Rev. Sci. Instrum. **68** (1997) 3728.
[2] R. Guillemin, W. C. Stolte, M.N. Piancastelli and D. W. Lindle, Phys. Rev. A **82** (2010) 043427.

III-3. MOLECULAR SPECTROSCOPY AND DYNAMICS

Topological Phase Transition in Ultrathin Bi Films on Bi_2Te_3 Substrates

T. Hirahara[1], M. Aitani[1], M. Yamada[1], H. Miyazaki[2], M. Matsunami[2], S. Kimura[2]
and S. Hasegawa[1]

[1]*Department of Physics, University of Tokyo, 7-3-1 Hongo, Bunkyo-ku, Tokyo 113-0033, Japan*
[2]*UVSOR Facility, Institute for Molecular Science, Okazaki 444-8585, Japan*

Topological insulators have become one of the model systems to study Dirac physics in solids. They are mathematically characterized by the Z_2 topological number with edge modes that cannot be backscattered [1]. An essential ingredient in realizing a topological insulator is the parity inversion induced by the strong spin-orbit coupling. From this viewpoint, bismuth (Bi), which is virtually the heaviest nonradioactive element, has been the main building block. Nowadays many Bi alloys are known as topological insulators. Although it is necessary to make alloys, inhomogeneity may be introduced in the grown samples. Therefore, searching for other ways to produce novel topological materials with simple, well-defined structures is important.

In this respect, driving a quantum topological phase transition [making a normal (trivial) material into a topological (nontrivial) one] in a simple system seems to be a rather smart approach. One example of such a transition is the case of Bi, where the three-dimensional (3D) trivial bulk becomes topological in two dimensions by making thin films of 1–8 bilayers (BL) [2, 3]. Another way to induce a topological phase transition is to apply pressure and change the lattice parameters slightly, which is experimentally not easy to do.

In this study, we have attempted to change the lattice constant by growing an ultrathin film. We have fabricated Bi films on Bi_2Te_3 substrates and measured the band dispersion with angle-resolved photoemission spectroscopy. Due to the small in-plane lattice mismatch between Bi and Bi_2Te_3 (~3.6 %), Bi can be grown epitaxially on Bi_2Te_3 from 1 BL [4]. Figure 1(a) shows the band dispersion of a 7 BL Bi film on Bi_2Te_3. Compared to the 7 BL Bi film grown on Si(111)-7x7 [Fig. 1(b)], the band dispersion is significantly different near the Γ point.

The change in the band dispersion of the Bi films shown in Fig. 1 can be explained by the change in the lattice constant. Our detailed LEED-IV measurements showed that due to the contraction of the in-plane lattice contraction by ~3.6 %, the out-of-plane lattice constant is expanded ~4 % [5]. The Poisson ratio, which is the ratio of the above two changes is as large as 1, meaning a very large distortion. We have further found that the lattice constant returns back to its original bulk value at ~15 BL.

The band dispersion in Fig. 1(a) is reproduced by *ab initio* calculations for a free standing Bi slab when the experimentally obtained lattice parameters are
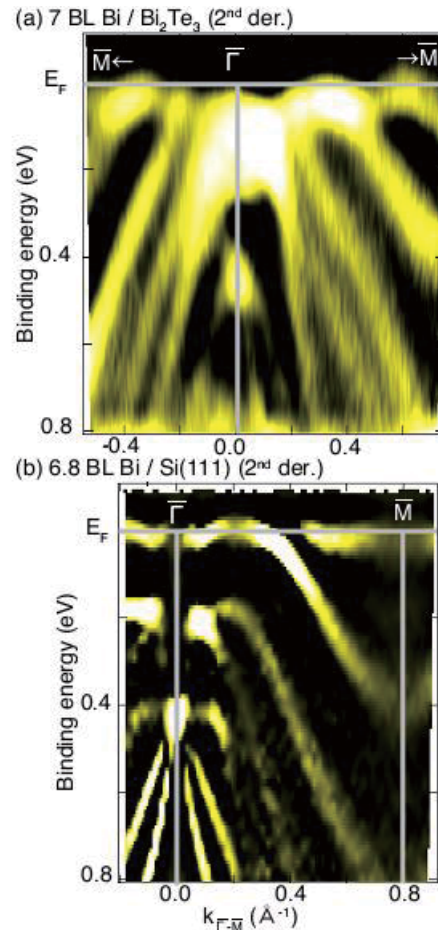

Fig. 1. The band dispersion of a 7 BL Bi(111) film grown on Bi_2Te_3 (a), and that on Si(111) (b).

used. Furthermore, by calculating the 3D Z_2 topological for this strained Bi, we have found that the originally trivial Bi becomes nontrivial. Thus it is shown that the topological properties of Bi can be changed by inducing a small change in the lattice parameters [5].

[1] M. Z. Hasan and C. L. Kane, Rev. Mod. Phys. **82** 3045 (2010).
[2] S. Murakami, Phys. Rev. Lett. **97** (2006) 236805
[3] Z. Liu *et al*., Phys. Rev. Lett. **107** (2011) 136805.
[4] T. Hirahara *et al.,* Phys. Rev. Lett. **107** (2011) 166801.
[5] T. Hirahara *et al.,* Phys. Rev. Lett. **109** (2012) 227401.

Ⅲ-4. SURFACE AND THIN FILMS

Hydrogen Reduction of Pd Catalysts Studied by Transmission Soft-X-Ray Absorption Spectroscopy

H. Kondoh[1,2], R. Toyoshima[1], K. Suzuki[1], M. Yoshida[1], H. Yuzawa[2], M. Nagasaka[2] and N. Kosugi[2]

[1]*Department of Chemistry, Keio University, Yokohama 223-8522, Japan*
[2]*Department of Photo-Molecular Science, Institute for Molecular Science, Okazaki 444-8585, Japan*

Hydrogenation of unsaturated hydrocarbon is one of key reactions both in the fundamental organosynthesis and in the chemical industry. Pd nanoparticles supported on amorphous carbon are well known as good catalysts for hydrogenation using atmospheric H_2 gas. Also Pd has a capability to absorb hydrogen in the bulk. Recently it was demonstrated that the absorbed hydrogen has a close relation to the catalytic activity for the hydrogenation of unsaturated hydrocarbon at the surfaces [1]. Furthermore, carbonaceous species included in the Pd catalysts give significant effects on the hydrogen absorption and hence on the hydrogenation activity. The oxidation state of Pd should be also important to the activity. However, chemical behavior of the Pd catalysts has been hardly observed under gas flow conditions. In this work, we studied Pd nanoparticles and Pd porous films from the viewpoint of chemical state of oxygen adsorbed on and/or included in the Pd catalysts under atmospheric H_2 gas flow conditions by means of transmission soft-x-ray absorption spectroscopy.

Transmission NEXAFS spectra were measured at BL3U using a photodiode detector mounted in He path [2]. The Pd nanoparticles were supported on amorphous carbon and the hydrogenation activity was checked for butene at 295 K with a flow cell and mass spectrometry. The Pd porous film was prepared by temporal immersion of a Pd foil into aqua regia and subsequent rinses with pure water and acetone. These Pd catalysts were loaded in the flow cell with a sandwiched configuration between two Si_3N_4 windows of 100 nm thickness.

O K-edge transmission NEXAFS spectra for the Pd nanoparticles supported on amorphous carbon were taken at 295 K before and under H_2 flow as shown in Fig. 1. Before H_2 flow, several peaks (A-D) are observed at a lower energy range from 532 to 538 eV, which are tentatively associated with adsorbed O-containing species on the Pd surfaces and surface oxides of Pd nanoparticles, while under H_2 flow these peaks diminish significantly. This decrease in intensity indicates reduction and removal of the O-containing surface species under H_2 flow even at room temperature. A prominent and broad peak is observed at around 540 eV. This peak is attributed to oxygen atoms of a Pd oxide included in the particles. This oxide peak does not disappear even under H_2 flow, which suggests that the Pd oxide included in the particles is not reduced even under hydrogen-rich

conditions. A similar trend was observed for a Pd porous film as shown in Fig. 2: The low-energy peaks (A-D) almost disappear, while main structures at 540 eV and 550-560 eV remain under H_2 flow.

The next step is in-situ monitoring of behavior of included carbon as well as included oxygen under hydrogenation reaction conditions, which will reveal the relation between the presence of carbon and oxygen in the Pd catalysts and the hydrogenation activity.
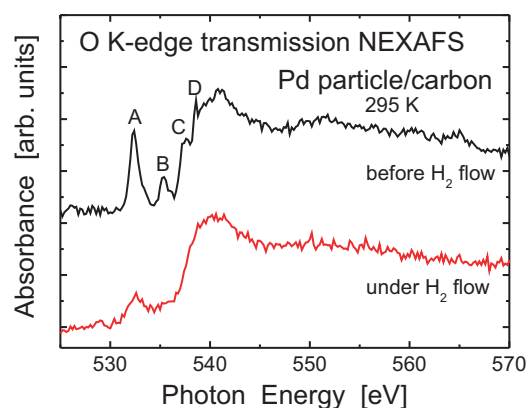

Fig. 1. O-K transmission NEXAFS spectra taken for Pd nanoparticles supported on amorphous carbon before (upper) and under (lower) H_2 gas flow (200 SCCM).
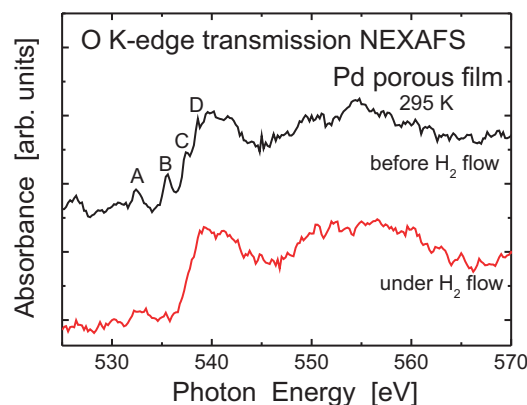

Fig. 2. O-K transmission NEXAFS spectra taken for a Pd porous film before (upper) and under (lower) H_2 gas flow (200 SCCM).

[1] M. Wilde *et al.,* Angew. Chem. Int. Ed. **47** (2008) 9289.
[2] M. Nagasaka *et al*., J. Electron. Spectrosc. Relat. Phenom. **177** (2010) 130.

The Study on Nickel-Borate Oxygen Evolution Catalyst by Soft X-ray Electrochemical XAFS

M. Yoshida[1], T. Mineo[1], T. Yomogida[1], H. Yuzawa[2], M. Nagasaka[2], N. Kosugi[2] and H. Kondoh[1,2]

[1]Department of Chemistry, Keio University, Yokohama 223-8522, Japan
[2]Department of Photo-Molecular Science, Institute for Molecular Science, Okazaki 444-8585, Japan

Electrochemical water splitting to hydrogen and oxygen gases is an attractive and promising approach toward highly efficient energy conversion. This reaction is derived from two half reactions of hydrogen evolution reaction (HER) and oxygen evolution reaction (OER). However, many electrode materials are known to be not active for OER due to the high overpotentials. Recently, a nickel-borate thin film was reported as an efficient electrocatalyst for OER [1]. The local structure around the nickel ions of this thin film was revealed by Ni K-edge XAFS measurements, while that around B species is still unclear. The structure and chemical state of the B species may change depending on the film growth. Thus, in this study, the nickel-borate thin film were investigated by B K-edge XAFS measurements under potential control conditions.

The soft X-ray electrochemical XAFS measurements were performed with the transmission mode at BL3U of UVSOR, according to the previous work [2]. Au/Cr/Si$_3$N$_4$ thin film substrates were used as working electrodes. A home-made electrochemical cell was used with a Pt mesh counter electrode and a Ag/AgCl (saturated KCl) reference electrode in a potassium borate aqueous solution.

Figure 1 shows B K-edge XAFS spectra taken for nickel-borate thin film electrodeposited at 2.0 V vs Ag/AgCl. Prominent peaks associated with B species were observed at ca. 192 eV. The peak positions were slightly different between the samples before and after cyclic voltammetry measurements, indicating that the chemical state of B in the nickel-borate thin film is likely to change by potential control.

In-situ B K-edge XAFS spectra for the nickel-borate deposition on the Au/Cr/Si$_3$N$_4$ electrode were measured as a function of time in a potassium borate aqueous solution containing nickel nitrate at 0.9 V, as shown in Fig. 2. A broad peak grows gradually at ca. 192 eV, suggesting that the nickel-borate thin film was deposited on the Au/Cr/Si$_3$N$_4$ electrode. The B species at the solid-liquid interface was successfully detected under potential control for the first time by the in-situ B K-edge XAFS measurement. This in-situ technique will be applied to investigation of structures and chemical states of nickel-borate thin films under working conditions as the OER electrocatalyst.
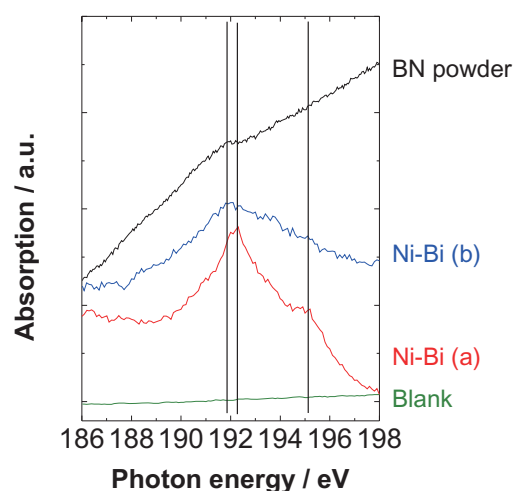

Fig. 1. B K-edge XAFS spectra taken for the nickel-borate thin film and BN powder reference. The samples were measured before (a) and after (b) cyclic voltammetry.
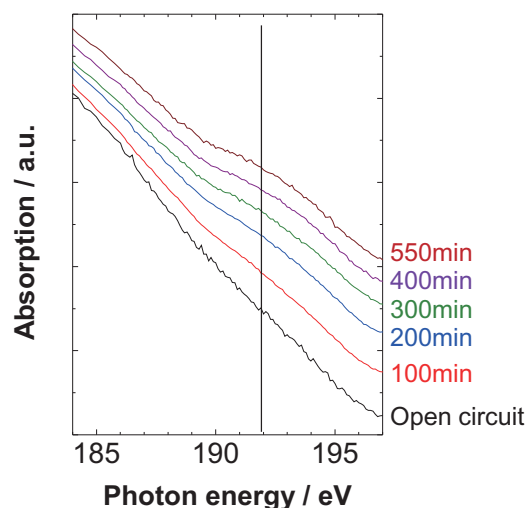

Fig. 2. Time course of in-situ B K-edge XAFS spectra during electrodeposition of nickel-borate thin film.

[1] D. K. Bediako *et al*., J. Am. Chem. Soc. **134** (2012) 6801.
[2] M. Nagasaka *et al*., J. Electron. Spectrosc. Relat. Phenom. **177** (2010) 130.

III-4. SURFACE AND THIN FILMS

Photoionization Threshold Measurement of Porphyrin Derivatives at the Surface of Water

T. Ishioka, K. Tomita, T. Morimoto and A. Harata

Molecular and Material Sciences, Kyushu University, Kasuga, Fukuoka 816-8580, Japan

Porphyrin derivatives play import roles in natural science such as photosynthesis and energy transfer systems in a cell. A number of research works have been carried out utilizing the ring molecule for converting photon energy to chemical structure [1]. In such cases, porphyrin molecules are usually dissolved into some kinds of solvents. Wavelength regions effective for reactions are limited by light absorption of the solvents. Water surfaces are ideal environments for utilizing photon energies since loss of photon energy can be minimized. Moreover, source molecules for chemical synthesis are easily supplied from both gas phase and solution. However, physical and chemical properties of such photoactive molecules are usually known for gas phase or solution phase. The properties of surface phase are not easily accessible, which are essential for designing photoinduced reactions at the surface. In this work, photoionization behavior of porphyrin derivatives has been analyzed by utilizing synchrotron light source. Solvation state of such molecules at the surface of water are also discussed by comparing the determined threshold values to those in vacuum.

In a typical photoionization measurement, mono-chromated light was emitted from the chamber to a He-purged cell through an MgF_2 window. The range of light energy was in 4-8 eV. The emitted light was reflected with an Al mirror and vertically irradiated on the sample surface. High voltage (400V) was applied between the mesh electrode that was 5 mm above the liquid surface and a Pt cell with 25 mm in diameter. Benzene solutions of porphyrin derivatives (tetraphynylporphyrin (TPP), Zn complex of TPP (Zn-TPP)) were prepared at the concentration of 1×10^{-4} M. The solution was added by 100 μL dropwisely on the surface of 5 mL water. After evaporating benzene for 5 min, the photoinduced current (~ 0.1 pA) was measured by a picoammeter (Keithley model 428).

Measured photoionization spectra were analyzed and threshold values were determined by fitting the spectra to the empirical formula of $I = (E - E_{th})^{2.5}$. Figure 1 shows the obtained photoionization current of Zn-TPP. The curve fits well and the threshold value was determined to 5.50 ±0.01 eV from repeated experiments (n = 5). The threshold values are listed in Table 1 as well as the reported values in vacuum [2].

All measured threshold lies higher in a vacuum because each molecule (E_{th}) satisfy the formula in the case of emitting electron into the air, $E_{th} = I_p + P^+$ where I_p and P^+ are the ionization potential and polarization energy of the photoionized molecule, respectively. P^+ is always negative since the polarization is exothermic. In the porphyrin case, the observed value P^+ is smaller than that for aromatic hydrocarbon (perylene, Table 1) because polarization energy reciprocally depends on the size of molecule and the size of porphyrin is approximately 2.1 times larger than perylene. However, this value is not enough for explaining the small polarization energy (1/2.5-3.0) compared to perylene. Further researches are now in progress for analyzing the result.
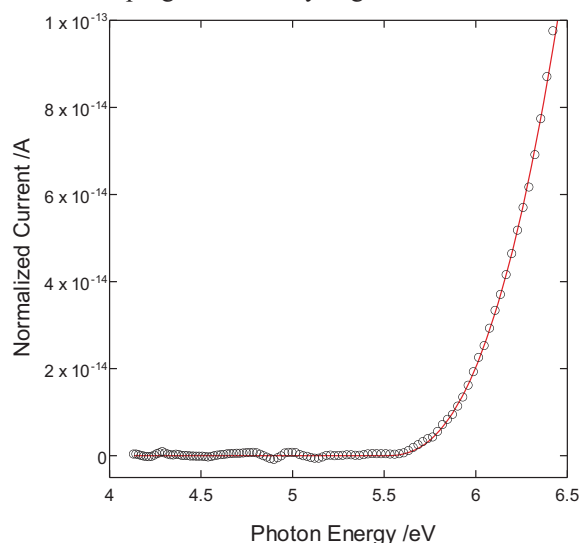

Fig. 1. Measured photoinduced current of Zinc Tetraphenylporphyrin at the surface of water. Inserted curve is the nonlinear fit using the formula $I = I_0 (E - E_{th})^{2.5}$.

Table 1. Photoionization threshold (E_{th}) of porphyrin derivatives at the water surface and their ionization potential (IP) in vacuum.

	E_{th} / eV	IP / eV
TPP	5.65 ± 0.04	6.3 ± 0.2*
Zn-TPP	5.50 ± 0.01	6.0 ± 0.2*
Pyrene	5.30 ± 0.04**	6.960

*) Ref.[2] **)Ref.[3]

[1] N. Inoue, T. Ishioka and A. Harata, Chem. Lett. **38** (2009) 358.
[2] Y. Nakano *et al.*, Chem. Phys. Lett. **39** (1976) 358.
[3] T. Ishioka, K. Tomita, Y. Imanishi and A. Harata, UVSOR Activity Report **39** (2012) 63.

Multi-Electron Spectroscopy for Condensed H₂O Molecules

Y. Konosu, M. Sawa, K. Soejima and Y. Hikosaka

Niigata University, Niigata 950-2181, Japan

Slow electron formation has received particular attention, in connection with DNA strand breaks in living cells exposed to ionizing radiations. The DNA strand breaks are caused, not only by direct ionization of the DNA itself, but also by the impact of secondary particles produced by the radiation. Here, the most abundant secondary particles are electrons emitted from the ionization of water molecules and biomolecules surrounding the DNA, where the majority of the electrons have kinetic energies of less than 20 eV. The efficiency of the DNA strand breaks is strongly dependent on the incident electron energy of the impacting electrons, due to its resonant character, and therefore the knowledge of the energy distribution of the slow electrons is important in modeling the radiation damages of living cells. In this study, we have investigated the slow electron emission process of condensed H₂O irradiated with soft x-ray.

The experiments were carried out by using a magnetic bottle-type electron energy analyzer. A copper wire of a 0.3-mm diameter was placed at the focus point of the monochromatized synchrotron radiation, and was cooled with liquid nitrogen, in order to condense H₂O vapor admitted into the chamber. Figure 1 shows total electron yield spectra around the O1s range, measured before and after the cooling of the copper wire. The spectrum measured before the cooling shows structures attributable to electrons from CuO formed on the copper wire surface. After cooling, the spectral feature changes drastically, implying that H₂O molecules are adsorbed on the surface.

The energy correlation between two electrons emitted from condensed H₂O is shown in Fig. 2. On the map clear structures due to coincidences between photoelectrons and Auger electrons are seen, which proves that the magnetic bottle-type electron energy analyzer enables us to investigate the energy correlations among electrons emitted from condensed H₂O. Figure 3 shows the energy correlation between photoelectrons and slow-electron observed in triple coincidence events including Auger electrons. The right panel represents the slow electron spectrum extracted by integrating the coincidence yields in the horizontal range for the O1s photoelectrons. It is estimated, from the total coincidence counts in this curve and the photoelectron yields, that the decay path emitting the slow electrons is about 0.18% of the $O1s^{-1}$ creation. This ratio for gas-phase H₂O is reported to about 13% [1], and the emission of slow electron is reduced in the condensation. The reasons of the less efficient sole electron formation from the condensed H₂O are as follows. In the case of

gas-phase H₂O, the main source of slow electron is autoionizing O^* fragment formed by double OH-bond breaking at highly-excited H_2O^{2+} states populated after Auger decay of the O1s core-hole state. This dissociation at the H_2O^{2+} states should be largely inhibited in the condensed phase by the neighboring H₂O molecules. Moreover, while such dissociations could occur and emit slow electrons, a considerable part of the slow electrons would fail to escape from the condensed H₂O molecules.
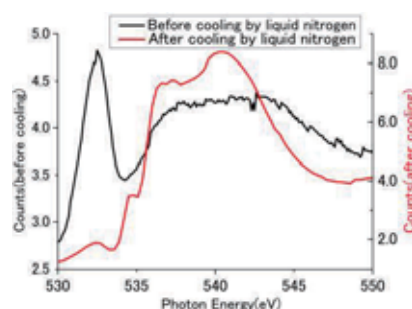

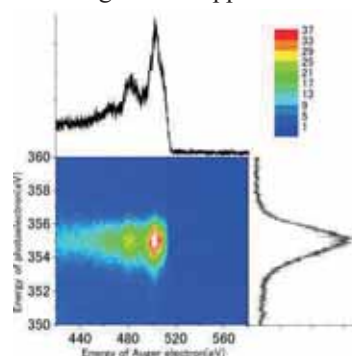Fig. 1. Total electron yield spectra measured before and after the cooling of the copper wire.

Fig. 2. Energy correlation between photoelectrons and Auger electron emitted from condensed H₂O. The photon energy was set to 900.1 eV.
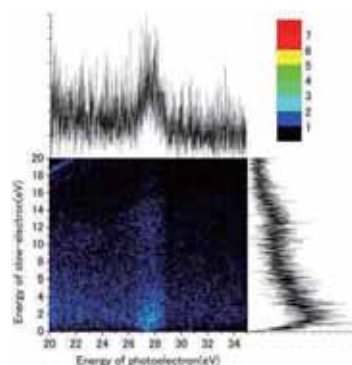

Fig. 3. Energy correlation between photoelectrons and slow-electron.

[1] Y. Hikosak *et al*., J. Chem. Phys. **137** (2012) 191101.

Ⅲ-4. SURFACE AND THIN FILMS

Molecular Orientation and Magnetic Property of Vanadium Phthalocyanine Multilayer on a Silver Surface Studied by XAS/XMCD

K. Eguchi[1], Y. Takagi[1, 2], T. Nakagawa[1, 2] and T. Yokoyama[1, 2]

[1] School of Physical Sciences, The Graduate University for Advanced Studies (SOKENDAI), Okazaki 444-8585, Japan

[2] Division of electronic structure, Institute for Molecular Science, Okazaki 444-8585, Japan

3d transition metal phthalocyanines (TMPcs) have attracted much interest in recent years because they show characteristic electronic, optical and magnetic properties. In our group, we have especially focused on the magnetic properties of TMPcs to understand their magnetic coupling in their films and between TMPcs and ferromagnetic surfaces [1-3]. For instance, iron phthalocyanine (FePc) in multilayer shows a ferromagnetic behavior [2]. Recently, we have succeeded in preparing a vanadium phthalocyanine (VPc) multilayer. In this study, we have investigated the molecular orientation and magnetic property of the VPc multilayer by means of x-ray absorption spectroscopy (XAS) and x-ray magnetic circular dichroism (XMCD).

The experiments were carried out in an ultra high vacuum condition at beam line 4B. A silver film was prepared on a clean Cu(111) substrate by the electron bombardment evaporation at room temperature (RT). Purified H_2Pc and Vanadium atoms were deposited on the substrate at RT using Knudsen cell and electron beam evaporation source, respectively. The N K-edge and V L-edge XAS/XMCD measurements were done using a system (JANIS: 7THM-ST-UHV) with a superconducting magnet and a liq. He cryostat. The XAS and XMCD spectra were taken at 5 K and the XMCD spectra were recorded with reversal magnetic field.

Figure 1 shows angle dependence of N K-edge XAS spectra of 10ML VPc. The π^* resonance intensity is observed at normal incidence and the intensities increase with increasing the incident angle. This result means that the framework of the phthalocyanines is slantingly tilted from the substrate surface plane.

Figure 2 shows V $L_{2,3}$-edge XMCD spectra of 10ML-VPc and VOPc [4] taken at an external magnetic field of 5 T and an incident angle of 55 degree. The spectra of VPc are obviously different from ones of VOPc at both V L-edge and O K-edge. The XMCD signal of VOPc is observed because it has one electron in 3d-orbital. On the other hand, that of VPc is very small in comparison to that of VOPc even though a vanadium atom in VPc has 3 electrons in 3d-orbital. This result might indicate that vanadium atoms in VPc are antiferromagnetically coupled. To reveal it, we need to investigate for the case of 1ML-VPc which has no magnetic interaction between them.
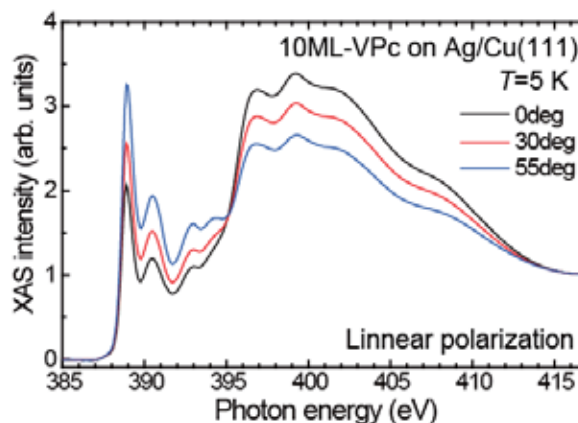

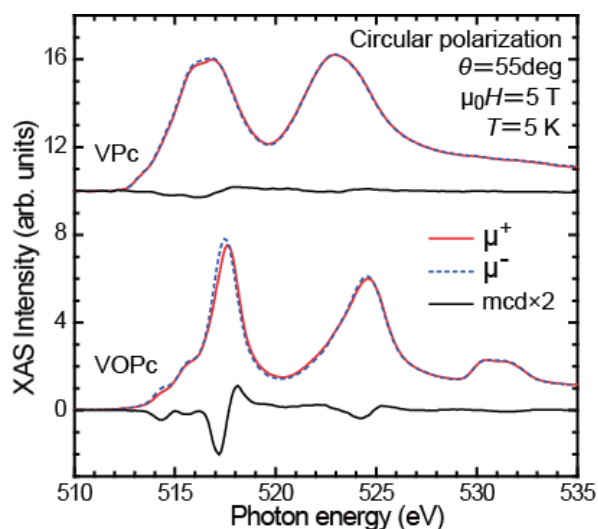Fig. 1. The angle dependent N K-edge XAS spectra of VPc multilayer.

Fig. 2. V $L_{2,3}$- (and O K) edges XAS and XMCD spectra of VPc and VOPc multilayers taken at the incident angle of 55 deg, μ_0H=5 T and T=5 K.

[1] I. Yamamoto, K. Eguchi, Y. Takagi, T. Nakagawa and T. Yokoyama, UVSOR Activity Report **37** (2010) 74.
[2] Y. Takagi, K. Eguchi, T. Nakagawa and T. Yokoyama, UVSOR Activity Report **38** (2011) 67.
[3] Y. Takagi, K. Eguchi, T. Nakagawa and T. Yokoyama, UVSOR Activity Report **39** (2012) 66.
[4] K. Eguchi, Y. Takagi, T. Nakagawa and T. Yokoyama, UVSOR Activity Report **39** (2012) 65.

XMCD Studies of Magnetization of Co Ultrathin Films on W(110)

T. Nakagawa[1, 2, 3], H. Nakano[2, 4], K. Eguchi[2, 3], Y. Takagi[2, 3] and T. Yokoyama[2, 3]

[1]*Department of Molecule and Material Sciences, Kyushu University, Kasuga 816-8580, Japan*
[2]*Institute for Molecular Science, Okazaki 444-8585, Japan*
[3]*The Graduate University for Advanced Studies (SOKENDAI), Okazaki 444-8585, Japan*
[4]*Department of Chemistry, Graduate School of Science, Kyoto University, Kyoto 606-8502, Japan*

Magnetic properties in ultra thin films have attracted interests because of their characteristics due to low dimensionality [1-3]. Co ultrathin films, including nano wire and nano dots, have been extensively studied since they exhibit large magnetic anisotropy [1, 2]. Co films grown on W surfaces have been investigated since it shows sharp interface without no alloying. One of the long standing issues on Co/W(110) is vanishing magnetization below 2 monolayer (ML).

We performed experiments at BL4B using x-ray magnetic circular dichroism (XMCD) end station equipped with a superconducting magnet under $H = 5$ T and $T_s = 5$ K. All the measurements were done below 1×10^{-10} Torr. The Co films were grown on W(110) at room temperature, which was cleaned by repeated cycles of oxidation at 1500 K and subsequent annealing at 2200 K. The Co film shows psedomorphic structure bwlow 0.6 ML, and above this coverage it shows close packed structures. All the XMCD results are taken on the close packed structures.

Figure 1(a) shows x-ray absorption spectra (XAS) using circularly polarized light with opposite magnetization directions and XMCD spectrum for 0.9 ML. The 0.9 ML Co film shows no detective XMCD signal even in the low temperature (5 K) and high magnetic field (5 T). This result ensures that the Co film is not in a ferromagnetic order or has extremely high magnetic anisotropy, but the latter case is unlikely since the magnetic anisotropy greater than 50 T is necessary to explain the negligible XMCD signal. This vanishing XMCD result is in good agreement with previous studies [1, 2].

Figure 1(b) shows a magnetization curve taken on 1.7 ML Co film. The 1.7 ML Co film exhibits perpendicular magnetic anisotropy with a coercive field of 1.7 T, which is large compared to that of the bulk Co (~0.1 T). Thus the magnetization easy axis for 1.7 ML Co film is perpendicular to the surface, which is revealed for the first time. In the previous measurements the Co film did not show ferromagnetic states between 1 and 2 ML. The failure to detect the perpendicular magnetization may come from its large coercivity.

Figure 1(c) shows a magnetization curve for 4 ML Co film. This shows in-plane magnetization with 1.5 μ_B, which is in agreement with the previous results [1, 2].

These result demonstrates that the Co film grown on W(110) surface undergoes a spin reorientation transition from the perpendicular to the in-plane axis with increasing the Co coverage. Below 1 ML the total magnetization is almost zero. The XMCD measurement rules out the existence of huge anisotropy. The vanishing magnetization would be caused by quenching of Co magnetic moment due to a strong hybridization between Co and W or anti-ferromagnetism (or spin density waves).

[1] G. Garreau, M. Farle, E. Beaurepaire and K. Baberschke, Phys. Rev. B **55** (1997) 330.
[2] A. Kleibert, V. Senz, J. Bansmann and P. M. Oppeneer, Phys. Rev. B **72** (2005) 144404.
[3] T. Nakagawa, Y. Takagi, T. Yokoyama, T. Methfessel, S. Diehl and H.J. Elmers, Phys. Rev. B **101** (2012) 144418.
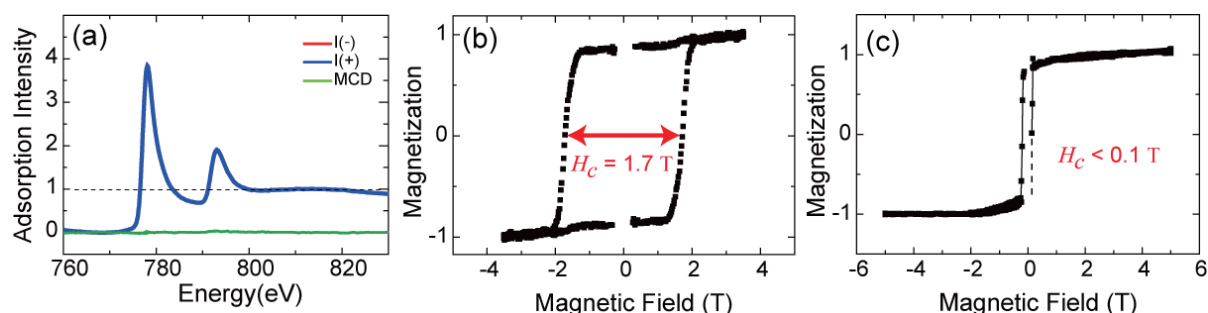
Fig. 1. XMCD results on Co/W(110) surfaces. (a) x-ray adsorption and XMCD result on Co(0.9 ML)/W(110) surface, showing no dichroic signal. (b) A magnetization curve obtained from XMCD measurement on Co(1.7 ML)/W(110) surface. Magnetic field is applied normal to the surface. (c) A magnetization curve obtained from XMCD measurement on Co(4.0 ML)/W(110) surface. Magnetic field is applied along the direction which is tilted 30° to the [1-10] direction.

X-ray Magnetic Circular Dichroism Studies of Monolayer Iron Phthalocyanine Molecules Grown on Single and Bilayer Graphene

M. Ohtomo[1], Y. Matsumoto[1], S. Entani[1], P. V. Avramov[1], H. Naramoto[1], T. Yokoyama[2] and S. Sakai[1]

[1]*Advanced Science Research Center, Japan Atomic Energy Agency, Tokai-mura, Ibaraki 319-1195, Japan*
[2]*Department of Materials Molecular Science, Institute for Molecular Science, Okazaki, Aichi 444-8585, Japan*

Graphene is a promising spintronics material for its long spin diffusion length as a consequence of small spin-orbit coupling [1]. There are also numbers of reports on the functionalization of graphene using finite geometries, adatoms or defects [2]. The adsorption of magnetic adatoms or molecules, for example, open the possibility for controlling the intrinsic spintronic properties of graphene through so-called Ruderman-Kittel-Kasuya-Yoshida ₁ (RKKY) coupling between magnetic molecules or defects.

Previous theoretical works on the RKKY coupling in graphene [3-5] have shown that for all bipartite lattices at halffilling, the RKKY coupling is ferromagnetic (FM) for impurities on the same sub-lattice but antiferromagnetic (AFM) for impurities on different sub-lattices. However, there are no reports of the experimental observation of RKKY interaction in graphene. In our beam time, we performed series of X-ray magnetic circular dichroism (XMCD) measurements on ultra-thin magnetic molecules/graphene hetero structure.

The monolayer film of Iron phthalocyanine (FePc) was grown on three graphene samples: bilayer graphene (BLG) on Cu(111), single layer graphene (SLG) on SiC(0001) and highly ordered pyrolytic graphite (HOPG) as a reference. The samples were thoroughly degassed in ultra-high vacuum chamber at 500˚C before the deposition of FePc.

Fig. 1 shows Fe $L_{2,3}$-edge XMCD of monolayer FePc/SLG hetero structure at magic angle (55˚) incidence (MI). The spectrum shape of $L_{2,3}$ edge adsorption was identical with that of FePc textured thin film [6], which suggest ^3E_g ground state meaning small interaction with the substrate. Similar X-ray adsorption spectra were observed for FePc/BLG and FePc/HOPG as well. Due to large orbital moment of FePc molecules, smaller XMCD signal was observed in case of normal incidence (NI) condition. The magnetic field dependence of the XMCD signals is shown in Fig. 2 for FePc/BLG sample, which did not show saturation behavior up to 5 T.

In order to confirm the possibility of super paramagnetic component, we assumed the blocking temperature around 50 K and measured XMCD at "field cool" and "zero-field cool" conditions, which showed no differences within experimental error (not shown). This result indicates two possibilities, that is, the blocking temperature was larger than 50 K, or magnetic coupling was negligibly small. It was recently reported that the conduction electrons in graphene interact with magnetic defects (carbon atomic vacancies) thorough Kondo effect [7]. This report together with our XMCD results suggest that the transport property of FePc/graphene nano composite should be investigated as well in order to understand the nature of electron-electron interaction in the system.
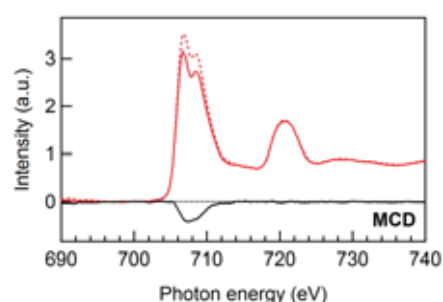

Fig. 1. Fe $L_{2,3}$-edge XMCD spectra of monolayer FePc/SLG hetero structure. The temperature was 5.4 K with applied magnetic field of ±50 kOe.
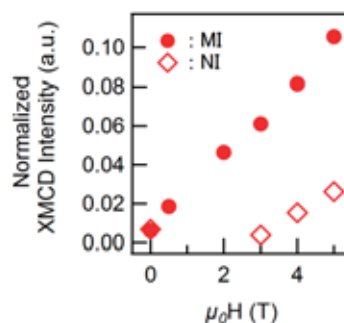

Fig. 2. The magnetic field dependence of XMCD signals in case of FePc/BLG nano-composite. The temperature was 5.5 K during the measurement.

[1] B. Dlubak *et al.*, Nature Phys. **8** (2012) 557.
[2] O. V. Yazyev, Reports on Progress in Physics **73** (2010) 056501.
[3] A. M. Black-Schaffer, Phys. Rev. B **81** (2010) 205416.
[4] E. Kogan, Phys. Rev. B **84** (2011) 115119.
[5] M. Sherafati *et al.*, Phys. Rev. B **84** (2011) 125416.
[6] J. Bartolomé *et al.*, Phys. Rev. B **81** (2010) 195405.
[7] J. H. Chen *et al.*, Nature Phys. **7** (2011) 535.

Temperature Dependence of the Electronic Structure
of K-doped EuO Ultrathin Film

H. Momiyama[1], H. Miyazaki[2], T. Hajiri[1,3], M. Matsunami[3,4],
T. Ito[1] and S. Kimura[3,4]

[1]*Graduate School of Engineering, Nagoya University, Nagoya 464-8603, Japan*
[2]*Center for Fostering Young and Innovative Researchers, Nagoya Institute of Technology, Nagoya 466-8555, Japan*
[3]*UVSOR Facility, Institute for Molecular Science, Okazaki 444-8585, Japan*
[4]*School of Physical Sciences, The Graduate University for Advanced Studies (SOKENDAI), Okazaki 444-8585, Japan*

Europium monoxide (EuO), a ferromagnetic semiconductor, with Curie temperature (T_C) of 69 K, is attracting attention due to its anomalous magneto-optical and transport properties [1, 2]. Especially, T_C achieves to as high as 200 K in the electron doping case, recently. Therefore EuO is one of the candidate compounds for next-generation spintronics applications such as spinfilter. So far, we successfully fabricated single-crystalline EuO ultrathin films with a few atomic layers for device development by using molecular beam epitaxy (MBE) method. Furthermore, we have performed angle-resolved photoemission spectroscopy (ARPES) to clarify the electronic structure and its relation to the anomalous properties. Consequently, we revealed that the T_C decreases with reducing the thickness because of the weakening of hybridization strength of Eu $4f$ – O $2p$ and Eu $4f$ – Eu $5d$ [3].

In this study, we had fabricated K-doped EuO ultrathin film to elevate T_C. And we performed ARPES at the beamline BL5U of UVSOR-Ⅲ combined with the MBE system.

Figure 1 shows the temperature-dependent ARPES spectra of single-crystalline K-doped EuO ultrathin film (5nm) measured at hν = 38 eV, which corresponds to the trace around the X point. Eu 4f state has two structures at 1.4 eV (A) and 2.2 eV (B) binding energies. According to the previous research on EuO single-crystalline ultrathin film (5nm) [4], the former originates from the Eu $4f$ – O $2p$ and Eu $5d$ hybridized states being attributed to the magnetic property, while the latter from the bare Eu $4f$ states. In Fig. 1, we found that the feature A gradually shifts to the lower binding-energies below 100 K. The observed shift could be originated in the exchange energy splitting below T_C of around 100 K. In turn, it is suggestive of the elevated T_C on the K-doped EuO than EuO ultrathin film. To clarify the detailed effect of K-doping, further studies are intended.
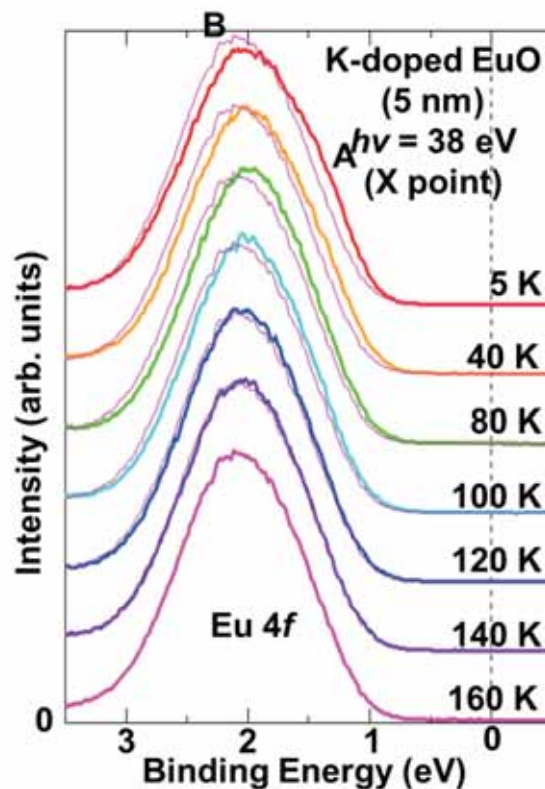

Fig. 1. Temperature dependent ARPES spectra of K-doped EuO ultrathin film (5nm) measured at hν = 38 eV. The thin lines are ARPES spectra in 160 K for comparison.

[1] N. Tsuda *et al*., *electronid Conduction in Oxides* (Springers College) (1976).
[2] A. Mauger *et. al.,* J. Phys. (paris) **39** (1978) 1125.
[3] H. Miyazaki *et al*., UVSOR Activity Report **39** (2012).
[4] H. Miyazaki *et al*., Phys. Rev. Lett. **101** (2009) 227203.

Ⅲ-4. SURFACE AND THIN FILMS

Soft X-ray Photoelectron Spectroscopy Study of Fe$_2$P(0001)

K. Edamoto[1, 2] and Y. Sugizaki[1]

[1]*Department of Chemistry, Rikkyo University, Nishi-Ikebukuro, Toshima-ku, Tokyo 171-8501, Japan*
[2]*Research Center for Smart Molecules, Rikkyo University, Nishi-Ikebukuro, Toshima-ku, Tokyo 171-8501,Japan*

The surface properties of transition metal phosphides (TMPs) have attracted much attention because these materials have been shown to have high catalytic activities for HDS and HDN [1]. Of all TMPs studied thus far, Ni$_2$P has the highest catalytic activity, while that of Fe$_2$P has been found to be very low [1]. The high catalytic performance of Ni$_2$P has been proposed to arise from the stabilization of active Ni sites induced by segregation of substrate P atoms toward the surface [2]. In order to elucidate the origin of the high activity of Ni$_2$P, we think that it is useful to elucidate the difference in surface properties of Ni$_2$P and Fe$_2$P. However, in contrast to the accumulation of data on Ni$_2$P, very limited information is available as to the Fe$_2$P surfaces. In this work, we performed a soft X-ray photoelectron spectroscopy (SXPES) study on Fe$_2$P(0001).

The experiments were performed at BL-5U of UVSOR, Institute for Molecular Science. The photoelectrons were collected by an electron energy analyzed of hemispherical type (MBS A-1), using an angle-integrated mode (acceptance angle of ±20°). The Fe$_2$P single-crystal was grown by Dr. S. Otani of National Institute for Materials Science. The sample was cut at an orientation of (0001) by spark erosion, and the surface was polished mechanically to a mirror finish. The surface was cleaned by several cycles of Ar$^+$ ion sputtering and annealing (600℃) in the UHV system.

Figure 1 shows SXPES spectra of Fe$_2$P(0001) measured at various photon energies of 48 – 60 eV. A clear cut-off at the Fermi edge is observed independent of the photon energy, indicating a metallic nature of Fe$_2$P. A band is observed at 0 – 4 eV independent of *hv*. The band is ascribed to a Fe 3d – P 3p hybrid band (main band). Satellite peaks are observed at 5 and 7 eV, and these peaks are increased in intensity around the photon energy region of Fe 3p photoexcitation threshold (*hv* = 54 eV). Therefore, the satellites are associated with the photoemission process including the Fe 3p – 3d photoexcitation and the following Fe 3d electron emission through a super-Coster-Kronig decay. At *hv* > 56 eV, an additional band composed of photoelectrons with constant kinetic energy (44 – 45 eV) is observed, and the band is ascribed to a Fe MVV Auger peak.

The overall spectral features of Fe$_2$P(0001) are similar to those of Ni$_2$P(0001) [3]. In Fig. 2, the normal-emission spectrum of Ni$_2$P(0001) is shown together with the spectrum of Fe$_2$P(0001). Both spectra are measured at *hv* = 48 eV. For Ni$_2$P(0001),

the main band is also observed at 0 – 4 eV. However, the main band is more stabilized and DOS around E$_F$ is more suppressed for Ni$_2$P(0001). It is considered that the stabilization of Ni 3d levels is essential to prevent the accumulation of S atoms on active metal sites in HDS for Ni$_2$P, which is less effective for Fe$_2$P.
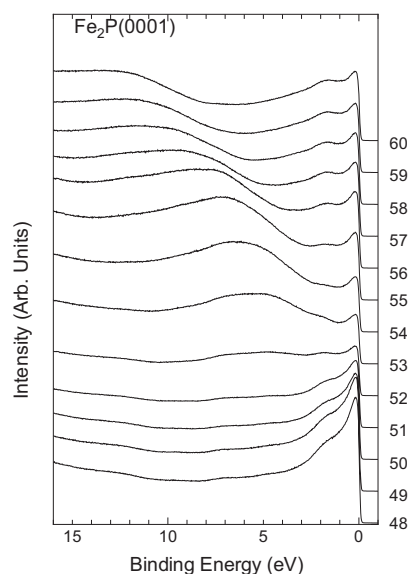

Fig. 1. Valence band spectra of Fe$_2$P(0001).
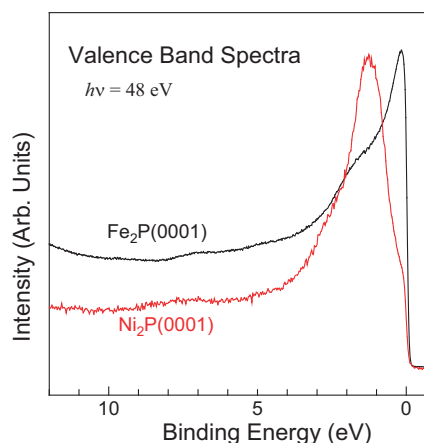

Fig. 2. Comparison of valence band spectra of Fe$_2$P(0001) and Ni$_2$P(0001).

[1] S. T. Oyama, J. Catal. **216** (2003) 343.
[2] K. Edamoto, Appl. Surf. Sci. **269** (2013) 7.
[3] K. Edamoto *et al.,* Solid State Commun. **148** (2008) 135.

Characterization of Electronic Structures of Ge and $Ge_{1-x}Sn_x$ Surfaces by Using Angle-Resolved Photoelectron Spectroscopy

O. Nakatsuka[1], S. Ike[1], T. Asano[1], M. Kurosawa[1,2], N. Taoka[1],
M. Matsunami[3], S. Kimura[3] and S. Zaima[1]

[1]*Graduate School of Engineering, Nagoya University, Furo-cho, Chikusa-ku, Nagoya 464-8603, Japan*
[2]*JSPS Research Fellow, 5-3-1 Kojimachi, Chiyoda-ku, Tokyo 102-0083, Japan*
[3]*UVSOR Facility, Institute for Molecular Science, Okazaki 444-8585, Japan*

Germanium (Ge), strained-Ge, and germanium-tin ($Ge_{1-x}Sn_x$) alloy are attractive candidates for high mobility channel material alternative to silicon (Si) in metal-oxide- semiconductor filed effect transistors (MOSFETs) in order to improve on ultra-large scale integrated circuits (ULSIs). $Ge_{1-x}Sn_x$ alloy with a Sn content high than 10% is also expected to be direct transition semiconductor. Theoretical calculation promises the reduction in the effective mass of holes in tensile strained Ge and compressive strained $Ge_{1-x}Sn_x$ compared to bulk-Ge and strained Si. Recently, we achieved the epitaxial growth of $Ge_{1-x}Sn_x$ thin films with wide Sn content (0~27%) on various substrates such as Ge, Si, and InP [1-3]. It is essentially important to understand the electronic properties of energy band dispersion, effective mass of electrons and holes, and carrier mobility of strained Ge and $Ge_{1-x}Sn_x$ alloy for ULSI applications. However, there are few reports about the electronic structure of strained Ge and $Ge_{1-x}Sn_x$.

In this study, we prepared the compressive-strained $Ge_{1-x}Sn_x$ epitaxial layers on Ge substrates, and investigated the electrical structures of Ge and $Ge_{1-x}Sn_x$ by using angle-resolved photoelectron spectroscopy (ARPES) measurement.

Ge(001) and Ge(110) wafers were used for substrates. After chemically cleaning, a Ge substrate was thermally cleaned in an ultra high vacuum chamber. Then, a 200 nm-thick $Ge_{1-x}Sn_x$ layer was deposited at 150~170°C on a Ge substrate. Sn content was ranging from 4.6% to 6.0%, which was estimated with x-ray diffraction two dimensional reciprocal space mapping. Successively, A 1~2 nm-thick Ge cap layer was deposited. Samples were brought to UVSOR/BL5U, and then introduced into a preparation UHV chamber connected to the ARPES measurement chamber. A sample was annealed at as high as 460°C in the preparation chamber in order to remove surface native oxide. Clean surface was confirmed from the surface reconstruction structure by using reflective high-energy electron diffraction (RHEED) observation. Samples were cooled at 15K during the ARPES measurement. ARPES measurement was performed with x-ray energies of 66 and 33 eV for $Ge_{1-x}Sn_x$/Ge(001) and $Ge_{1-x}Sn_x$/Ge(110) samples, respectively.

Figure 1 shows a typical ARPES result for the $Ge/Ge_{0.968}Sn_{0.032}$/n-Ge(001) sample. The spectra were measured for various take-off-angles (TOA). We can clearly see the energy dispersion related to the valence bands of light and heavy holes at the Γ-point. We have also obtained photoemission spectra from the strained-$Ge_{1-x}Sn_x$/Ge(110) and tensile-strained Ge/ $Ge_{1-x}Sn_x$/Ge(001) samples. The analysis of electronic structures and effective mass for holes are ongoing and will be reported in future.
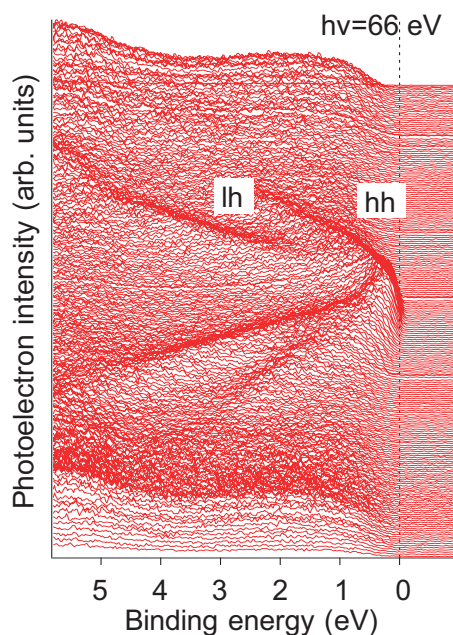
Fig. 1. Photoemission spectra with various TOAs (126 slices) for the $Ge/Ge_{0.968}Sn_{0.032}$/n-Ge(001) sample.

[1] S. Zaima, O. Nakatsuka, Y. Shimura, S. Takeuchi, B. Vincent, F. Gencarelli, T. Clarysse, J. Demeulemeester, K. Temst, A. Vantomme, M. Caymax and R. Loo, ECS Trans. **41** (2011) 231.
[2] S. Zaima, O. Nakatsuka, M. Nakamura, W. Takeuchi, Y. Shimura and N. Taoka, ECS Trans. **50** (2012) 897.
[3] O. Nakatsuka, Y. Shimura, W. Takeuchi, N. Taoka and S. Zaima, Solid-State Electron. **83** (2013) 82.

Characterization of TiO$_2$/Sapphire Beam Splitter for High-Order Harmonics

H. Kumagai[1], M. Sanjo[1] and T. Shinagawa[2]

[1]*Graduate School of Engineering, Osaka City University, 3-3-138 Sugimoto, Sumiyoshi-ku, Osakashi, Osaka 558-8585, Japan*
[2]*Inorganic Materials Lab., Osaka Municipal Technical Research Institute, 1-6-50 Morinomiya,Joto-ku,Osaka 536-8553, Japan*

High-intensity high-order harmonic generation has been investigated intensively in recent years because of application to nonlinear optics with magnificent spatial coherence and with an ultrashort pulse duration for high peak power. In the development of beam line for high-intensity high-order harmonics, however, utilizing a conventional beam splitter (BS) (Si or SiC) that absorbs fundamental waves causes serious problems such as its thermal distortion [1]. To resolve these problems, we proposed and investigated novel BS with transparent materials that transmitted the fundamental waves and then reflected the high-order harmonics. In BS for the high-order harmonics, reflection of the fundamental waves should be prevented by entering the p-polarized fundamental waves at the Brewster's angle θ_B, which could improve the separation between the fundamental waves and the high-order harmonics.

Atomic layer deposition (ALD) and atomic layer epitaxy (ALE) are gas phase deposition methods that are based on sequential surface chemical reaction where the growth rate is dependent solely on the number of growth cycles. These deposition methods have emerged as the excellent techniques to fabricate a wide variety of thin films [2-6]. The main difference between ALE and chemical vapor deposition (CVD) is the way to introduce precursor into the reaction chamber. Unlike CVD, each precursor is alternately pulsed to the chamber in ALE process. ALE has self-limiting nature of the surface saturation, allowing the formation of a full or a sub-monolayer of atoms because adsorption of precursor gases stops due to covered surface reactive sites or steric hindrances of ligands of adsorbed molecules. It can coat complex shapes with excellent uniformity and control thickness with precision over large areas.

We have already studied and fabricated TiO$_2$ thin films on sapphire (0001) substrates by controlled growth with ALD or ALE. One of authors has already demonstrated that rutile TiO$_2$ (200) thin films were grown epitaxially on sapphire (0001) substrates by ALE using sequentially fast pressurized titanium tetrachloride (TiCl$_4$) and water (H$_2$O) vapor pulses [7].

Figure 1 shows reflectivity (p polarization) of TiO$_2$/sapphire BS. Incident angle θ_B was set at 70.5° for TiO$_2$ and at 65.56° for sapphire, which corresponded to the Brewster angles θ_B of the 800-nm pump pulse. Figure 1 indicated that the peak

reflectivities of TiO$_2$/sapphire BS were high reflectivity of 44.8% (incident angle θ_B =70.5° for TiO$_2$) and 31.9% (incident angle θ_B =65.56° for sapphire) at 21.24 nm, which corresponded to the 37th order harmonics of the 800-nm pump pulse, respectively. Thus, the incident angle θ_B was set at 70.5° for TiO$_2$, which corresponded to the Brewster angle θ_B of the 800-nm pump pulse.
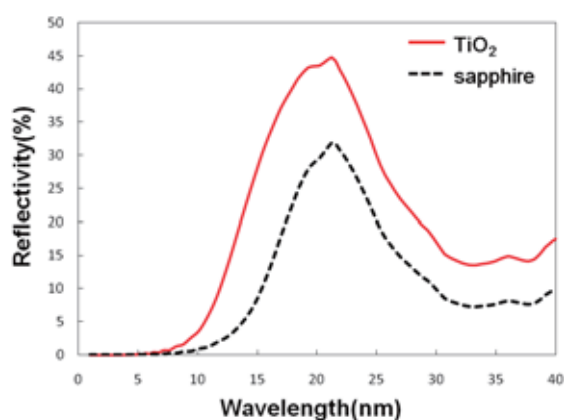

Fig. 1. Reflectivities of TiO$_2$/sapphire BS at the Brewster angles for TiO$_2$ (solid line) and sapphire (dashed line) at the pump pulse.

[1] E. J. Takahashi *et al.*, Opt. Lett. **29** (2004) 507.
[2] S. M. George *et al.*, J. Phys. Chem. **100** (1996) 13121.
[3] D. M. Hausmann *et al.*, Thin solid Films **443** (2003) 1.
[4] S. J. Kwon, Jpn. J. of Appl. Phys. **44** (2005) 1062.
[5] M. Ishii *et al.*, J. crystal Growth **180** (1997) 15.
[6] H. Kumagai *et al.*, J. Mater. Sci. Lett. **15** (1996) 1081.
[7] H. Kumagai *et al.*, J. Crystal Growth **314** (2011) 1.

Spin-Orbit Coupled Gold Atomic Chains on Vicinal Si Surfaces

S. Won Jung[1], W. Jong Shin[1], H. Yamane[2], N. Kosugi[2] and H. W. Yeom[1]

[1] *Department of Physics and Center for Low Dimensional Electronic Symmetry,*
Pohang University of Science and Technology, Pohang 790-784, Korea
[2] *Department of Photo-Molecular Science, Institute for Molecular Science, Okazaki 444-8585, Japan*

One dimensional (1D) electronic system has been studied for its exotic phenomena such as Peierls instability [1], and non-Fermi liquid behavior [2]. For the non-Fermi liquid, most experimental researches focused on the spin-charge separation [3] and the power-law dependent density of states near the Fermi level [4].

However, there has been almost no such study for the non-Fermi liquid state with the spin-orbit coupling [2-4]. Moreover, 1D systems with the spin-orbit coupling becomes important for spintronic applications and for finding Majorana Fermions [5, 6]. Therefore, 1D electronic system with a substantial spin-orbit coupling would be an important topic with a chance to observe exotic states such as Spiral Luttinger liquids and Helical Luttinger liqids [7].

In the present study, we performed angle-resolved photoelectron spectroscopy (ARPES) measurements, using BL6U of UVSOR, in order to measure the band structure of gold atomic wires formed on a vicinal silicon surface, Si(553). Gold atomic wires on vicinal Si surfaces has been known to possess multiple 1D metallic bands [8], Peierls instability [9], and Rashba-type spin-orbit coupling [10].

Fig. 1 shows low energy electron diffraction (LEED) images of two phases of Au atomic wires on Si(553) surface at different gold coverages. The periods along [1 1 -2] direction (perpendicular with wires) is $(4+1/3)a_0$ [Fig. 1 (a), A phase] , $(9+2/3)a_0$ [Fig. 1 (b), B phase]. The B phase is found for the first time in this work. However, in Fig. 2, the electronic structures have strong similarity with surface states, S1 and S2 (known as the Rashba spin splitting [10]) and S3. Therefore, we can assume that the two phases features the same gold chain structure with different density.

In this study, we measured high-resolution band spectra of the B phase, which is thought to have a lower wire density and thus a large interwire distance. We thus expect that this low density wire phase would exhibit a more ideal 1D electronic property and thus is a good candidate to investigate the possibility of non-Fermi liquid state with the spin-orbit interaction. The analysis of the spectra functions is underway along with a scanning tunneling microscopy study.
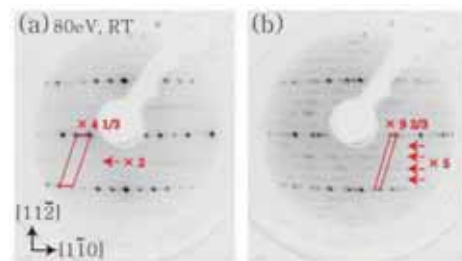

Fig. 1. Measured LEED images of Au atomic wires on Si(553). The coverage of Gold is about (a) 0.48ML, (b) 0.22ML. [1 -1 0] is the direction of atomic wires.
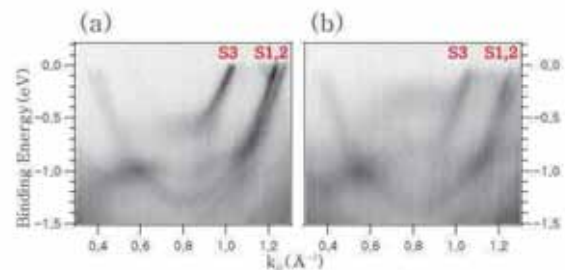

Fig. 2. Measured ARPES Spectra of Au atomic wires along [1 -1 0] direction with 46eV photon. The coverage of Gold is about (a) 0.48ML , (b) 0.22ML.

[1] H. W. Yeom *et al*., Phys. Rev. Lett. **82** (2009) 4898.
[2] T. Giamarchi, *Quantum Physics in One Dimension* (Clarendon Press, OXFORD, 2003).
J. N. Crain and F. J. Himpsel, Appl. Phys. A **82** (2006) 431.
[3] C. Kim *et al*., Phys. Rev. Lett. **77** (1996) 4054.
[4] Marc Bockrath *et al*., Nature **397** (1999) 598.
C. Blumenstein *et al*. ,Nature Physics **7** (2011) 776.
[5] R. M. Lutchyn, J. D. Sau, and S. Das Sarma, Phys. Rev. Lett. **105** (2010) 077011.
[6] J. Park *et al*., Phys. Rev. Lett. **110** (2013) 036801.
[7] B. Brauecker, C. Bena and P. Simon, Phys. Rev. B **85** (2012) 035136.
[8] J. N. Crain *et al*., Phys. Rev. Lett. **90** (2003) 176805.
J. N. Crain *et al*., Phys. Rev. B **69** (2004) 125401.
[9] J. R. Ahn, P. G. Kang, K. D. Ryang and H. W. Yeom, Phys. Rev. Lett. **95** (2005) 196402.
[10] I. Barke *et al*., Phys. Rev. Lett. **97** (2006) 226405.

Systematic Study on Intermolecular Interaction in Crystalline Films of Metal Phthalocyanine

H. Yamane and N. Kosugi

Department of Photo-Molecular Science, Institute for Molecular Science, Okazaki 444-8585, Japan

The intermolecular electronic band dispersion, originating from the periodicity of the molecular stacking structure, is essential to investigate the charge transport mechanism related to organic electronics. Recently, we have succeeded in observation of quite small intermolecular band dispersions for crystalline films of metal phthalocyanines (MPc, M = metal), such as ZnPc, MnPc, and $F_{16}ZnPc$, by the precise angle-resolved photoemission spectroscopy (ARPES) experiments [1]. These observations enable us to do systematic study of the intermolecular interaction in terms of the intermolecular distance along the π-π stacking direction ($a_\perp$) by changing terminal groups or central metals in the MPc molecule.

Figure 1(a) shows the normal-emission ARPES spectra as a function of the incident photon energy (hv) for a crystalline film of CoPc on Au(111) at 15K. The relative peak intensity between the highest occupied molecular orbital (HOMO) and HOMO-1 levels changes with hv. At hv = 50 eV, the HOMO intensity is stronger than the HOMO-1 intensity. At $hv \geq$ 58 eV, the HOMO-1 intensity is getting stronger than the HOMO intensity due to different ionization cross sections between the HOMO and HOMO-1 characters. This evidence indicates that the HOMO of CoPc is derived from the C 2p orbital; on the other hand, the HOMO-1 of CoPc is derived from the Co 3d orbital. These assignments agree well with theoretical results [2]. The HOMO (C 2p) and HOMO-1 (Co 3d) derived peaks show the clear periodic shift with hv. The periodicity of these dispersive peaks in the wavevector space is explained by $a_\perp$ of 3.318 Å, which is evaluated from the X-ray diffraction (XRD) shown in Fig. 1(b). Therefore, it is concluded that the observed dispersive behavior for the HOMO and HOMO-1 peaks is ascribed to the delocalized band formation due to the intermolecular van der Waals interaction in the crystalline CoPc film.

From the observed band dispersions of the C-2p-derived band for crystalline films of various MPc molecules, the intermolecular transfer integral ($t_\perp$) can be evaluated with respect to $a_\perp$ as shown in Fig. 2. From the $t_\perp$-vs.-$a_\perp$ relation, we found that (i) the $t_\perp$ value is getting large with decreasing the $a_\perp$ value due to the stronger intermolecular electronic coupling and that (ii) the $t_\perp$-vs.-$a_\perp$ relation seems to be fitted by a linear function in the present narrow $a_\perp$ range. From the least-squares fitting, the slope parameter of $t_\perp/a_\perp$ is determined to be 70 meV/Å for the C-2p-derived band of α-crystalline MPc films.

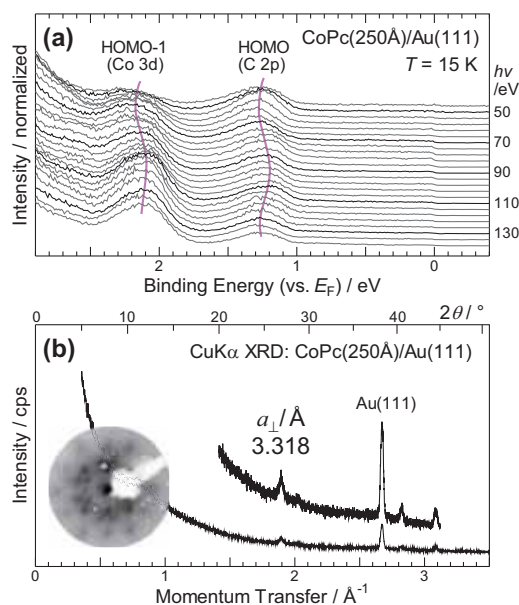Fig. 1. (a) The photon energy (hv) dependence of the normal-emission ARPES spectra shown with the hv step of 4 eV and (b) the CuKα X-ray diffraction (XRD) spectrum, measured for the crystalline CoPc film on Au(111). In panel (b), the low-energy electron diffraction image, taken at the incident electron energy of 34 eV, is also shown.
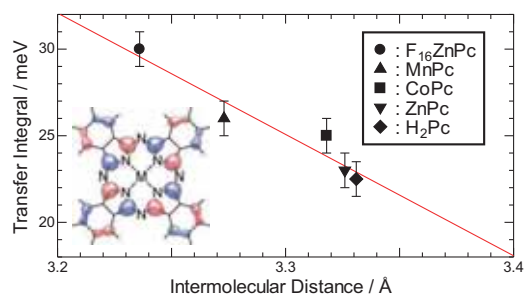

Fig. 2. The intermolecular transfer integral ($t_\perp$) with respect to the intermolecular distance along the π-π stacking direction ($a_\perp$) in flat-lying crystalline films of MPc on Au(111) at 15 K. The LCAO (linear combination of atomic orbitals) pattern of the C 2p derived level of MPc is shown in the inset.

[1] H. Yamane and N. Kosugi, submitted.
[2] For example, M.-S. Liao and S. Scheiner, J. Chem. Phys. **114** (2001) 9780.

Crystallinity-Dependent Excited-Electron Dynamics in $F_{16}ZnPc$ Films

H. Yamane and N. Kosugi

Department of Photo-Molecular Science, Institute for Molecular Science, Okazaki 444-8585, Japan

Resonant photoemission spectroscopy (RPES) has been applied to the study of the charge transfer dynamics at molecule/electrode interfaces [1, 2], which is called as a core-hole clock (CHC) experiment. The CHC method is based on the normal decay time of a core excitation (6 fs for N 1s) as a reference clock for other processes in the target system. That is, RPES signals depend on the timescale of excited electron motions with respect to that of the core-hole lifetime. Here we have applied the CHC method to the thick molecular films for the study of the excited-electron dynamics by the weak intermolecular interaction.

In the present work, we have used an archetypal n-type organic semiconductor of $F_{16}ZnPc$. In order to study the effect of the weak intermolecular interaction on the excited state, we have prepared an amorphous and a crystalline film of $F_{16}ZnPc$. The amorphous $F_{16}ZnPc$ film is obtained by the molecular deposition onto a polycrystalline Au surface kept at the low temperature ($T \sim 180$ K). On the other hand, the crystalline $F_{16}ZnPc$ film is obtained by the molecular deposition onto a single-crystalline Au(111) surface kept at the elevated temperature ($T \sim 360$ K). The sample crystallinity was confirmed by the N K-edge X-ray absorption spectroscopy (XAS), the low-energy electron diffraction, and the X-ray diffraction. For the crystalline $F_{16}ZnPc$ film, furthermore, we confirmed that the valence band dispersion by the intermolecular interaction is observable. In order to avoid the effect of the molecular orientation on the core-level excitation, the N K-edge RPES and XAS spectra were measured at the magic-angle incidence geometry.

Figure 1 shows the color contour map of the N-K RPES spectra for (a) the amorphous and (b) crystalline $F_{16}ZnPc$ film, measured at $T = 15$ K. We found that the ionization energy and the RPES intensity depend on the sample crystallinity. Among these, the RPES intensity, plotted in the upper panel of Fig. 1 together with the N-K XAS spectrum, is related to the excited-electron dynamics. The XAS spectra of both the amorphous and crystalline $F_{16}ZnPc$ films show the first, second, and third N 1s $\rightarrow \pi^*$ transition peaks at the photon energy ($h\nu$) of 397.0, 399.4, and 401.4 eV, respectively. At these $h\nu$, the RPES spectra for the amorphous $F_{16}ZnPc$ film also show the intensity maxima. On the other hand, for the crystalline $F_{16}ZnPc$ film, the RPES intensity at $h\nu = 399.4$ and 401.4 eV is decreased significantly. This evidence in RPES and XAS indicates that the timescale of the intermolecular charge transfer in the crystalline $F_{16}ZnPc$ film is faster than that of the N 1s core-hole lifetime (6 fs) due to the delocalization of the excited electron. The inter-

molecular charge transfer time (τ_{CT}) can be determined from the modified equation given in Ref. [1] of

$$\tau_{CT} = \tau_{CH} (I_{cry\text{-}PE}/I_{cry\text{-}XA})(I_{amo\text{-}PE}/I_{amo\text{-}XA} - I_{cry\text{-}PE}/I_{cry\text{-}XA})^{-1},$$

where τ_{CH} is the core-hole lifetime, $I_{cry\text{-}PE}/I_{cry\text{-}XA}$ is the RPES/XAS intensity ratio for the crystalline film, and $I_{amo\text{-}PE}/I_{amo\text{-}XA}$ is the RPES/XAS intensity ratio for the amorphous film. Using this equation, the τ_{CT} in the crystalline $F_{16}ZnPc$ film is determined to be 2.1 fs.
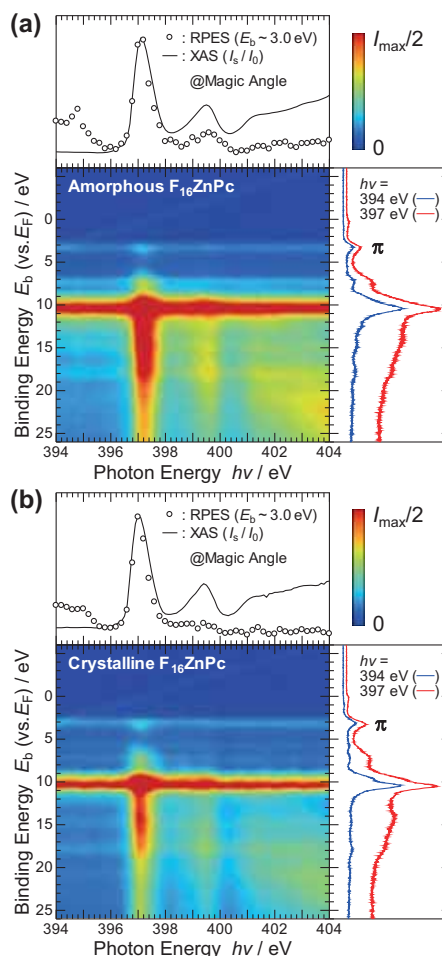

Fig. 1. Color contour map of the N-K RPES spectra for (a) amorphous and (b) crystalline films of $F_{16}ZnPc$ at 15 K. Upper panel shows the intensity-vs-$h\nu$ profile at $E_b = 3.0$ eV (○), together with the XAS spectrum (–). Side panel shows the intensity-vs-E_b profile (*i.e.*, RPES spectrum) at $h\nu = 394$ and 397 eV.

[1] P. A. Brühwiler, O. Karis and N. Mårtensson, Rev. Mod. Phys. **74** (2002) 703.
[2] L. Wang, W. Chen and A. T. S. Wee, Surf. Sci Rep. **63** (2008) 465, and references therein.

III-4. SURFACE AND THIN FILMS

Anisotropy of Electron-phonon Coupling for Pentacene Monolayer

S. Kera[1], F. Bussolotti[1], H. Shinotsuka[1], N. Ueno[1], M. Matsunami[2] and S. Kimura[2]

[1]*Graduate School of Advanced Integration Science, Chiba University, Chiba 263-8522, Japan*
[2]*UVSOR, Institute for Molecular Science, Okazaki 444-8585, Japan*

Over the past decade, organic electronic devices have increased considerable attentions due to their potential applications. Fine features of the highest occupied molecular orbital (HOMO) state in highly-resolved ultraviolet photoelectron spectrum (UPS) of organic semiconductor can offer a variety of key information that is necessary to unravel fundamental mechanism in carrier-transport(transfer) properties in organic devices. Here, we present high-resolution angle-resolved UPS (ARUPS) studies on the HOMO hole in pentacene monolayer (ML) by using low-energy photon to access dynamic events of photohole.

ARUPS spectra were measured at photon incidence angle $\alpha=45^{\circ}$, hv = 7 to 10 eV and T=15 K at BL7U. The molecules were evaporated onto a clean graphite (HOPG) substrate. The coverage/thickness of the pentacene ML was confirmed by the binding energy (E_B) of HOMO[1,2]. No significant band dispersion is detected for the ML.

Figure 1 shows the angle-integrated UPS (for 36°) of pentacene ML. HOMO band is appeared at 1.3 eV. Vibronic satellites bands denoted by v = 1, 2, 3 and Lorentzian-like-tail feature are observed at higher-E_B and lower-E_B side, respectively [2]. We found the intensity ratio of hole-vibration coupling and the tail feature largely depends on the photoelectron kinetic energy.

To reveal the differences more precisely, photon energy dependences of ARUPS were recorded as shown in Fig.2. We found clear differences in the ARUPS intensity maps by using different photon energy of 0.8eV. The vibrational progression should follow a Poisson distribution under Frank-Condon approximation. The intensity of hole-vibration coupling, however depends largely on the momentum number, hence the momentum distribution curve (MDC) of vibronic peak is different from that of the
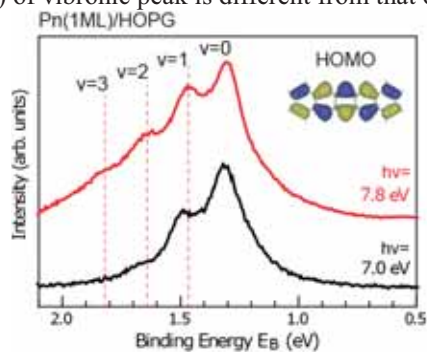
main peak. It demonstrates that we have to consider a violation of Born-Oppenheimer approximation and dynamic photoemission processes for large-π conjugated materials.

Moreover, the low-E_B tail feature appears at around Γ point, which was accessible by observing low-kinetic-energy photoelectrons. The results may give a chance to discuss the origin of the HOMO band shape of molecular solids, which would be closely related to following topics: (i) accurate contribution of electron-phonon (hole-vibration) coupling to the hopping conduction. (ii) dynamics of polarization (molecular polaron and Holstein polaron) which is affected by lifetime of the photohole to give a the high-kinetic-energy tail of HOMO shape. To elucidate the anomalous features and their anisotropy, further studies are intended.
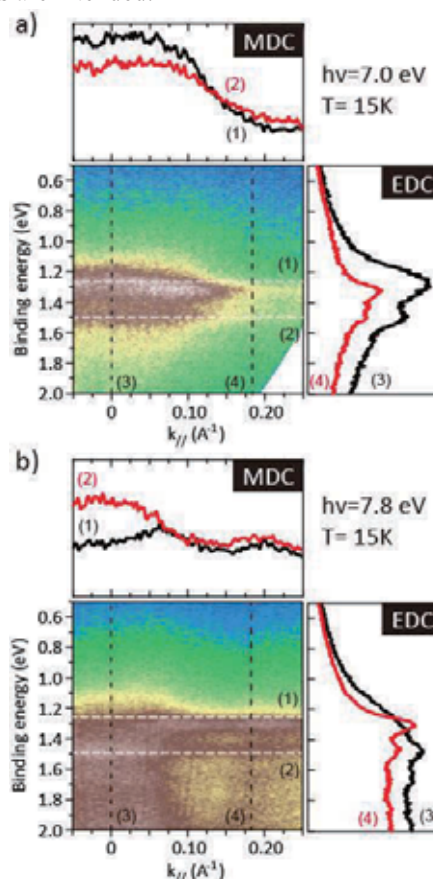

Fig. 1. Photon energy dependence of angle-integrated UPS of pentacene ML film prepared on a clean graphite (HOPG) (background subtracted).

Fig. 2. ARUPS intensity map for pentacene ML/HOPG measured at hv=7.0eV a) and hv=7.8eV b). EDCs at $k_{//}$ = 0 and 0.18 (Δk= 0.04Å^{-1}) are shown in right panels. MDCs at E_B= 1.25 and 1.50 eV for ΔE= 0.05eV are shown in top panels.

[1] H. Yamane *et al.,* Phys. Rev. B **72** (2005) 153412.
[2] S. Kera *et al.*, Prog. Surf. Sci. **84** (2009) 135.

Low-Energy Angle-Resolved Photoemission Study on Ultrathin Bi Films

T. Hirahara[1], M. Matsunami[2], T. Hajiri[2], S. Kimura[2] and S. Hasegawa[1]

[1]Department of Physics, University of Tokyo, Tokyo 113-0033, Japan
[2]UVSOR Facility, Institute for Molecular Science, Okazaki 444-8585, Japan

Semimetal bismuth (Bi) is one of the most extensively studied elements in solid state physics because of its extreme physical properties, such as the highest resistivity and Hall coefficient of all metals. Bi has tiny hole and electron pockets at T and L points, respectively, [Fig.1(a) and 1(b)], and therefore the Fermi wavelength λ_F is very large (about 30 nm). Because of this large λ_F, nanosized objects of Bi in the range of several tens of nanometers have been examined extensively toward the development of quantum-size-effect-based devices [1–3]. For example, the oscillation of the film resistance with the film thickness d was reported [4] and, furthermore, it was predicted that when the lowest quantized subband of the electron pocket is raised to an energy higher than the highest hole subband, a band gap will develop [semimetal-to-semiconductor (SMSC) transition at $d\sim$30 nm, Fig. 1(c)] [1, 5]. However, although many angle-resolved photoemission (ARPES) measurements have been performed on ultrathin Bi films, none has actually been able to verify whether this SMSC transition occurs or not [6-14]. The main reason is that the cross section for the bulk bands depends dramatically on the photon energy and polarization.

Therefore in the present study, we have performed ARPES measurements on ultrathin Bi films by systematically changing the photon energy (7-40 eV) and polarization (P- and S- polarization). Figures 2(a) and (b) show the band dispersion near the Fermi level at the $\overline{\Gamma}$ point (hv =9 eV). Whereas the well-studied surface states are observed clearly for the P-polarization data (a), they completely disappear in the S-polarization data (b). The hole-like dispersion in (b) suggests the detection of the bulk hole band and its maximum seems to be located below the Fermi level. This may be suggesting the occurrence of a SMSC transition. Further sophisticated study is needed to reach a definite conclusion.
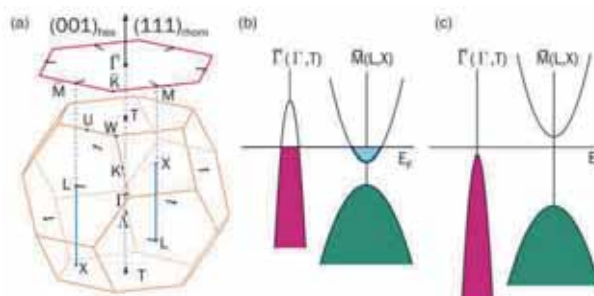

Fig. 1. (a) The Fermi surface of bulk Bi depicted in bulk (orange) and its projection to the surface (red) Brillouin zone. Electron (hole) pockets are filled with light blue (purple). (b), (c) Schematic drawing of the Bi bulk band projection near the Fermi level before (b) and after (c) the SMSC transition as predicted in Ref. [5].
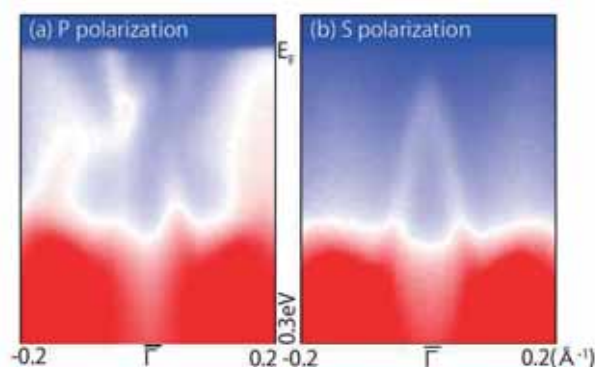

Fig. 2. The ARPES image of the band dispersion of Bi(111) films measured at hv=9eV for P- (a) and S- (b) polarized photons.

[1] C. A. Hoffman *et al.,* Phys. Rev. B **48** (1993) 11431.
[2] Z. Zhang *et al.,* Phys. Rev. B **61**, 4850 (2000).
[3] T. E. Huber *et al.,* Appl. Phys. Lett. **84** (2004) 1326.
[4] Yu. F. Ogrin *et al.,* JETP Lett. **3** (1966) 71.
[5] V. B. Sandomirskii, Sov. Phys. JETP **25** (1967) 101.
[6] T. Hirahara *et al.,* Phys Rev. Lett. **97** (2006) 146803.

[7] T. Hirahara *et al.,* Phys. Rev. B **75** (2007) 035422.
[8] T. Hirahara *et al.,* Phys. Rev. B **76** (2007) 153305.
[9] T. Hirahara *et al.,* New Jour. Phys. **10** (2008) 083038.
[10] A. Takayama *et al.,* Phys. Rev. Lett. **106** (2011) 166401.
[11] A. Takayama *et al.,* Nano Lett. **12** (2012) 1766.
[12] H. Miyahara *et al.,* eJSSNT **10** (2012)153.
[13] T. Okuda *et al.,* Rev. Sci. Inst. **82** (2011) 103302.
[14] G. Bian *et al.,* Phys Rev. B **80** (2009) 245407.

Secondary Electron Emission from the Graphite Surface

S. Tanaka[1], M. Matsunami[2,3] and S. Kimura[2,3]

[1]*The institute of Scientific and Industrial Research, Osaka University, Ibaraki 567-0047, Osaka, Japan*
[2] *UVSOR Facility, Institute for Molecular Science, Okazaki 444-8585, Japan*
[3]*School of Physical Sciences, The Graduate University for Advanced Studies (SOKENDAI), Okazaki 444-8585, Japan*

When the condensed matter is electronically excited, the following relaxation process leads to the emission of many particles/waves such as phonons, photons, and electrons. For example, Graphite, one of the 'textbook' materials, emits 3.3-eV electrons when excited no matter what photon energy is used as shown in the right panel of Fig. 1, where other peaks change their kinetic energies as a function of the photon energy. This phenomenon is important not only from the scientific point of view, because it reveals the relaxation dynamics in solids, but also from the technical one, because it may leads to the development of the monochromatic electron emitter.

Previously, this 3.3eV peak has been ascribed to the electron emission from the unoccupied band located at 3.3eV above the vacuum level of the Graphite [1]. The photoexcitation process provides the electrons located at the unoccupied band, and they may be emitted with conserving their energies and momentum if its wavefunction is connected to the free-electron-like wavefunction in the vacuum. In this study, we chalenge this interpretation with using the two-dimensional photoelectron spectroscopy where both of the photon and kinetic energies are scanned.

The experiments were carried out at BL7U of UVSOR-III. The HOPG (highly oriented pyrolytic graphite) was cleaved *in-situ* and the surface-normal photoelectron spectra were recorded with the photon energy is scanned by 0.3-eV step for hν=6-16eV and 1-eV step for hν=16-26eV. The sample temperature was 13K for hν=6-16eV and 50K for hν=16-26eV. Significant differences were not observed when temperature was changed except anomalous peaks just below the Fermi level at lower temperature [2]. The photon intensity was calibrated by using the photo-diode.

The results for the surface-normal photoelectron emission, which correspond to the electron at the Γ-point in the Brillouin zone, are shown in center panel of Figure 1 as a colored map (red is higher than blue) where the x-axis indicates the photon energy and the y-axis indicates the kinetic energy of the photoelectron. The photoelectron intensities as a function of the electron-kinetic energy are plotted at the right panel at some photon energies and those as a function of the photon energy at some photon energies are shown in the upper panel. Dotted diagonal lines in the center panel shows the position of the peaks corresponding the photoexcitation from
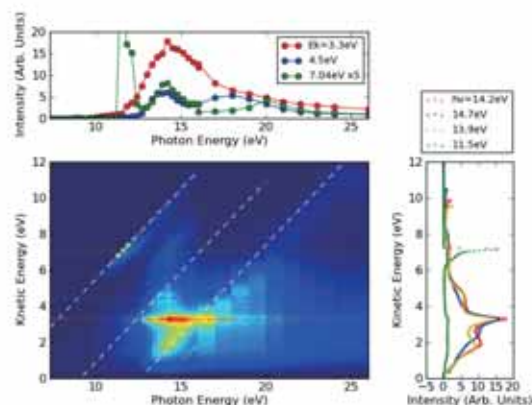

Fig. 1. Two-dimensional photoelectron spectra for HOPG Graphite.

the π-band (backfolded from the K-point [2]), the σ-band and the π-band, respectively, from the top to the bottom. The σ-band is hardly seen because it is prohibited by the dipole selection rule. Meanwhile, the horizontal lines correspond to the photoexcitation into a specific unoccupied state. Dotted lines are kinetic energies where high intensities are observed for several photon energies. The one who has the highest intensity is the 3.3-eV peak. According to the Fermi's golden rule, the photoexcitation probability resonantly increased when the photon energy agrees with the difference in energy between the occupied and unoccupied bands. These should be observed at the intersection points among the diagonal and horizontal lines. In the case of 3.3-eV peak, however, there is no particular enhancement at those photon energies. It clearly excludes the interpretation that the 3.3-eV peak is due to the unoccupied state of the Graphite. Thus, there should be another true mechanism to emit the 3.3-eV electrons. Our next goal will be finding it and is now under progress by using the photoelectron-secondary electron coincidence spectroscopy.

[1] R. F. Willis, B. Fitton, and G. S. Painter, Phys. Rev. B **9** (1974) 1926.
[2] S. Tanaka M. Matsunami and S. Kimura, Phys. Rev. B **84** (2011) 121411(R) .

Interface Electronic Structure of Diindenoperylene on Cu(111)

S. Kera[1], K. Kato[1], K. Yonezawa[1], K. Sato[1], Y. Liu[1], N. Ueno[1] and T. Hosokai[2]

[1]*Graduate School of Advanced Integration Science, Chiba University, Chiba 263-8522, Japan*
[2]*Faculty of Engineering, Iwate University, Morioka 020-8551, Japan*

Electric property of organic semiconductor materials is dominated by the density-of-states at the band gap and wavefunction spread of the electronic states. The molecule-substrate interaction crucially influences electronic and geometric properties at the interface [1]. The adsorption geometry of large π-conjugated molecules on metal surfaces, therefore is one of the key targets to understand the variety of peculiar interface properties. Diindenoperylene (DIP: $C_{32}H_{16}$) (inset in Fig 2b) is a typical organic semiconductor. The DIP monolayer (ML) films are prepared on Cu(111) substrate to reveal the interface electronic structure by using angle-resolved ultraviolet photoelectron spectroscopy (ARUPS).

ARUPS spectra were measured at photon incidence angle $\alpha=45^o$, hv=28 eV and T=295 K. The molecules were evaporated onto the Cu(111). The coverage/thickness of the monolayer was confirmed by work function of the densely-packed ML film which shows a clear LEED pattern.

Figure 1 shows the ARUPS of DIP 1ML on the Cu(111). The azimuthal angle (ϕ) dependence is recorded at photoemission angle of $\theta= 37^o$ by rotating the ϕ_s. The interface states (IS) denoted by B_1, B_2 and B_3 are observed. The features B_1 and B_2 (B_3) would be related to the former LUMO and former HOMO of DIP as reported similarly in PTCDA/Ag(111) and PTCDA/Cu(111), respectively [2]. There is no clear energy-band dispersion for the ISs. The feature B_1 is appeared as a broadened feature and hardly to discuss the origin of electronic state at the present results. On the other hand, the features B_2 and B_3 show a clear angular distribution in the ϕ rotation.

Figure 2(a) shows the photoelectron angular distribution (PAD) of features B_2 and B_3. The PAD of B_2 shows the maximum at around $\phi_s=0^o$, while B_3 gives the minimum. Fig. 2(b) represents the simulated PAD for the LUMO and HOMO distribution of isolated DIP molecule by using multiple-scattering theory combined with molecular orbital calculation (MS/MO) [3]. The molecule is placed that the molecular longer axis sets in the plane of electric vector ($\phi_m=0^o$) as seen in Fig. 2(b). The observed PAD of features B_2 and B_3 would be represented by the PAD pattern of HOMO for different molecular azimuthal orientation in the crystal domains. The results of LEED and STM indicate that the ML film consists of at least two different molecular unit cell. Depending on the lattice constant and molecular arrangement the absorption energy would be modified, hence they give the different binding energies. A molecular azimuthal orientation will be analyzed by considering the LEED, STM and simulated PAD. To reveal each orbital character of ISs, a full-spherical map of the PAD is requested to be measured.
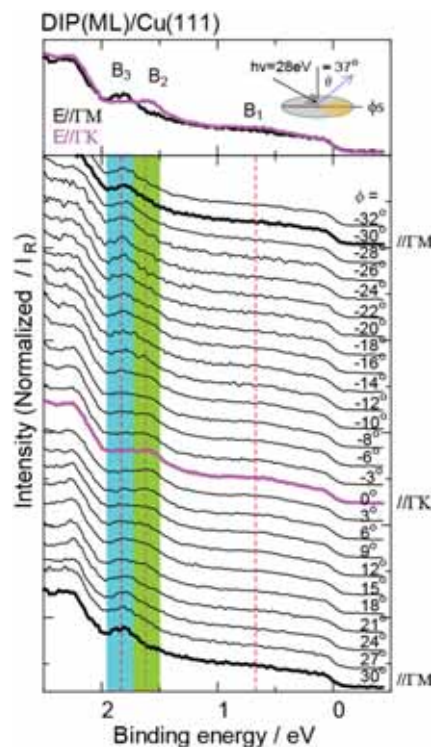

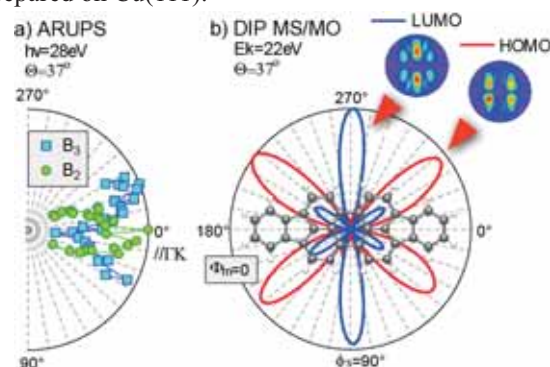Fig. 1. ϕ dependence of ARUPS for DIP ML film prepared on Cu(111).

Fig. 2. Observed PAD of features B_2(circles) and B_3(squares) (a) and calculated PAD of LUMO and HOMO distribution by MS/MO (b). Full-spherical PAD images are also shown. The simulated patterns are displayed by slicing the image at $\theta=37^0$. Scheme view of DIP molecule at $\phi_m=0$ is also shown.

[1] G. Heimel *et al.,* Nature Chem. **5** (2013) 187.
[2] J. Ziroff *et al.,* Phys. Rev. Lett. **104** (2010) 233004.
[3] S. Kera *et al.*, Chem. Phys. **325** (2006) 113.

III-4. SURFACE AND THIN FILMS

Role of Oxygen Side Group on Interface State Formation in π-conjugated Organic Molecule/metal System

T. Hosokai[1], K. Yonezawa[2], K. Kato[2], N. Ueno[2] and S. Kera[2]

[1]*Department of Materials Science and Technology, Iwate University, Morioka 020-8551, Japan*
[2]*Graduate School of Advanced Integration Science, Chiba 263-8522, Japan*

Electronic structure of organic/metal (O/M) interfaces is crucial for Organic Electronics, in which charge carrier injection at the interface dominates device efficiency. Therefore, enormous effort has been devoted for understanding the interface electronic structure by using (angle-resolved (AR)) ultraviolet photoelectron spectroscopy (UPS). One remaining issue in this research field is an interface state (IS). In some O/M systems the IS appears unexpectedly near the Fermi level. It has been elucidated that this state is caused by a charge-transfer from metal substrate to the former lowest unoccupied molecular orbital (LUMO) state of the adsorbates. From x-ray standing waves (XSW) experiments on monolayers of perylene compound with acyl groups (PTCDA: $C_{24}H_8O_6$)(Fig. 2)) on noble metal substrates (Au(111), Ag(111) and Cu(111)), it was implied that a shorter bonding distance of the adsorbates onto the substrates may trigger to form the IS [1]. In such case, however, a role of chemical bonding of the side acryl groups to the substrates for the IS is not yet clarified.

To address this issue, we have focused diindenoperylene (DIP: $C_{32}H_{16}$) (Fig. 2), a perylene compound consisting of only carbon and hydrogen atoms. From XSW we confirmed that the bonding distance of DIP to noble metal substrates was similar to that of PTCDA [2]. Here we performed ARUPS study of DIP monolayer (ML) films deposited on Ag(111) and Cu(111), and also on polycrystalline-Ag and -Cu surfaces.

ARUPS spectra were measured at photon incidence angle α=45°, $h\nu$=28 eV and 40 eV and T=295 K. The molecules were evaporated onto each substrate. The ML formation was confirmed by saturation of the work function shift.

As shown in Fig. 1, the ML spectrum of DIP on Ag(111) and Cu(111) shows some spectral features (as denoted to $A_1 - A_4$ for Ag(111) and $B_1 - B_3$ for Cu(111)) distinct from theoretical one or multilayer (island) film spectrum (b_2). This is a direct evidence of IS formation on Ag(111) and Cu(111) surfaces. Notably, such ISs are also seen on polycrystalline surfaces, suggesting the importance of IS in organic devices employing those metal electrodes and DIP.

Figure 2 shows comparison of the energy level alignments of DIP and PTCDA on Ag(111) and Cu(111). ISs are located at nearly the same positions for both molecular films. This clearly indicates that the O-atoms are not necessarily required to form the IS. A strong interaction between the π-conjugated

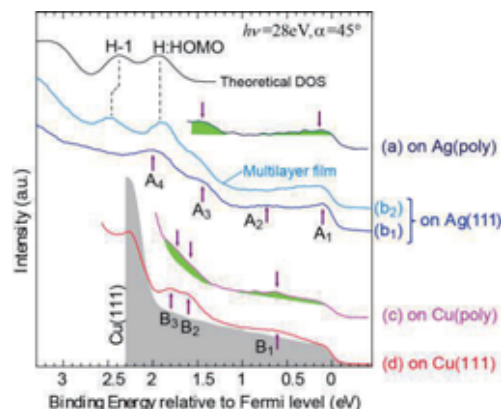carbons and substrate atoms, which may be realized by a short bonding distance, can be also a key for the IS.

Fig. 1. Valence band structure of DIP ML on Ag(poly) (θ=0°) (a), Ag(111) (θ=40°) (b_1), Cu(poly) (θ=0°) (c) and Cu(111) (θ=37°) (d). Multilayer (island) film (1 nm) of DIP/Ag(111) (θ=30°, $h\nu$=40eV) (b_2). A calculated density-of-state (DOS) of DIP molecule based on B3LYP/6-31G(d) is also shown at the top.
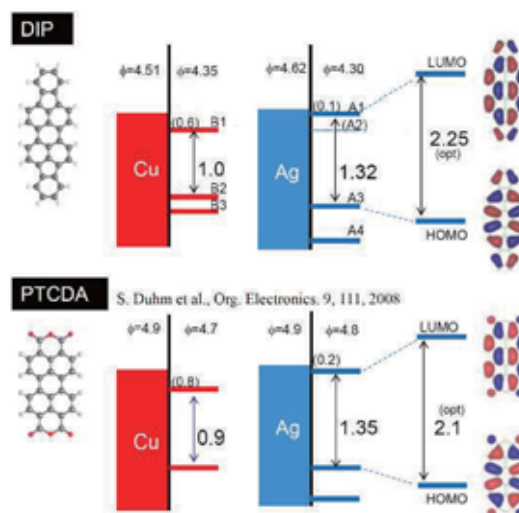

Fig. 2. Energy-level alignment of DIP/Ag(111) and Cu(111) systems compared with PTCDA from ref [1]. The energy levels of multilayer films and orbital pattern of HOMO and LUMO are depicted at the right-hand side, respectively.

[1] S. Duhm *et al.*, Org. Electronics, **9** (2008) 111.
[2] C. Bürker *et al.*, submitted.

Quantitative Analysis of Anisotropic Molecular Orientation of Pentacene Thin Film

K. K.Okudaira, T. Ishii and N. Ueno

Association of Graduate Schools of Science and Technology, Chiba Univererity,
1-33 Yayoi-cho Inage-ku, Chiba 263-8522, Japan

In recent years, organic semiconductor materials have proven to be one of the most popular materials used in the fabrication of thin-film transistor The performance of organic-TFT such as the field-effect mobility depends not only on the molecular structure of the semiconducting films but also the degree of molecular orientation, since charge transport in organic materials is realized by π-π interactions between molecules through the hopping mechanism. The anisotropic mobility could be useful in isolating neighboring components so as to reduce cross-talk. We apply a method to control both the molecular and crystal orientation of organic semiconductors, producing films with strong anisotropy. The anisotropic orientation of pentacene (Pn) film can be obtained by evaporating pentacene on the uniaxially oriented PTFE thin films onto the uniaxially polished Cu plate To obtain the quantitative analysis on the molecular orientation; we compare observed take-off angle dependence of π band and calculated one by the independent-atomic-center (IAC)/MO approximation [1].

ARUPS measurements were performed at the beam line BL8B of the UVSOR storage ring at the Institute for Molecular Science. The take-off angle (θ) dependencies of photoelectron spectra were measured at incident angle of photon (α) = 45° with the photon energy (hν) of 40 eV. Pentacene was evaporated to a final thickness of 10 nm on the uniaxially PTFE(5nm)/Cu (Pn(10nm)/ PTFE (5nm)/ Cu).

We observed take-off angle (θ) dependence of HOMO peak in UPS of (Pn(10nm)/ PTFE (5nm)/ Cu). Figure 1 shows the θ dependence of photoelectron from HOMO band with the parallel and perpendicular condition Under the parallel and perpendicular condition, the polarization plane of incidence photon is parallel and perpendicular to the direction of the groove of Cu plate, respectively. the θ dependences with parallel condition have a sharp maxima at θ= 65°. On the other hand, with the perpendicular condition, the θ dependence of HOMO band does not show a strong θ dependence. (θ for the maximum of is lower than that with parallel condition).

Figure 2 (a) and (b) show the calculated θ-dependence of HOMO peak for two geometries. With the geometry (1) and (2), the polarization plane is parallel and perpendicular to the a-axis of bulk phase pentacene crystal, respectively. For the geometry (1). the calculated θ-dependence of HOMO

Fig. 1. Take-off angle (θ) dependences of photoelectron intensities of HOMO peak of n(10nm)/ PTFE (5nm)/ Cu) with parallel (●) and perpendicular condition (●).

peak shows a maximum of θ =70°. It is similar with observed one with parallel condition. On the other hand, for the geometry (2) the calculated θ-dependence of HOMO peak shows a maximum of θ =40°, which is lower than that for the geometry (1). From the comparison between observed and calculate ones,. it can be expected that pentacene molecules have the anisotropic molecular orientation on uniaxial PTFE film, where the a-axis of pentacene crystal is parallel to the direction of groove of Cu plate.

Fig. 2. Calculated θ-dependence of HOMO peak for two geometries. where the polariaion plane of incidence photon is parallel (a) and perpendicular (b) to the a-axis of bulk phase pentacene crystal.
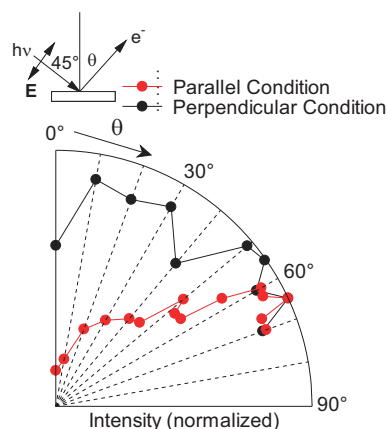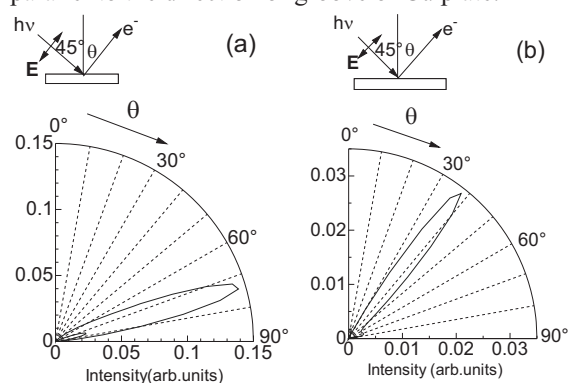
[1] S. Hasegawa *et al*., Phys. Rev. B **48** (1993) 2596.

Ⅲ-4. SURFACE AND THIN FILMS

Ultraviolet Photoelectron Spectroscopic Study on the Electronic Structure of the L-cysteine Ad-layers on the Noble Metal Surfaces

K. K. Rasika, Y. Nakayama and H. Ishii

Center for Frontier Science, Chiba University, Chiba 263-8522, Japan

In recent years the possibility to use proteins in bioelectronic devices has attracted much attention. In order to use proteins for bioelectronic applications, it is essential to investigate on the electronic structures of amino acids as the building blocks of proteins to elucidate functionality such as transport properties, adsorption properties, interface, and so on. As the initial step, we selected L-cysteine from the amino acids for the investigation, because it has been reported that the cysteine with its sulfanyl as a promising candidate for bioelectronics [1].

In the present study, we systematically elucidated the electronic structure at the interfaces of L-cysteine over layers and the noble metal surfaces Au(111), Ag(111), and Cu(111) by means of ultraviolet photoelectron spectroscopy (UPS) at BL8B.

Figure 1 shows the thickness-dependent UPS spectra of L-cysteine on (a) Ag(111), (b) Au(111), and (c) Cu(111) at photon energy of 28 eV. In each figure, on the left, the secondary energy cutoff (SECO) is shown on a magnified scale. On the right, the region between Fermi level of the metal substrate and the HOMO of the L-cysteine measured with relatively small energy step is also shown.

It was observed that the electronic structures of the L-cysteine thin films are different from each other and also from that of the L-cysteine thick film, which indicates strong dependence on the kind of substrate. On the thin films, a new structure appears in between Fermi level and the HOMO of the L-cysteine and the structure may be due to bonding of S $3sp$ orbital with Ag $4d$, Au $5d$, and Cu $3d$ states for each substrate, respectively. Further, the peak at ~5 eV for thin films shifts to the higher binding energy (e.g., Au by ~ 0.3 eV) (Fig.1., dotted line), may be due to the interaction of O $2sp$ orbital with metal substrates. The maximum SECO shifts were estimated to be 0.46, 0.83, and 1.01 eV to a higher binding energy for Ag, Au, and Cu, respectively. The direction of the shifts corresponding to a net transfer of negative charge from the cysteine to the substrates and the low value for Ag may be due to relatively large energy difference of S $3sp$ and Ag $4d$ states (a weak Ag-S bonding) [2].

Despite the difference in electronic structure for thin films, the electronic structure of thick film is identical for each substrate. Thus, for the thick films, photon energy-dependent UPS spectra were measured in the range of 20-120 eV. The results are shown that the top of valance band (VB) has a different origin from the other structure. By considering the results of Ogawa *et al.* [2], and DV-Xα molecular orbital calculation, it is attributed that the top of VB is
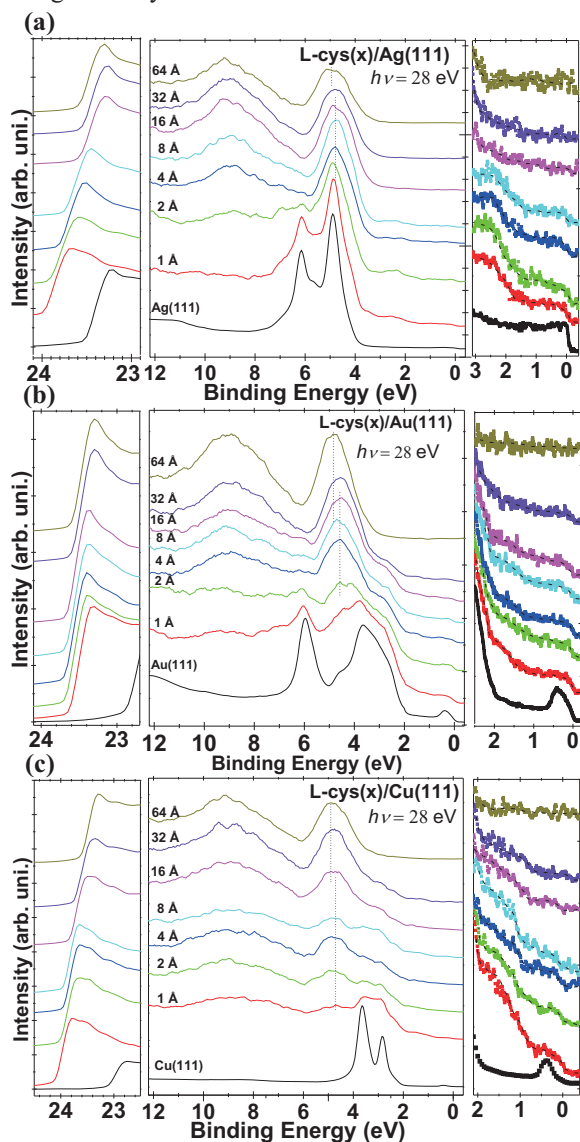
originated by sulfur.

Fig. 1. Thickness-dependent UPS of L-cysteine on (a) Ag(111), (b) Au(111), and (c) Cu(111) at photon energy of 28 eV. In each figure, on the left, the SECO is shown on a magnified scale. On the right, it is shown that the region between Fermi level of the substrate and the HOMO of the cysteine, which was measured with relatively small energy step and the dashed curves are plotted as a guide for eye.

[1] L. Willner and E. Katz, *Bioelectronics*: *From Theory to Applications* (Wiley-VCH, Weinheim, 2005).
[2] K. Ogawa *et al.*, J. Appl. Phys. **112** (2010) 023715.

Characterization of Calcium in Hydroxyapatite by an XAFS Method

T. Kurisaki[1], Y. Nagino[1], S. Yokoyama[1] and H. Wakita[1,2]

[1] *Department of Chemistry, Faculty of Science, Fukuoka University, Nanakuma, Jonan-ku, Fukuoka 814-0180, Japan*
[2]*Advanced Materials Institute, Fukuoka University, Nanakuma, Jonan-ku, Fukuoka 814-0180, Japan*

Hydroxyapatite is a kind of calcium phosphate. This compound can be found in tooth and born in the human body. In addition, it is commonly used as a filler to replace amputated born or as a coating to promote bone ingrowth into prosthetic implants. However, the local structure and electronic structure of calcium in a tooth and hydroxyapatite (HAP) are not determined. For various light element compounds, we have studied the electronic structure by X-ray absorption spectroscopy [1]. These results suggested that there is a correlation between XANES spectra and the local structures.

In this work, we performed the XANES spectra measurement about tooth, decayed tooth and hydroxyapatite. The obtained experimental XANES spectra are analyzed using the calculated theoretical spectra from DV-Xα calculations. The X-ray absorption spectra were measured at BL2A of the UVSOR in the Institute of Molecular Science, Okazaki [2]. The ring energy of the UVSOR storage ring was 750MeV. Ca K-edge absorption spectra were recorded in the regions of 4000-4200eV by use of two InSb crystals. The absorption was monitored by the total electron yield using a photomultiplier.
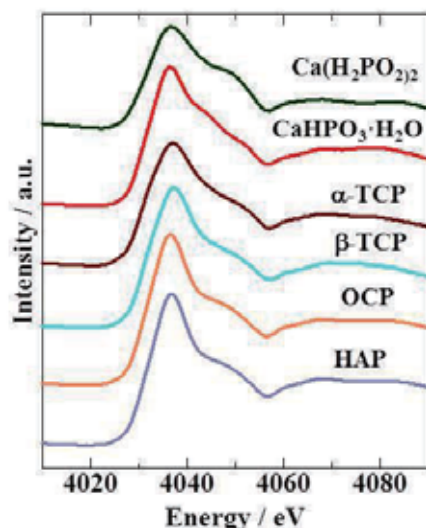

Fig. 1. Ca K-edge XANES spectra of the calcium phosphate compounds.
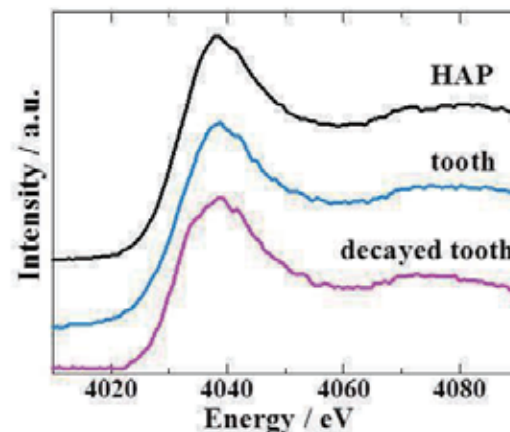

Fig. 2. Ca K-edge XANES spectra of the HAP, tooth and decayed tooth.

The samples were spread onto the carbon tape on the first photodynode made of CuBe of the photomultiplier.

Figure 1 shows the observed Ca K-edge XANES spectra for the calcium phosphate compounds. This result suggested that the measured Ca K-edge XANES spectra shows different peak profiles depending on the electronic structure and local structure of the these compounds.

Figure 2 shows the observed Ca K-edge XANES spectra for the HAP, tooth and decayed tooth. The Ca K-edge XANES spectra of HAP and tooth show the same peak profiles. On the other hand, the Ca K-edge XANES spectra of decayed tooth show a little difference of the peak profiles at 4037eV in comparison with the Ca K-edge XANES spectra of HAP and tooth. These results indicated that the electronic structure and local structure around the calcium in decayed tooth is different from those of HAP and tooth.

[1] T. Kurisaki S. Matsuo, I. Toth and H. Wakita, *Anal. Sci*. **24** (2008) 1385.
[2] S. Murata, T. Matsukawa, S. Naoè, T. Horigome, O. Matsuodo and M. Watatabe, *Rev. Sci. Instrum*. **63** (1992) 1309.

Ⅲ-5. SOLID STATE PHYSICS

Defects in Metal Oxide Studied by X-ray Absorption Fine Structure Spectroscopy

E. Kobayashi[1], K. K. Bando[2] and T. Okajima[1,3]

[1]*Kyushu Synchrotron Light Research Center, 8-7 Yayoigaoka, Tosu, Saga 841-0005, Japan*
[2]*National Institute of Advanced Industrial Science and Technology, 1-1-1, Higashi, Tsukuba, Ibaraki 305-8565, Japan*
[3]*Research Center for Synchrotron light applications, Kyushu University, 6-1 Kasugakoen, Kasuga, Fukuoka 816-8580, Japan*

Metal oxide is an important material from a fundamental physical point of view and is widely used in the field of catalytic, optical and electrical applications. It is recognized that the defects in metal oxide is important for applications because it can significantly affect the material characteristics. To understanding of the character of the defects is of importance for the development of new materials.

MgO plays a prototype of metal oxides and is also a wide-gap insulator [1]. The important defects in MgO are oxygen vacancies. We have investigated the MgO surface defects induced by ion bombardment in metal oxide. In this study, the annealing behavior of hydrogen defects of MgO bulk was studied by Mg *K*-edge NEXAFS spectroscopy using fluorescence yield (FY) method.

X-ray absorption fine structure spectra in the soft X-ray region can be obtained by detecting either the electrons or the fluorescence. For insulating materials, the total electron yield (TEY) method cannot be used due to the charge up. The FY can be measured for metal oxide, but the intensity is very low in the soft x-ray region, this is sensitive to the bulk material whereas the TEY is surface-sensitive.

The samples were MgO pellets after annealing at 673 K ~ 1073 K for 2 hours in hydrogen atmosphere and MgO reference powder. NEXAFS spectra were measured at the beamline 2A of the UVSOR in the Institute of Molecular Science. The NEXAFS spectra were obtained by measuring the fluorescence from the sample. The incident angle of the synchrotron radiation was 0° from the surface normal. The FY was normalized to the incident photon flux, recorded as a photocurrent at a photon-flux monitor consisting of a gold-evaporated mesh.

Figure 1 shows the NEXAFS spectra for the Mg *K*-edge region of MgO pellets after annealing at 673 K ~ 1073 K for 2 hours in hydrogen atmosphere and MgO reference powder. Three strong peaks are observed at around 1309.1 eV, 1314.7 eV and 1316.9 eV, respectively. The spectrum exhibits an overall similarity with those previously obtained by experiments [2]. The edge of the spectrum is shifted by annealing under a hydrogen atmosphere. This indicates that the hydrogen reduction of MgO was carried out. The oxygen of MgO is reduced by the hydrogen, the edge is shifted to the low energy.

After the hydrogen reduction, the strongest peaks become broad peak. In addition, the intensity of the peaks decreases with increasing temperature. These results indicate that the oxygen vacancies were induced by hydrogen reduction and the amorphous phase increased with annealing.
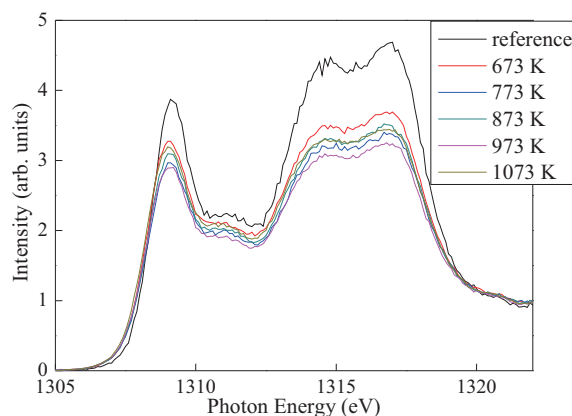

Fig. 1. NEXAFS spectra for the Mg *K*-edge region of MgO pellets after annealing at 673 K ~ 1073 K for 2 hours in hydrogen atmosphere and MgO reference powder.

[1] D. M. Roessler and W. C. Walker, Phys. Rev. **159** (1967) 733.
[2] P. Luches, S. D'Addato, and S. Valeri, E. Groppo, C. Prestipino and C. Lamberti, F. Boscherini, Phys. Rev. B **69** (2004) 045412.

Ultraviolet Emission of AlGdN by Inner-Core Excitation

K. Fujita, R. Ikematsu and K. Fukui

Department of Electrical and Electronics Engineering, University of Fukui, Fukui 910-8507, Japan

III-V nitride compound semiconductors doped with rare earth (RE) elements are attractive systems because of the possibility of magnetic ordering coupled with a semiconducting natures and luminescence properties, so-called spintronics. However, even in light emitter the III-V nitride wide band-gap host materials with REs have potential for development. In the case of ultraviolet (UV) region where is used as sterilization lamp and excitation lamp for phosphors in the visible region, Gd^{3+} is known as the light emitting material having ~ 3.9 eV emission (UVE) by $^6P_{7/2} \rightarrow {}^8S_{7/2}$ $4f$ intra-transition of Gd^{3+}. Since the UVE is higher than the band-gap energy of the GaN (3.4 eV), the realistic host materials are AlGaN or AlN. In our previous work [1], we studied photoluminescence (PL) and PL excitation (PLE) spectra of AlN doped with Gd^{3+} in the band-to-band excitation region. A sharp line of the UVE was clearly observed, and its PLE spectra revealed that this emission process is host excitation. It means that there is a process which transfers energy from the band-to-band excitation of AlN to $4f$ intra-transition of Gd^{3+} ion, and also means that UVE does not observed if the excitation light photon energy is less than that of AlN bandgap. Then, we have performed the ultraviolet (UV) emission of AlGdN thin films by Al 1s and Gd 3d core excitations to investigate the emission process of AlGdN.

AlGdN thin films were grown in a MBE system with a RF-plasma assisted radical cell on the Si-face of (0001)-oriented 6H-SiC substrates. The thickness of the sample is about 120 nm. Concentration of Gd^{3+} ions are 2 % ($Al_{0.98}Gd_{0.02}N$) and 13 % ($Al_{0.87}Gd_{0.13}N$). The details of the crystal growth have been reported elsewhere [2]. All visible (VIS) – UV region photoluminescence (PL) measurements were carried out at ~ 20 K with a conventional 30 cm VIS – UV monochromator and CCD image detector. PL excitation (PLE) and total yield (TY) spectra were measured around both Al K-edge (~ 1.5 keV) and Gd M_{IV}-edge (~ 1.2 keV). TY measurements were carried out at RT.

Figure 1 shows the PL spectrum of $Al_{0.98}Gd_{0.02}N$. The excitation energy is 1569 eV. A sharp line of the UVE is observed. Figures 2(a) and 2(b) show the TY and the PLE spectrum of $Al_{0.98}Gd_{0.02}N$, respectively. The intensity of the PLE spectrum is integrated intensity of the UVE shown in fig. 1. Both TY and PLE spectra around Al K-edge in fig. 2 are in good agreements with TY spectrum of AlN [3]. Since TY spectrum in this energy region is similar to the absorption spectrum, these results are consistent with our previous works as mentioned above.

Figures 3(a) and 3(b) represent the TY and the PLE

spectrum of $Al_{0.87}Gd_{0.13}N$, respectively. These spectra of $Al_{0.98}Gd_{0.02}N$ were not observed. Both TY and PLE spectra near Gd M_{IV}-edge are in good agreements with TY spectrum of Gd^{3+} ion which is well explained by the $3d^{10}4f^7 \rightarrow 3d^9 4f^8$ transition array [4].
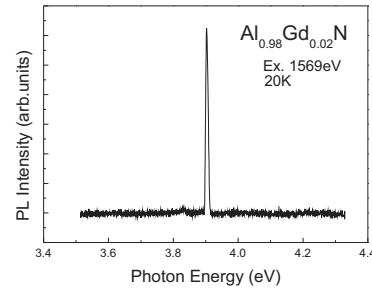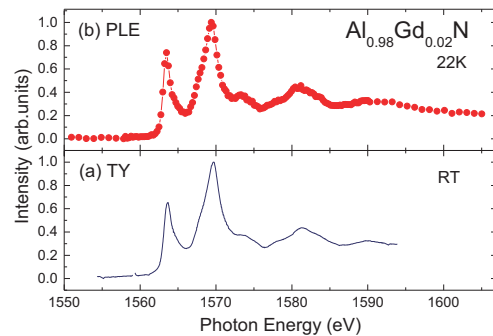

Fig. 1. PL spectrum of $Al_{0.98}Gd_{0.02}N$

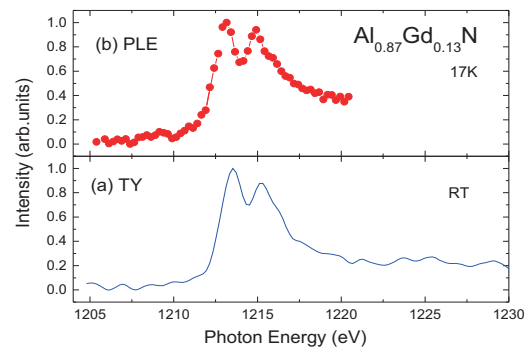Fig. 2. TY (a) and PLE (b) spectra of $Al_{0.98}Gd_{0.02}N$ around Al K edge.

Fig. 3. TY (a) and PLE (b) spectra of $Al_{0.87}Gd_{0.13}N$ around Gd M_{IV} edge.

[1] K. Fukui *et al*., Phys. Stat. Sol. (c) **7** (2010) 1878.

[2] N. Teraguchi *et al*., J. Cryst. Growth **230** (2001) 392.

[3] K. Fukui *et al*., Phys. Stat. Sol. (b) **228** (2001) 461.

[4] C. Bonnelle *et al*., J. Phys. B **10** (1977) 795.

Ⅲ-5. SOLID STATE PHYSICS

Optical Spectra of NaCl:Ag⁻ Crystals up to the VUV Energy Region

T. Kawai[1], T. Hirai[2] and K. Bando[3]

[1]Graduate School of Science, Osaka Prefecture University, Sakai 599-8531, Japan
[2]Faculty of Science and Engineering, Ritsumeikan University, Kusatsu 525-8577, Japan
[3]Faculty of Science, Shizuoka University, Shizuoka 422-8529 , Japan

Ag⁻ ions belong to the family of the so-called Tl⁺-type ions and exhibit the optical bands called A, B, and C [1, 2]. In alkali halide crystals doped with the Tl⁺-type ions, the absorption bands labeled D are often observed in the energy region between the C band and the fundamental absorption edge of the host crystals [3]. However, the existence of the D bands has not been reported for the Ag⁻ centers in alkali halides. In this study, optical spectra of NaCl:Ag⁻ crystals have been investigated in the energy region between the C absorption band and the fundamental absorption edge.

NaCl:Ag⁺ crystals were grown by the Bridgman method from the NaCl powders containing the AgCl concentration of 0.01 mol%, which corresponds to the Ag⁺ ion concentration of about 2.3×10^{18} number/cm³ in the crystal. The conversion from the Ag⁺ to Ag⁻ ions in the crystals was achieved by an electrolytic coloration technique. The optical measurements were performed at the BL-3B of UVSOR.

Figure 1 shows the absorption spectra of NaCl:Ag⁺ and NaCl:Ag⁻ crystals. In NaCl:Ag⁺, an absorption band peaking at 6.9 eV and the steep rise from 7.2 eV can be seen. The absorption band at 6.9 eV is attributed to the partially-allowed transition of $4d^{10} \rightarrow 4d^9 5s$ in the Ag⁺ ion. The steep rise from 7.2 eV corresponds to the lower tail of the absorption band due to an electronically allowed transition in the Ag⁺ ion [4].

In NaCl:Ag⁻, the absorption band at 6.9 eV disappears and the steep rise from 7.2 eV shifts to the higher energy side. The C absorption band due to the Ag⁻ centers is obviously observed at 4.6 eV [2]. The fact implies that the Ag⁺ ions are efficiently transformed to the Ag⁻ ions by the electrolytic coloration. In addition to the C absorption band, the intense and small absorption bands are observed at 6.51 and 7.10 eV, respectively.

Figure 2 shows the excitation spectra for the A' and C' luminescence bands due to the Ag⁻ centers, which are shown in the insert of Fig. 2. The C' luminescence band is efficiently excited at around 6.9 eV corresponding to the C absorption band. The A' luminescence band is excited at the higher energy region in the C absorption band. It should be noted that the excitation spectrum for the A' luminescence has the peaks at 7.10 and 7.60 eV. The peak energy of 7.10 eV is equal to that of the small absorption band of NaCl:Ag⁻, as shown in Fig. 1. Thus, the small absorption band at 7.1 eV will be related to the Ag⁻

centers and might be assigned to the D band. On the other hand, both the A' and C' luminescence bands are not excited at around 6.5 eV, where the intense absorption band is located. This fact indicates that the 6.5 eV absorption band in NaCl:Ag⁻ has no relationship with the Ag⁻ centers. The 6.5 eV absorption band might be associated with the Ag⁰ atoms which were not converted to the Ag⁻ ions through the electrolytic coloration.
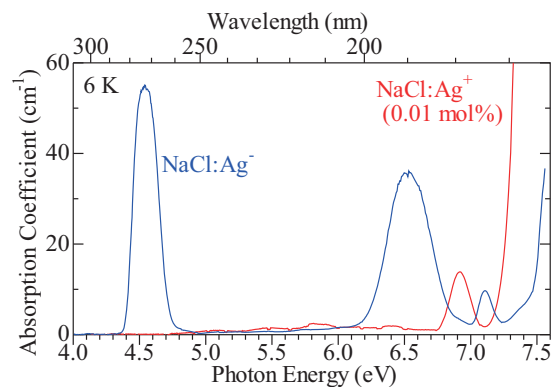

Fig. 1. Absorption spectra of NaCl:Ag⁺ (red)   and NaCl:Ag⁻ (blue) crystals.
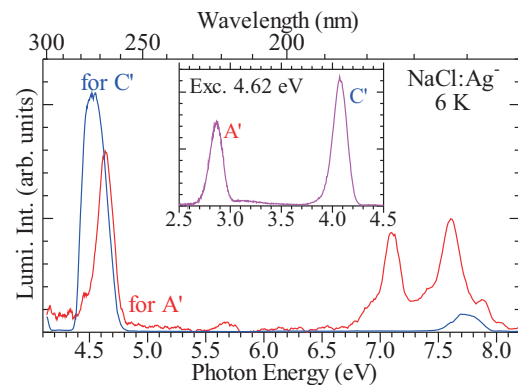

Fig. 2. Excitation spectra for the A' (red) and C' (bule) luminescence bands. Insert is the lumi- nescence spectrum under excitation at 4.62 eV

[1] W. Kleemann, Z. Physik **234** (1970) 362.
[2] S. Shimanuki, J. Phys. Soc. Jpn. **35** (1973) 1680.
[3] A. Ranfagni *et al.*, Advances in Physics **32** (1983) 823.
[4] R. Onaka *et al.*, Jpn. J. Appl. Phys. **4** (1965) Suppl.1, 631.

Experimental Evidence for Migration and Trapping of Excited Electrons in Ce:Gd$_3$(Al,Ga)$_5$O$_{12}$ Single Crystals

A. Satoh[1], M. Kitaura[1], K. Kamada[2], A. Ohnishi[1] and M. Sasaki[1]

[1]*Dept. of Physics, Faculty of Science, Yamagata University, 1-4-12 Kojirakawa, Yamagata 990-8560, Japan*
[2]*Materials laboratory of Furukawa Co. Ltd, 1-25-13 Kannondai, Tsukuba 305-0856, Japan*

Rare-earth doped A$_3$B$_5$O$_{12}$ (A=Y, Lu, Gd; B=Sc, Al, Ga) garnet crystals attract much attention as a material group of inorganic scintillators useful for x- and γ-ray detection. Scintillation properties of this group have been remarkably improved by the combination of band-gap engineering and rare-earth 5*d* level positioning strategies [1, 2]. By such great efforts, a novel Ce^{3+} doped Gd$_3$(Al,Ga)$_5$O$_{12}$ (Ce:GAGG) scintillator crystal has been recently developed [3]. Further improvement of crystal quality is necessary in order to meet the demand for the application into various scientific and industrial fields. For this purpose, it is expected that spectroscopy experiment bring valuable information. In the present study, we have measured absorption spectra and excitation spectra of the 2.34 eV emission band due to 5*d* - 4*f* transitions of Ce^{3+} ions at various temperatures, in order to clarify migration and trapping processes of photo-carriers in GAGG crystals. Crystals of Ce:GAGG and GAGG were grown in Ar + O$_2$ (2%) atmosphere from melt by the Czochralski method. Experiment was performed at the BL3B beam line of UVSOR. The absorption and excitation spectra measured were corrected with a calibrated silicon photodiode sensor for the distribution of an excitation light.

Figure 1 shows absorption spectra of a Ce:GAGG single crystals observed at 6 K and 300 K. The concentration of Ce^{3+} ions in the Ce:GAGG crystal was determined to 0.08 mol%. The absorption spectra exhibit broad bands at 2.82 eV and 3.62 eV, and narrow lines around 4 - 5 eV. The broad bands appear by the incorporation of Ce^{3+} ions, and they are thus assigned to the 4*f* - 5*d* transitions of Ce^{3+} ions. The narrow lines were observed in absorption spectra of GAGG single crystals. We connect these lines to the 4*f* - 4*f* transitions of Gd^{3+} ions. The absorption coefficient is abruptly increased in the photon energy range from 5.75 to 6 eV. This is due to the fundamental absorption edge of the host GAGG crystal, the photon energy of which is determined to be 5.96 eV at 6 K and 5.69 eV at 300 K.

Excitation spectra for the 2.34 eV emission band of Ce:GAGG (0.08 mol%) are shown in Fig. 2. The intensity of the 2.34 eV emission band does not almost depend on temperature under excitation in the lowest energy Ce^{3+} 4*f* - 5*d* absorption band at 2.81 eV. In contrast, the intensity is varied with increasing temperature, when the crystal is excited in the energy region higher than 2.81 eV absorption peak. This result is explained as follows. At low temperature,

excited electrons are partially trapped at defect levels. With increasing temperature, trapped electrons are released from the defect levels via a thermal activation process, and they migrate to electron-lost Ce^{4+} sites. The excited states of Ce^{3+} ions are more increased, compared to those at low temperature, and the 2.34 eV emission band is thus enhanced. The origin of defects responsible for such an enhancement is now in investigation.
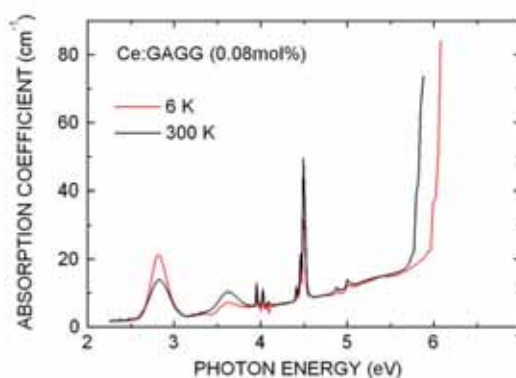

Fig. 1. Absorption spectra of a Ce:GAGG (0.08 mol%) single crystal observed at 6 K (red line) and 300 K (black line).
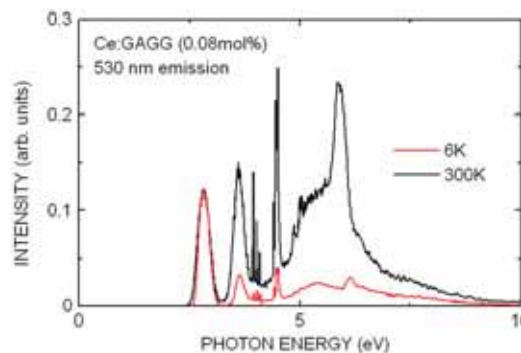

Fig. 2. Excitation spectra for the 2.34 eV emission band of a Ce:GAGG (0.08 mol%) single crystal, observed at 6 K (red line) and 300 K (black line).

[1] K. Kamada *et al*., Cryst. Growth & Des. **11** (2011) 4484.
[2] M. Fasoli *et al*., Phys. Rev. B **84** (2011) 081102(R).
[3] K. Kamada *et al*., J. Cryst. Growth **352** (2012) 88.

Ⅲ-5. SOLID STATE PHYSICS

Combined Excitation-Emission Spectroscopy of Boron-Doped Diamond Films

T. Toyoda[1], K. Fukui[1] and T. Inushima[2]

[1]*Department of Electrical and Electronics Engineering, University of Fukui, Fukui 910-8507, Japan*
[2]*Department of Electronics, Tokai University 4-1-1 Kitakaname, Hiratsuka 259-1292, Japan*

Boron-doped diamond (BDD) is one of the p-type wide band-gap (5.5eV) semiconductors. Recently, the superconductivity has been discovered in heavily BDD [1]. In this study, we have measured the CEES (Combined Excitation Emission Spectroscopy) around the band-gap (excitation energy 4.5 ~ 7.0eV) in order to clarify the electron state of BDD whose boron concentrations is in the metal-semiconductor transition region.

The BDD films used in this study are grown on Ib-synthesized diamond substrates by the MPCVD (Microwave Plasma Chemical Vapor Deposition) method and their boron concentration are 1000, 2000, 5000 and 10000 ppm [2]. All CEES measurements including the diamond substrate (0 ppm) have been performed at BL3B.

Figure 1(A) and 1(B) show the CEES spectra at 9 K of the 1000 ppm and 10000 ppm BDDs, respectively. The horizontal axis represents the emission energy, and the vertical the excitation energy. A strong emission region around 2.4 eV (white color region in Fig. 1(A)) consists of two emission bands. One is shown at lower excitation energy side which has clear higher energy cut of the emission spectrum shape at 2.5 eV. This characteristic emission band is known as the band due to the H3 center (H3 band) which is nitrogen defect related center in diamond. In fact, the H3 band is clearly observed in diamond substrate (0 ppm) sample. The difference of the H3 band in between 0 ppm and 1000 ppm is the existence or nonexistence of the higher excitation energy limit, because there is no limit in the case of 0 ppm sample but about 6.0 eV in the case of 1000 ppm. The other emission band has a broad Gaussian like line shape and is observed at higher excitation energy side. The lower excitation energy limit is about 5.5 eV where is almost same energy as the indirect band-gap energy of the diamond. This emission band is often observed in the BDD and is considered donor-acceptor pair (DAP) emission (G band), where the acceptor is boron [3]. These results suggest that (i) the higher excitation energy side emission band is the G band of the BDD, (ii) the lower side band is H3 band of the diamond substrate, (iii) 1000 ppm BDD has the direct band-gap of ~ 6.0 eV.

In the case of the 10000 ppm BDD (fig. 1(B)), the strong regions clearly separate two regions. One is shown in the emission energy around 2.4 eV (white color region in fig. 1(B)). This band is H3 band of the diamond substrate as mentioned above. A new band around 2.8 eV (red color circle in fig. 1(B)) is

observed. The origin of this band is not clear at present, but it is clear that this emission is caused by the band to band excitation and there is no overlap of the excitation energy between this new band and the H3 band. These behaviors are consistent with the previous work [2, 4].
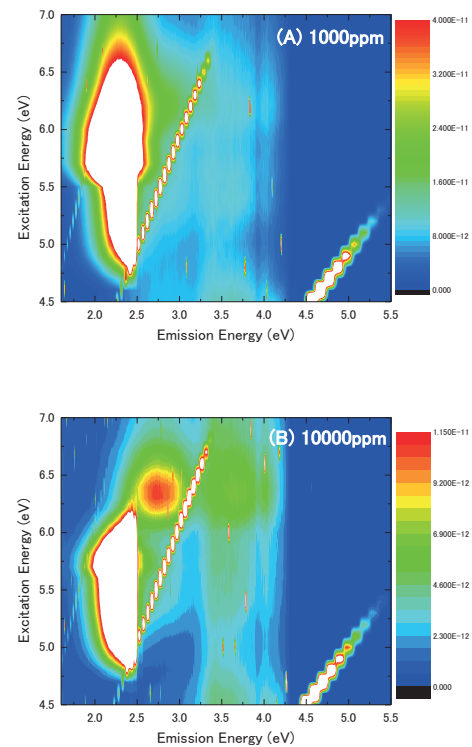

Fig. 1. CEES of BDD (A) 1000 ppm and (B) 10000 ppm at 9 K.

[1] E. A. Ekimov, V. A. Sidorov, E. D. Bauer, N. N. Mel'nik, N. J. Curro, J. D. Thompson and S. M. Stishov, Nature **428** (2004) 542.
[2] A. Ogasawara, T. Inushima, T. Shiraishi, S. Ohya, S. Karasawa and H. Shiomi, Diamond Relat. Mater. **6** (1997) 835.
[3] E. Gaillou, Jeffrey E. Post, D. Rost and J. E. Butler, Am. Mineral. **97** (2012) 1.
[4] T. Inushima, Y. Ota, K. Fukui, UVSOR Activity Report **38** (2010) 101.

Valence State Analysis of Mn Ions in In_2O_3:(Mn, TM) (TM = Cr, Fe, Co)

S. Nishida[1], T. Yoshioka[1] and T. Yamamoto[1, 2]

[1] Faculty of Science and Engineering ,Waseda University, Tokyo 169-8555, Japan
[2] Institute of Condensed-Matter Science, Waseda University, Tokyo 169-8555, Japan

The dilute magnetic materials (DMMs) have been extensively studied through experiments and theoretical calculations [1, 2], which have ferromagnetic properties with dilute magnetic elements, because of the possibility of their future applications in spintronics. Although the Curie temperature of most DMMs were quite low, it was recently reported that some DMMs show room-temperature ferromagnetism [3, 4]. Among them, a sintered polycrystalline specimen of Mn- and Fe-codoped In_2O_3 (In_2O_3:(Mn,Fe)) shows the property [4]. For a deeper understanding of the mechanism of ferromagnetism in In_2O_3:(Mn,Fe), substitution mechanism of magnetic elements was investigated, in which Mn and Fe ions are substituted at the In sites in In_2O_3 [5]. In addition, it was found that the coexistence of Mn^{2+} and Mn^{3+} is mandatory for room-temperature ferromagnetism in In_2O_3:(Mn,Fe) [6]. In the present study, the valence state analysis of doped Mn ions have been carried out using Mn–L_3 X-ray Absorption Near-Edge Structure (XANES) measurements in order to investigate the difference in electronic structure between ferromagnetic In_2O_3:(Mn,Fe) and paramagnetic In_2O_3:(Mn,Cr) and In_2O_3:(Mn,Co).

All polycrystalline specimens, In_2O_3:(Mn,TM) (($In_{0.94}Mn_{0.03}TM_{0.03})_2O_3$, TM=Cr, Fe, Co), were synthesized by the conventional solid-state reaction method. Mn-L_3 XANES spectra were collected at BL4B in UVSOR by the total electron yield (TEY) method. All the sample powders were mounted on the first Be-Cu dinode using the carbon adhesive tape. The incident beam was monochromatized by the varied-line-spacing plane grating (800 lines/mm). The energy resolution of the incident beams, E/ΔE was set to 3000 by tuning the slit height settled at the upper and lower reaches of the grating.

Prior to the XANES analysis, all the samples were characterized by the X-ray diffraction (XRD). No extra peaks were found in these XRD patterns except for the peaks originating from the bixbyite-structured In_2O_3. Then all the samples were determined to be crystallized in a single-phased cubic bixbyite-structured (*I*a3). The observed Mn-L_3 XANES spectra of In_2O_3:(Mn,TM) are shown in Fig. 1, together with the reference spectra of Mn^{2+} (MnO) and Mn^{3+} (Mn_2O_3). The profiles of the Mn–L_3 XANES spectra of Mn^{2+} (MnO) and Mn^{3+} (Mn_2O_3) are clearly different and can be easily distinguished from the characteristic peak energies of their peaks. By comparing to these standard spectra of Mn oxides, the observed Mn–L_3 XANES spectra of In_2O_3:(Mn,Cr) and In_2O_3:(Mn,Fe) can be determined to be a mixture of the spectra of Mn^{2+} and Mn^{3+}, on the other hand, that of In_2O_3:(Mn,Co) can be determined to be Mn^{3+}.

Mn ions are trivalent in paramagnetic In_2O_3:(Mn,Co), which support our previous report that the coexistence of Mn^{2+} and Mn^{3+} is mandatory for room-temperature ferromagnetism in In_2O_3:(Mn,Fe) [6], while coexistence of Mn^{2+} and Mn^{3+} is also found in paramagnetic In_2O_3:(Mn,Cr). It should be noted here that the ratios between Mn^{2+} and Mn^{3+} are different in In_2O_3:(Mn,Cr) and In_2O_3:(Mn,Fe), which suggests that the ratio between Mn^{2+} and Mn^{3+} is also quite important for the appearance of room-temperature ferromagnetism.
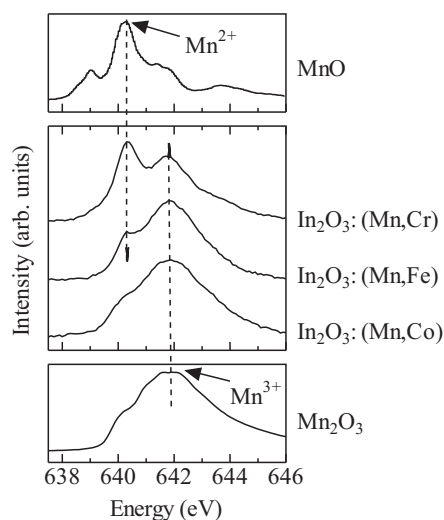
Fig. 1. Observed Mn-L_3 XANES spectra of In_2O_3:(Mn,TM) (TM=Cr, Fe, Co). Top and bottom spectra are those of MnO [7] and Mn_2O_3, respectively.

[1] H. Ohno *et al.*, Phys. Rev. Lett. **68** (1992) 2664.
[2] T. Dietl *et al.*, Science **287** (2000) 1019.
[3] P. Sharma *et al.*, Nat. Mater. **2** (2003) 673.
[4] G. Peleckis *et al.*, Appl. Phys. Lett. **88** (2006) 132507.
[5] T. Yamamoto *et al.*, J. Phys. : Condens. Matter **21** (2009) 104211.
[6] T. Okazaki *et al.*, Solid State Comm. **151** (2011) 1749.
[7] B. Gilbert *et al.*, J. Phys. Chem. A **107** (2003) 2839.

Ⅲ-5. SOLID STATE PHYSICS

Angle-Resolved Photoemission Study of CaCu$_3$Ti$_4$O$_{12}$

H. J. Im[1], M. Tsunekawa[2], T. Sakurada[1], M. Iwataki[1], K. Kawata[1], T. Watanabe[1],
K. Takegahara[1], H. Miyazaki[3], M. Matsunami[4, 5], T. Hajiri[4, 6] and S. Kimura[4, 5]

[1]*Department of Advanced Physics, Hirosaki University, Hirosaki 036-8224, Japan*
[2]*Faculty of Education, Shiga University, Shiga 522-8522, Japan*
[3]*Department of Environmental and Materials Engineering, Nagoya Institute of Technology, Nagoya 466-8555, Japan*
[4]*UVSOR Facility, Institute for Molecular Science, Okazaki 444-8585, Japan.*
[5]*School of Physical Sciences, The Graduate University for Advanced Studies, Okazaki 444-8585, Japan.*
[6]*Graduate School of Engineering, Nagoya University, Nagoya 464-8603, Japan*

A-site ordered perovskite CaCu$_3$Ti$_4$O$_{12}$ has been attracted much attention due to the extremely high dielectric constant and Mott-type insulator, respectively [1]. However, there have been difficulties to realize applications and understand the underlying physics, e.g. strong correlation effects, due to the absence of experimental band structures. Therefore, we have been studied the electronic structure by the photoemission spectroscopy [2, 3]. In this report, we present the band dispersions obtained the angle-resolved photoemission (ARPES) measurements and discuss the strong correlation effects by comparing with the band calculations within the local-density approximation (LDA).

ARPES experiments were performed at the beamline BL5U. The used photon energy and the total energy resolution are 90 eV and 165 meV, respectively. Measurement temperature is about 300 K. The clean surface was prepared in the (100) plane by cleaving *in situ* in a vacuum better than 2×10^{-8} Pa.

Figure 1 (a) and (b) are the image of the ARPES spectra obtained by the second derivatives of the energy distribution curves and the band dispersions obtained from the LDA calculations, respectively. In Fig. 1 (a), the calculated band dispersions are superimposed on the ARPES image, shifting to the higher binding energy by 1.7 eV. Before comparing the ARPES results and the LDA calculations, it should be noted that there are 51 bands in the valence band region as shown in Fig. 1 (b). Unfortunately, the ARPES experiments cannot resolve these bands due to the limitation of energy- and momentum-resolution. Therefore, the band dispersions observed in ARPES experiments should be interpreted as a bundle of bands with the similar tendency.

In the region of 0 - 2.5 eV, we find the flat band with weak intensity. Even though the exact size of band dispersion cannot be estimated in the ARPES measurements due to the band broadening, we find that the band width is very narrow compared with the LDA calculations. This indicates that the bands are more localized than the expectation of the LDA calculations. These bands are assigned to three bands from 64 to 66 which cross the Fermi level and

disperse by about 1 eV in the LDA calculations. In the region of 2.5 - 5 eV, there are bands around 3 eV and bands around 3.8 eV, which are well consistent with the LDA calculations. The former and the latter bands are assigned to bands from 60 to 63 and from 55 to 59, respectively. Particularly, the bands around 3.8 are not dispersive and show the localized character.

In the region of 5 - 8 eV, ARPES data show the highly dispersive bands, which consist of many bands from 16 to 50 in the LDA calculations.

As discussed above, we attribute the differences between ARPES results and the LDA calculations to the strong correlation effects.
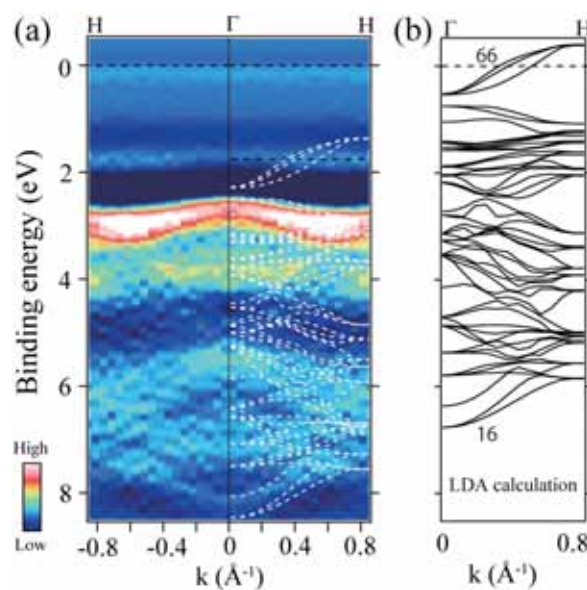

Fig. 1. (a) ARPES image of CaCu$_3$Ti$_4$O$_{12}$ obtained at hv = 90 eV and T = 300 K and the band dispersions obtained from the LDA calculations.

[1] M. A. Subramanian *et al.*, J. Solid State Chem. **151** (2000) 323.
[2] H. J. Im *et al.,* UVSOR Activity Report **38** (2011) 87.
[3] H. J. Im *et al.,* UVSOR Activity Report **39** (2012) 90.

Photoemission Study of Pyrite-type $Ni_{1-x}Cu_xS_2$

K. Soda[1,2,3], K. Usui[2], S. Osawa[3], H. Kondo[1], M. Kato[1,2,3], J. Iwasaki[4], K. Niwa[2,3,4],
K. Kusaba[2,3,4] and M. Hasegawa[2,3,4]

[1]*Department of Quantum Engineering, Graduate School of Engineering, Nagoya University, Nagoya 464-8603, Japan*
[2]*Department of Physical Science and Engineering, School of Engineering, Nagoya University, Nagoya 464-8603, Japan*
[3]*Department of Materials, Physics and Energy Engineering, Graduate School of Engineering, Nagoya University, Nagoya 464-8603, Japan*
[4]*Department of Crystalline Materials Science, Graduate School of Engineering, Nagoya University, Nagoya 464-8603, Japan*

Pyrite-type transition-metal dichalcogenides MX_2 (M = Fe, Co, Ni, Cu, Zn; X = S, Se) show rich variety of electronic and magnetic properties due to the electron correlation and hybridization effects. NiS_2 is classified as a charge-transfer-type insulator and $NiS_{2-x}Se_x$ reveals a metal-insulator transition [1, 2]. CuS_2 is a p-band metal, exhibiting superconductivity [3]. It is interesting to clarify the effects of solid solution between metallic CuS_2 and insulating NiS_2 on the electronic structure and related properties. Here, we will report the first preliminary results.

Photoelectron measurements were performed at 10 K at BL5U in angle-integrated mode. Polycrystalline specimens of $Ni_xCu_{1-x}S_2$ were synthesized under a high pressure of 6.5 GPa at a temperature of ~920 K. Their clean surfaces for the measurement were prepared by scraping them with a diamond file. Total energy resolution was estimated as ~0.07 eV at the excitation photon energy of 40 eV. The origin of the binding energy E_B was set to the Fermi energy E_F determined by measuring the Fermi edge of an evaporated Au film electrically connected to the specimen.

In Fig. 1, typical valence-band photoelectron spectra of $Ni_xCu_{1-x}S_2$ are compared with their X-ray ones obtained at SPring-8 (dots) and calculated results: configuration-interaction cluster model (bars) [4] and band structure (curves) [1, 5] calculations. Each spectrum is normalized with the intensity integrated up to E_B = 16 eV and the excitation photon energy is indicated in the figure. Calculated semiconductor-like electronic structure of NiS_2 is presented so as to locate the valence-band maximum at E_F. For CuS_2, the observed valence-band spectrum agrees well with the calculated band structure [5], while the present NiS_2 spectra are in less agreement but consistent with both the calculated results [1, 4]. The intensity at E_F for CuS_2 is 50 % of the edge jump, indicating its metallic nature, while that for NiS_2 is ~20 %, suggesting that NiS_2 has a semimetallic or semiconducting (insulating) feature, as reported [2, 3]. Bands at 2.0 and 2.6 eV in NiS_2 and CuS_2 are ascribed to the Ni and Cu 3d states, respectively. In $Ni_{0.5}Cu_{0.5}S_2$, peaks are recognized at E_B = 1.7 and 2.6 eV, and the intensity at E_F is ~40 % of the edge jump,

which is in the middle of NiS_2 and CuS_2. Thus the valence band of $Ni_{0.5}Ni_{0.5}S_2$ seems superposition of those of NiS_2 and CuS_2, although the Ni 3d peak in $Ni_{0.5}Ni_{0.5}S_2$ is 0.3 eV lower in E_B than in NiS_2, which suggests the hybridization between Ni and Cu states.

Further study is intended on the x-dependence of the spectral shape as well as the electric and magnetic properties. In comparison to the reported results [1-4], some modifications are also found in the high binding energy region. Further examination will be tried in different experimental conditions including sample preparation.
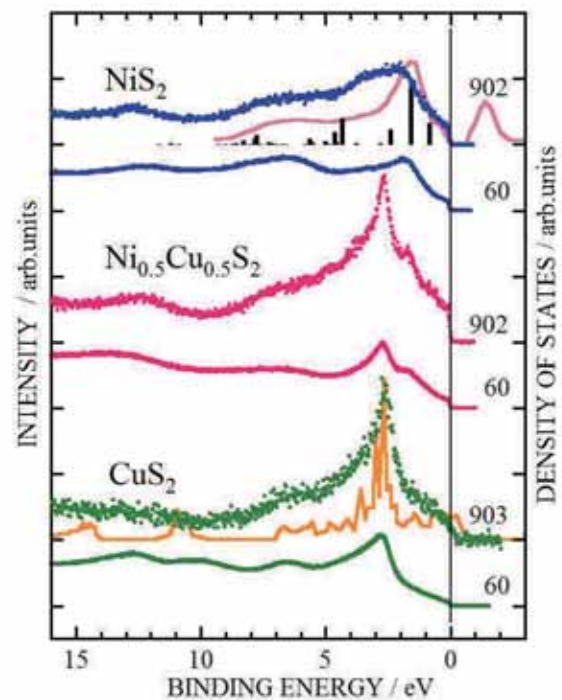

Fig. 1. Valence-band spectra of $Ni_{1-x}Cu_xS_2$.

[1] J. Kunes *et al*., Phys. Rev. B **81** (2010) 035122.
[2] K. Mamiya *et al*., Phys. Rev. B **58** (1998) 9611.
[3] H. Ueda *et al*., Phys. Rev. B **65** (2002) 155104.
[4] A. Fujimori *et al*., Phys. Rev. B **54** (1996) 16329.
[5] D. W. Bullett, J. Phys. C **15** (1982) 6163.

III-5. SOLID STATE PHYSICS

Angle-Resolved Photoemission Study on $Sm_{1-x}Y_xS$

M. Kaneko[1, 2], M. Saito[3], T. Ito[1, 5], K. Imura[4], T. Hajiri[1, 2], M. Matsunami[2, 6], S. Kimura[2, 6], H. S. Suzuki[7] and N. K. Sato[4]

[1] Graduate School of Engineering, Nagoya University, Nagoya 464-8603, Japan
[2] UVSOR Facility, Institute for Molecular Science, Okazaki 444-8585, Japan
[3] School of Physical Sciences, Nagoya University, Nagoya 464-8603, Japan
[4] Graduate School of Physical Sciences, Nagoya University, Nagoya 464-8603, Japan
[5] Nagoya University Synchrotron Radiation Research Center, Nagoya University, Nagoya 464-8603, Japan
[6] School of Physical Sciences, The Graduate University for Advanced Studies (SOKENDAI), Okazaki 444-8585, Japan
[7] National Institute for Materials Science, Tsukuba 305-0047, Japan

Samarium monosulfide (SmS) is a prototypical valence fluctuating compound inducing insulator (Black phase) – metal (Golden phase) transition by applying external pressure. To directly observe the pressure-induced change of the electronic structure, we have performed angle-resolved photoemission spectroscopy (ARPES) on $Sm_{1-x}Y_xS$ where the analogous insulator – metal transition is achieved as a function of chemical pressure (Sm-Y substitution).

Single crystals of $Sm_{1-x}Y_xS$ ($x = 0, 0.17, 0.33$) were grown by the Bridgman technique using a high-frequency induction furnace installed at NIMS. ARPES measurement on these crystals was performed at the VUV-ARPES beamline BL5U of UVSOR-III. The inner potentials V_0 have been 0.17, and 0.33, respectively, by analyzing $h\nu$ - dependence (27 - 84 eV) of energy distribution curve of highly-dispersive S 3p bands.

Figure 1 (a), (b) and (c) show the ARPES image of $Sm_{1-x}Y_xS$ ($x = 0, 0.17$ and 0.33) near the X point. From the comparison with the reported ARPES on black SmS [1], the highly dispersive features at 3 – 6 eV are ascribed to S 3p band, while nondispersive structures, respectively. By Sm-Y substitution, the latter structure gradually shifts to EF, while the former to higher binding energies from $x = 0.17$ to 0.33 (see Fig.1 (d)).

To investigate the electronic structure, we show the ARPES image of $Sm_{0.83}Y_{0.17}S$ near EF around the X point at the Brillouin zone boundary [Fig. 1(e)]. We clearly found EF crossing of highly dispersive band around the X point, where the Sm 5d states locate just above EF on black SmS [2]. Around the bottom of the dispersive band, the Sm 4f state pushed up to around 0.5 eV show sizable dispersion. The observed Sm 4f dispersion strongly suggests the existence of the Sm 4f-5d hybridization, which causes the insulator to metal transition with Sm-Y substitution.

In conclusion, as the Sm^{2+} 4f multiplet structure shifts to EF from $x = 0$ to 0.17, the electron pocket appears due to the Sm 4f-5d hybridization band formation, which is the possible origin of insulator-metal transition. On the other hand, the S 3p bands pushed down to high binding energy side from $x = 0.17$ to 0.33 since the Sm 5d – S 3p hybridization becomes stronger in the metallic phase.

[1] T. Ito, A. Chainani, H. Kumigashira, T. Takahashi and N. K. Sato, Phys. Rev. B **65** (2002) 155202.
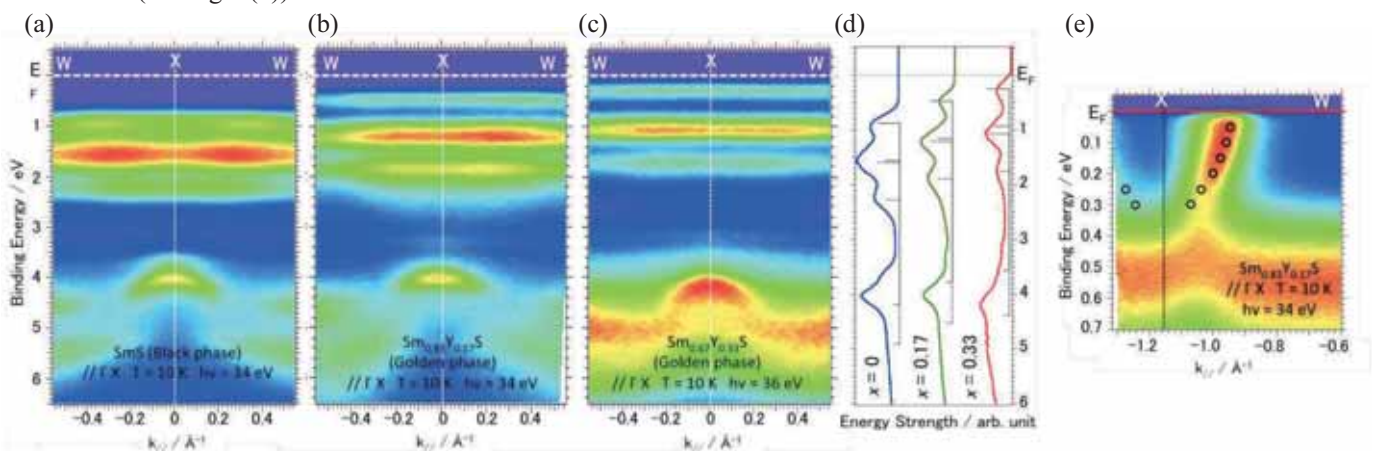[2] V. N. Antonov et al., Condensed Matter Physics, **7** (2004) 38.

Fig. 1. The ARPES image of (a) x = 0, (b) 0.17 and (c) 0.33 near the X point.
(d) The elemental substitution dependence of the ARPES spectrum at X point (x = 0, 0.17 and 0.33)
(e) The thorough ARPES image of x = 0.17. Open circles indicate the peak positions of the bands estimated by the second derivative of EDC data.

Annealing Behavior of Ultrashallow Thermal Donors Formed in Carbon- and Hydrogen-Doped Czochralski Silicon Crystals

A. Hara and T. Awano

Electronic Engineering, Tohoku Gakuin University, Tagajo 985-8537, Japan

In the past, we have reported on ultrashallow thermal donors (USTDs) in carbon- and hydrogen-doped Czochralski silicon (CZ Si) crystals after annealing at 480°C [1]. USTDs are hydrogen-like donors with slightly different energy levels, some of which show negative central-cell correction, and to the best of our knowledge, are the shallowest energy levels as compared to many types of previously reported donors in Si crystals [2]. In this study, we evaluated the relationship between the intensity of USTDs and annealing time to investigate their formation mechanism.

Carbon-doped CZ Si samples were doped with hydrogen by annealing them in wet oxygen at 1300°C for 60 min. The samples were then cooled to room temperature by rapidly exposing them to air. For carbon doping, the Si melt used for preparing the ingot was doped with carbon powder during CZ Si crystal growth. The formation of USTDs at 480°C in wet oxygen was investigated using the far-IR spectrometer of the BL6B beamline at Liq. He temperature obtained using a flowing cryostat.

Figure 1 shows the annealing behavior of USTDs and shallow thermal donors (STDs). It has been reported that STDs are hydrogen-like donors and are generated in hydrogen-doped CZ Si crystals at around 450°C [3]. STDs are generated rapidly within the first 10 h and then decrease with the annealing time. However, USTDs are generated slowly and increase with increasing annealing time.

Figure 2 shows that the intensity of STDs after annealing at 480°C for 40 h is equal to that after 10 h of annealing in hydrogen-doped but without carbon CZ Si crystals. Moreover, USTDs are not generated.

Figures 1 and 2 show that carbon impurities act as atomic elements essential for the generation of USTDs and reduction of STDs. Carbon impurities occupy substitution sites; therefore, its diffusion coefficient (D) is very small given by D = $1.9\exp(-3.2eV/k_BT)$ cm^2/s [4]. However, the value of D for interstitial carbons is significantly greater than this value. Thus one tentative explanation for the results shown in Figure 1 and 2. They are that some STDs, which are generated in the initial stage at 480°C owing to their rapid generation rate, are transformed to USTDs during long-term annealing by combining with interstitial carbons. Interstitial carbon is thought to be generated in CZ Si by the formation of SiO$_2$ precipitates.
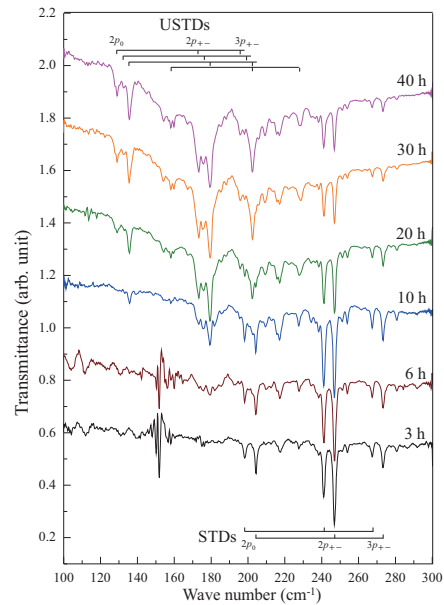
Fig. 1. Variations in USTDs and STDs after annealing at 480°C in carbon- and hydrogen-doped CZ Si crystals.
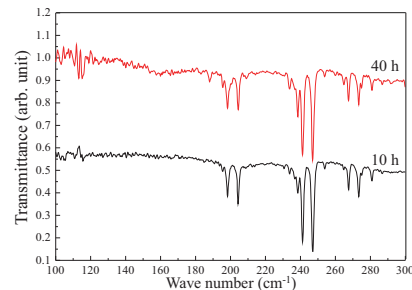
Fig. 2. Spectra for STDs after annealing at 480°C for 10 and 40 h in hydrogen-doped but without carbon CZ Si crystals.

[1] A. Hara, T. Awano, Y. Ohno and I. Yonenaga, Jpn. J. Appl. Phys. **49** (2010) 050203.

[2] A. Hara, Jpn. J. Appl. Phys. **34** (1995) 3418.

[3] R. C. Newman, J. H. Tucker, N. G. Semaltianos, E. C. Lightowlers, T. Gregorkiewicz, I. S. Zevenbergen and C. A. J. Ammerlaan, Phys. Rev. B **54** (1996) R6803.

[4] F. Shimura, Semiconductor Silicon Crystal Technology (Acadenic Press, 1988)

III-5. SOLID STATE PHYSICS

Study of Electronic States of Solids Probed by a Microspectroscopy Using the Synchrotron Radiation

A. Irizawa[1], S. Kobayashi[2], K. Yoshimura[2] and S. Kimura[3, 4]

[1]*The Institute of Science and Industrial Research, Osaka University, Ibaraki 567-0047, Japan*
[2]*Division of Chemistry, Graduate School of Science, Kyoto University, Kyoto 606-8502, Japan*
[3]*School of Physical Sciences, The Graduate University for Advanced Studies (SOKENDAI),*
Okazaki 444-8585, Japan
[4]*UVSOR Facility, Institute for Molecular Science, Okazaki 444-8585, Japan*

The optical study using infrared light sources is one of the most powerful techniques for the investigation of electronic states on solids. There can be obtained the direct information about the change of electronic band structure, the symmetry of crystal structure, and the dielectric property. In the respect of experimental affinity, the optical study is extremely compatible with the multiple conditions such as low temperature, high magnetic field, and high pressure. In the case of strongly correlated electron systems, it is well known that the temperature is one of the decisive factors for the electronic state. The considerable types of phase transition are induced by the change of the temperature. Particularly, the multiferroic compounds can be controlled of its physical properties mutually by the external fields such as magnetic, electronic, and elastic ones. The other particular condition, the pressure will directly affect the electron-electron interactions through the change of lattice constants. The beamline 6B in UVSOR is adjusted for the investigations at low temperature and high pressure in the extremely low-energy region of FIR-THz (far infrared-terahertz). There equips two type interferometers of both Michelson and Martin-Puplett type. In this report, we tried the optical reflectivity measurements in the longest wavelength region by a micro spectrometer for the single crystals of newly synthesized compound $CrSe_2$ showing a discontinuous resistive change and a pressure-dependent magnetization.

The experiments are performed using a micro spectrometer having 1D array detector and a liquid-He flow type cryostat for controlling the temperature from 300 K down to 20 K. The reflectivity was obtained from the ratio of optical reflections between the sample and Au as a standard with mirrored surfaces. They were installed on the sample holder and were measured through a polypropylene window of the cryostat.

The reflectivities are obtained in the energy range between 200 and 700 cm^{-1} as shown in Fig. 1. This compound shows two discontinuous temperature changes at 195 K and at 175 K with hysteresis loop in electrical resistivity [1] and magnetization [1, 2], but from the results of optical reflectivity experiments there is no significant change in the energy range of FIR. At this moment it comes out that the lower energy experiments using larger samples are demanded as a future study for this compound.
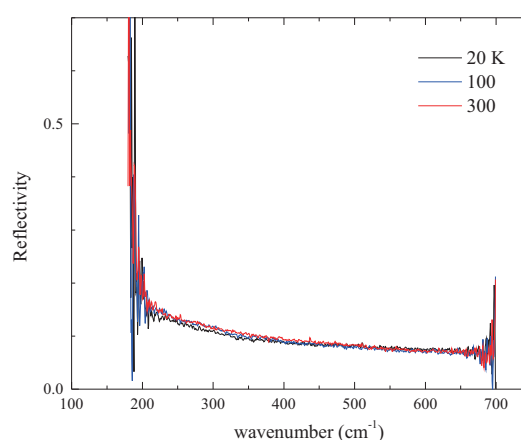

Fig. 1. Temperature change of reflectivity of $CrSe_2$.

[1] S. Kobayashi *et al*., 18pGB-12 (2012) JPS meeting in Yokohama.
[2] C.F. van Bruggen *et al*., Physica B+C **99** (1980) 166.

Increase of Quasiparticle Lifetime in FeSb₂ Kondo-Semiconductor

T. Takeuchi[1,2,3], T. Shimada[3], M. Matsunami[4] and S. Kimura[4]

[1]*EcoTopia Science Institute, Nagoya University, Nagoya 464-8603, Japan*
[2]*PRESTO, Japanese Science and Technology Agency, Tokyo 102-0075, Japan*
[3]*Department of Applied Physics Graduate School of Engineering, Nagoya University, Nagoya 464-8603, Japan*
[4] *UVSOR, Institute for Molecular Science, Okazaki 444-8585, Japan*

FeSb₂ has attracted interest because it possesses a huge magnitude of Seebeck coefficient $|S|$ exceeding 40 mV/K at low temperature below 40 K [1]. The origin of this huge $|S|$ has not been revealed yet. Seebeck coefficient is generally determined by the electronic structure near the chemical potential of conduction electrons. Thus it is of great importance to investigate its electronic structure in detail. Since the unusual increase of $|S|$ is observed at low temperatures below 50 K, one has to use experiments that are capable of investigating the detailed electronic structure with a high-energy resolution.

In this study, therefore, we prepared high-quality single grained FeSb₂ samples and measured their electronic structure in detail by means of high-resolution angle resolved photoemission spectroscopy measurements (ARPES) with synchrotron radiation as the photon source at BL7U of UVSOR. We also measured Seebeck coefficient, low temperature specific heat, and magnetization over a wide temperature range from 2 K to 100 K.

The single grained FeSb₂ samples were grown in antimony flux under the vacuum atmosphere. The electrical resistivity shows a very large but finite value at low temperature. This result indicates a finite number of electronic states persisting at the Fermi energy (ε_F). We also confirmed that the electronic specific heat coefficient of samples was distributed

over the range of 0.001 < γ < 0.01 mJ mol⁻¹K⁻². These small γ definitely indicate the very small but finite value of electronic density of states at ε_F.

We also realized that the shape of ARPES spectra drastically changes with varying temperature. The sharp peak persisting at temperatures below 20 K starts to be broadened above 30 K. The drastic increase of the energy-width of spectral function indicates that the quasiparticle lifetime is fairly reduced. Notably, this temperature dependence was observed over the whole momentum-range where the present ARPES measurement was performed.
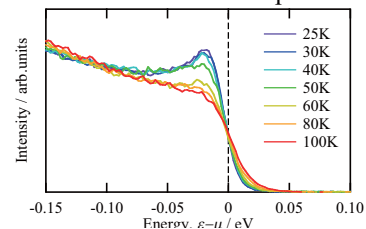

Fig. 2. Energy distribution curves observed at a momentum near the Fermi surface. With decreasing temperature, the peak intensity drastically increased at the temperature range below 60 K where the large magnitude of Seebeck coefficient was observed.

At the same temperature range, the magnitude of Seebeck coefficient and electrical resistivity decreases with increasing temperature, while the magnitude of magnetic susceptibility increases. All the experimental facts unambiguously indicate that the electronic structure change in association with destruction of Kondo-lattice occurs with increasing temperature in this particular temperature range. If we assume the formation of Kondo-peak a few meV above the chemical potential at the temperature range below 30 K, the large magnitude of Seebeck coefficient with negative sign is reasonably accounted for with it. The behavior of electrical resistivity above 30 K is understood as that in the disordered Kondo materials where the lifetime of quasiparticle is limited to be short by the strong spin scatterings. The constant value of electrical resistivity below 30 K is regarded as that observed for Kondo lattice under the unitary limit in good consistency with the rather long lifetime of quasiparticles. The increase of magnetic susceptibility with increasing temperature above 30 K is also accounted for with the destruction of Kondo lattice leading to the development of local magnetic moment.

[1] T. Bentien *at al*., EPL **80** (2006) 17008.

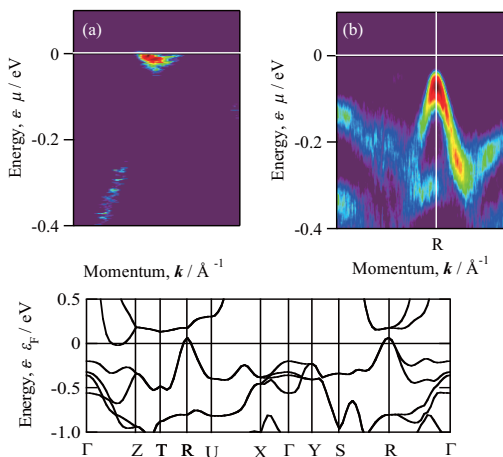Fig. 1. (a) Electron pocket observed in the second momentum derivative of ARPES intensity $\partial I(k_{\Gamma Z},\varepsilon)/\partial k_{\Gamma Z}$ measured aling Γ-Z line. (b) Second energy derivative of ARPES intensity $\partial I(k_{\Gamma R},\varepsilon)/\partial \varepsilon$ obtained at a momentum line near R. The band dispersion calculated by FLAPW-GGA is shown in the bottom.

III-5. SOLID STATE PHYSICS

Investigation of the Electron-phonon Scattering in the Graphite by Using the Angle-Resolved Photoelectron Spectroscopy: Direct Observation of the Indirect Transition

S. Tanaka[1], M. Matsunami[2,3] and S. Kimura[2,3]

[1]*The institute of Scientific and Industrial Research, Osaka University, Ibaraki 567-0047, Osaka, Japan*
[3]*UVSOR Facility, Institute for Molecular Science, Okazaki 444-8585, Japan*
[3]*School of Physical Sciences, The Graduate University for Advanced Studies (SOKENDAI), Okazaki 444-8585, Japan*

The electron-phonon scattering is one of the key issues in the solid state physics and has been extensively studied for long years. Angle-resolved photoelectron spectroscopy (ARPES) is a very powerful tool to investigate the electronic properties of the condensed matter, since it allows us to measure the band of the electron resolving both in energy and momentum. Then, it has been used to understand the electron-phonon scattering in solids by many researchers. With the ARPES spectrum, however, the electron-phonon interaction was investigated only through the self-energy of the quasiparticle-spectral function in an integrated manner over their branches and momentum. In this study, our aim is observing directly the process of electron-phonon scattering with resolving the energy and momentum. If the energy and momentum of the electron before the scattering are known, the measurements for those of the scattered electron allow us to determine the energy and momentum of the phonons that scattered the electron thanks to the law of the conservation.

For this purpose, we took the Graphite as a target material. HOPG (highly oriented pyrolytic graphite) sample was cleaved *in-situ* and investigated with the ARPES at BL7U of the UVSOR-III. The sample temperature was kept at 50K, that is higher than the critical temperature for the CDW transition [1]. Figure 1(a) shows the surface-normal photoelectron spectra taken at photon energies from 6 to 16eV. The spectra vary drastically depending on the photon energy, and Fig. 1(b) shows the typical spectra in detail. The step-like edges are clearly observed not at the Fermi level, where an edge is observed for the Au film, but at 68meV and 155meV with respect to the Fermi level. Differentials of the spectra are shown in Fig. 1(c) for a convenience to eye, and the peaks are clearly observed at the edge positions. The electronic band crosses the Fermi level at K(H)-point in the Brillouin zone of Graphite and highest occupied band at the Γ(A)-point is located at ~4eV below the Fermi level. Therefore, the electron emission observed in Fig. 1(a) is due to the electron scattering from the K(H)-point to the Γ(A)-point. When the electron-phonon interaction occurs, the electron loses (emission) or gains (absorption) its energy as much as the phonon energy. Since temperature is low (50K), the phonon-absorption probability is negligible in this case. Thus, the peak positions should indicate the
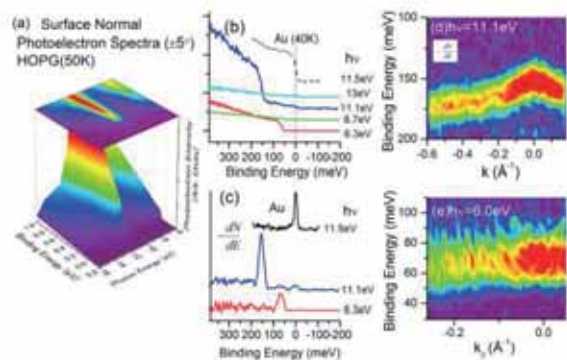

Fig. 1. ARPES Spectra for Graphite (HOPG) and their differentials with respect to the binding energy of the electrons.

energies of the phonons that scattered the electron. Moreover, considering the conservation rule for the momentum, the angle-resolved measurement of the photoelectron enables us investigate the dispersions of the phonons around the K(H)-point. The angle-resolved differential spectra are shown in Figs. 1(d) and (e) taken at hv=11.1eV and 6.0eV, respectively. They clearly show the dispersions of the phonons.

68meV and 155meV phonons are attributed to the ZA and/or ZO, and LO and/or LA modes, respectively. The strong photon-energy-dependence observed in Fig. 1(a) indicates that the final state of the photoexcitation determines the phonon branch that can scatter the electron during the photoexcitation process. It should be ascribed to the dipole selection rules both for the optical transition and the electron-phonon scattering, those of which can be predicted by using the group theory. The detail will soon be published elsewhere.

[1] S. Tanaka, M. Matsunami and S. Kimura, Phys. Rev. B **84** (2011) 121411(R).

Change in the Electronic Structure of the Single Crystalline Graphite as a Result of the CDW Transition

S. Tanaka[1], M. Matsumoto[2], M. Matsunami[3,4] and S. Kimura[3,4]

[1]*The institute of Scientific and Industrial Research, Osaka University, Ibaraki 567-0047, Osaka, Japan*
[2]*Institute of Industrial Science, The University of Tokyo, 4-6-1 Komaba, Meguro-ku, Tokyo 153-8505, Japan.*
[3]*UVSOR Facility, Institute for Molecular Science, Okazaki 444-8585, Japan*
[4]*School of Physical Sciences, The Graduate University for Advanced Studies (SOKENDAI), Okazaki 444-8585, Japan*

Charge-density-wave (CDW) transition is one of the topics that have been extensively studied in solid state physics. This phenomenon is a rearrangement of the atomic structure of low-dimensional solids due to the electron-photon interaction. When the temperature is below critical temperature for the CDW transition, the superstructure is formed accompanying the opening of the gap near the Fermi level in the electronic structure. Recently, we found the experimental evidence that the $p(\sqrt{3} \times \sqrt{3})R30°$ superstructure is formed at lower temperature than 30K on the HOPG (Highly Oriented Pyrolytic Graphite) with Angle-resolved photoelectron spectroscopy (ARPES), and interpreted it as the CDW transition according to the temperature-dependent measurement [1]. When the superstructure is formed, the folding of the Brillouin zone occurs, and the dispersion (originally) at the K-point can be observed at the Γ-point with the ARPES. However, a change in the electronic states as a result of the CDW transition was not observed in the previous work. This is somewhat paradoxical. In this paper, therefore, we examine a change in the electronic structure due to the CDW transition on the single-crystal of Graphite.

The experiments were carried out at BL-7U. The single-crystalline Graphite samples exhibited sharp (1x1) LEED (Low Energy Electron Diffraction) pattern. A clean surface was made by cleaving using the Scotch tape in the ultrahigh vacuum at low temperature. The superstructure formed at low temperature below 30K was confirmed using the 11.5eV-photons in the same manner as the previous study [1]. The photon energy used below was 39eV.

The left panel of Fig.1 shows the comparison of the ARPES spectra near the K-point along the Γ-K-M' direction when the sample temperature is changed from 15K to 50K, those are respectively below and above the critical temperature of the CDW transition. No significant differences are observed in the main features, which show the dispersion of the π-band of the Graphite as previously reported. However, there is a striking change for a dispersive band indicated by circles in the left panel of Fig.1. For showing more detail, we display the EDC curves at several $k_{//}$ values in the right panel of Fig. 1. At top curves, where the π
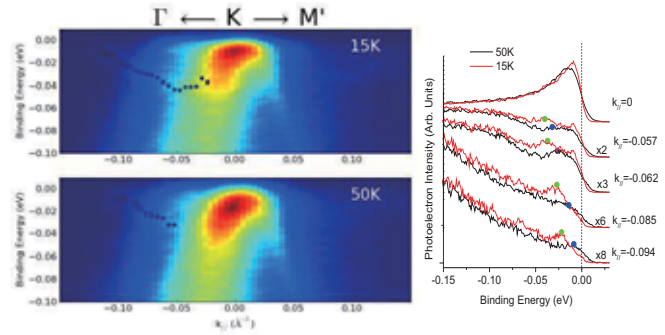

Fig. 1. ARPES Spectra near the K-point of the single-crystalline Graphite at 15K and 50K.

band at the K-point is only observed, there is no change except the thermal broadening at 50K. Meanwhile, the spectrum at higher $k_{//}$ show changes with changing temperature. The energy positions of the green (15K) and blue (50K) circles correspond to those of the circles in the left panel of Fig. 1. This band shifts in energy to by about 0.01eV when the temperature is changed. At 50K, this band crosses the Fermi level at $k_{//} \sim 0.1 A^{-1}$ while the gap seems open at 15K where the CDW is formed.

According to the report by Zhou et al. [2], this band is ascribed to the edge state of the zig-zag step on the Graphite surface. Sugawara et al. also reported a similar band [3]. Therefore, we can conclude that the CDW transition is strongly related to the edge state. The band folding at low temperature may be ascribed to the surface Umklapp process that is due to the CDW transition at domains near to the step edge on the Graphite surface. This is consistent with the theoretical calculation by Hamada et al. [4].

[1] S. Tanaka M. Matsunami and S. Kimura, Phys. Rev. B **84** (2011) 121411(R) .
[2] S.Y. Zhou, G.-H. Gweon and A. Lanzara, Ann. of Phy. **321** (2006) 1730–1746.
[3] K. Sugawara, T. Sato, S. Souma, T. Takahashi and H. Suematsu, Phys. Rev. B. **73** (2006) 045124.
[4] I. Hamada and Y. Morikawa, Phys. Rev. B **85** (2012) 237401.

Ⅲ-5. SOLID STATE PHYSICS

Angle-Resolved Photoemission Study on FeSb₂

S. Imada[1], K. Terashima[1], H. Eto[1], K. Sano[1], K. Tsukamura[1] and H. Nakamura[2]

[1]*Faculty of Sci. and Eng., Ritsumeikan Univ., Shiga 525-8577 Japan*
[2]*Grad. School of Eng., Kyoto Univ., Kyoto 606-8501, Japan*

$FeSb_2$ shows a metal-insulator crossover; it is metallic around room temperature, while it is insulating at low temperatures with an upturn of the resistivity curve at ~50 K. A number of experimental reports have indicated the existence of the energy gap at low temperatures [1-3], while the mechanism for the formation of the energy gap has not been settled yet. So far, mainly two scenarios have been proposed, one is that $FeSb_2$ is a Kondo insulator [2], and the other is that $FeSb_2$ is a narrow-gap semiconductor [1, 3]. $FeSb_2$ has an orthorhombic structure with $a = 5.82$ Å, $b = 6.51$ Å and $c = 3.17$ Å at 100 K [2].

In our previous study on $FeSb_2$ at UVSOR [4], we have measured temperature dependence of the density of states (DOS) near E_F. As we reduce the temperature, the DOS suppression is observed, but finite intensity in the vicinity of E_F remains even at 15 K where the resistivity shows insulating behavior. We also find a free-electron like band crossing E_F at 15 K, indicative of the surface state. Thus it is important to separate the surface contribution from photoemission spectra to discuss bulk property and its mechanism.

We have also performed angle-resolved photoemission (ARPES) on $FeSb_2$ to reveal the mechanism of the crossover by directly observing the temperature dependence of the energy gap. We have observed dispersive bands but interpretation was left ambiguous due to the small amount of data.

In this study, we have preformed normal emission measurement with larger photon energy region than the previous measurement and succeeded in observing a clear dispersion.

A single crystal of $FeSb_2$ has been synthesized by Sb-flux method. High-resolution ARPES study has been performed at BL-7U in the UVSOR facility. Energy resolution was set at ~13 meV. We have obtained a clean surface of the sample by fracturing in an ultrahigh-vacuum of ~1x10⁻⁸ Pa.

Figure 1 (a) shows the normal emission spectra from the (100) surface of $FeSb_2$ at 100 K using photon energy ($h\nu$) from 12 to 40 eV, where each $h\nu$ corresponds to different k points along Γ-X axis. As in Fig. 1(a), we have observed a number of dispersive bands of $FeSb_2$, such as Fe $3d_{3z^2-r^2}$ band [5] located at binding energy (E_B) of ~0.3 eV, Fe $3d_{x^2-y^2}$ band [5] at $E_B \sim 1$ eV, and so on. By comparing the dispersion with the calculated bands [6], we estimate that in the spectrum taken at $h\nu$~35 eV, the bottom of the valence band at the Γ point is observed at around E_B

~ 6 eV. Reflection of a band around $E_B \sim 2.5$ eV at X point is found at around $h\nu \sim 23$ eV. Between these points, a clear dispersion is found. Further ARPES study, clarifying (i) the bulk Fermi surfaces near the Zone edge and corner [5], (ii) the location of the surface bands, (iii) the temperature dependence of bulk bands, is necessary to elucidate the origin of the metal-insulator crossover in $FeSb_2$
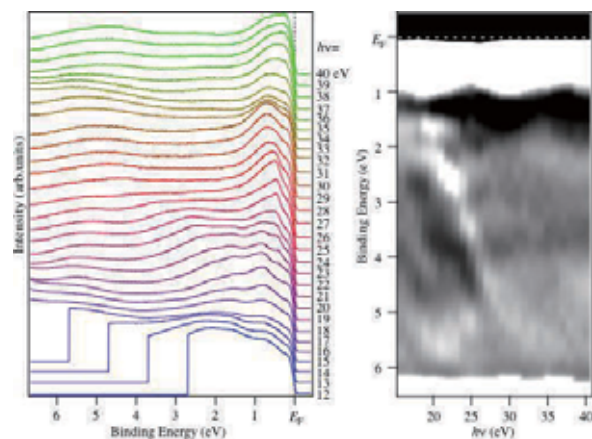
Fig. 1. (a) ARPES spectra derived by normal emission method using $h\nu$ = 12-40 eV at BL-7U. (b) Plot of second derivative of (a). White area corresponds to bands.

[1] Z. Schlesinger *et al*., Phys. Rev. Lett. **71** (1993) 11.
[2] C. Petrovic *et al*., Phys. Rev. B **72** (2005) 045103.
[3] T. Koyama *et al*., Phys. Rev. B **76** (2007) 073203.
[4] S. Imada *et al*., UVSOR Activity Report **37** (2010) 106.
[5] A. V. Lukoyanov *et al*., Euro. Phys. J. **53** (2006) 205.
[6] J. M. Tomczak *et al*., Phys. Rev. B **82** (2010) 085104.

Three-Dimensional Electronic Structure of Over-Doped BaFe$_{1.8}$Co$_{0.2}$As$_2$

T. Hajiri[1,2], T. Ito[1,3], M. Matsunami[2,4], B. H. Min[5], Y. S. Kwon[5] and S. Kimura[2,4]

[1]*Graduate School of Engineering, Nagoya University, Nagoya 464-8603, Japan*
[2]*UVSOR Facility, Institute for Molecular Science, Okazaki 444-8585, Japan*
[3]*Nagoya University Synchrotron radiation Research Center, Nagoya University, Nagoya, 464-8603, Japan*
[4]*School of Physical Sciences, The Graduate University for Advanced Studies (SOKENDAI), Okazaki 444-8585, Japan*
[5] *Department of Emerging Materials Science, DGIST, Daegu 711-873, Republic of Korea*

In iron pnictides, it is one of the most interest issues that where the nodes appear in three-dimensional (3D) electronic structures. In BaFe$_2$As$_{2-x}$P$_x$ system, there are different two reports. One is that there are the nodes on the hole Fermi surface (FS) of d_{z^2} orbital character around Z point [1], and the other is that on the electron FS at the longer edge of the ellipsoid-shaped FS cross-section [2]. The former can be explained by spin fluctuation mediated superconductivity theory [3], while the latter by taking into account for not only spin fluctuations but also orbital fluctuations. On the other hand, the fundamental physical properties of BaFe$_{2-x}$Co$_x$As$_2$ system suggest the existence of orbital fluctuations in the wide doping range [4], despite spin fluctuation cannot. Therefore, it is important to determine 3D superconducting gap symmetry.

To elucidate this, we performed a 3D angle-resolved photoemission spectroscopy of over-doped BaFe$_{1.8}$Co$_{0.2}$As$_2$ (T_c ~ 22.5 K) at BL7U, UVSOR-III.

Figure 1(a) shows a 3D hole FSs measured in the ΓMAZ plane at T = 12 K. The red open circles indicate the hole FSs determined by the peak positions of the momentum distribution curves. One and two hole FSs are clearly visible at Γ and Z point, respectively [Fig. 1(b, c)].

Figure 2(a) shows the symmetrized energy distribution curve (EDC) at Γ point. The symmetrized EDC spectrum at T = 35 K (> T_c) shows the pseudogap [5] at around 8 meV. On the other hand, at T = 12 K, the additional shoulder structure appears at around 6 meV. Interestingly, when we divide the symmetrized EDC at T = 12 K by one at T = 35 K, we found that only the low-energy shoulder remains. This suggests that the low-energy shoulder can be identified as superconducting gap, while the high-energy one as 'pseudogap'. Figure 2(b, c) shows the symmetrized EDC spectra and summarized gap size at several photon energies at 12 K. We can recognize the superconducting gap between 5~7 meV at each photon energy and almost isotropic superconducting gaps. These results imply that there is no horizontal line nodes, at least, on the outer hole FS in this system.
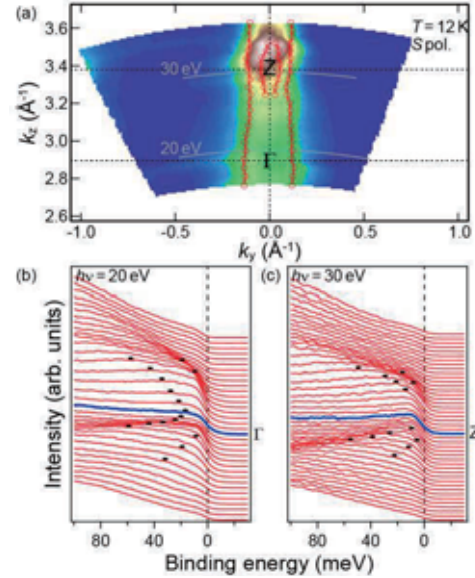
Fig. 1. (a) Out-of-plane FSs in the ΓMAZ plane at T = 12 K. (b, c) EDC along gray-lines marked by 20 (b) and 30 eV (c) in panel (a), respectively.
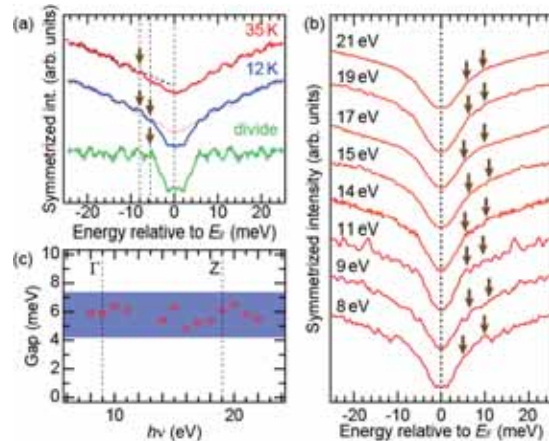
Fig. 2. (a, b) Temperature (a) and photon energy (b) dependent symmetrized EDC. (c) Size of the superconducting gaps estimated from panel (b).

[1] Y. Zhang *et al*., Nature Phys. **8** (2012) 371.
[2] T. Yoshida *et al*., arXiv:1301. (2013) 4818.
[3] K. Suzuki *et al*., J. Phys. Soc. Jpn. **80**, 013710 (2011).
[4] H. Kontani *et al*., Solid State Commun. **152** (2012) 718.
[5] S. Kasahara *et al*., Nature **486** (2012) 382.

Ⅲ-5. SOLID STATE PHYSICS

Angle-Resolved Photoemission Study on Quasi-One-Dimensional Organic Conductor $(TMTSF)_2X$ (X = SbF_6, AsF_6, PF_6)

M. Mitamura[1], S. Hirate[2], T. Hajiri[2], T. Ito[2, 4], S. Kimura[3, 5] and T. Nakamura[3, 5]

[1]*School of Engineering, Nagoya University, Nagoya 464-8603, Japan*
[2]*Graduated School of Engineering, Nagoya University, Nagoya 464-8603, Japan*
[3]*UVSOR Facility, Institute for Molecular Science, Okazaki 444-8585, Japan*
[4] *Nagoya University Synchrotron Radiation Research Center, Nagoya University, Nagoya 464-8603, Japan*
[5] *School of Physical Sciences, The Graduate University for Advanced Studies (SOKENDAI), Okazaki 444-8585, Japan*

The Bechgaard salts $(TMTSF)_2X$ (TMTSF: tetramethyl-tetraselenafulvalene, X = SbF_6, AsF_6, PF_6, *etc*.) are the well-known models of quasi-one-dimensional (Q1D) organic conductor. At low temperatures, this quasi-one-dimensionality results in an intriguing ground state such as a spin-density-wave (SDW) state, a superconducting state, etc., depending on anion X (or pressure) [1].

In this study, we have performed angle-resolved photoemission spectroscopy (ARPES) on single-crystalline $(TMTSF)_2X$ (X = SbF_6, AsF_6, PF_6) to clarify the intrinsic electronic structure and its relation to the anomalous properties by utilizing the bulk-sensitive microfocus low-energy photons (hν = 8 eV, 15×150 μm^2).

Figure 1 shows the second derivative of the ARPES image near the Fermi level (E_F) along the ΓX high-symmetry line measured at T = 30 K of $(TMTSF)_2X$ (X = SbF_6(a), AsF_6(b), PF_6 (c)), respectively. Three clear band dispersions (h, s and p) successfully observed on each compounds. From the comparison with the first principle calculation on analogous $(TMTSF)_2ClO_4$, the hole-like dispersion of main feature (p) around the Γ point can be assigned as the TMTSF band [2]. Though the theory expects only one TMTSF band, the observed multi dispersive features could be attributed to, so called, spin-charge separation. Actually, the separation of $\underline{h}$ and p dispersions on $(TMTSF)_2X$, respectively, shows good correspondence with holon and spinon bands on inorganic Q1D conductor $SrCuO_2$ [3].

In the one-dimensional Hubbard model, it is known that, the width of holon and spinon band corresponds to transfer integral along TMTSF chain t_a (red) and spin-exchange interaction constant J (blue), respectively. Table 1 shows the comparison of the J and t_a estimated by the present ARPES with those by the thermodynamic experiments [4-6]. From the comparison, we found qualitative agreement of J and t_a between the experiments. Furthermore, gradual increase of t_a / J from X = SbF_6 to PF_6 has been revealed, while t_a shows discontinuity. The results suggests that the balance of bandwidth between holon and spinon should .reflect the nature of TMTSF π electrons (localized or itinerant) and scale with the physical properties as well.
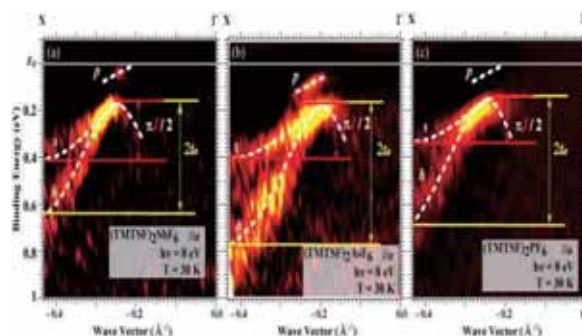
Fig. 1. Second derivative of ARPES image near E_F of $(TMTSF)_2X$ (X = SbF_6(a), AsF_6(b), PF_6 (c)).

Table 1. J and ta of $(TMTSF)_2X$ (X = SbF_6, AsF_6, PF_6) estimated by thermodynamic [4-6] and present ARPES experiments.

X=	Thermodynamic		ARPES		
	J (meV)	t_a (meV)	J (meV)	t_a (meV)	t_a / J
SbF_6	—	—	139	212	1.53
AsF_6	120[4]	250[5]	135	276	2.04
PF_6	120[4]	230[6] -250[5]	83	200	2.41

[1] T. Ishiguro *et al*., *Organic Superconductors* (Springer-Verlag, Berlin, 1998).
[2] S. Ishibashi, Sci. Techonol. Adv. Mater. **10** (2009) 024311.
[3] B. J. Kim *et al*., Nat. Phys. **2** (2006) 397.
[4] M. Dumm *et al*., Phys. Rev. B **62** (2000) 6512.
[5] C. S. Jacobsen *et al*., Phys. Rev. B **28** (1983) 7019.
[6] L. Ducasse *et al*., J. Phys. C **19** (1986) 3805.

Hybridized Band Dispersion of YbAl$_2$

M. Matsunami[1, 2], T. Hajiri[1], H. Miyazaki[3], M. Kosaka[4] and S. Kimura[1, 2]

[1]*UVSOR Facility, Institute for Molecular Science, Okazaki 444-8585, Japan*
[2]*School of Physical Sciences, The Graduate University for Advanced Studies (SOKENDAI), Okazaki 444-8585, Japan*
[3]*Center for Fostering Young and Innovative Researchers, Nagoya Institute of Technology, Nagoya 466-8555, Japan*
[4]*Graduate School of Science and Engineering, Saitama University, Saitama 338-8570, Japan*

The most important concept in the heavy fermion systems is a hybridization effect between conduction (*c*) and *f* electrons. The *c-f* hybridization-derived electronic structure can be directly probed by the angle-resolved photoemission spectroscopy (ARPES). In this work, we focus on YbAl$_2$, which is known as one of the prototypical valence fluctuation systems, with the Yb mean valence of +2.2 [1]. Thus, YbAl$_2$ is a suitable system to investigate the *c-f* hybridized band structure in relation with the extremely strong valence fluctuations.

The ARPES experiment was carried out at the undulator beamline BL7U [2]. The single crystals of YbAl$_2$, which were grown by the Lithium flux method, were cleaved *in situ* along the (111) plane. The Brillouin zone of YbAl$_2$ is shown in the Fig. 1. The total energy resolution and the measurement temperature were set to 20 meV and 12 K, respectively. The LDA band structure calculations were performed using the WIEN2k code.

Figures 2 (a)-(d) show the series of ARPES spectra and the ARPES intensity plot near the Fermi level along the Γ-K and Γ-M' directions, measured at $h\nu$= 20 eV [2]. The band dispersions obtained by the LDA calculation are also plotted in Figs. 2 (b) and (d). Their overall feature is well described in terms of the LDA calculation. In particular, the observed Yb 4$f_{7/2}$ band around the binding energy of 0.17 eV shows good agreement of energy with the calculation without any shift. This finding strongly suggests an extremely small renormalization in YbAl$_2$. In the lower-binding energy region compared with the 4$f_{7/2}$ band, the anti-bonding bands of the *c-f* hybridization are clearly observed, responsible for the valence fluctuations in YbAl$_2$. For the Γ-K direction, the position of the innermost band matches very well with that of LDA calculation. On the other hand, the experimental outer band has a slightly weaker dispersion. This band might not be separated from the more outer band, which does not cross the Fermi level as shown in the LDA calculation. For the Γ-M' direction, the experimental inner and outer bands are highly mixed, unlike those of the LDA calculation. The "mixed" band is located on the inside of the calculated ones and has almost same Fermi vector as the inner band in the Γ-K direction. This finding suggests that the inner Fermi surface is more circular than that of the LDA calculation [2].
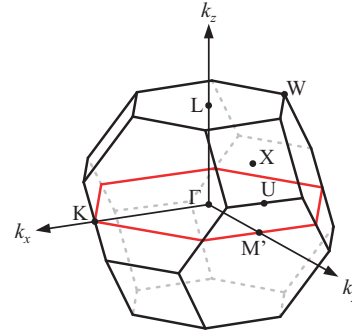
Fig. 1. Brillouin zone of YbAl$_2$, in which k_z corresponds to the (111) direction of the fcc Brillouin zone. In the k_x-k_y plane, the midpoint of the zone edge (K) is referred to as M' point, which is also equivalent to the midpoint between L and U points.
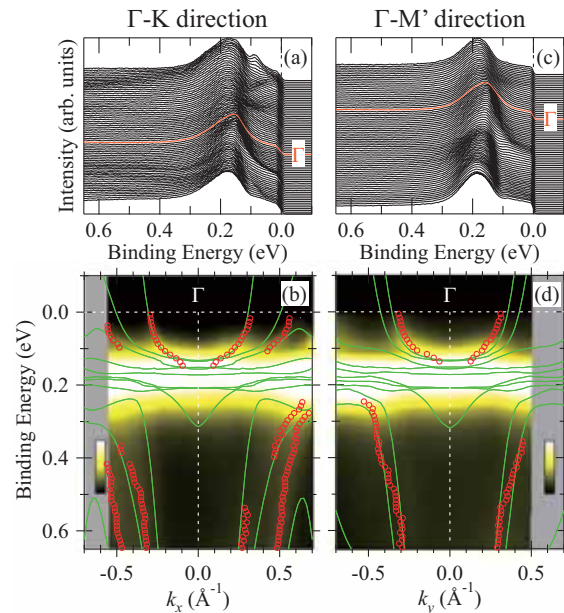
Fig. 2. (a) and (c) Series of ARPES spectra along the Γ-K and Γ-M' directions, respectively. (b) and (d) ARPES intensity plots of (a) and (c), respectively. The band dispersions obtained by MDC fitting (open circle) and LDA calculation are overlapped.

[1] M. Matsunami *et al*., J. Phys. Soc. Jpn. **81** (2012) 073702.
[2] M. Matsunami *et al*., Phys. Rev. B **87** (2013) 165141.

Ⅲ-5. SOLID STATE PHYSICS

Unique Fermi-Surface Topology Originated from Pt Atoms: An ARPES Study of the Electronic Structure of $Ca_{10}(Pt_4As_8)(Fe_{2-x}Pt_xAs_2)_5$

X. P. Shen[1], S. D. Chen[1], Q. Q. Ge[1], Z. R. Ye[1], H. C. Xu[1], F. Chen[1], M. Xia[1],
B. P. Xie[1], M. Matsunami[2], S. Kimura[2] and D. L. Feng[1]

[1]*State Key Laboratory of Surface Physics, Department of Physics, and Advanced Materials Laboratory,*
Fudan University, Shanghai 200433, People's Republic of China
[2]*UVSOR Facility, Institute for Molecular Science and*
The Graduate University for Advanced Studies, Okazaki 444-8585, Japan

Recently, superconductivity up to 38 K was discovered in the novel iron-based superconductor $Ca_{10}(Pt_4As_8)(Fe_{2-x}Pt_xAs_2)_5$ [1]. In these compounds the metallic Pt_4As_8 layer was introduced as a new intermediary layer, which distinguished them from other usual iron pnictides.

To study whether the Pt_4As_8 layer contribute density of states (DOS) at the Fermi energy (E_F) and estimate the strength of interlayer coupling between Pt_4As_8 and FeAs layers, we have conducted angle-resolved photoemission spectroscopy (ARPES) studies on $Ca_{10}(Pt_4As_8)(Fe_{2-x}Pt_xAs_2)_5$ at beamline BL7U at UVSOR. The variable photon energies and polarizations enable us to successfully resolve the low-energy electronic structure and corresponding orbital characters in the 3-dimensional momentum space.
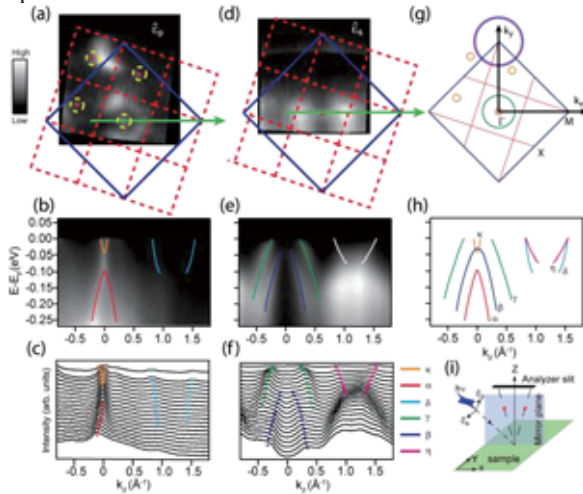

Fig. 1. The polarization-dependent ARPES data around Γ taken with 26 eV photons.

Figure 1 reveals the polarization dependent photoemission intensity maps and corresponding photoemission intensity plots along Γ-M. As shown in Fig. 1(a) and (b), the 2D blue BZ is from FeAs layer and the red dash one is from Pt_4As_8 layer. The most remarkable feature here is that there are four small electron pockets (κ) arranged around the zone centers of the Pt_4As_8 BZs, as enclosed by the dash lines in Fig. 1(a), which is very likely from Pt atoms as proposed in the recent first-principles calculation[3]. Besides, we resolved two hole-like bands (α, β), one hole pocket (γ) around the zone

center and two electron pockets (δ, η) around the zone corner, which show good correspondence to the electronic structures of other prototype pnictides and could be attributed to the Fe-$3d_{xz}$, -$3d_{yz}$, and -$3d_{xy}$ orbitals, respectively [3].
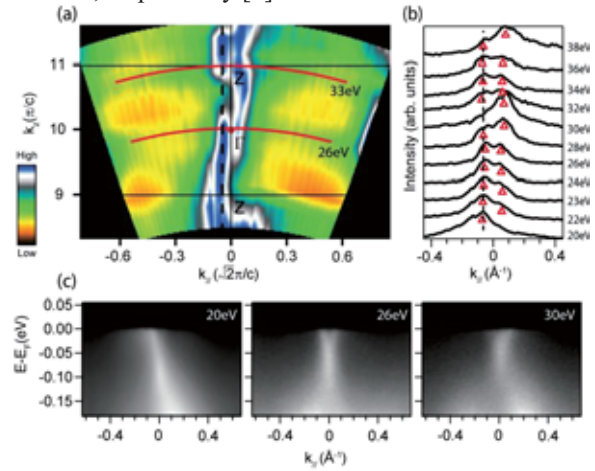
Fig. 2. The Fermi surface as a function of k_z in the p geometry.

Further k_z dependence of the κ electron pocket is shown in Fig. 2. The intensity distribution of the κ band shows a periodic variation in Fig. 2(a) if we take the inner potential to be 13 eV. By tracing the MDC's at E_F at each k_z [Fig. 2(b)], we could conclude that the κ electron pocket shows weak dispersion along the k_z direction.

In general, our data demonstrate that the Pt atoms indeed provide DOS at E_F and the κ electron pocket may participate in superconductivity in this novel material. However, the interlayer coupling between Pt_4As_8 and FeAs layers is considerably weak according to the rather two-dimensional electronic structure and absence of obvious hybridization between κ and α bands. Our results might open up new avenues for the exploration of high-Tc superconductor by tuning the interlayer coupling between FeAs layer and additional metallic-like intermediary layers.

[1] N. Ni *et al*., Proc. Natl. Acad. Sci. USA **108**, E 1019 (2011).
[2] H. Nakamura *et al*., Physica C **484** (2013) 39.
[3] Y. Zhang *et al*., Phys. Rev. B **83** (2011) 054510.

Circular Dichroism ARPES Studies on Dresselhaus Effect in Non-Magnetic Semiconductors

W. Jung[1], S. Cho[1], Y. Kim[1], B. Kim[1], Y. Koh[1], M. Matsunami[2], S. Kimura[2] and C. Kim[1]

[1]Institute of Physics and Applied Physics, Yonsei University, Seoul, Korea
[2]UVSOR Facility, Institute for Molecular Science, Okazaki 444-8585, Japan

GaAs and InSb have been studied by many researchers and received attention. One of the issues in studying these semiconductors is the band splitting at the Γ-point. GaAs and InSb have a zinc blende structure and such materials have three hole bands that belong to the bulk band at the Γ-point. It is known that band splitting is due to the inversion symmetry breaking in the bulk. We studied this phenomena in light of the Dresselhaus effect.

Semiconductors with zinc blende and Wurtzite structures with a bulk inversion asymmetry such as ZnTe, ZnSe, CdS, CdSe, GaAs and InSb have been theoretically studied within a tight-binding model [1]. The effective one-body Hamiltonian with Dresselhaus effect is:

$$H = H_0 + H_D$$

$$H_D = \gamma[\sigma_x k_x (k_y^2 - k_z^2) + cyclic\ permutations]$$

Here, H_D is the Hamiltonian for the Dresselhaus effect, σ Pauli matrix, and γ the material dependent spin-orbit coupling constant. GaAs and InSb have a strong spin-orbit coupling and consequently show the Dresselhaus effect [2].

Topological insulators have strong spin-orbit coupling and have been studied in our group. According to our recent results, the orbital angular momentum (OAM) plays an important role in the formation of a Rashba-type surface band splitting [3]. We expect that OAM also greatly affects the electronic structure of semiconductors such as GaAs and InSb and that one should be able to obtain key evidences for the role of OAM in the Dresselhaus-type bulk band splitting. It was also recently reported that OAM can be measured by Circular Dichroism ARPES (CDARPES) [4, 5]. Therefore, we tried to study the OAM effect on the Dresselhaus effect by using circular and linear dichroism ARPES.

GaAs and InSb single crystals were purchased as wafer. ARPES measurement was performed at the beam line 7U of UVSOR-III. Crystals were cleaved *in-situ* at room temperature and the chamber pressure was better than 5×10^{-11} Torr. ARPES spectra were acquired with a hemispherical photoelectron analyzer (MBS A-1). We used linearly polarized as well as left and right circularly polarized (LCP and RCP) photons of 9–21 eV photons to avoid signal from the surface states.

Figure 1 shows ARPES data from GaAs. It is confirmed that GaAs has two hole bands at the Γ-point.
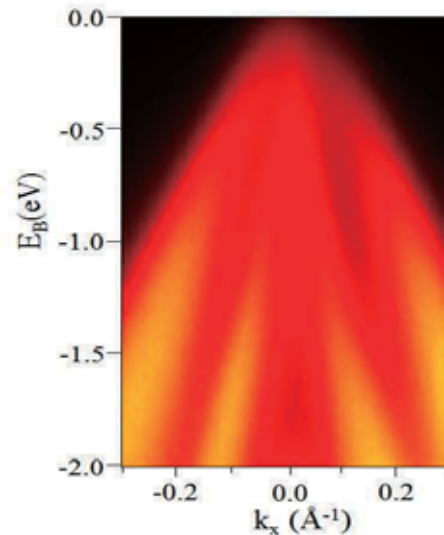
Fig. 1. ARPES image from GaAs (110) bulk state measured with linearly polarized 21 eV photon. The image is taken along the $k_y = 0$ line.

To obtain the evidence for the Dresselhaus effect in ARPES, we performed CDARPES experiments on the GaAs and InSb with circularly polarized 9 eV photons, because the Dresselhaus effect gives a 3θ symmetry in the CDARPES $(I_{LCP} - I_{RCP})/(I_{LCP} + I_{RCP})$. However, we could not reach the Γ point with low-energy photons owing to the limitation of the beamline. It is expected that three-dimensional bulk band structure of GaAs and InSb gives us new information. Therefore, we will perform the three-dimensional ARPES to obtain the complete bulk electronic structure.

[1] W. T. Wang *et al*., Appl. Phys. Lett. **91** (2007) 082110.
[2] J. W. Luo *et al*., Phys. Rev. Lett. **102** (2009) 056405.
[3] S. R. Park *et al*., Phys. Rev. Lett. **107** (2011) 156803.
[4] B. Y. Kim *et al*., Phys. Rev. B **85** (2012) 195402.
[5] J. H. Park *et al*., Phys. Rev. B **85** (2012) 195401.

Temperature-Dependent Dispersive In-Gap State of The Kondo Semiconductor SmB_6

H. Miyazaki[1, 2], T. Hajiri[2, 3], M. Matsunami[2, 4], T. Ito[3], S. Kunii[5] and S. Kimura[2, 4]

[1]*Nagoya Institute of Technology, Nagoya 466-8555, Japan*
[2]*UVSOR Facility, Institute for Molecular Science, Okazaki 444-8585, Japan*
[3]*Nagoya University, Nagoya 464-8603, Japan*
[4]*The Graduate University for Advanced Studies (SOKENDAI), Okazaki 444-8585, Japan*
[5]*Tohoku University, Sendai 980-8578, Japan*

Samarium hexaboride (SmB_6) is one of typical Kondo semiconductors/insulators with a valence fluctuation between Sm^{2+} ($4f^6$) and Sm^{3+} ($4f^5$) ions [1]. The electrical resistivity decreases on cooling, like a metal, above the temperature of 100 K, and then reveals a semiconductor-like character with activation energy of 15 meV, but the resistivity saturates below 20 K [2]. Though the origin of the constant resistivity at low temperatures has not been resolved for a long time, recently this behavior has been suggested to originate from metallic behavior at the edge state on the surface [topological Kondo insulator (TKI)] [3]. To clarify the origin of the anomalous electrical resistivity behavior of SmB_6, we performed three-dimensional angle resolved photoemission spectroscopy (3D-ARPES) to determine the electronic band structure directly.

A SmB_6 (001) single crystal was cleaned by Ar^+ ion sputtering and 1400 °C annealing cycles in the ultrahigh vacuum chamber with a base pressure of ~ 2 × 10^{-8} Pa. Clean surface of SmB_6 with the 2 × 1 and 1 × 1 (001) patterns was confirmed by a low energy electron diffraction method and no contamination, such as carbon, was observed by an Auger electron spectroscopy. The 3D-ARPES measurements were performed at the beamline 7U of UVSOR-III. The total energy and momentum resolutions for the ARPES measurement were set to 13 meV and 0.006 $Å^{-1}$ at the Γ point ($h\nu = 26$ eV) and 12 meV and 0.003 $Å^{-1}$ at the X point ($h\nu = 10.6$ eV), respectively.

Figure 1 shows the temperature-dependent ARPES spectra divided by the Fermi-Dirac distribution curve along the X−M line. At $T = 40$ K, the k-dependence of the peak at $E_B = 15$ meV, marked by open circles, is almost flat. The band becomes slightly dispersive at temperature below 20 K, i.e., the *c-f* hybridization gap opens near the X point. At $T = 10$ K, another band dispersion, with an electron pocket at $k \sim 0.25$ $Å^{-1}$, appears at $E_B \sim 5$ meV, as shown by vertical lines. The dispersive in-gap state behavior suggests that the in-gap state is not a local state, such as an impurity state, but has the periodicity of the SmB_6 unit cell. The ARPES data seem to be consistetnt with the electrical resistivity; i.e., the formation of the hybridization gap is visible above 20 K, while the in-gap state becomes dominant below 10 K. The band dispersion of the in-gap state is consistent with theoretical calculation [4, 5], i.e., the dispersive

in-gap state suggests the existence of an edge state. To determine the origin of the in-gap state, further studies are intended.
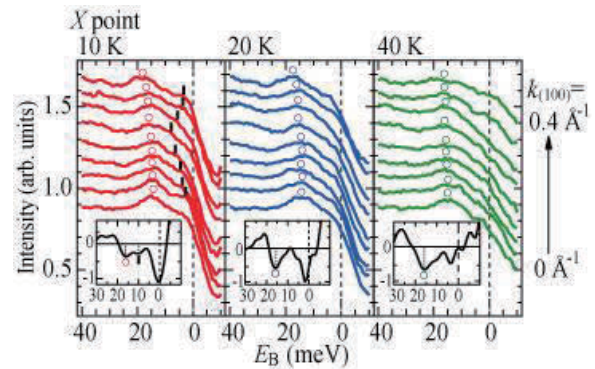
Fig. 1. Temperature dependence of ARPES spectra divided by the Fermi-Dirac distribution curve along the X − M line. The hybridization band dispersions are shown by open circles, and the observed dispersion in-gap state is shown by vertical lines. Insets show the second derivative curves of the ARPES spectra at $k_{(100)} = 0.25$ $Å^{-1}$.

[1] R. L. Cohen *et al*., J. Appl. Phys. **41** (1970) 898.
[2] T. Tanaka *et al*., J. Appl. Phys. **51** (1980) 3877.
[3] M. Dzero *et al*., Phys. Rev. Lett. **104** (2010) 106408.
[4] M. Dzero *et al*., Phys. Rev. B **86** (2012) 075105.
[5] F. Lu *et al*., arXiv: 1211.5863.

High-Resolution ARPES study of $Sn_{1-x}In_xTe$: Implication to Topological Superconductivity

T. Sato[1], Y. Tanaka[1], K. Nakayama[1], S. Souma[2], T. Takahashi[1,2], S. Sasaki[3], Z. Ren[3], A. A. Taskin[3], K. Segawa[3] and Y. Ando[3]

[1]*Department of Physics, Tohoku University, Sendai 980-8578, Japan*
[2]*WPI Research Center, Advanced Institute for Materials Research, Tohoku University, Sendai 980-8577, Japan*
[3]*Institute of Scientific and Industrial Research, Osaka University, Ibaraki, Osaka 567-0047, Japan*

Topological insulators (TIs) are a novel quantum state of matter where the bulk band gap induced by a strong spin-orbit coupling leads to the appearance of unusual gapless edge/surface states protected by time-reversal symmetry [1, 2]. The discovery of TIs triggered the search for their superconducting (SC) analogues, topological superconductors (TSCs). TSCs are accompanied by gapless Andreev bound states inside the SC gap which are often comprised of Majorana fermions. Very recently, point-contact spectroscopy revealed that indium-doped tin telluride ($Sn_{1-x}In_xTe$, called In-SnTe here) is possibly a new type of TSC [3]. This result is particularly intriguing in view of the fact that SnTe was recently elucidated to be materializing a new type of topological state called topological crystalline insulator (TCI) [4, 5] associated with topologically-protected surface states that emerge due to a combination of band inversion and mirror symmetry [4, 5]. It is thus of great importance to experimentally clarify the electronic states of In-SnTe relevant to the possible occurrence of topological superconductivity.

In this study, we have performed high-resolution angle-resolved photoemission spectroscopy (ARPES) of In-SnTe. By utilizing the low energy and variable photon energy ($h\nu$) characteristics of the beamline BL7U, we have succeeded in directly observing topological surface state [6].

To clarify the effect of indium substitution on the electronic states of SnTe, we paid particular attention to the momentum space around the $\bar{X}$ point of the surface Brillouin zone [Fig. 1(a)], because the topological surface states appear in this momentum region in SnTe [5]. Figures 1(b) and (c) represent a direct comparison of near-E_F ARPES intensity between pristine and In-doped SnTe measured along a **k** cut crossing the $\bar{\Lambda}$ point. In SnTe, we observed a highly dispersive holelike band which is attributed to an admixture of the bulk and surface states with dominant contribution from the surface state near E_F, as confirmed by the $h\nu$ independence. While the overall dispersive feature is significantly broader in In-SnTe, it is still possible to extract an intrinsic band dispersion for In-SnTe by taking second derivatives [see Fig. 1(d)]. The result of such an analysis clearly shows a linearly dispersive holelike band approaching E_F, which is similar to what is found in pristine SnTe. This result demonstrates that the topological surface state is likely to be present in In-SnTe. This

conclusion is further supported by the observation of the "M"-shaped band dispersion along the $\bar{\Gamma}$ $\bar{X}$ cut [Fig. 1(e)], which can be regarded as a fingerprint of the Dirac-cone surface state of a TCI [5] where the calculated bulk-band structure never shows any M-shaped dispersion near E_F.

The present experiments elucidate that the bulk band inversion, which makes SnTe a TCI, is kept unchanged in In-SnTe. This band inversion and our observation of the topological surface state in In-SnTe assure that this material provides a fertile ground for the study of TSC [6].
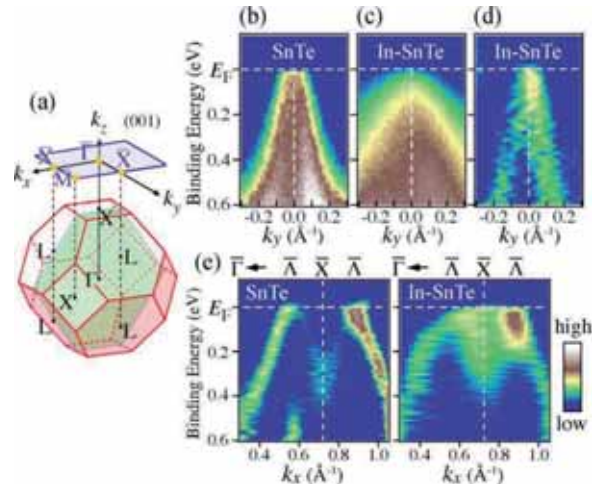
Fig. 1. (a) Bulk fcc Brillouin zone and corresponding tetragonal (001) surface Brillouin zone. (b) and (c) Comparison of near-E_F intensity measured with $h\nu =$ 21 eV plotted as a function of k_y and binding energy across the $\bar{\Lambda}$ point. (d) Second derivative of the data in (c). (e) Comparison of the band dispersion derived from the second derivatives of the MDCs along the $\bar{\Gamma}$ $\bar{X}$ cut between pristine SnTe (left) and In-doped SnTe (right).

[1] M. Z. Hasan and C. L. Kane, Rev. Mod. Phys. **82** (2008) 3045.
[2] X.-L. Qi and S.-C. Zhang, Rev. Mod. Phys. **83** (2011) 1057.
[3] S. Sasaki *et al.*, Phys. Rev. Lett. **109** (2012) 217004.
[4] L. Fu, Phys. Rev. Lett. **106** (2011) 106802.
[5] Y. Tanaka *et al.*, Nature Phys. **8** (2012) 800.
[6] T. Sato *et al.*, arXiv:1212.5886.

III-5. SOLID STATE PHYSICS

Temperature Dependence of Auger-Free Luminescence in Cs$_2$ZnCl$_4$

A. Ohnishi[1], M. Kitaura[1], M. Sasaki[1] and M. Itoh[2]

[1]Depeartment of Physics, Yamagata University, Yamagata 990-8560, Japan
[2]Department of Electrical and Electronic Engineering, Shinshu University,
Nagano 380-8553, Japan

In the present study, temperature dependence of Auger-free luminescence (AFL) in Cs$_2$ZnCl$_4$ has been investigated in the temperature range T =15–300 K. Experiments were performed at the BL-7B beam line of UVSOR. This report is one of results published in ref. 1.

Temperature dependence of emission spectra of Cs$_2$ZnCl$_4$ were measured under photo-excitation at 21.4 eV. Typical results at several different temperatures are shown in a relative scale in Fig. 1. Three bands peaking at 3.3, 4.2 and 4.8 eV at 15 K are the AFL in Cs$_2$ZnCl$_4$, which come from radiative transitions between the Cl $3p$ valence band and the Cs $5p$ outermost-core band. On increasing the temperature, spectral widths of the 3.3 and 4.8 eV bands become broaden appreciably, while that of the 4.2 eV band is almost unchanged. This situation is clearly recognized in Fig. 2, where the full width at half maximum (FWHM) of the three bands is plotted as a function of temperature.

The existence of two AFL bands peaking at 4.2 and 4.8 eV is discussed. As shown in Fig. 2, when T is increased from 15 K, the spectral width of the 4.8 eV band indicates a remarkable broadening, while that of the 4.2 eV band is almost unchanged. Meanwhile, their decay times were identical to each other. It is, therefore, supposed that the difference in thermal broadening is attributed to the difference in the final state of the Auger-free transition, not the difference in the initial state. In this connection, it is worth noting that the 4.2 and 4.8 eV bands in Cs$_2$ZnCl$_4$ are very similar in nature to the AFL in CsCl [2], in which two bands at 4.5 and 5.2 eV are also ascribed to radiative transitions between the Cl $3p$ valence band and the Cs $5p$ outermost-core band. For CsCl, Fukaya *et al.* [3]. have theoretically studied the temperature dependence of AFL spectra by an extended deformable cluster model, which is based on a supposition that a core hole self-traps weakly by inducing lattice deformation around itself. Their theoretical study gives a satisfactory agreement with the experimental observation. By referring to their arguments, we consider on the existence of two AFL bands at 4.2 and 4.8 eV as follows. The high-energy band at 4.8 eV comes from the Auger-free transition of a self-trapped core hole to a localized state in the valence band due to an attractive potential of lattice deformation created in the initial state. The final state of the low-energy band at 4.2 eV, on the other hand, is an extended state in the valence band without lattice deformation. It is also supposed that the lattice relaxation of core holes may play an important role for the 3.3 eV band, because this band becomes broadened significantly with increasing the temperature.

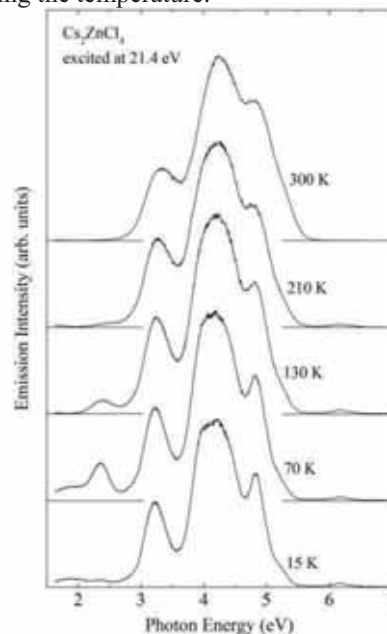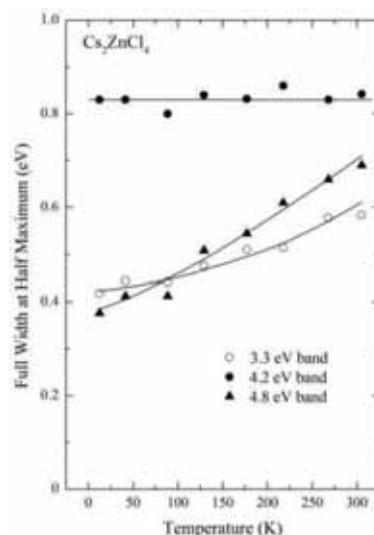Fig. 1. Emission spectra measured at T = 15, 70, 130, 210 and 300 K under photo-excitation at 21.4 eV.

Fig. 2. Temperature dependence of the FWHMs of the 3.3, 4.2 and 4.8 eV bands.

[1] A. Ohnishi, M. Kitaura, M. Itoh and M.Sasaki, J. Phys. Soc. Jpn. **81** (2012) 114704.
[2] M. Itoh, M. Kamada and N. Ohno, J. Phys. Soc. Jpn. **66** (1997) 2502.
[3] M. Fukaya, Y. Kayanuma and M. Itoh, J. Phys. Soc. Jpn. **71** (2002) 2557.

Luminescence of CsCl Heavily Doped with CsI

N. Ohno and K. Sakae

Graduate School of Engineering, Osaka Electro-Communication University, Neyagawa, Osaka 572-8530, Japan

Stimulation in iodine absorption bands of dilute I⁻-doped alkali chlorides produces characteristic luminescence bands under excitation with UV light or with X-rays at low temperatures. These luminescence bands have been well explained in terms of localized relaxed excitons at ICl⁻ molecule (I⁻ monomer) and a complex of two iodine ions (I⁻ dimer) [1, 2]. However, optical and luminescence properties of heavily iodine-doped alkali chloride crystals have not been examined sufficiently for applying to high efficient scintillation materials. The present report describes the results of CsCl heavily doped with CsI.

The crystals of CsCl:I were grown by the Bridge-man method from reagent grade CsCl added with an appropriate amount of CsI (up to 3 mol%). The photo-luminescence and photoexcitation spectra were measured at BL7B station. The photoluminescence spectra excited with photons near the exciton absorption region of CsCl were almost the same as those of the previous studies [3, 4]: two luminescence bands peaking at 3.92 eV (monomer) and 5.12 eV (dimer) at 15 K. Figure 1 shows the photoexcitation spectra for the monomer (blue) and the dimer emission (red) for 3 mol% CsCl:I. The excitation spectrum for the monomer is quite similar with that for the dilute case [3]. However, the spectrum for the dimer band is found to show a quite different behavior with heavily doped crystals [4]. This clear low energy tail of the excitation band for the dimer emission suggests that there coexist dimers, trimers and lager sizes of I⁻ ions (CsI cluster) in heavily-doped CsCl:I crystal as can been found in heavily-doped KCl:I [5].

The luminescence energies of the trimers and clusters of I⁻ ions in heavily doped CsCl:I crystals are expected to be different from that of I⁻ dimers. We have examined the dimer emission spectra excited at various photon energies. The results are shown in Fig. 2. It is clearly confirmed that the peak energy of the dimer band moves towards the low energy side when excited with photons of lower energy. Therefore, the luminescence bands are supposed to be the composite bands due to radiative annihilation of the relaxed exciton at dimers, trimers and clusters of I⁻ ions [5].

In CsCl crystals containing CsI above 1 mol %, there exists a small amount of dimer centers as compared with monomers, and moreover the amount of trimers and clusters of CsI is extremely smaller than those of monomers and dimers. The present results suggest that the excitons trapped in CsI clusters in heavily doped CsCl:I crystals would give the high luminescence efficiency.
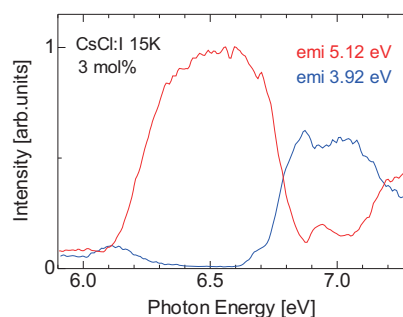
Fig. 1. Photoexcitation spectra of CsCl:I (3 mol%) crystal for the monomer (blue) and dimer (red) bands.
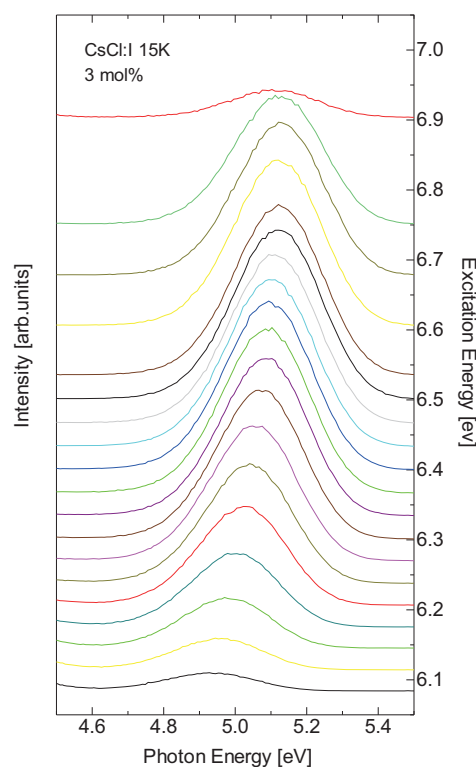
Fig. 2. Luminescence spectra of CsCl:I (3 mol%) crystal excited with photons of various energies ranging from 6.08 to 6.90 eV.

[1] N. Nagasawa, J. Phys. Soc. Jpn. **27** (1969) 1535.
[2] K. Kan'no, K. Tanaka and T. Hayashi, Rev. Solid State Sciences **4** (1990) 383, and references therein.
[3] M. Yoshida and N. Ohno, *Proc. Int. Conf. on Excitonic Processes in Condensed Matter* (1996) 231.
[4] N. Ohno and A. Ohno, UVSOR Activity Report **38** (2012) 83.
[5] A. Ohno and N. Ohno, Phys. Status Solidi C **8** (2011) 112.

Ⅲ-5. SOLID STATE PHYSICS

Electronic Structure of the ZnO Treated by Microwave

K. Yoshida[1], T. Sonobe[2], H. Zen[1], K. Hachiya[2], K. Okumura[1], K. Mishima[1], M. Inukai[1],
H. Negm[1], M. Omer[1], Y.-W. Choi[1], R. Kinjo[1], T. Kii[1], K. Masuda[1] and H. Ohgaki[1]

[1]Institute of Advanced Energy, Kyoto University, Gokasyo, Uji, Kyoto 611-0011, Japan
[2]Graduate School of Energy Science, Kyoto University, Yoshida-honmachi, Sakyo-ku, Kyoto 606-8501 Japan

Microwave (MW) heating is considered as an advanced method for a material processing, since it has several unique advantages such as rapid and selective heating over conventional methods. To date, several approaches have been investigated. For example, K.M Parida and S. Parija achieved the enhancement of a photocatalitic activity of ZnO by irradiating the ZnO with MW [1]. In addition, the activity as a catalyst of MgO in chemical reaction was also improved by irradiating the MgO catalyst with MW [2]. In this way, MW heating is considered as a one of useful techniques for improving properties of the functional materials. However, the change of the physical property, especially electronic structure, by MW irradiation has not been clarified well. The clarification of the effect of MW irradiation on electronic structure is important for design of materials such as photocatalyst, solar cells or material processing. Therefore, we investigated the electronic structure of the material treated by MW.

The photoluminescence was measured for the analysis of the electronic structure. BL7B was used as the light source and photon energy was changed from 2.92 eV (425 nm) to 3.54 eV (350 nm). A CCD array cooled by liquid nitrogen was used as the detector. The exposure time was 10 s. The measurement temperature was room temperature. Two types of ZnO were prepared. One was sintered at 873 K for 2 hours and not irradiated with MW. The other was sintered at 873 K for 2 hours and irradiated with MW of 500 W for 10 minutes. The treatment method of MW irradiation is shown in the reference [3].

Figure 1 is the photoluminescence spectra of ZnO with the MW irradiation. The sharp peaks from 1.5 eV to 1.8 eV and from 2.5 eV to 3.7 eV are the second order diffraction light of light source and fundamental excitation light, respectively. A broad band whose peak energy is 2.4 eV was observed.

In addition, the black and red dots in Fig. 2 show the PLE (photoluminescence excitation) spectra for the intensity of photoluminescence at 2.4 eV from ZnO with and without MW irradiation. In Fig. 2, the peak intensity of ZnO without MW irradiation is seen constant in any excitation energy. In contrast, in the case of the ZnO with MW irradiation, the intensity of the broad band peaks showed strong dependency on the excitation photon energy. The maximum intensity was observed at excitation energy of 3.21 eV. The black arrow in Fig. 2 shows the band gap energy (3.27 eV) of ZnO. From these results, it is considered

that a new energy band was created at lower energy than the conduction band by MW irradiation, and the excitation and relaxation process of electron was changed by the effect of the new energy band. As the conclusion, we found that the MW irradiation made significant change of the electronic structure of ZnO.
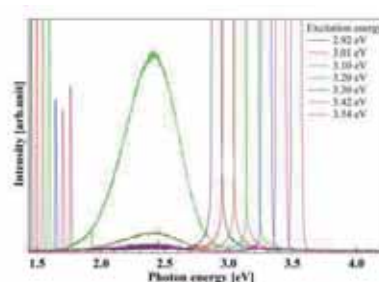

Fig. 1. Photoluminescence spectra of ZnO with MW irradiation.

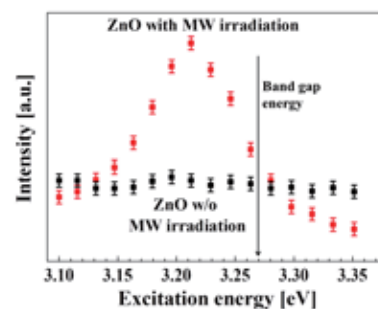

Fig. 2. PLE spectra of the intensities at 2.4 eV from ZnO with and without MW irradiation.

[1] K. M. Parida, et al., Solar Energy **80** (2006) 1048.
[2] H. Mirzaei, et al., Chin. J. Catal. **33** (2012) 1502.
[3] T. Sonobe, et al., Jpn. J. Appl. Phys. **49** (2010) 080219.

Ultraviolet Photoelectron Spectra of Lu Encapsulated Fullerenes (I)

T. Miyazaki[1], R. Sumii [2,3], H. Umemoto[4], H. Okimoto[4], T. Sugai[4], H.Shinohara[4] and S. Hino[1]

[1] *Graduate School of Science and Engineering, Ehime University, Matsuyama, 790-8577, Japan*
[2] *Institutes for Molecular Science, Okazaki, 444-858, Japan*
[3] *Research Center for Materials Science, Nagoya University, Chikusa-ku, Nagoya, 464-8602, Japan*
[4] *Graduate School of Science, Nagoya University, Chikusa-ku, Nagoya, 464-8602, Japan*

Fullerene cages encapsulate single as well as multiple metal atoms, metal nitrides and metal-carbides. Encapsulated metal atom(s) donate electrons to the cage, and affect the electronic structure of the fullerene cage [1, 2]. The amounts of the transferred electrons depend on the entrapped species and the fullerene cages. Recently, Lutetium atom(s) and lutetium-carbide encapsulated C_{82} fullerenes, $Lu@C_{82}$ (I), $Lu_2@C_{82}$ (II), $Lu_2@C_{82}$ (III), $Lu_2C_2@C_{82}$ (II) and $Lu_2C_2@C_{82}$ (III) have been isolated. The NMR study revealed their cage symmetry, C_{2v} (82:9) for $Lu@C_{82}$ (I), $Lu_2@C_{82}$ (II) and $Lu_2C_2@C_{82}$ (II), C_{3v} (82:8) for $Lu_2@C_{82}$ (III) and $Lu_2C_2@_{82}$ (III). In the current work, the UPS of $Lu@C_{82}$ (I), $Lu_2@C_{82}$ (II), $Lu_2@C_{82}$ (III), $Lu_2C_2@C_{82}$ (II) and $Lu_2C_2@C_{82}$ (III) will be presented and validity of the empirical rule is examined. Ultraviolet photoelectron spectra were measured at BL8B2 of Ultraviolet Synchrotron Orbital Radiation Facility of Institute for Molecular Science. The measured UPS were referenced against the Fermi level (E_F) of gold deposited on the sample disk before the measurements.

The valence band UPS of $Lu@C_{82}$ (I), $Lu_2@C_{82}$ (II) and $Lu_2C_2@C_{82}$ (II) obtained with $hv = 20－55$ eV. Their onset energy (E_{onset}) are 0.2_5 eV ($Lu@C_{82}$ (I)) and 0.6_4 eV ($Lu_2@C_{82}$ (II) and $Lu_2C_2@C_{82}$ (II)), which are much smaller than that of empty C_{82} (1.2eV). These are the results of electron transfer from the entrapped species to the cage. These fullerenes are semi-conductive. There are several structures labeled $\alpha － \delta$ and A – E in the UPS of $Lu@C_{82}$ (I), $Lu_2@C_{82}$ (II) and $Lu_2C_2@C_{82}$ (II). The UPS of $Tb@C_{82}$, $Er@C_{82}$ and $Y_2C_2@C_{82}$ all of them have the same C_{2v} symmetry are also shown in Fig. 4. Remarkable difference among these UPS is observed in the $9－11$ eV region. While there is only one structure labeled ϵ is observed in the UPS of Tb, Er, Y_2C_2 entrapped fullerenes, two structures labeled X and Y are observed in the UPS of Lu entrapped fullerenes. The ionization energies of Lu $4f_{7/2}$ and $4f_{5/2}$ levels of Lu metal are 7.5 eV and 8.9 eV, respectively. Binding energies of X and Y are ranging from $9.3－9.8$ eV and $10.8－11.2$ eV, respectively, and they are much higher than those of Lu metal atoms by $2.0－2.5$ eV. Further, energy separation between structures X and Y is $1.4－1.5$ eV, which coincides with that of $Lu4f_{7/2}$ and $Lu4f_{5/2}$. Thus, structures X and Y might be due to entrapped Lu atom(s). This could be the first observation of the photoelectrons of entrapped species in the ultraviolet photoelectron spectroscopy.

The UPS of $Lu_2C_2@C_{82}$ and $Y_2C_2@C_{82}$ are almost identical but that of $Lu_2@C_{82}$ shows slight differences from them. These differences might be attributed to the difference in the amounts of transferred electrons. Probably, the amounts of transferred electrons in $Lu_2@C_{82}$ and $Lu_2C_2@C_{82}$ are so different that their electronic structure is modified differently. $Lu4f_{7/2}$ and $4f_{5/2}$ levels may be helpful to estimate them. The oxidation state of entrapped Lu atom might be +3. Since $Lu4f_{7/2}$ and $Lu4f_{5/2}$ binding energies of $Lu@C_{82}$ and $Lu_2@C_{82}$ are almost the same, the electronic configuration might be $(Lu^{3+})_2@C_{82}{}^{6-}$. Possibly the original oxidation state of Lu atoms in $Lu_2C_2@C_{82}$ is +3, but entrapped C_2 might receive two electrons from them and hybridization or back donation takes place among Lu atoms and C atoms resulting $Lu^{-3+\delta}$ state.
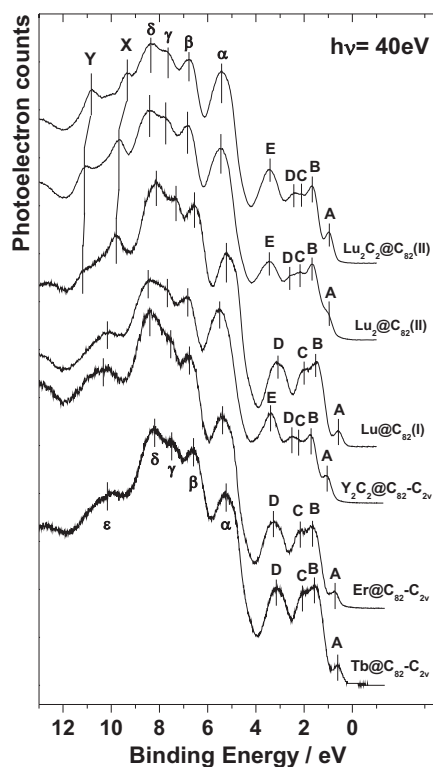

Fig. 1. UPS of endohedral fullerenes at hυ= 40eV.

[1] T. Miyazaki *et al.*, Chemical Physics **378** (2010) 11.
[2] T. Miyazaki *et al.*, Chemical Physics **397** (2012) 87.

Ⅲ-5. SOLID STATE PHYSICS

Scintillation and Luminescence Properties of Sn^{2+}-doped Oxide Glass[1]

H. Masai[1], T. Yanagida[2], Y. Fujimoto[2], M. Koshimizu[3], T. Yoko[1] and K. Asai[3]

[1]*Institute for Chemical Research, Kyoto University, Kyoto 611-0011, Japan*
[2]*Kyushu Institute of Technology, Kitakyushu 808-0196, Japan*
[3]*Department of Applied Chemistry, Graduate School of Engineering, Tohoku University, Sendai 980-8579, Japan*

RE (rare-earth)-free phosphors have long been developed in terms of abundance as natural resource. Among them, RE-free glasses have advantage that various kinds of elements can be incorporated to control the emission properties. One application of the RE-free glasses may be scintillators, because most of conventional scintillators include RE ions as luminescent centers and as the constituent of the host matrix. In this study, we demonstrated the applicability of RE-free glasses for scintillators.

The SnO-SrO-B$_2$O$_3$ and SnO-ZnO-P$_2$O$_5$ glass samples were fabricated by a conventional melt-quenching technique. The raw materials were melted in platinum crucibles, and subsequently were quenched on a stainless steel at 473 K. The glass samples were annealed at the glass transition temperatures.

The pulse height spectra of the α-ray from ^{241}Am were obtained for the scintillation detectors quipped with sample scintillators. The emission and excitation spectra of samples were measured at room temperature under the irradiation of synchrotron radiation having energies of 6–20 eV at the UVSOR facility (BL7B).

Figure 1 shows the pulse height spectra of the samples. Because the experimental set up and the excitation source was the same for each sample, the multichannel analyzer (MCA) channel is roughly proportional to the number of photoelectrons. A clear peak was observed for each sample. This result indicates that the light yield was sufficient for detection of ionizing radiation whose energy is on the order of MeV, although the light yield was significantly smaller than that of Li-glass.

Figure 2 shows contour plot of emission and excitation spectra of the 0.5SnO-24.5SrO-75B$_2$O$_3$ and 5.0SnO-60ZnO-40P$_2$O$_5$ glass. Each contour plot shows the photon energy of excitation (ordinate) and emission (abscissa), and the intensity axes are shown on an identical linear scale. We observed two excitation bands; one is the band at ~6 eV corresponding to the S$_0$-S$_2$ transition of Sn^{2+}. We observed another peak at above 20 eV. Assuming that this band corresponds to the excitation in the host glass, the emission occurs via the energy transfer from the host to the Sn^{2+} center. The observation of the high-energy band suggests that effective scintillation occurs, because the energy transfer is essential in obtaining effective scintillation.

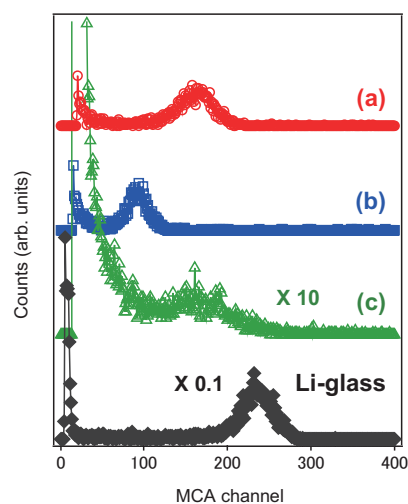Fig. 1. Pulse-height spectra of the samples for ^{241}Am α-ray; (a): 5SnO-60ZnO-40P$_2$O$_5$,
(b): 0.5SnO-24.5SrO-75B$_2$O$_3$,
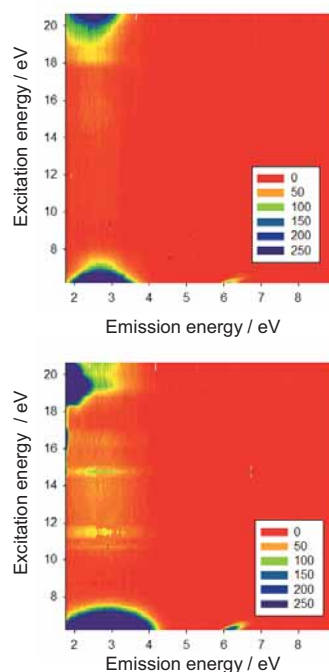(c): 0.1SnO-24.9SrO-75B$_2$O$_3$.

Fig. 2. Contour plot of emission and excitation spectra of the 5.0SnO-60ZnO-40P$_2$O$_5$ (lower) and 0.5SnO-24.5SrO-75B$_2$O$_3$ (upper).

[1] Hirokazu Masai, *et al*., Appl. Phys. Lett., **101** (2012) 191906.

Ⅲ-6. APPLIED MATERIALS

Mo L$_{III}$-Edge XANES Study of MoO$_3$-Modified H-GaAlMFI Catalysts for Methane Dehydroaromatization

H. Aritani[1], T. Sugawara[1], N. Naijo[1], K. Takanashi[1], S. Mogi[1] and A. Nakahira[2]

[1]*Department of Life Science & Green Chemistry, Saitama Institute of Technology, Fukaya 369-0293, Japan*
[2]*Graduate School of Engineering, Osaka Prefecture University, Sakai 599-8531, Japan*

MoO$_3$-modified H-MFI (Mo/H-MFI) is a typical catalyst for methane dehydroaromatization, which is an important reaction for direct GTL (Gas to Liquid) processes. The H-MFI zeolite (SiO$_2$/Al$_2$O$_3$=28-40) shows unique properties for dehydroaromatization of light alkanes such as propane and ethane. The catalytic activity is based on strong acidity and selective sieving effects. By MoO$_3$ modification, it shows high activity for methane dehydro-aromatiozation (MTB reaction). In this reaction, MoO$_x$ species are reduced and carbonized to form Mo$_2$C-like carbide species. The carbide species plays a key role in methane dehydrogenation. As a same time, carbon contamination on Mo/H-MFI proceeds. It is a major source for catalytic deactivation. Because the deactivation relates to the strong acidity on H-MFI, an improvement of H-MFI support is called for. In the present study, Ga-containing H-MFI (GaAl-MFI) supports have been synthesized hydrothermally [1], and MoO$_x$-modified GaAl-MFI catalysts have been applied to employ the methane dehydroaromatization. By substitution of Ga ions onto H-MFI framework, the acidity weakens slightly. The effect of Ga ion onto H-MFI, highly active and durable catalysts can be expected. In the present report, Mo species on GaAl-MFI catalysts have been characterized by Mo L$_{III}$-edge XANES to evaluate the carbide species after the MTB reaction.

Catalysts were prepared by impregnation of H-GaAlMFI support with MoO$_2$(acac)$_2$−CHCl$_3$ solution, and followed by drying overnight and calcination at 773 K for 3 h. The amount of MoO$_3$-loading is 5.0 wt% in this study. H-GaALMFI supports were synthesized hydrothermally at 413 K for a week, and followed by ion-exchanging with NH$_4$Cl and calcination at 873 K. The catalytic activity of methane dehydroaromatization was evaluated by means of fixed bed flow reaction, as described in a separate paper [2]. The catalyst samples are denoted as Mo/GamMFIn, in which m=Ga/Al and n=Si/Al$_2$ atomic ratios. Mo L$_{III}$-edge XANES spectra were measured in BL2A of UVSOR-IMS in a total-electron yield mode using InSb double-crystal monochromator. Photon energy was calibrated by using Mo metal-foil at Mo L$_{III}$-edge, and normalized XANES spectra and their second derivatives are presented. REX-2000 (Rigaku) software was used by normalization of each XANES spectrum.

Figure 1 shows the Mo/H-MFI28(Ga-free), Mo/GaAl-MFI28 (intraframework Ga onto MFI with Ga/Al=10-50), and Mo-Ga/H-MFI28 (Ga$_2$O$_3$-MoO$_3$
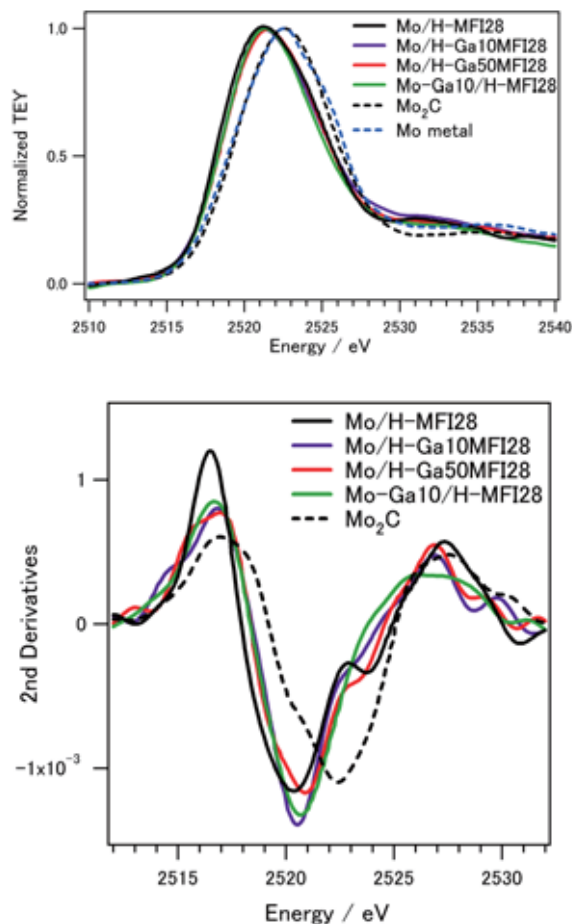
Fig. 1. Mo L$_{III}$-edge XANES spectra (top) and their second derivatives (bottom) over MoOx- modified GaAl-MFI catalysts after MTB reaction.

co-impregnation) catalysts after MTB reaction. For all the catalysts, the edge energy values of L-XANES are lower than bare Mo$_2$C, suggesting the formation of micro-particles which consist of metallic and carbonized Mo. Mo/H-Ga50MFI28 shows the maximum reactivity for MTB reaction, and thus, Ga ions do not affect the Mo carnbonization. Mo-Ga interaction can not be seen in both the structural evaluation and catalytic properties. It is concluded that formation of active Mo carbide species proceeds independently of Ga modification.

[1] K. Nagashima, S. Nakamura, K. Okada, A. Nakahira and H. Aritani, Bull. Chem. Soc. Jpn. **82** (2009) 1203.
[2] H. Aritani, H. Shibasaki, H. Orihara and A. Nakahira, J. Environm. Sci. **21** (2009) 736.

BL2A

Local Structure of Na-K and K-K edge of Artificial Zeolites Prepared from Blast Furnace Slag

M. Sato[1], K. Kumadani[2], T. Shirai[2] and A. Nakahira[1, 2]

[1]Kansai Center for Industrial Materials Research, Tohoku University, Osaka 599-8531, Japan
[2]Department of Material Science and Engineering, Osaka Prefecture University, Osaka 599-8531, Japan

The depletion of natural resources is one of the our serious problems. Therefore, the development of the novel recycling technology has been performed energetically. Blast furnace slag (BF slag) is one of the waste materials that the development and establishment of the effective recycling technology and system become the urgent assignment. The BF slag has been produced approximately 25 million tons per year, and it is recycled as Portland cement, base coarse materials, fine aggregate for concrete and ground improvement materials, and so on. However, recycling rate of BF slag is insufficient by comparing to the amount of generation. In this study, A and Y type zeolite were prepared using BF slag as a starting material to reduce an emission of waste materials, and local structure of Na-K and K-K edge of products were measured in order to investigate the condition of exchanged cation in zeolite.

BF slag and sodium aluminate were used as starting materials. Firstly, BF slag was ground to become their particle size less than 70 μm. Ground slag powder was undergone an acid treatment to remove Ca component. Then, Ca removed slag powder was hydrothermally treated in NaOH solution at 368 K. In this study, the ratio of Si to Al was changed in the range from 0.5 to 2.4 by addition of sodium aluminate. Obtained samples were ion exchanged in 1000 ppm KNO_3 solution at room temperature for several periods. K-K edge XANES spectra of obtained samples were measured by a total electron yield mode at room temperature using InSb double-crystal monochromater, and Na-K edge XANES spectra was also measured by a total electron yield mode at room temperature using Beryl double-crystal monochromater at BL-2A station of UVSOR.

Figure 1 shows Na-K edge XANES spectra of A type zeolite prepared from BF slag before and after ion exchange. Commercial A type zeolite and A type zeolite prepared using reagents were used as references. The position of second peak around 1080 eV was different between references and sample. This result shows that Na environment in zeolite prepared from BF slag more distorts than references [1].
In the case of K-K edge XANES spectra of A type zeolite prepared from BF slag after ion exchange. Although clear spectra did not obtain for the sample ion exchanged for 5 and 30 min, obtained spectra were similar spectra with zeolite 3A, which is the potassium form of the type A crystal structure. This result shows that exchanged K^+ ions in zeolite prepared from BF slag exist in similar environment with zeolite 3A.
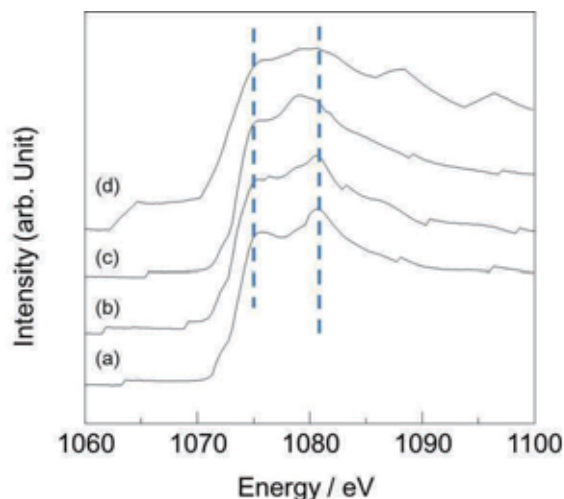

Fig. 1. Na-K edge XANES spectra of A type zeolite prepared from BF slag and references. (a) Commercial A type zeolite, (b) A type zeolite prepared using reagents, (c) A type zeolite prepared from BF slag, (d) after ion exchange for 30 min.

[1] D. R. Neuville, L. Cormire, A-M. Flank, R. J. Prado and P. Lagarde, Eur. J. Mineral **16** (2004) 809-816.

Ⅲ-6. APPLIED MATERIALS

Investigation of Local Structure of P-K edge of Fe doped Amorphous Calcium Phosphate Powders

M. Sato[1], T. Nagayasu[2], S. Hayashi[2] and A. Nakahira[1, 2]

[1]*Kansai Center for Industrial Materials Research, Tohoku University, Osaka 599-8531, Japan*
[2]*Department of Material Science and Engineering, Osaka Prefecture University, Osaka 599-8531, Japan*

Hydroxyapatite ($Ca_{10}(PO_4)_6(OH)_2$, HAp) has been well understood as an alternate materials of our hard tissue because of their excellent osteoconductivity and biocompatibility. Besides, HAp also has good protein adsorption ability and ion exchange ability. Therefore, many studies for bioactivity and degradable behavior of Mg, Mn, Fe, Si, Zn doped HAp have been performed.

In a previous study, we prepared Fe doped HAp powders by co-precipitation and hydrothermal method, and investigated the effect of Fe addition on the crystal phase, microstructure, local structure around Fe, Ca and P atoms and other properties [1, 2]. From the result of XAFS measurement, it was suggested that the added Fe mainly existed as α-FeOOH and α-Fe_2O_3 phase, and small amount of Fe was substituted into the HAp structure. Since the generation of α-FeOOH phase is caused by the alkali condition of preparation method, sol-gel method, which does not require the alkali condition and typical method to obtain amorphous calcium phosphate, was used as a preparation method.

Metal Ca, phosphoric acid and Fe acetylacetonate were used as starting materials. These were mixed up in ethanol solution at 353 K for 4 hours becoming the Ca/P ratio of 1.67 and the ratio of Fe from 1 to 10 mol% for Ca. After that, they were filtered and dried at 323 K for overnight. P-K edge XANES spectra of obtained HAp powders were measured in a total electron yield mode at room temperature using InSb double-crystal monochrometer at BL-2A station of UVSOR.

Figure 1 shows P-K edge XANES spectra of Fe doped amorphous calcium phosphate powders prepared by sol-gel method. Commercial HAp was used as a reference. The obtained spectra of Fe doped sample showed similar spectra independent from the ratio of Fe. This result indicates that the local structure around P atom of Fe doped samples does not change by Fe addition. Besides, clear peak shift to high energy site and spectrum broadening were observed by comparison with the commercial HAp.

From these results, it is suggested that relatively higher amount of Fe can be doped than our previous studies [1, 2], and this data is important to clarify the condition and solid solubility limit of Fe in the HAp structure.
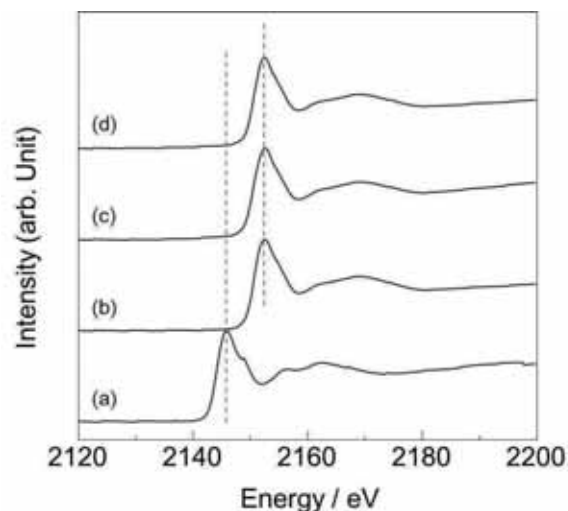

Fig. 1. P-K edge XANES spectra of Fe doped amorphous calcium phosphate powder prepared by sol-gel method.

[1] M. Sato, S. Yamamoto, Y. Nishio, Y. Takamatsu and A. Nakahira, UVSOR Activity Report **38** (2011) 115.
[2] M. Sato, Y. Kawabe, S. Misu, S. Hayashi and A. Nakahira, UVSOR Activity Report **39** (2012) 81.

Study of the Local Strucures of LTA-type Zeolite Nanopowder by XANES Evaluations

A. Nakahira[1, 2], T. Tagami[1], T. Shirai[1], M. Sato[2], T. Nagayasu[1] and H. Aritani[3]

[1]Faculty of Engineering, Osaka Prefecture University, Gakuencho, Sakai 599-8531, Japan

[2]Osaka Center, IMR, Tohoku University, Gakuencho, Sakai 599-8531, Japan

[3]Saitama Institute of Technology, Fukaya 369-0293, Japan

It is well-known that zeolites are microporous, aluminosilicate minerals commonly used as various commercial adsorbents. In fact, zeolites are widely used in industry for water purification, as catalysts, for the preparation of advanced materials and Cs purification in nuclear reprocessing. In addition, they purification are used to extract nitrogen from air to increase oxygen content for both industrial and medical purposes. However, the modification of microstructures and morphology is needed for zeolites to expand their applications in various industrial fields. [1-3]

Recently, as one approach for the modification of microstructures and morphology of zeolites, much attention are paid to the synthesis of the finely nanosized zeolite powders by the novel processing. Various processing are attempted to synthesize the nanosized zeolite powders.

In this study, the finely nanosized zeolite powders were synthesized by the mechanical mixing processing with high energy grinding forces and the local structures were investigated for finely nanosized zeolite powders prepared by the mechanical mixing processing.

Zeolite was synthesized by the following method. LTA type zeolites were synthesized at 60 ℃ to 90 ℃ by the soft chemical solution processing using sodium silicate as s silicon source and aluminum silicate as an aluminum source. The mixture of sodium silicate and aluminum silicate was aged for 12h and then treated under hydrothermal conditions for 12 h to 48 h without stirring. The solid product was filtered, frequently washed, and air-dried at room temperature. Subsequently, the powder of this LTA type zeolites powder was milled by the mechanical milling method with the high energy forces for 1h to 24 h. After the milled and ground nanosized LTA type zeolite powder were characterized by Xrd method and TG/DTA. The microstructures of nanosized LTA type zeolite powder were observed by scanning electron microscopy. The local structures around Al for the products of nanosized LTA type zeolite powder were characterized by measuring X-ray adsorption near edge structure (XANES) at BL2A in UVSOR.

The results of XRD for synthesized zeolite indicated that the obtained products were LTA type zeolites. XRD results showed that after the mechanical mixing processing for 2 hs the ground products were also identified to be LTA type. Products obtained after the mechanical mixing processing had the average particle of a few hundred nanometer in diameter. Suggesting the nanosized LTA zeolite powders were successfully obtained by after the mechanical mixing processing for 2 hs.

Fig.1 shows the XANES spectra of zeolites and reference materials. As shown in Fig. 1, XANES spectra of sample obtained after the mechanical mixing processing for 2h the same spectra as the LTA without mechanical mixing. These results suggest nanosized LTA zeolite powders possess the good crystallinity and also the same local structure of Al after the mechanical mixing processing.
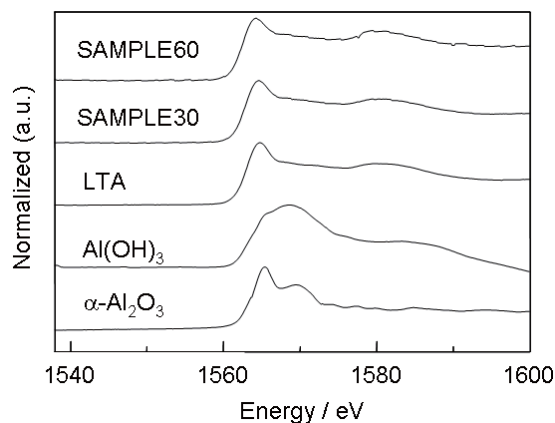

Fig. 1. Al XANES spectra of zeolites and reference materials.

[1] M. E. Davis and R. F. Lobo, Chem. Mater., **4** (192) 756.

[2] A. Nakahira, S. Nishimura, H. Aritani, T. Yamamoto and S. Ueda, J. Mater. Sci. **36** (2001) 1885.

[3] A. Nakahira, S. Yamamoto, M. Sato, Y. Takamatsu, S. Misu, Y. Kawabe, Y. Nishio and H. Aritani, UVSOR Activity Report **38** (2011) 112.

Ⅲ-6. APPLIED MATERIALS

XANES Evaluation of Zeolites obtained from Waste Glass

A. Nakahira[1, 2], T. Tagami[1], T. Shirai[1], K. Kumadani[1], M. Sato[2] and H. Aritani[3]

[1]*Faculty of Engineering, Osaka Prefecture University, Gakuencho, Sakai 599-8531, Japan*
[2]*Osaka Center, IMR, Tohoku University, Gakuencho, Sakai 599-8531, Japan*
[3]*Saitama Institute of Technology, Fukaya 369-0293, Japan*

Glass is widely used in many fields and an ideal material for recycle, whereas it is used for new glass container manufacture it is virtually infinitely recyclable. The glass component in municipal waste is usually made up of bottles, broken glassware, light bulbs and other items. Glass makes up a large component of household and industrial waste. The use of the recycled glass as aggregate in concrete and others has become popular in modern times, although large scale researches have been carried out long year. It is expected that glass recycling is the process of turning waste glass into usable products because the use of recycled glass in new containers helps save energy. In fact, recycling of waste glass and other sources help in brick and ceramic manufacture, and it conserves raw materials, reduces energy consumption [1-4].

As one approach of the recycle of waste glass, much attention are paid to the synthesis of zeolites for waste glass by soft chemical processing, that is, eco-processing with low environmental load. Especially, the finely zeolite powders are expected to synthesize by the novel soft chemical eco-processing. Various eco-soft chemical processing with low environmental load are attempted to synthesize the novel zeolites.

In this study, the finely LTA zeolite powders were synthesized by the novel soft chemical eco-processing with low environmental load and the local structures were investigated for zeolite powders prepared by the novel eco-soft chemical processing with low environmental load.

Glass was prepared from the waste glass, such as a window sheet glass. Zeolite was synthesized by the following eco-soft chemical processing with low environmental load. LTA type zeolites were synthesized at 90 °C by the eco-recycle soft chemical processing using sodium silicate as s silicon source and aluminum silicate as an aluminum source. The mixture of both sodium silicate and aluminum silicate was aged for 24h and then heat-treated under hydrothermal conditions for 48 h with magnetic stirring. The solid product was filtered, frequently washed, and air-dried at room temperature. Subsequently, the powder of the zeolite was milled by the mortar. The solid products were evaluated by XRD method and TG/DTA equipments. The microstructures of the solid product powder were observed by scanning electron microscopy (SEM). The local structures around Si for the products of the solid product powder were characterized by measuring X-ray adsorption near edge structure (XANES) at BL02A in UVSOR.

The results of XRD indicated that the products synthesized under the optimum synthetic conditions were identified to be a LTA type zeolite without other phase, although some products contained LTA and other phases. These results suggest that the fine LTA zeolite powders were successfully obtained from waste glass by eco-soft chemical processing with low environmental load.

The XANES spectra of products and reference materials are shown in Fig.1. XANES spectra of sample obtained the same spectra as the commercial LTA. These results suggest the fine LTA zeolite powders possess the good crystallinity and also the same local structure of Si as the commercial LTA (com LTA).
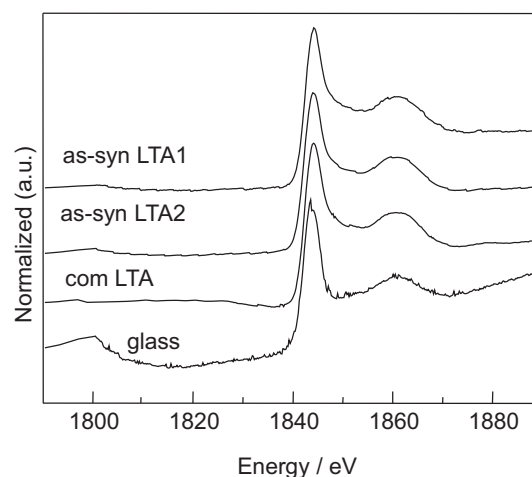
Fig. 1. Si XANES spectra of zeolites and reference materials.

[1] Y. Shaoa, T. Leforta, S. Morasa and D. Rodriguezb, Cement and Concrete Research. **30** (2000) 91.
[2] A. R. Boccaccini, M. Bücker, J. Bossert and K. Marszalek, Waste Management. **17** (1997) 39.
[3] A. Nakahira, S. Yamamoto, M. Sato, Y. Takamatsu, S. Misu, Y. Kawabe, Y. Nishio and H. Aritani, UVSOR Activity Report. **38** (2010) 112.
[4] M. Sato, S. Yamamoto, Y. Nishio, Y. Takamatsu, K. Kumadani and A. Nakahira, UVSOR Activity Report . **38** (2010) 114.

Photoluminescence of Si-O-C(-H) Ceramics Derived from Polysiloxanes

T. Kawai[1] and M. Narisawa[2]

[1] *Graduate School of Science, Osaka Prefecture University, Sakai 599-8531, Japan*
[2] *Graduate School of Engineering, Osaka Prefecture University, Sakai 599-8531, Japan*

The photoluminescence (PL) properties of Si-O-C materials derived from organosilicon polymers have been attracting widespread attention in recent years [1, 2]. Simple chemical composition of such Si-O-C without special activator was promising for use in light-emitting diode (LED) systems. Though some Si-O-C transparent materials were synthesized by sol-gel methods or CVD methods, the precise adjustment of resulting chemical composition was not easy in such sol-gel or CVD methods. Recently, we succeeded in synthesizing Si-O-C(-H) ceramics with a white appearance by using hydrogen in the pyrolysis process for silicone resin particles [3, 4]. In this study, we have investigated the PL properties of the Si-O-C(-H) ceramics decarbonized at different temperatures.

Figure 1 shows the PL spectra of the Si-O-C(-H) ceramic decarbonized at 750 °C. Under excitation on the shorter wavelength than 240 nm, the broad PL bands are observed around 320 and 450 nm. The 450 nm bands have a long tail on the longer wavelength region. On the other hand, the excitation on the longer wavelength than 250 nm induces the broad PL bands peaking at 420 nm and having a shoulder structure around 540 nm. The shape of the PL bands indicates that the Si-O-C(-H) ceramic decarbonized at 750 °C has several PL centers.

Figure 2 shows the PL spectra of the Si-O-C(-H) ceramics decarbonized at 1100 °C under excitation at various wavelength. The broad PL bands with a peak at 500 nm are observed. The peak energy and band-shape of the PL bands are independent of the excitation wavelength. The fact indicates that the decarbonization at 1100 °C leads to the transformation to the more stable PL centers.

In the simple chemical composition of Si-O-C(-H), the oxygen deficiency centers called ODC (II) are often proposed as possible PL centers. The excitation and emission due to the transition between S_0 (singlet ground state) and S_1 (singlet excited state) in ODC (II) occur around 5.0 eV (245 nm) and 4.3 eV (290 nm), respectively [5]. Since the 320 nm PL band of the Si-O-C(-H) ceramic decarbonized at 750 °C appears only under excitation on the shorter wavelength than 240 nm, the 320 nm PL band would be attributed to the $S_1 \rightarrow S_0$ radiative transition in ODC(II). On the other hand, the 450 nm PL band might come from the transition between S_0 and T_1 (triplet excited state) in ODC (II). The appearance of the 450 nm PL band under excitation on the shorter wavelength than 240 nm implies the existence of

transfer from the S_1 to T_1 states. In order to obtain information on the PL centers of the Si-O-C(-H) ceramics, the shape of the PL bands is carefully analyzed.
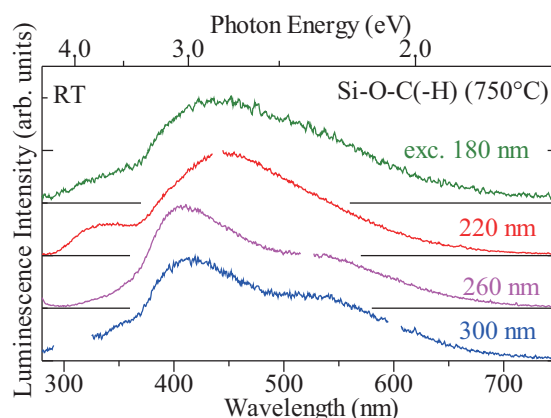
Fig. 1. Luminescence spectra of the Si-O-C(-H) ceramics decarbonized at 800 °C.
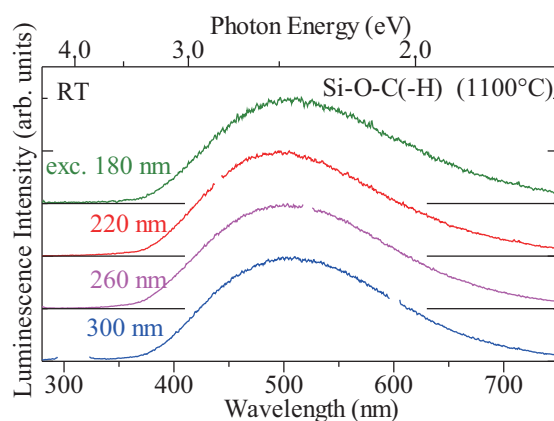
Fig. 2. Luminescence spectra of the Si-O-C(-H) ceramics decarbonized at 1100 °C.

[1] A. Karakuscu *et al*., J. Am. Ceram. Soc. **92** (2009) 2969.
[2] S. Gallis *et al*., Appl. Phys. Lett. **97** (2010) 081905.
[3] M. Narisawa *et al*., Bull. Chem. Soc. Jpn. **85** (2012) 724726.
[4] M. Narisawa *et al*., J. Am. Ceram. Soc. **95** (2012) 3935.
[5] L. Skuja: J. Non-Cryst. Solids **239** (1998) 16.

Ⅲ-6. APPLIED MATERIALS

Intrinsic Luminescence and Host Sensitization of Rare-earth Ions in Lanthanum Scandium Borate upon VUV Excitation

N. Kodama, Y. Morisawa, A. Abe, T. Sakashita and T. Takahashi

Faculty of Engineering and Resource Science, Akita University, Akita 010-8502, Japan

Host sensitization of rare-earth ions ($RE^{3+} = Gd^{3+}$ and Ce^{3+}) has been observed in some phosphates and borates [1-3]. The intrinsic luminescence characteristics of lanthanum scandium borate, $LaSc_3(BO_3)_4$ (LSB) were investigated, in which the absorption of vacuum ultraviolet (VUV) light by the host may facilitate efficient energy transfer to Re^{3+} ions. Here, energy transfer was observed from the self-trapped exciton (STE) to Sm^{3+} and Tb^{3+} ions.

Emission and excitation spectra were measured at temperatures in the range of 7.8-293 K using the UVSOR facility. Figures 1(a) and (b) show emission spectra observed for an undoped LSB polycrystal with various excitation wavelengths at 293 and 7.8 K. The emission spectrum with VUV excitation at 70 and 160 nm consists of three intrinsic broad bands at 253, 323, and 379 nm. The feature of the emission spectrum for a LSB single crystal is the same as that for the polycrystal. Figure 2 shows excitation spectra at 293 K for both the LSB polycrystal and single crystal, which consist of fairly broad bands between 50 and 215 nm. The band edge of the single crystal is observed around 215 nm and the broad bands are assigned as bandgap excitations or molecular transitions of the $BO_3^{3-}$ group. Both the single crystal and polycrystal spectra exhibit the same features with a sharp rise below 215 nm.

The three intrinsic emissions can be assigned to recombination of the distinct STEs (I, II, and III) that could be associated with bandgap excitations or molecular transitions of the BO_3^{3-} group. The decay times of the emissions, I (253 nm), II (323 nm) and III (379 nm) are less than 10 ns, 115 ns, and 3.4 μs, respectively. By analogy with the STE states in alkali halides [4], the I (fast) and II (fast) STE emissions originate from singlet transitions on center and off-center configurations, respectively, whereas the III (slow) STE emission is suggested to originate from a triplet transition on the off-center configuration. The emission spectra of undoped LSB, Sm^{3+}-doped LSB polycrystals (LSB:Sm), and Tb^{3+}-doped LSB polycrystals (LSB:TB) excited at 70 and 160 nm at 296 K are shown in Figs. 3(a)-(c).

For LSB:Sm, the intrinsic emissions (STE emission) decrease with increase in the Sm^{3+} concentration (1-30 at.%) (Fig. 3(a)) and this is accompanied by the appearance of intense emissions from the $^4G_{5/2}\rightarrow^6H_J$ transitions of Sm^{3+} (Fig. 3(b)). This suggests efficient energy transfer from the STE to Sm^{3+} ions. The Sm^{3+} emission intensity passes through a maximum at 3-5 at.% with increasing Sm^{3+}

concentration and then decreases monotonically at higher concentrations, which indicates concentration quenching by energy transfer between two Sm^{3+} ions.

For LSB:Tb, the STE emission decreases with increase in the Tb^{3+} concentration (1-40 at.%), as shown in Fig. 3(c). An increase in the $^5D_4\rightarrow^7F_J$ transition of Tb^{3+} accompanies the decrease of the STE emission, which also indicates efficient energy transfer from the STE to Tb^{3+} ions. The two decay times of the intrinsic emissions, II (85 ns) and III (2.5 μs), become shorter in the Tb^{3+}-doped samples, which is consistent with the decrease in the time-averaged STE emission intensity with increasing Tb^{3+} concentration.

The Sm^{3+}/STE or Tb^{3+}/STE ratios gradually increase in intensity with temperatures from 7.8 to 293 K, which suggests that the energy transfer from the STE to Sm^{3+} or Tb^{3+} is thermally activated.
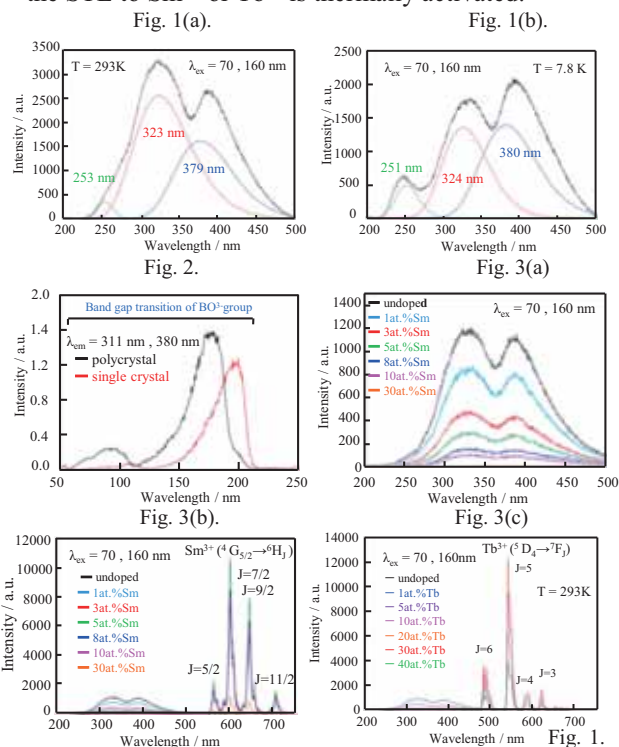
Fig. 1.
Emission spectra observed in undoped LSB excited at 70 nm and 160 nm at 293 K (a) and 7.8 K (b).
Fig. 2. Excitation spectra of undoped LSB poly- and single-crystal.
Fig. 3. Emission spectra of undoped LSB (a), LSB:Sm (b) and LSB:Tb excited at 70 nm and 160 nm.

[1] S.P. Feofilov *et al*., Phys.Rev.B. **74** (2006) 085101.
[2] S.P. Feofilov *et al*., J. Lumin. **125** (2007) 80.
[3] N. Kodama *et al*., *Abstract of 15th Int. Conf. on Defects in Insulating Materials* (2010) A90.
[4] K.Kan'no *et al*., Pure & Appl. Chem. **69** (1997) 1227.

Effect of Ion Implantation on the Crystallinity of YAlO$_3$ Single Crystal

Y. Horii, T. Morimoto and Y. Ohki

Waseda University, 3-4-1 Ohkubo, Shinjuku-ku, Tokyo 169-8555, Japan

Yttrium aluminate (YAlO$_3$) is a promising candidate for a gate insulator in advanced MOS devices. However, ion implantation, which is usually required after the deposition of a gate insulator, would cause damage to the gate insulator. Therefore, the effects induced by implantation of ions were examined by measuring optical absorption, photo-luminescence (PL) and X-ray diffraction (XRD) spectra.

The samples examined are commercially available YAlO$_3$ (100) single crystals in the shape of a plate with a thickness of 0.5 mm. Positive phosphorus (P$^+$) or boron (B$^+$) ions were implanted to the samples at a fluence of 1.0×10^{15} cm^{-2}. Before and after the ion implantation, optical absorption, in-plane XRD and PL were measured.

Optical absorption increases significantly at energies slightly lower than the gap energy as shown in Fig. 1. The XRD peak shown in Fig. 2 shifts after the implantation of P$^+$ and B$^+$ ions. Furthermore, its peak height becomes smaller. Figure 3 shows PL spectra induced by 6.4, 7.7 and 8.2 eV photons, where curve A represents PL spectra observed before ion implantation, while curves B and C represent those observed after the implantation of P$^+$ and B$^+$ ions, respectively. Among several photoluminescence bands observable in YAlO$_3$, two bands due to Cr^{3+} at around 1.70 eV induced by 6.4 eV photons [1], another one due to self-trapped exciton at 4.2 eV induced by 7.7 eV photons [2], and another one due to an antisite defect at 5.5 eV induced by 8.2 eV photons [3] become smaller or disappear by the ion implantation. These three PLs appear only when the sample is crystalline [1, 3, 4]. All these facts indicate that the appearance of localized electronic states in the band gap and the degradation of crystallinity are induced by the ion implantation.
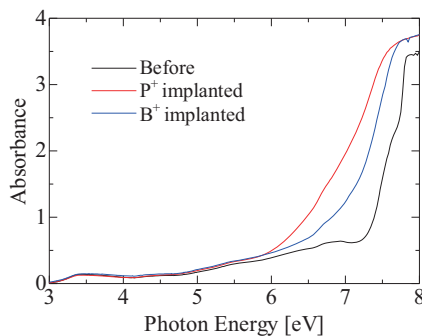
Fig. 1. Absorption spectra of YAlO$_3$ single crystals implanted with P$^+$ or B$^+$ ions.
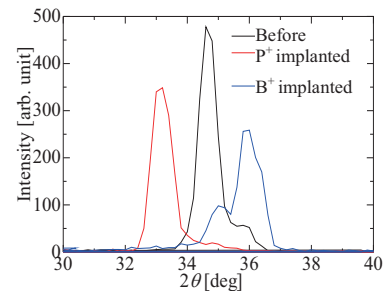
Fig. 2. In-plane XRD patterns observed before and after the implantation of P$^+$ or B$^+$ ions.

(a)

(b)

(c)
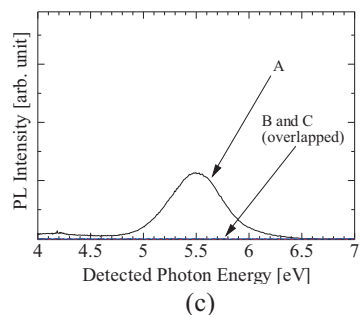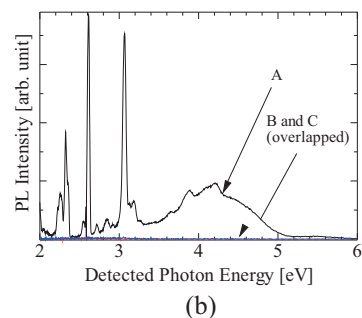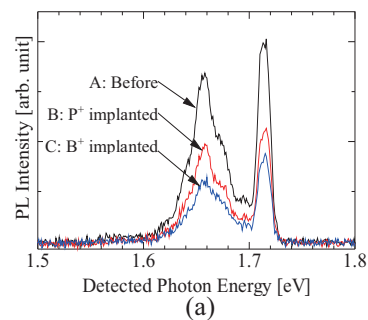
Fig. 3. PL spectra observed before and after P$^+$ or B$^+$ ion implantation, induced by 6.4 eV (a), 7.7 eV (b) and 8.2 eV (c) photons.

[1] E. Hirata *et al*., Jpn. J. Appl. Phys. **49** (2010) 091102.
[2] Ch. Lushchik *et al*., J. Phys. Condens. Matter **6** (1994) 11177.
[3] Y. V. Zorenko *et al*., Opt. Spectrosc. **96** (2004) 536.
[4] M. Murakami *et al*., J. Appl. Phys. Lett. **78** (2001) 2664.

Optical Spectroscopy of Eu^{3+} in GaN Codoped with Mg and Eu

M. Yamaga, S. Tsuda and K. Takagi

Department of Mathematical and Design Engineering, Gifu University,Gifu 501-1193, Japan

Europium doped GaN is a candidate of red light-emitting diodes (red LEDs). Recent optical spectroscopy of Eu^{3+} in GaN(Mg) has revealed the electronic structure of Eu^{3+} associated with defects and temperature-dependence hysteresis of the Eu^{3+} luminescence [1]. However, the quantum efficiency of the Eu^{3+} luminescence was less than 1 %. In order to improve the quantum efficiency, it is very important to examine the relaxation process from the band-to-band excitation to the Eu^{3+} excited state.

GaN films, grown by hydride vapor phase epitaxy (HVPE) on (0001) sapphire substrates and doped with Mg (p-type) were implanted with 300 keV Eu ions. The GaN(Mg):Eu sample was supplied by Prof. K. P. O'Donnell at University of Strathclyde, UK.

Figure 1 shows the absorption spectrum of GaN(Mg):Eu at 300 K. The sharp step around 360 nm is corresponding to the band-edge energy of GaN. The interference fringes due to the thin film structure were observed in the spectrum.

The band-to-band excitation below 360 nm produces fairly strong Eu^{3+} luminescence lines around 620 nm, and three broad bands with peaks at 440, 540 and 600 nm as shown in Fig. 2. The Eu^{3+} luminescence lines decrease drastically beyond 360 nm and the two broad bands at 440 and 540 nm appeared clearly. These broad bands may be assigned to localized centers, for example, donors, acceptors or defects.

Relaxation to Eu^{3+} and emitting processes of Eu^{3+} are strongly associated with the rise and falling components of the decay curves of the Eu^{3+} luminescence, respectively. The decay curve of the Eu^{3+} luminescence in GaN:Eu can fit a single exponential function with the decay time of 0.23 ms [2]. However, the decay curve from GaN(Mg):Eu does not fit to a single exponential, but multi-exponential, at least three components. Otherwise, the decay curve fits to a sum of a single exponential function and power function of t^{n} (n=-1), assuming that there are two different relaxation processes to Eu^{3+}; one is rapid relaxation from band-to-band excitation immediately to the Eu^{3+} excited states; the other is relaxation to Eu^{3+} via donor-acceptor recombination process. Namely, the long decay time (larger than 2 ms) of Eu^{3+} may be due to fairly long feeding time. The possible model is shallowly trapped centers, for example, donors or acceptors trapping weakly electrons or holes, respectively. These bands with the double peaks at 440 nm and 540 nm in Fig. 2 may be associated with

splitting of the acceptor bands consisting of Mg and N wavefunctions.
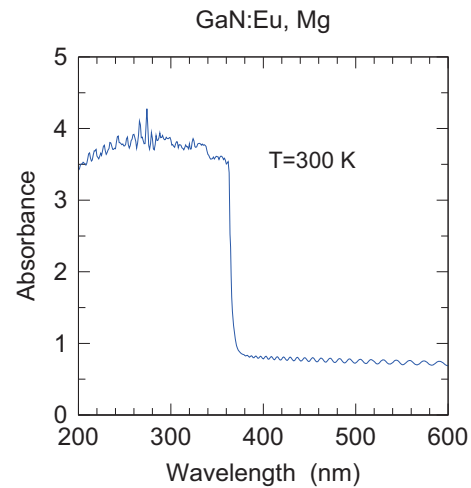
Fig. 1. The absorption spectrum of GaN(Mg):Eu.
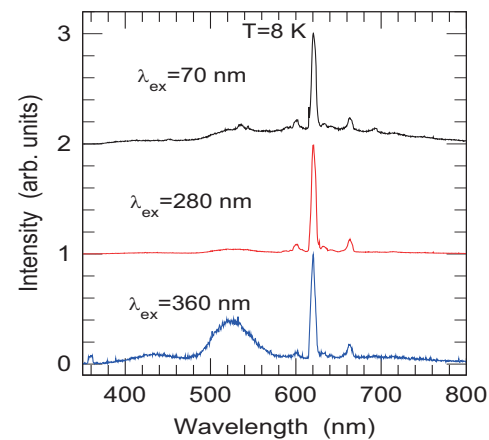

Fig. 2. Photoluminescence of Eu^{3+} in GaN(Mg):Eu excited with various wavelengths in the band-to-band transitions.

[1] K. P. O'Donnell, P. R. Edwards, R. W. Martin, K. Lorenz, V. Darakchieva, A. Alves and M. Bockowski, to be published (2013).
[2] I. S. Roqan, K. P. O'Donnell, R. W. Martin, P. R. Edwards, S. F. Song, A. Alves and M. Bockowski, Phys. Rev. B **81** (2010) 085209.

Photoluminescence due to Intraionic *4f-4f* Transitions of Gd^{3+} Ions in Gd$_3$(Al,Ga)$_5$O$_{12}$ Single Crystals

S. Ishii[1], M. Kitaura[1] K. Kamada[2], A. Ohnishi[1] and M. Sasaki[1]

[1]*Dept. of Physics, Faculty of Science, Yamagata University, 1-4-12 Kojirakawa, Yamagata 990-8560, Japan*
[2]*Materials laboratory of Furukawa Co. Ltd, 1-25-13 Kannondai, Tsukuba 305-0856, Japan*

Resonant energy transfer between impurity ions has been studied in the viewpoint of fundamentals and applications in inorganic phosphor materials [1]. The control of this process is one of conventional methods to enhance the luminescence yield in the development of phosphor materials. The main work is to hunt for better combinations of donor and acceptor ions on the basis of an overlap of absorption and luminescence spectra. The pair of Ce^{3+} and Gd^{3+} ions is known to be one of such combinations. In most ionic crystals, the absorption due to *4f-5d* transitions of Ce^{3+} ions and the emission due to *4f-4f* transitions of Gd^{3+} ions are located in the near ultraviolet range [2]. Since they have a strong overlap with each other, resonant energy transfer from Gd^{3+} to Ce^{3+} ions are possible in crystals including them.

Gd$_3$Ga$_3$Al$_2$O$_{12}$ (GAGG) belongs to the cubic system with garnet structure. Ce^{3+} doped GAGG (Ce:GAGG) attracts much attention as an inorganic scintillator for the detection of x- and γ–rays, because it has scintillation properties superior to other optical crystals [3]. As mentioned above, since the Ce:GAGG crystal contains Gd^{3+} and Ce^{3+} ions, there is the possibility that host sensitization of the Ce^{3+} 5d-4f emission occurs by the energy transfer from Gd^{3+} to Ce^{3+} ions. An investigation of the host sensitization process is of great significance for the realization of higher luminescence yield and shorter decay time, so it is worthwhile to investigate photoluminescence (PL) properties of GAGG crystals with vacuum ultraviolet (VUV) photons. In the present study, we have measured PL and PL-excitation (PLE) spectra of GAGG crystals with use of synchrotron radiation. Experiment was carried out at the BL3B beam line of UVSOR. Here, we report a part of results in our experiment.

Figure 1 shows the absorption spectrum of GAGG at 6K. Narrow peaks are observed around 4 –5 eV. Similar peaks have been observed for Gd^{3+} activated phosphors [2]. We thus assign them to *4f-4f* transitions of Gd^{3+} ions. The strong absorption occurs at 5.96 eV. This corresponds to the fundamental absorption edge of GAGG.

Figure 2 shows PL and PLE spectra of a GAGG crystal. The PL spectrum was obtained at 6 K under excitation at 6.52 eV. A sharp peak appears at 3.92 eV in the PL spectrum. The PLE spectrum for the 3.92 eV peak exhibits narrow peaks, due to *4f-4f* transitions of Gd^{3+} ions, around 4 – 5 eV. The 3.92 eV PL peak is also assigned to *4f-4f* transitions of Gd^{3+} ions, because this peak is efficiently excited in

the same position as narrow peaks in Fig. 1. As the photon energy is increased, the excitation for the 3.92 eV peak occurs at the fundamental absorption edge at 5.96 eV again, and it continues for the high-energy side above 5.96 eV. The intensity of the 3.92 eV peak is gradually increased around 20 eV, and reaches twice at 30 eV. This is interpreted as an appearance of the multiplication of electron-hole pairs in GAGG.
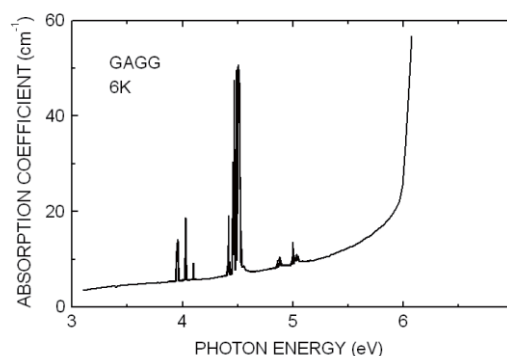
Fig. 1. Absorption spectra of a GAGG single crystal observed at 6 K.
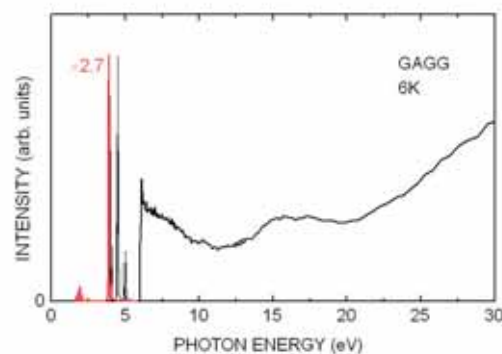
Fig. 2. Emission (red line) and excitation (black line) spectra of a GAGG single crystal observed at 6 K. The emission spectrum was observed under excitation at 6.52 eV. The excitation spectrum was measured for the 3.92 eV emission peak.

[1] D. L. Dexter, J. Chem. Phys. **21** (1953) 836.
[2] T. Kano, *Phosphor Handbook*, CRC Press (Boca Raton) 2nd ed., Chap.3, Sect.3 .
[3] K. Kamada *et al*., J. Cryst. Growth **352** (2012) 88.

133

Nitrogen Doped TiO$_2$ Photocatalyst Prepared by Low Energy N$^+$ Implantation

T. Yoshida[1], E. Kuda[2] and H.Yoshida[2]

[1]*EcoTopia Science Institute, Nagoya University, Nagoya 464-8603, Japan*
[2]*Department of Applied Chemistry, Graduate School of Engineering, Nagoya University, Nagoya 464-8603, Japan*

Photocatalytic reactions at the surface of titanium dioxide (TiO$_2$) under UV light irradiation have been attracting much attention in view of their practical applications to environmental cleaning such as self cleaning of tiles, glasses, and windows. Asahi *et al.* reported that the substitutional doping of N into TiO$_2$ contributes to band gap narrowing to provide visible-light response [1].

In our previous study, we prepared visible-light response TiO$_2$ photocatalysts by the implantation of 50 keV N$^+$ ions [2]. We found that the photocatalytic active nitrogen species, i.e., nitrogen substituting for the O sites in TiO$_2$, are preferentially formed in the samples implanted with a low N$^+$ fluence (< 3 x 10^{21} m^{-2}). In the samples prepared with a higher N$^+$ fluence, the inactive N-O species generated to reduce photocatalytic activity. In the present study, a low energy, 5 keV N$^+$ implantation was performed in order to inject nitrogen atoms near the surface of TiO$_2$.

The samples used in this study were TiO$_2$ (1 0 0) single crystals (5 x 5 x 0.5 mm^3). Mass analyzed 10 keV N$_2^+$ (5 keV N$^+$) ions were injected into the samples at room temperature, perpendicular to the sample surface. As calculated by a Monte Carlo simulation using SRIM code (Fig. 1), the implanted nitrogen distributes up to ca. 25 nm, peaking around 10 nm in depth from the surface, and they would increase monotonously with N$^+$ fluence. Thus, the 5keV N$^+$ implantation enables to inject nitrogen atoms in the shallower region compared with the 50 keV N$^+$ implantation in our previous study.

N K-edge XANES spectra of the samples were measured at the BL-4B. Data were recorded at room temperature in total electron yield mode.

Figure 2 shows N K-edge XANES spectra of the N$^+$-implanted TiO$_2$ and TiN samples. Common XANES features in (b) and (d) suggest that N in the sample implanted by 3 x 10^{21} m^{-2} (TiO$_2$-N(3)) is in a chemical environment similar to that in TiN. Careful observation led us to notice that two peaks around 400 eV for the catalyst sample shift to lower energy side than those for the TiN sample, which was well reproduced by the theoretical prediction using FEFF code when N occupies one of the O sites of TiO$_2$.

On the other hand, the XANES spectra of the sample implanted by 1 x 10^{21} m^{-2} (TiO$_2$-N(1)) and that implanted by 3 x 10^{21} m^{-2} followed by heating at 573 K (TiO$_2$-N(3)-H) showed a distinct single peak around 401 eV. This peak could be empirically attributed to formation of the species such as NO bonds near the surface [3], and which also indicates that the inactive N-O species dominates in TiO$_2$-N(1) and the active nitrogen formed in TiO$_2$-N(3) changed to the inactive N-O species by oxidation at 573 K. These results are in conflict with our previous study, in which the photocatalytically active nitrogen was preferentially produced by 50keV N$^+$ implantation with the lower nitrogen concentration.
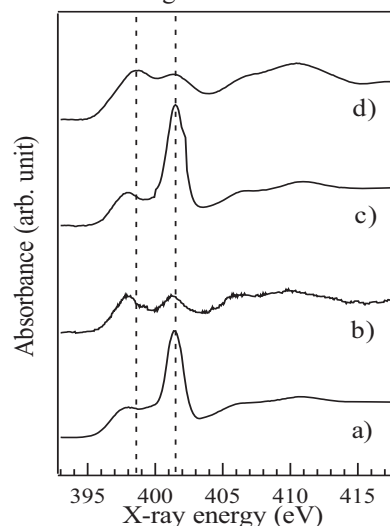
Fig. 2. N K-edge XANES spectra of (a) N$^+$-implanted at 1 x 10^{21} m^{-2}, (b) N$^+$-implanted at 3 x 10^{21} m^{-2}, (c) N$^+$-implanted at 3 x 10^{21} m^{-2} followed by heating at 573 K for 2 h, and (d) TiN.

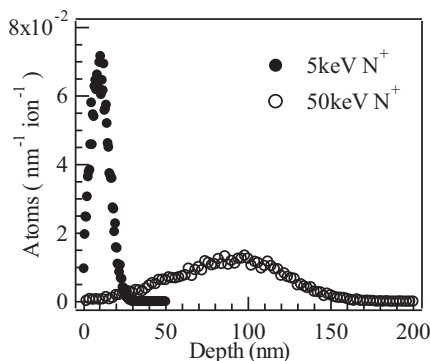

Fig. 1. Depth distributions of implanted nitrogen per incident N$^+$ ion calculated by SRIM code for 5 and 50 keV N$^+$ implantations.

[1] R Asahi *et al.,* Science **293** (2001) 269.
[2] T. Yoshida *et al.,* Mater. Trans. **48** (2007) 2580.
[3] J-H. Wang *et al.,* Anal. Chim. Acta, **476** (2003) 93.

Surface-Structure Change in Lithium-Ion Battery Using Anti-Fluorite Type Positive Electrode

T. Okumura, M. Shikano and H. Kobayashi

National Institute of Advanced Industrial Science and Technology (AIST), Ikeda, Osaka 563-8577, Japan

Fe-based materials as positive electrodes of lithium-ion batteries have been paid much attention to due to their advantages of being low cost and environmentally benign. For example, $LiFePO_4$ is used as the positive electrode material of commercial lithium-ion batteries in spite of relatively lower capacity. To improve battery performance, the positive electrode materials of high capacity are required. Defect anti-fluorite-type structure Li_5FeO_4 is one of the candidate because its theoretical capacity reaches ~694 mAh g^{-1} (four Li in a formula unit) [1, 2]. In previous work, the relatively rechargeable capacity of Li_5FeO_4 could be obtained after first charging until two Li per Li_5FeO_4 formula unit [1]. However, the changes in electronic and crystal structure of Li_5FeO_4 during the electrochemical reaction have not been clarified yet. Recently, we have analyzed the structural changes of Li_5FeO_4 during charging process using XRD, hard-XAFS and ^{7}Li MAS NMR. In this study, the surface-structure change during electrochemical reaction was analyzed by O *K*-edge XAFS spectra using total-electron-yield (TEY) mode.

Li_5FeO_4 was synthesized by solid-state reaction. The positive electrodes were made from a mixture containing 60 wt% Li_5FeO_4, 32 wt% acetylene black and 8 wt% polytetrafluoroethylene, which were casted and pressed on nickel mesh. Coin cells were assembled using metallic lithium foil as a negative electrode. A 1 mol dm^{-3} ethylene carbonate/dimethyl carbonate solution of $LiPF_6$ was used as electrolyte. Electrochemical test was carried out at a constant current density of 1/30 C. For measuring XAFS spectra, samples (#1~5) were obtained from the cells after charging or discharging, as shown in Fig. 1.

The O *K*-edge spectra were shown in Fig. 2+. 3*d*-transition metal (*TM*) oxides generally have the two peaks around 532-538 eV since O 2*p* orbital hybridized with *TM* 3*d* t_{2g} and e_g as shown in the spectrum of Fe_2O_3. However, this specific shape could not be observed in the all samples in this study (#1~5). This result indicates that the surface of the samples is covered with another phase containing lithium salts, and iron oxide phase could not be detected by TEY mode. To identify the surface phase, the spectra of various lithium salts were measured as partially shown in Fig. 2. The spectrum of pristine sample (#1) is similar to that of Li_2O, that is, the surface of #1 would be covered with Li_2O since the lattice parameters of anti-fluorite-type structure Li_2O is close to those of Li_5FeO_4. The shapes of the spectra around 535-538 eV were changed during charging

battery (#1 to #4). Thus, the surface Li_2O also reacts as well as the oxidation of internal Li_5FeO_4 phase. For example, Li_2O_2 is one of the candidates of product compounds. After that, the Li_2O re-formed after discharging battery (#5). Thus, the electrochemical reaction of the surface Li_2O phase would also contributed on the charge / discharge properties in the battery using anti-fluorite Li_5FeO_4 positive electrode.

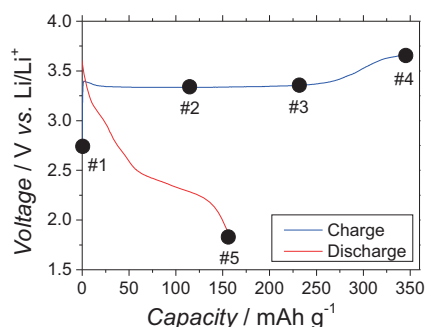
Fig. 1. First cycle of lithium-metal half cell using Li_5FeO_4 positive electrode. Circles indicate the samples measured XANES spectra.
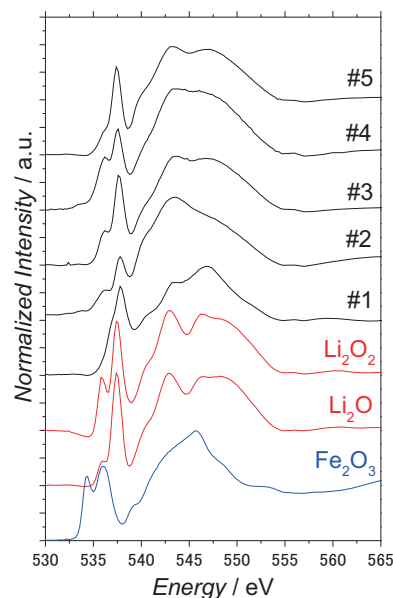
Fig. 2. O *K*-edge XANES spectra measured by total-electron-yield mode.

[1] A. Hirano *et al.,* Solid State Ionics **176** (2005) 2777.
[2] C.S. Johnson *et al.,* Chem. Mater **22** (2010) 1263.

Ultrahigh-Resolution Direct Observation of Mini-bands Formed in InGaAs/AlGaAs Superlattice

D. Shimura[1], F. Ichihashi[1], K. Nishitani[1], S. Harada[1], M. Kuwahara[2], T. Ito[1],
M. Matsunami[3], S. Kimura[3], M. Tagawa[1] and T. Ujihara[1]

[1]*Department of Materials Science and Engineering, Nagoya University, Nagoya 464-8603, Japan*
[2]*Department of Applied Physics, Nagoya University, Nagoya 464-8603, Japan*
[3]*UVSOR Facility, Institute for Molecular Science, Okazaki 444-8585, Japan*

Intermediate-band solar cells have attracted great attention for their potential to achieve 74.6 % efficiency over the Shockley-Queisser limit of a single gap solar cell [1-3]. The concept of the intermediate-band solar cell is to increase photocurrent by using electrons excited to a conduction band via the intermediate-bands. Mini-bands formed in superlattice structures are often utilized for the formation of the intermediate-bands. Indeed, recently, it has been demonstrated that quantum-well superlattice solar cells induced two step photon absorption and photocurrent generation at room temperature [4]. In addition, these reports indicated that the transport of the carriers in the mini-bands was essential in order to the photocurrent generation based on two step absorption. Therefore it is very important to figure out the mini-band structures which influence the transport properties and the conversion efficiency. In this study, we directly observed the dispersions of mini-bands formed in InGaAs/AlGaAs quantum-well superlattice by angle-resolved photoemission spectroscopy (ARPES) with synchrotron radiation.

The structure of the specimen is shown in Fig. 1. The superlattice was grown by a low-pressure metalorganic vapor phase epitaxy. On the evaluation of the mini-band structure, normal-emission and in-plane ARPES measurements in the vacuum-ultraviolet region were performed at BL5U of the UVSOR-III storage ring. The measurements were carried out at 10 K under the ultrahigh vacuum atmosphere (less than 1×10^{-8} Pa).

The ARPES intensity mapping image of the X-valley of InGaAs which was originated from the surface of the superlattice specimen is shown in Fig. 2. The zero energy indicates the valence-band maximum and the zero wave vector indicates the X-valley. The valence band of InGaAs and As $3d$ core level-derived peaks were observed. In addition, it was noticed that the peaks which were not existed in the InGaAs bulk were observed ranging from -2.0 to 0 eV of energy. The yellow circles indicate the mini-band-derived peaks of the second order differential, which indicate the mini-band structures formed in the superlattice structure. These peaks were good consistent with the theoretical values calculated by Kronig-Penney model, especially the heavy hole mini-bands.

By ARPES measurement at high resolution, we can experimentally evaluate the mini-band structures.
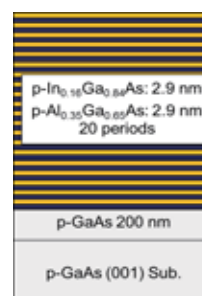
Fig. 1. Details of the structures of the specimen.
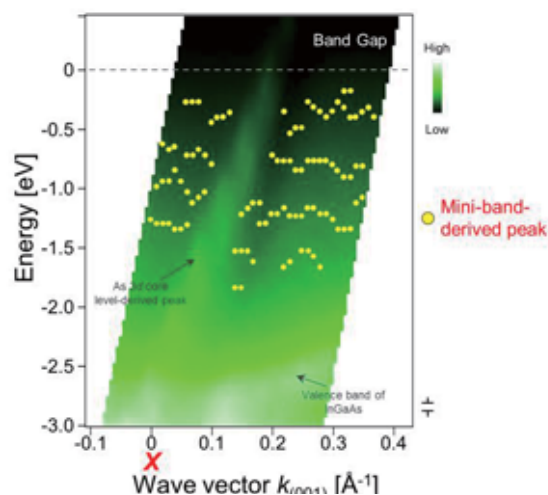
Fig. 2. The ARPES intensity mapping image of InGaAs/AlGaAs superlattice. The yellow circles indicate the mini-band-derived peaks of the second order differential.

[1] A. Luque and A. Martí, Phys. Rev. Lett. **78** (1997) 5014.
[2] T. Nozawa and Y. Arakawa, Appl. Phys. Lett. **98** (2011) 171108.
[3] W. Shockley and H. J. Queisser, J. Appl. Phys. **32** (1961) 510.
[4] M. Sugiyama, Y. Wang, K. Watanabe, T. Morioka, Y. Okada and Y. Nakano, IEEE J. Photovoltaics **2** (2012) 298.

Characterization of Amorphous Chalcogenide Films by Vacuum Ultraviolet Absorption Spectroscopy

K. Hayashi

Department of Electrical and Electronic Engineering, Gifu University, Gifu 501-1193, Japan

Amorphous semiconductor materials are very expected as a potential material for optoelectronic devices because these materials are very sensitive to the light and show a variety of photoinduced phenomena [1-3]. For the device application, it is necessary to sufficiently understand the physical property of these materials. Although a large number of studies have been done on the photoinduced phenomena of these materials, little is known about the details of these mechanisms. These phenomena were studied by exciting outer core electrons with the irradiation of light with the energy corresponding to the optical bandgap or sub-bandgap. The interest has been attracted for the change of the optical properties in the energy region of the visible light. We are interesting for the changes of the optical properties in the higher energy region. To obtain a wide knowledge of the photoinduced phenomena, it is necessary to investigate to the photoinduced effects on wide energy region. In previous reports, we reported the photoinduced change at the VUV reflection and total photoelectron yield spectra of the amorphous chalcogenide thin films induced by bandgap light. Recently, we became able to measure directly the VUV absorption spectra of amorphous thin films [4]. In this paper we report results on the study of the difference of the structure between the as-deposited and well-annealed films by the VUV absorption spectroscopy.

Samples used for the measurement of the VUV absorption spectrum were amorphous chalcogenide (a-As$_2$S$_3$ and a-As$_2$Se$_3$) semiconductor thin films prepared onto aluminum thin films by conventional evaporation technique. Typical thickness of the samples and the aluminum films were around 180nm and 100nm respectively. The aluminum film was also used in order to eliminate the higher order light from the monochromator in the VUV region. The measurements were carried out at room temperature at the BL5B beam line of the UVSOR facility of the Institute for Molecular Science. And the spectrum was measured by using the silicon photodiode as a detector. A pinhole of 1.5mm in a diameter was inserted between the monochromator and sample to remove stray light. The intensity of the VUV light was monitored by measuring the TPEY of a gold mesh. The positions of the core levels for the samples were calibrated by referencing to the 2p core level absorption peak of the aluminum film.

Figure 1 shows VUV absorption spectra of As 3d core level for the as-deposited and the well-annealed amorphous chalcogenide films. As shown in the figure, the As 3d core level absorption peaks of the as-deposited film show significant differences in shapes and positions in comparison with those obtained for the well-annealed film. It can explain the difference by the reports [5] that many dangling bonds and homo bonds (As-As and S-S bonds etc.) exist in the as-deposited amorphous films. In the next step, the structural changes by the irradiation of the bandgap light will be investigated by the VUV absorption spectroscopy.
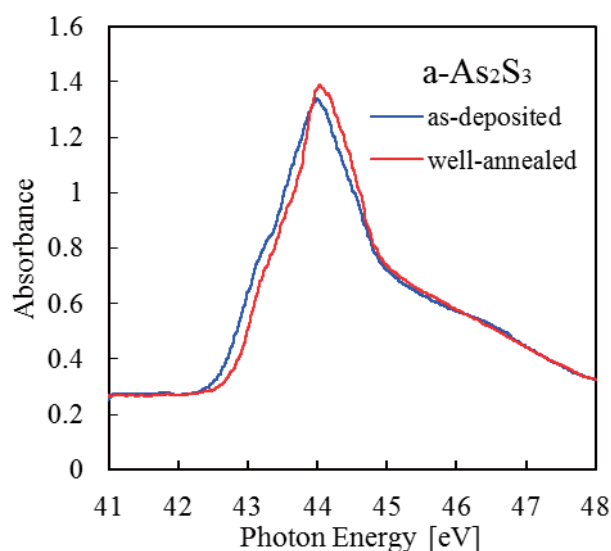
Fig. 1. VUV absorption spectra of As 3d core level for as-deposited and well-annealed amorphous chalcogenide films.

[1] Ke. Tanaka, Rev. Solid State Sci. **4** (1990) 641.
[2] K. Shimakawa, A.Kolobov, and S. R. Elliott, Adv. Phys. **44** (1995) 475.
[3] Ke. Tanaka, Encyclopedia of Nanoscience and Nanotechnology, **7** (2004) 629.
[4] K. Hayashi, UVSOR Activity Report **34** (2007) 79.
[5] Ka. Tanaka, Researches of the Electrical Laboratory, **779** (1977) 35.

Ⅲ-6. APPLIED MATERIALS

Highly Ordered Multilayer Films of Fragile Bio-Molecules - The Band Dispersion in Adenosine and Guanosine Assemblies

R. Friedlein[1], S. Z. N. Demon[1], H. Yamane[2] and N. Kosugi[2]

[1]*School of Materials Science, Japan Advanced Institute of Science and Technology, Nomi, Ishikawa 923-1292, Japan*

[2]*Dept. of Photo-Molecular Science, Institute for Molecular Science, Okazaki 444-8585, Japan*

Guanosine and adenosine are purine nucleosides that are composed of guanine or adenine units, respectively, attached to a ribose sugar. Their molecular structure is depicted in Figure 1 a and b, respectively. As the basic units of RNA and DNA, as well as in the case of adenosine-triphosphate (ATP) as the primary energy source for most bio-molecular processes, they are in the center of life itself.

Since these fragile bio-molecules decompose at elevated temperatures, however, it has been intrinsically difficult to investigate the electronic properties of their assemblies using surface science techniques. In the present study, thin multilayer films of adenosine, guanosine as well as of the Na salt of guanosine triphosphate (Fig. 1c) have been processed at about 100 °C onto graphite (0001) surfaces by spray deposition from solution inside a home-based ultra-high vacuum system. Films were then exposed *in situ* to water vapor before being transferred on air to the experimental set-up at BL 6U.

Photon-energy dependent photoelectron spectra of about an about 2-4 nm thick adenosine film were obtained at normal emission with photon energies in between 43 and 130 eV. As shown in Fig. 1d), a pronounced feature related to the highest occupied molecular orbital (HOMO), centered at a binding energy of about 2.8 eV, is composed of at least two bands, denoted "A" and "B". While the dispersion of the one at lower energy, "A", can be traced over several periods, "B" appears to be non-dispersing. As shown recently for guanine and adenine thin films [1, 2], the presence of dispersing π electronic states indicates the formation of homeotropically aligned, highly-ordered columnar assemblies. A more precise evaluation of the band dispersion of "A" with a one-dimensional tight-binding fit reveals the band width of 384 ± 20 meV and the length of the repeat unit of 6.78 ± 0.03 Å which is consistent with two inequivalent molecules per unit cell and the size of the overlap integral of 96 ± 5 meV. Note that the stacking is distinguishably different from that in adenine assemblies with its four molecules per unit cell [2] and also from DNA and RNA spiral configurations.

Guanosine triphosphate within films of its Na salt and guanosine have been found to form thin films which are structurally and electronically similar to those of adenosine. Our results show that the presence of water molecules within the crystal does not prevent the formation of extended electronic states as required for a band-like charge transport along quasi-one-dimensional assemblies.

Fig. 1. Photon-energy dependent photoelectron valence band spectra of the hydrated adenosine multilayer films. "A" and "B" denote features related to HOMO-derived electronic states.
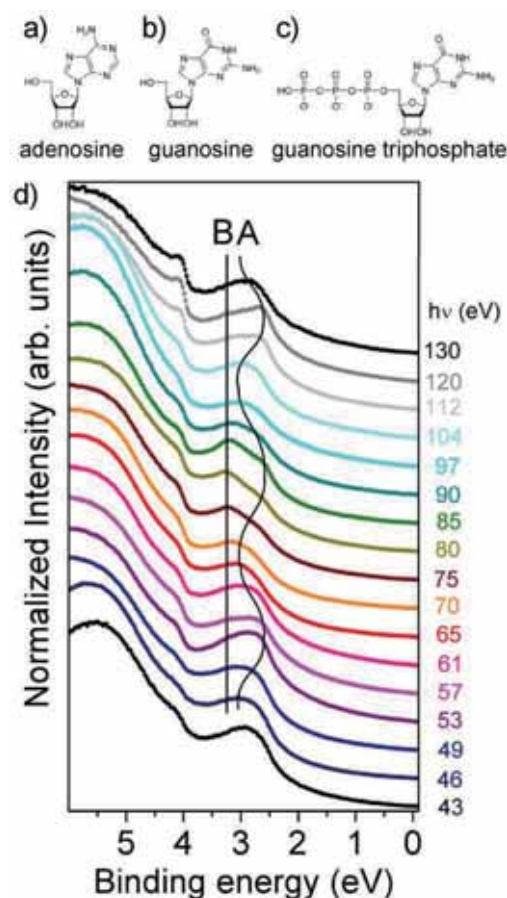
[1] R. Friedlein, Y. Wang, A. Fleurence, F. Bussolotti, Y. Ogata and Y. Yamada-Takamura, J. Am. Chem. Soc. **132** (2010) 12808.
[2] Y. Wang, A. Fleurence, Y. Yamada-Takamura and R. Friedlein, Chem. Commun. **47** (2011) 12349.

Far-Infrared Reflective Study of Alkali Niobate Ceramics

T. Nishi, K. Tsuchida, K. Kato, N. Kato, M. Watanabe and K. Kakimoto

Graduate School of Engineering, Nagoya Institute of Technology, Nagoya 466-8555, Japan

Alkali niobate ceramics are one of the promising candidates for lead-free piezoelectric materials. Especially, Li-doped $(Na,K)NbO_3$ (LNKN) solid solution shows excellent piezoelectric properties. Although it has been expected that the distortion of lattice structure due to the small ionic diameter of substited-Li ion would contribute to the good ferroelectric properties, the particular reason for this is still unclear. In our previous work, we evaluated the local lattice structure of alkali niobate ceramics using FT-IR analysis. The present work reports the spectroscopic characterization of LNKN ceramics using infrared (IR) technique.

The $Li_x(Na_{0.5}K_{0.5})_{1-x}NbO_3$ ceramic samples were produced by a solid-state reaction method. The surfaces of the LNKN ceramics were polished for IR reflectivity measurement. The reflectivity spectra were recorded in the range of $20 – 8000$ cm^{-1} at room temperature using a synchrotron radiation source. The spectra were corrected by using a Michelson interferometer (Bruker, IFS66v). The IR reflectivity spectra were fitted by :

$$\varepsilon\,(\omega) = \varepsilon\,_\infty + \sum_n \omega^2_{pn} / \omega^2_{on} - \omega^2 - n\gamma_n\omega \qquad (1)$$

where, ε_∞ is the high-frequency dielectric constant, ω_p and ω_o are the plasma and longitudinal frequencies, and γ is the damping constant. The complex dielectric function is related to the reflectivity spectrum by the equation,

$$R = |\sqrt{\varepsilon\,(\omega)} – 1 / \sqrt{\varepsilon\,(\omega)} + 1|^2 \qquad (2)$$

Figure 1 shows the reflectivity spectra of LNKN ceramics ($x = 2$ mol %) at room temperature. Figure 2 shows the complex permittivity (imaginary part) calculated from the fitting results (using eq. (1) and (2)). A weak phonon peak was observed around 100 cm^{-1}. This peak cannot be assigned with the only orthorhombic *Bmm*2 which represents NKN crystal structure ($x = 0$ mol %). Therefore, it can be found that Li substitution led to another phase in the NKN crystal structure. From XRD analysis, it has been obtained that LNKN ceramics possess the distorted monoclinic *Pm* phase. Therefore, this peak could be assigned with the mixed phase structure including monoclinic *Pm* phase. Figure 3 shows the phonon analysis results of LNKN ceramics by using FT-IR data. The phonon intensity around 100 cm^{-1} are increased with Li concentration. This result suggests that the proportion of *Pm* phase in LNKN ceramics increases with increasing the amount of Li content.
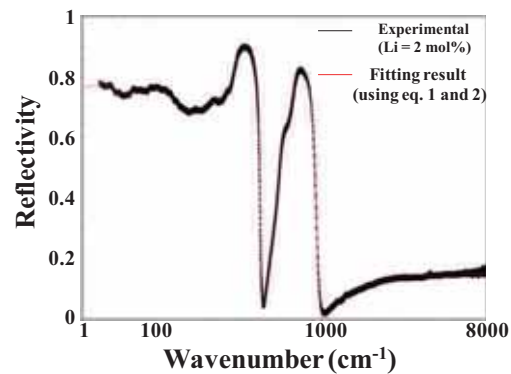
Fig. 1. Infrared reflectance spectra of $Li_{0.02}(Na_{0.5}K_{0.5})_{0.98}NbO_3$ ceramics at R.T. and red line represented fitting result using equations (1) and (2).
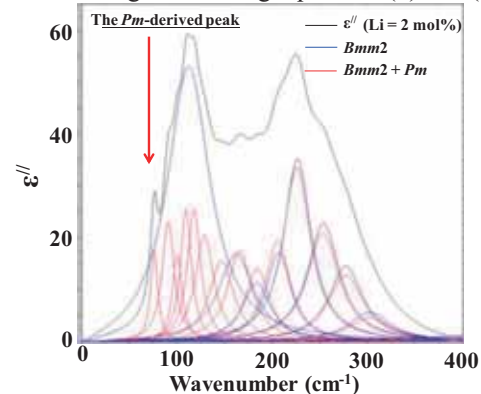
Fig. 2. Variation of imaginary part of permittivity with wavenumber for $Li_{0.02}(Na_{0.5}K_{0.5})_{0.98}NbO_3$ ceramic.
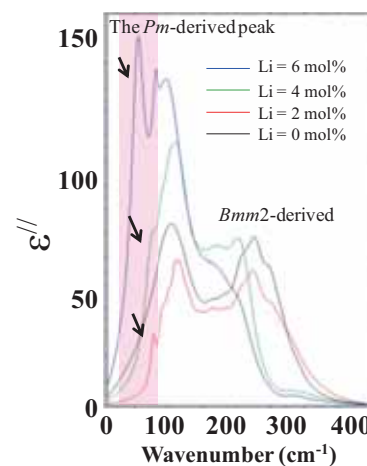
Fig. 3. Dependence of the imaginary part of permittivity on Li content in LNKN ceramics.

In the LNKN phonon spectra, more phonon modes are observed due to the existence of Li in the lattice. It is concluded that Li substation distorted the unit cell of the NKN ceramics and introduced the monoclinic *Pm* phase.

VUV Reflection Spectroscopy of Mg-Ni Alloy Thin Films

S. Sato, R. Matsushima, K. Hirasawa, M. Anzai and H. Matsumoto

School of Science & Technology, Meiji University, Kawasaki 214-8571, Japan

Magnesium nickel (Mg–Ni) alloy are well-known metallic alloys for hydrogen storage, and they exhibit switching mirror behavior from metal to transparent films. This behavior is due to the fact that the hydrides of the Mg–Ni alloys are transparent. The alternant hydrogenation and dehydrogenation reactions depend on their switching behavior. Therefore, the optical properties of these alloys are significantly changed by hydrogenation. However, there have been no reports about the optical properties of these Mg–Ni alloy materials in the vacuum ultraviolet (VUV) region. The transparent hydride forms of the Mg–Ni alloy films exhibit a large energy gap and fundamental absorption in the VUV region. VUV reflection spectroscopy is the one of the most important analysis methods for verifying the fundamental absorption properties of such transparent films [1, 2]. On the basis of VUV reflection spectroscopy, the refraction spectra of the hydride and dehydride forms of Mg–Ni alloy thin films prepared by the radio-frequency (RF) magnetron sputtering method were systematically investigated.

A switching Mg–Ni alloy film was prepared by the RF magnetron sputtering method according to Reference [3]. Metallic Mg (99.9%) and Ni plates (99.9%) were used as targets. The incident RF power was 100 W for Ni and 30–50 W for Mg. The sputtering was performed under an argon gas atmosphere at a total gas pressure of 0.8 Pa, and the argon flow was fixed at 20 sccm. The films were sputtered onto silica substrates at 100°C. The film thicknesses were approximately 100 nm. In addition, a 5-nm-thick palladium layer was deposited onto the films at room temperature. These films were maintained under a hydrogen (H_2) atmosphere for 24 h to prepare the hydride forms of the films.

Reflection spectra of the films were measured in the vacuum ultraviolet region up to 40 eV with a 3 m normal incidence monochromator (gratings: G1, G2, and G3) using the BL7B beamline at UVSOR-III. A silicon photodiode sensor was used as the detector for the reflected light.

Figure 1 shows the refraction spectra of Mg, Ni, and Mg-Ni alloy thin films before and after they were exposed to H_2. A change in the refraction spectra before and after H_2 exposure was observed only in the case of the Mg–Ni alloy thin film. The change in the spectra was more pronounced in the case of the Mg–Ni alloy thin film deposited with a Mg RF power of 40 W. As evident in the Fig. 1, no spectral changes were observed in the Mg and Ni films before and after the films were exposed to H_2. However, some strong peaks were observed in the region beyond 10 eV in the spectrum of the Mg–Ni alloy thin film after it was exposed to H_2. The positions of these peaks were 11, 14, 21, and 32 eV. The hydrogenation reaction of the Mg and Mg–Ni alloys is represented as follows [3]:

$$Mg_2Ni + 2H_2 \rightarrow Mg_2NiH_4$$
$$Mg + H_2 \rightarrow MgH_2$$
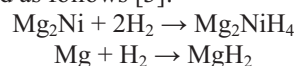
The peaks beyond 10 eV were assigned Mg_2NiH_4, which is the hydride form of the Mg–Ni alloy, because no changes were observed in the spectra of the Mg film. The transparent hydride of the Mg–Ni alloy film exhibited a large energy gap and fundamental absorption in the VUV region.
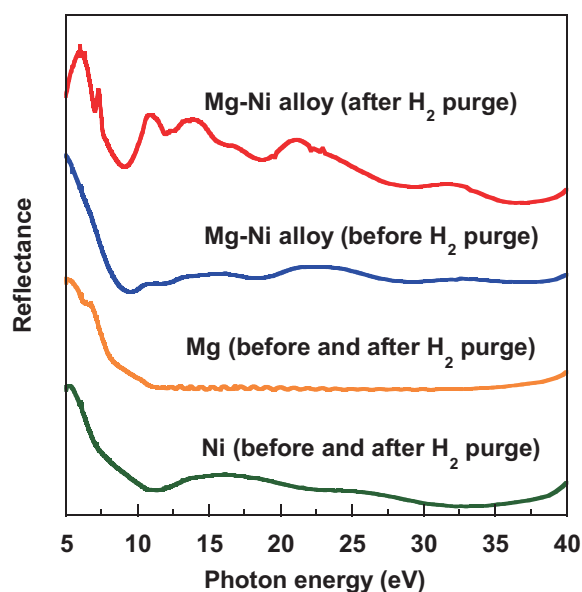
Fig. 1. Reflection spectra of Mg, Ni, and Mg-Ni alloy thin films before and after H_2 purge.

[1] K. Nakagawa *et al*., UVSOR Activity Report **32** (2005) 88.
[2] Y. Iwai *et al*., UVSOR Activity Report **35** (2008) 96.
[3] K. Yoshimura, J. Surf. Finish. Soc. Jpn **56** (2005) 882.

Photoluminescence upon Vacuum Ultraviolet Excitation in Gd^{3+} Ion Doped Inorganic Materials

Y. Inaguma, R. Horiguchi, S. Sasaki and D. Mori

Department of Chemistry, Faculty of Science, Gakushuin University, Tokyo 171-8588, Japan

Recently phosphor materials emitting UV light upon vacuum ultra violet (VUV) excitation are desired as the substitutes of mercury lamp due to the toxicity of mercury. Among them, Gd^{3+} ion doped compounds are expected to be candidates of the UV phosphors since the f-f transition from ^6P_J to $^8S_{7/2}$ in $Gd^{3+}$ corresponds to UV region [1-4]. The UV emission would be observed when the band gap energy of the host material is in the VUV region. In this study we then chose alkaline-earth phosphates with the band gap energy in the VUV region. Herein, we synthesized $A_3(PO_4)_2$:Gd^{3+}(A = Ca, Sr, Ba) and investigated the luminescence properties upon VUV excitation.

The polycrystalline samples of $A_3(PO_4)_2$:Gd^{3+}(A = Ca, Sr, Ba) were synthesized by a conventional solid state reaction at elevated temperature. The mixture of starting materials: alkaline-earth carbonate such as $A CO_3$ (A = Ca, Sr, Ba), $(NH_4)H_2PO_4$ and Gd_2O_3 or Gd nitrate solution were calcined at 1000°C in air. The calcined powder was pressed into pellets and sintered at 1000-1200°C in air. The phase identification for the samples was carried out by the powder X-ray diffraction (XRD) using a Rigaku RINT 2100 diffractometer with a Bragg Brentano geometry (graphite-monochromatized CuKα radiation). The emission and excitation spectra were recorded by a JASCO FP-6500 fluorometer upon the photo excitation using a Xe excimer lamp (λ = 172 nm) or in the beamline BL7B at the UVSOR facility.

The obtained samples were crystallized to be the hexagonal β-type form of tricalcium phosphates for A = Ca, and hexagonal form with a space group $R\overline{3}m$ for A = Sr and Ba. Figure 1 shows the emission spectra upon photo excitation of 172 nm for $A_3(PO_4)_2$: Gd^{3+} 5% (A = Ca, Sr, Ba) at room temperature. As seen in Fig.1, the UV emission peaks at 307 nm, 310 nm were observed for all compounds, which correspond to the f-f transitions, from $^6P_{5/2}$ to $^8S_{7/2}$, from $^6P_{7/2}$ to $^8S_{7/2}$ states of Gd^{3+}, respectively, and $Sr_3(PO_4)_2$: Gd^{3+} exhibited the highest emission intensity. Figure 2 shows the excitation spectrum emission-monitored at 310 nm for $Sr_3(PO_4)_2$: Gd^{3+} 1% at room temperature. Here, the excitation spectrum was corrected for the spectral distribution of excitation light source. In the excitation spectrum, the peaks around 142, 275, and 155 nm correspond to the f-f transitions from the ground state of $^8S_{7/2}$ to $^2Q_{23/2}$ state, $^8S_{7/2}$ to $^2Q_{23/2}$ of Gd^{3+}, and the host absorption band, i.e. the intra charge transfer of PO_4^{3-} [5, 6], respectively. While another peak at 130 nm has not

been assigned at the present time.

Consequently, it was found that $A_3(PO_4)_2$: Gd^{3+} (A = Ca, Sr, Ba) exhibits UV emission corresponding to the f-f transition and they are candidates of UV phosphors upon VUV excitation.
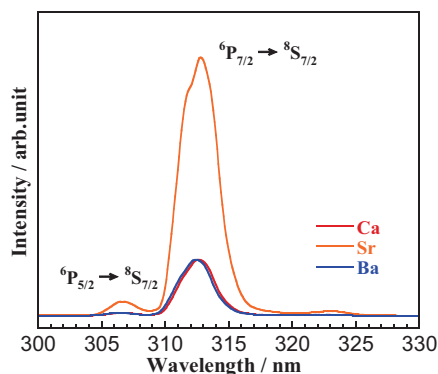
Fig. 1. Emission spectrum upon excitation of 172 nm for $A_3(PO_4)_2$:Gd^{3+}5% (A = Ca, Sr, Ba).
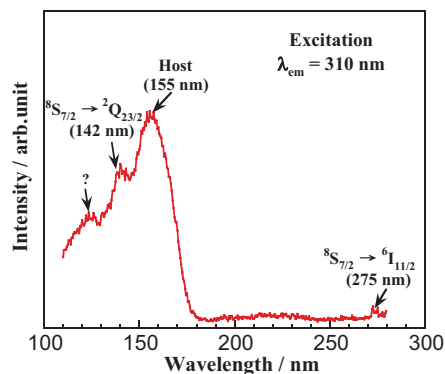
Fig. 2. Excitation spectrum monitored at 310 nm for $Sr_3(PO_4)_2$: Gd^{3+} 1%.

[1] H. Yoshida, R. Yoshimatsu, S. Watanabe and K. Ogasawara, Jpn. J. Appl. Phys. Part .1 **45** (2006) 146.
[2] N. Yokosawa, G. Sato and E. Nakazawa, J. Electrochem. Soc. **150** (2003) H197.
[3] T. Hirai, H. Yshida, S. Sakuragi and N. Ohno, Jpn. J. Appl. Phys. Part .1 **46** (2007) 146.
[4] S. Okamoto, R. Uchino, K. Kobayashi and H. Yamamoto, J. Appl. Phys.,**106** (2009) 013522.
[5] E. Nakazawa and F. Shiga, J. Lumin. **15** (1977) 255.
[6] H. Liang, Y. Tao, J. Xu, H. He, H. Wu, W. Chen, S. Wang and S. Su, J. Solid State Chem. **177** (2004) 901.

Ⅲ-6. APPLIED MATERIALS

Ascription of the Luminescent Components of Cs_2ZnCl_4 Single Crystal

N. Yahaba[1], M. Koshimizu[1], T. Yanagida[2], Y. Fujimoto[3], R. Haruki[4], F. Nishikido[5],
S. Kishimoto[6] and K. Asai[1]

[1]*Department of Applied Chemistry, Graduate School of Engineering, Tohoku University, Sendai 980-8579, Japan*
[2] *Graduate School of Life Science and Systems Engineering, Kyushu Institute of Technology, Kitakyushu 808-0196, Japan*
[3]*Institute of Materials Research, Tohoku University, Sendai 980-8579, Japan*
[4]*Advanced Science Research Center, Japan Atomic Energy Agency, Tokai-mura 319-1195, Japan*
[5]*Molecular Imaging Center, National Institute for Radiological Sciences, Chiba 263-8555, Japan*
[6]*Institute of Materials Structure Science, High Energy Accelerator Research Ogranization, Tsukuba 305-0801, Japan*

Scintillation materials exhibiting short decay are highly required for detection of high-energy X-ray photons at high counting rate. Recently, we have found that Cs_2ZnCl_4 crystals have excellent scintillation characteristics. In this report, we present the luminescence and scintillation dynamics of Cs_2ZnCl_4.

Figure 1 shows the scintillation time profile excited with 50 keV X-ray. The profile was expressed as a sum of two exponential components. The fast and slow ones have lifetimes of 1.8 and 10 ns, respectively. The relative intensity of each component was different for different crystals. The relative intensity hardly depended on the raw materials. In contrast, the contribution of the slow component increased after annealing the crystal.

Figure 2 shows the luminescence spectra. Under excitation at 88 nm, two luminescence bands were observed at 290 and 380 nm. This result is quite similar to a previous report [1, 2], and these bands are ascribed to the Auger-free luminescence. In the case of excitation at 198 nm, luminescence was observed at 320 nm. In this case, the excitation photon energy was lower than the bandgap energy of Cs_2ZnCl_4, and thus the observed luminescence band was ascribed to defects or impurities.

Figure 3 shows the luminescence time profile under VUV excitation. The lifetime of the decay at 290 and 380 nm was estimated to be 2 ns, which is consistent with the fast component in the scintillation time profile. In contrast, the lifetime of the decay at 320 nm was estimated to be approximately 10 ns. These results indicate that the slow component is ascribed to defects would be eliminated by treating the crystal after growth.

[1] A. Ohnishi, M. Kitaura, T. Otomo and M. Sasaki, J. Phys. Soc. Jpn. **72** (2003) 2400.
[2] A. Ohnishi, M. Kitaura, M.Itoh and M. Sasaki, J. Phys. Soc. Jpn. **81** (2012) 114704.
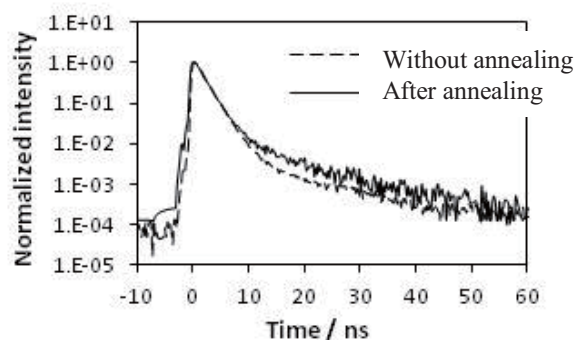
Fig. 1. Scintillation time profiles of Cs2ZnCl4 crystals before and after annealing.
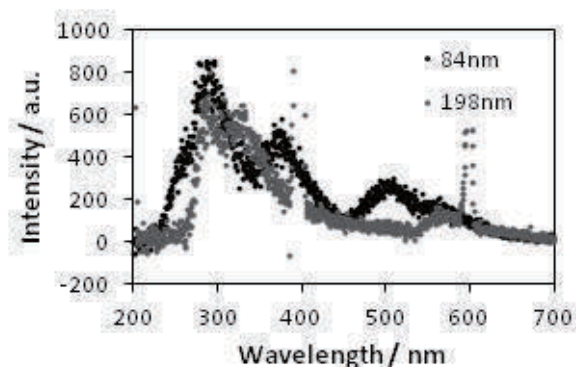
Fig. 2. Luminescence spectra of Cs_2ZnCl_4 under VUV excitation.
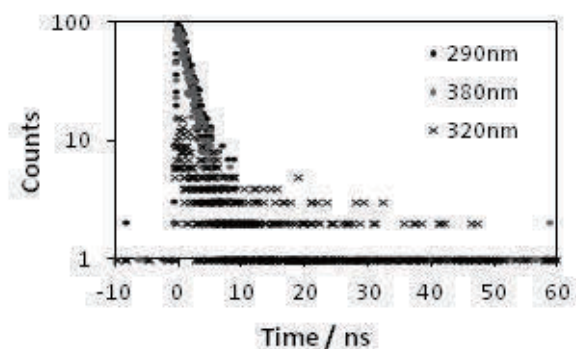
Fig. 3. Luminescence time profile at different wavelength.

Electronic Status of Pr³⁺ in Glass Host by Characterizing Photoluminescence of Pr³⁺ Doped APLF Glass Scintillator

T. Nakazato[1], M. Tsuboi[1], K. Takeda[1], Y. Minami[1], T. Hori[1], T. Shimizu[1],
R. Arita[1], K. Yamanoi[1], R. Nishi[1], Y. Shinzato[1], R. Sogi[1], N. Sarukura[1], H. Azechi[1],
M. Cadatal-Raduban[2], T. Murata[3], S. Fujino[4], H. Yoshida[5], T. Suyama[6], K. Fukuda[6],
A. Yoshikawa[7], N. Sato[8], H. Kan[8] and K. Kamata[8]

[1]*Institute of Laser Engineering, Osaka University, 2-6 Yamadaoka, Suita, Osaka 565-0871,Japan*

[2]*Centre for Theoretical Chemistry and Physics, Institute of Natural and Mathematical Sciences, Massey University, Albany, Auckland, 0632 New Zealand*

[3]*Kumamoto University, 2-39-1 Kurokami, Kumamoto 860-8555, Japan*

[4]*Kyushu University, 6-10-1 Hakozaki, Higashi-ku, Fukuoka 812-8581, Japan*

[5]*Ceramic Research Center of Nagasaki, 605-2 Hasami-cho, Higashisonogi-gun, Nagasaki 859-37, Japan*

[6]*Hamamatsu Photonics K.K., 325-6 Sunayama-cho, Naka-ku, Hamamatsu City, Shizuoka 430-8587, Japan*

[7]*Institute for Materials Research, Tohoku University, 1-1-2 Katahira, Aoba-ku, Sendai, Miyagi 980-8577, Japan*

[8]*Furukawa Co. Ltd., 2-6-1 Marunouchi, Chiyoda-ku, Tokyo 100-8370, Japan*

The realization of nuclear fusion is highly expected to satisfy the energy demand in the future. Fusion plasma diagnostics at higher plasma areal density than 3 g/cm^2 is one of the biggest breakthrough in nuclear fusion research. Scattered-neutron diagnostics [1] utilizing Pr³⁺-doped $20Al(PO_3)_3$-$80LiF$ (APLF+Pr) glass scintillator [2] is expected to achieve plasma areal density measurement in fusion core. APLF+Pr, which have high sensitivity for scattered neutrons and fast response time about 5.4 ns, is the key factor of the measure.

In this work, we report the luminescence properties of APLF+Pr at different Pr³⁺ concentrations (0.5mol%∼3mol%).

We have measured Photoluminescence (PL) spectra and Photoluminescence Excitation (PLE) spectra of APLF+Pr at 30K, 100K, 200K, and 300K. The experiment was conducted at BL7B utilizing G2 grating. PL spectra are measured with excitation wavelength at 180nm, 200nm and 217 nm. The APLF+Pr samples, having Pr³⁺ density at 1mol%, and cut into 10 mm × 10 mm × 2.5 mm, were prepared. PL and PLE spectra of Pr³⁺-doped $LiCaAlF_6$ (Pr:LiCAF) was measured as well for comparison.

The PL spectra of APLF+Pr excited by 180 nm radiation at 27 K, 100 K, 200 K and 300 K are shown in Fig. 1. 2 sharp peaks and 3 broad peaks have been found from 200 nm to 300 nm. The 2 peaks strongly depend on temperature and intensities decrease with increasing temperature. However the 3 broad peaks do not strongly depend on the temperature as compared with the 2 sharp peaks. The broad peaks of 227 nm, 236 nm and 261 nm are ascribe to 4f5d-⁵H_4, 4f5d-⁵H_5, and 4f5d-⁵H_6, ⁵F_2 and ⁵F_3 respectively based on the results of Pr:LiCAF PL spectra. The sharp peaks of 253 nm and 273 nm are also ascribed to ¹S_0-⁵F_4 and ¹S_0-¹G_4 respectively.
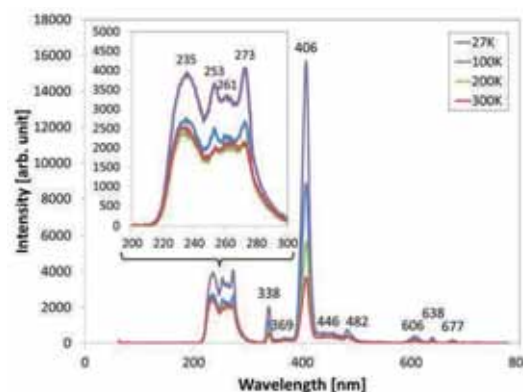
Fig. 1. PL spectra of APLF at various temperature.

[1] M. Moran *et al.*, Rev. Sci. Instrum. **75** (2004) 3592.

[2] T. Murata *et al.*, IEEE Trans. Nucl. Sci., **57** (2010) 1426.

Ⅲ-6. APPLIED MATERIALS

Photoelectric Emission from Ag/zinc-phthalocyanine Surface Under Near-UV Light Irradiation

S. Tanaka, K. Fukuzawa, T. Otani and I. Hiromitsu

Interdisciplinary Graduate School of Science and Engineering, Shimane University,
1060 Nishikawatsu, Matsue, Shimane 690-8504, Japan

The organic semiconductors have gained significant importance in the optoelectronic devices in the last decade. The electronic structure of the organic semiconductor has attracted interest from the view point of not only the basic science but also the practical application. For example, the electronic structure of the organic semiconductor/metal interface has an important role on the device performance of the organic solar cells [1]. Recently, we have studied the light irradiation effects on the electronic structure of the organic/metal and organic/organic interfaces to investigate the electronic structure under the working condition of the solar cells [2]. During the research, we found an anomalous photoelectric emission from the organic thin films with a surface treatment by metal deposition.

Figure 1 shows the photoelectric emission from the zinc phthalocyanine (ZnPc) film with Ag deposition under the 360 nm (= 3.44eV) laser irradiation. The nominal thickness of the ZnPc and Ag layer were 10 nm and 0.05 nm, respectively. The work function of Ag (~4.5 eV) and the ionization potential of ZnPc (~5.0 eV) are larger than the energy of the laser light. Thus, the present photoelectric emission could be an anomalous phenomenon at a particular condition of the organic/metal interface. The threshold of light energy for the photoelectron emission was approximately 3.3 eV.

To investigate the effect of the Ag deposition on the electronic structure of the sample surface, photoelectron spectroscopy was performed. The ZnPc layer was deposited on the indium tin-oxide (ITO) substrate by vacuum deposition at the preparation chamber. Ag was also deposited on the ZnPc layer by vacuum deposition. The thickness of the each material was monitored by quartz microbalance. The sample was transferred to the measurement chamber without breaking the vacuum. All the photoelectron measurements were carried out at room temperature. Figure 2 shows the variation of the photoelectron spectra of Ag deposited on the ZnPc substrate with increasing thickness. The highest occupied molecular orbital of ZnPc was shifted approximately 0.5 eV toward lower kinetic energies by the deposition of 0.5 nm of Ag. The secondary electron cutoff was also showed a corresponding shift. These results infer that the potential barrier for the photoelectric emission at the sample surface was decreased by the Ag deposition. However, the estimated value of the work function of the sample surface is much larger than the

3.3 eV. The shift of vacuum level is frequently observed at the organic/metal interface [3], although no anomalous photoelectric emission has been reported. The surface structure of the Ag/ZnPc sample was observed by atomic force microscope (AFM). The AFM images showed that Ag was deposited on the ZnPc surface with grain sizes of few nano meters. The structure of the Ag particles could be related to the reduction of the surface barrier potential. The fact that the anomalous photoelectric emission was suppressed at the thicker Ag region (Fig. 2. inset) could support this hypothesis.
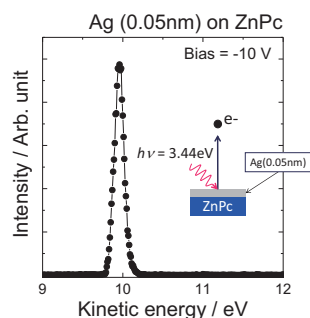
Fig. 1. Photoelectric emission from the Ag (0.05nm) /ZnPc (10nm) /ITO emitted by near-UV light irradiation ($h\nu$ = 3.44 eV). The sample was biased by −10 V to measure the electron with small kinetic energies.
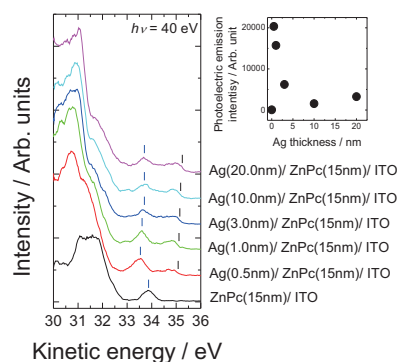
Fig. 2. Photoelectron spectra of ZnPc and Ag/ZnPc sample near the Fermi level. Inset: The Ag thickness dependence of the photoelectric emission intensity.

[1] S. Tanaka *et al*., Appl. Phys. Lett. **97** (2010) 253306.
[2] S. Tanaka *et al*., UVSOR Activity Report **39** (2012) 130.
[3] H. Ishii *et al*., Adv. Mater., **11** (1999) 605.

Does Polarity of the Giant Surface Potential Impacts Charge Transfer at Organic-Organic Interfaces?

H. S. Lim[1], Y. Ozawa[1], Y. Uragami[1], Y. Nakayama[2], Y. Noguchi[1,2] and H. Ishii[1,2]

[1]Graduate School of Advanced Integration Science, Chiba 263-8522, Japan
[2]Center for Frontier Science, Chiba University, Chiba 263-8522, Japan

Ito *et al.* reported spontaneous building up of the surface electric potential (giant surface potential; GSP) in vacuum deposited films of tris(8-hydroxyquinolinato) aluminum(III) (Alq$_3$) [1]. The origin of GSP can be attributed to a slight alignment of dipole moment of the molecules in average. The polarity of GSP in the case of Alq$_3$ is positive in increasing the film thickness.

We have reported how the existence/absence of GSP in an overlayer impacts the electronic nature at organic hetero-interfaces [2]. These works, however, are conducted on overlayers of non-GSP or positive GSP materials. In this context, an Alq$_3$-derivative tris(7-propyl-8-hydroxyquinolinato) aluminum(III) (Al(7-prq)$_3$) is an interesting material because this reveals a negative GSP [3].

In this experiment, we investigated the influence of different GSP direction at organic interfaces of a N,N'-bis(1-naphthyl)-N,N'-diphenyl-1,10-biphenyl-4,40-diamin (α-NPD) film capped with the Alq$_3$ or Al(7-prq)$_3$ overlayer.

Ito is used as substrate and is cleaned by ultrasonication in neutral detergent, isopropanol and acetone. 5nm-thick α-NPD layers were then deposited onto the ITO substrate. Alq$_3$ or Al(7-prq)$_3$ was subsequently deposited onto α-NPD from 0.1nm to 10.0nm in a step-by-step manner. Ultraviolet photoelectron spectroscopy (UPS) was performed at BL8B at UVSOR. 40 eV of photon energy was used. -5 V bias was applied during secondary electron cutoff (SECO) measurement. The experiment is carried out at room temperature.

At the α-NPD/Alq$_3$ interface, the highest occupied molecular orbital (HOMO) peak of α-NPD (as well as the SECO position) moved with growing the thickness of Alq$_3$ by 0.1 eV to low kinetic energy side. This implies that deposition of Alq$_3$ induces downward band-bending in the α-NPD layers, namely charge transfer from α-NPD to Alq$_3$. As growing the Alq$_3$ overlayer further thicker, the SECO position shifted down proportionally to the Alq$_3$ thickness representing GSP.

α-NPD HOMO peak moved to low kinetic energy side also at the α-NPD/Al(7-prq)$_3$ interface, yet the shifting value (~0.06 eV) was a little less than the case of the unsubstitued Alq$_3$. While SECO did not exhibit apparent shift in the thin coverage region, it moved to the high kinetic energy side in increasing the Al(7-prq)$_3$ thickness, which can be attributed to GSP of the opposite polarity to the Alq$_3$ layers.

The present results implies occurrence of charge transfer from α-NPD to the overlayers irrespective of the polarity of GSP, which is contradicting to our previous proposition [2]. In order to figure out the electronic phenomena at the topical organic-organic interface, further systematic studies by altering the overlayer characteristics are highly anticipated.
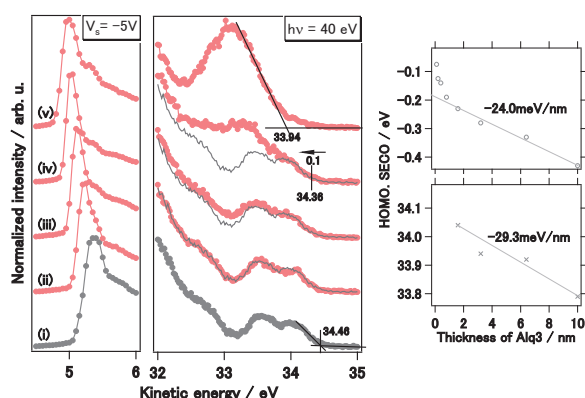
Fig. 1. UPS spectra of the Alq$_3$ [(i) : 0nm, (ii) : 0.1nm, (iii) : 0.4nm, (iv) : 1.6nm, (v) : 6.4nm] on α-NPD (5nm) interfaces. The gray line shows the spectra contribution of α-NPD, which is derived from a procedure described in Ref. [2].
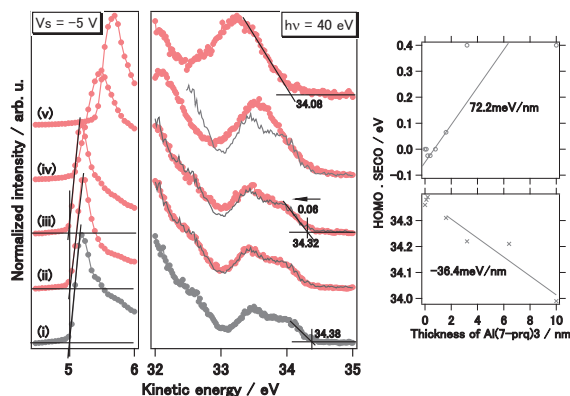
Fig. 2. UPS spectra of the Al(7-prq)$_3$ [(i) : 0nm, (ii) : 0.1nm, (iii) : 0.4nm, (iv) : 1.6nm, (v) : 10.0nm] on α-NPD (5nm) interfaces.

[1] E. Ito *et al.*, J. Appl. Phys. **92** (2002) 7306.
[2] Y. Nakayama *et al.*, Organic Electrons **13** (2012) 2850.
[3] T. Isoshima *et al.*, *submitted.*

List of Publications

M. Adachi, H. Zen, T. Konomi, J. Yamazaki, K. Hayashi and M. Katoh, "**Design and Construction of UVSOR-III**", J. Phys.: Conf. Ser. **425** (2013) 042013.

C. Evain, C. Szwaj, S. Bielawski, M. E. Couprie, M. Hosaka, A. Mochihashi and M. Katoh, "**Suppression of Self-Pulsing Instabilities in Free-Electron Lasers Using Delayed Optical Feedback**", Phys. Rev. ST Accel. Beams **15** (2012) 040701.

F. Chen, Q. Ge, M. Xu, Y. Zhang, X. Shen, W. Ji, M. Matsunami, S. Kimura, J. Hu and D. Feng, "**The Orbital Characters of Low-energy Electronic Structure in Iron-Chalcogenide Superconductor $K_xFe_{2-y}Se_2$**", Chin. Sci. Bull. **57** (2012) 3829.

J. W. Chiou, S. C. Ray, S. I. Peng, C. H. Chuang, B. Y. Wang, H. M. Tsai, C. W. Pao, H.-J. Ln, Y. C. Shao, Y. F. Wang, S. C. Chen, W. F. Pong, Y. C. Yeh, C. W. Chen, L.-C. Chen, K.-H. Chen, M.-H. Tsai, A. Kumar, A. Ganguly, P. Papakonstantinou, H. Yamane, N. Kosugi, T. Reigier, L. Liu and T. K. Sham, "**Nitrogen-Functionalized Graphene Nanoflakes (GNFs:N): Tunable Photoluminescence and Electronic Structures**", J. Phys. Chem. C **116** (2012) 16251.

V. Guritanu, S. Seiro, J. Sichelschmidt, N. Caroca-Canales, T. Iizuka, S. Kimura, C. Geibel and F. Steglich, "**Optical Study of Archetypical Valence-Fluctuating Eu-Systems**", Phys. Rev. Lett. **109** (2012) 247207.

V. Guritanu, P. Wissgott, T. Weig, H. Winkler, J. Sichelschmidt, M. Scheffler, A. Prokofiev, S. Kimura, T. Iizuka, A. M. Strydom, M. Dressel, F. Steglich, K. Held and S. Paschen, "**Anisotropic Optical Conductivity of the Putative Kondo Insulator $CeRu_4Sn_6$**", Phys. Rev. B **87** (2013) 115129.

T. Hirahara, N. Fukui, T. Shirasawa, M. Yamada, M. Aitani, H. Miyazaki, M. Matsunami, S. Kimura, T. Takahashi, S. Hasegawa and K. Kobayashi, "**Atomic and Electronic Structure of Ultrathin Bi(111) Films Grown on Bi_2Te_3(111) Substrates: Evidence for a Strain-Induced Topological Phase Transition**", Phys. Rev. Lett. **109** (2012) 247401.

M. Hosaka, N. Yamamoto, Y. Takashima, C. Szwaj, M. Le Parquire, C. Evain, S. Bielawski, M. Adachi, T. Tanikawa, S. Kimura, M. Katoh, M. Shimada and T. Takahashi, "**Saturation of the Laser-induced Narrowband Coherent Synchrotron Radiation Process: Experimental Observation at a Storage Ring**", Phys. Rev. ST Accel. Beams **16** (2013) 020701.

H. Iwayama, M. Nagasono, J. R. Harries and E. Shigemasa, "**Demonstration of Up-Conversion Fluorescence from Ar Clusters in Intense Free-Electron-Laser Field**", Opt. Express **20** (2012) 23174.

H. Iwayama, N. Sisourat, P. Lablanquie, F. Penent, J. Palaudoux, L. Andric, J. H. D. Eland, K. Bučar, M. Žitnik, Y. Velkov, Y. Hikosaka, M. Nakano and E. Shigemasa, "**A Local Chemical Environment Effect in Site-Specific Auger Spectra of Ethyl Trifluoroacetate**", J. Chem. Phys. **138** (2013) 024306.

H. Kanamori, T. Yoshioka, K. Hirose and T. Yamamoto, "**Determination of Valence State of Mn Ions in $Pr_{1-x}A_xMnO_{3-\delta}$ (A = Ca, Sr) by $Mn-L_3$ X-ray Absorption Near-Edge Structure Analysis**", J. Electron Spectrosc. Relat. Phenom. **185** (2012) 129.

T. Kawai, Y. Kishimoto and K. Kifune, "**Photoluminescence Studies of Nitrogen-doped TiO_2 Powders Prepared by Annealing with Urea**", Philos. Mag. **92** (2012) 4088.

S. Kimura, T. Iizuka, Y. Muro, J. Kajino and T. Takabatake, "**Anisotropic Gap Formation in CeM_2Al_{10} (M = Ru, Os)**", J. Phys.: Conf. Ser. **391** 012030.

S. Kimura, E. Nakamura, K. Imura, M. Hosaka, T. Takahashi and M. Katoh, "**Design of a Dedicated Beamline for THz Coherent Synchrotron Radiation at UVSOR-III**", J. Phys. Conf. Ser. **359** (2012) 012009.

S. Kimura and H. Okamura, "**Infrared and Terahertz Spectroscopy of Strongly Correlated Electron Systems under Extreme Conditions**", J. Phys. Soc. Jpn. **82** (2013) 021004.

Y. S. Kwon, J. B. Hong, Y. R. Jang, H. J. Oh, Y. Y. Song, B. H. Min, T. Iizuka, S. Kimura, A. V. Balatsky and Y. Bang, "**Evidence of a Pseudogap for Superconducting Iron-Pnictide $Ba_{0.6+\delta}K_{0.4-\delta}Fe_2As_2$ Single Crystals from Optical Conductivity Measurements**", New J. Phys. **14** (2012) 063009.

T. Maruyama, S. Sakakibara, S. Naritsuka, W. Norimatsu, M. Kusunoki, H. Yamane and N. Kosugi, "**Band Alignment of a Carbon Nanotube/N-Type 6H-SiC Heterojunction Formed by Surface Decomposition of SiC Using Photoelectron**

Spectroscopy", Appl. Phys. Lett. **101** (2012) 092106.

H. Masai, T. Yanagida, Y. Fujimoto, M. Koshimizu and T. Yoko, "**Scintillation Property of Rare Earth-Free SnO-doped Oxide Glass**", Appl. Phys. Lett. **101** (2012) 191906.

K. Mitsuke, H. Katayanagi, B. Kafle and Md S. Prodhan, "**Design of Velocity Map Imaging Spectrometer Equipped with a Mass Gate Discriminating Particular Photofragments**", ISRN Phys. Chem. **2012** (2012) 959074.

T. Miyazaki, R. Sumii, H. Umemoto, H. Okimoto, T. Sugai, H. Shinohara and S. Hino, "**Ultraviolet Photoelectron Spectra of Lu Atoms Encapsulated C_{2v}-C_{82} Fullerenes**", Chem. Phys. Lett. **555** (2013) 222.

M. Nagasaka, N. Kosugi and E. Rühl, "**Structures of Small Mixed Krypton-Xenon Clusters**", J. Chem. Phys. **136** (2012) 234312.

M. Nagasaka, E. Serdaroglu, R. Flesch, E. Rühl and N. Kosugi, "**Structures of Mixed Argon-Nitrogen Clusters**", J. Chem. Phys. **137** (2012) 214305.

T. Nakagawa, Y. Takagi, T. Yokoyama, T. Methfessel, S. Diehl and H. J. Elmers, "**Giant Magnetic Anisotropy Energy and Coercivity in Fe Island and Atomic Wire on W(110)**", Phys. Rev. B **86** (2012) 144418.

Y. Nakayama, S. Machida, Y. Miyazaki, T. Nishi Y. Noguchi and H. Ishii, "**Electronic Structures at Organic Heterojunctions of N,N' -bis(1-naphthyl)-N,N'-diphenyl-1,1' -biphenyl-4,4'-diamin (NPB)-based Organic Light Emitting Diodes**", Org. Electron. **13** (2012) 2850.

A. Ohnishi, M. Saito, M. Kitaura, M. Itoh and M. Sasaki, "**Auger-free Luminescence due to Interatomic p-d Transition and Self-Trapped Exciton Luminescence in Rb_2ZnCl_4 Crystals**", J. Lumi. **132** (2012) 2639.

A. Ohnishi, M. Saito, M. Kitaura, M. Itoh and M. Sasaki, "**Electronic Structure and Auger-Free Luminescence in Cs_2ZnCl_4 Crystals**", J. Phys. Soc. Jpn. **81** (2012) 114704.

T. Okumura, M. Shikano and H. Kobayashi, "**Contribution of Oxygen Partial Density of State on Lithium Intercalation/de-intercalation Process in $Li_xNi_{0.5}Mn_{1.5}O_4$ Spinel Oxides**", J. Power Sources (2013) DOI:10.1016/j.jpowsour.2013.01.189

O. M. Ozkendir, E. Cengiz, E. Tırasoglu, M. Kaya, I. H. Karahan and N. Orhan, "**Traces of Defects in the Electronic Structure of Porous NieTi Alloys**", J.

Mater. Sci. Technol. **29** (2013) 344.

O. M. Ozkendir, "**Chromium Substitution Effect on Magnetic Structure of Iron Oxides**", Chin. Phys. Lett. **29** (2012) 057502.

O. M. Ozkendir, "**Structural and Magnetic Study of $Cu_xFeCr_{1-x}O_2$ Oxides under High External Magnetic Fields**", J. Electron. Mater. **42** (2013) 1055.

J. Park, S. W. Jung, M.-C. Jung, H. Yamane, N. Kosugi and H. W. Yeom, "**Self-Assembled Nanowires with Giant Rashba Split Bands**", Phys. Rev. Lett. **110** (2013) 036801.

J. Sichelschmidt, A. Herzog, H. S. Jeevan, C. Geibel, F. Steglich, T. Iizuka and S. Kimura, "**Far-Infrared Optical Conductivity of $CeCu_2Si_2$**", J. Phys. Condens. Matter. **25** (2013) 065602.

S. B. Singh, L. T. Yang, Y. F. Wang, Y. C. Shao, C. W. Chiang, J. W. Chiou, K. T. Lin, S. C. Chen, B. Y. Wang, C. H. Chuang, D. C. Ling, W. F. Pong, M.-H. Tsai, H. M. Tsai, C. W. Pao, H. W. Shiu, C. H. Chen, H.-J. Lin, J. F. Lee, H. Yamane and N. Kosugi, "**Correlation Between P-Type Conductivity and Electronic Structure of Cr-Deficient $CuCr_{1-x}O_2$ (x = 0-0.1)**", Phys. Rev. B **86** (2012) 241103(R).

P. Thoma, A. Scheuring, S. Wuensch, K. Il'in, A. Semenov, H-W Huebers, V. Judin, A-S. Mueller, N. Smale, M. Adachi, S. Tanaka, S. Kimura, M. Katoh, N. Yamamoto, M. Hosaka, E. Roussel, C. Szwaj, S. Bielawski and M. Siegel, "**High-Speed Y-Ba-Cu-O Direct Detection System for Monitoring Picosecond THz Pulses**", IEEE Trans. Terahertz Sci. Technol. **3** (2013) 81.

M. Yamaga, Y. Oda, H. Uno, K. Hasegawa, H. Ito and S. Mizuno, "**Energy Transfer from Ce to Nd in $Y_3Al_5O_{12}$ Ceramics**", Phys. Status Solidi C **9** (2012) 2300.

M. Yamaga, Y. Oda, H. Uno, K. Hasegawa, H. Ito and S. Mizuno, "**Formation Probability of Cr-Nd Pair and Energy Transfer from Cr to Nd in $Y_3Al_5O_{12}$ Ceramics Codoped with Nd and Cr**", J. Appl. Phys. **112** (2012) 063508.

H. Yamane and N. Kosugi, "**Hybridized Electronic States in Potassium-Doped Picene Probed by Soft X-ray Spectroscopies**", AIP Advances, **2** (2012) 042114.

T. Yoshioka, T. Yamamoto and A. Kitada, "**Co-L_3 X-ray Absorption Near-Edge Structure Analysis of $Pr_{1-x}Ca_xCoO_{3-\delta}$ and $Pr_{1-x}Sr_xCoO_{3-\delta}$**", Physica B **407** (2012) 4114.

STXM Users Meeting

Date: June 4, 2012
Place: Conference Room C, Okazaki Conference Center, Okazaki, Japan

June 4th (Mon)

<Session 1: Reports of UVSOR Facility, Chair: A. Ito>
13:30-13:35 M. Katoh (UVSOR)
     Introduction from director
13:35-13:50 T. Ohigashi
     Current status of BL4U beamline
13:50-14:00 H. Arai (UVSOR)
     Introduction of STXMs of oversea synchrotron radiation facilities
14:00-14:10 M. Adachi (IMS)
     Current status of UVSOR-III
14:10-14:20 N. Kosugi (IMS)
     Collaboration programs of IMS

14:20-14:45 Coffee Break

<Session 2, Chair: T. Ohigashi>
14:45-15:00 A. Ito (Tokai Univ.)
     Soft X-ray spectro-microscopy of biological samples
15:00-15:15 T. Araki (TOYOTA Central R&D Lab.)
     (Untitled)
15:15-15:30 H. Yabuta (Osaka Univ.)
     Innovative researches by STXM; outer space, the earth and life
15:30-15:45 J. Usukura (Nagoya Univ.)
     Spatial structure of actin cytoskeletons revealed by various imaging methods
15:45-16:00 N. Iwata (Ricoh)
     Imaging of organic materials by using STXM
16:00-16:15 Y. Ishii (Nagoya Institute Tech.)
     Development of functional materials based on nano-carbon
16:15-16:30 A. Matsuura (Fujita Health Univ.)
     Early diagnosis of pediatric patients with Wilson disease by synchrotron copper imaging
16:30-16:45 K. Shinohara (Waseda Univ.)
     Observation of living cells by a contact microscope with laser-produced plasma X-rays

16:45-17:00 Coffee Break

<Session 3, Chair: T. Araki>
17:00-17:15 K. Ono (KEK)
     Observation of the magnetic domains of NdFeB magnet
17:15-17:30 Y. Takeichi (KEK)
     Summary of the STXM project at PF
17:30-17:45 N. Inami (KEK)
     Development of the real-time control and the measurement system for the STXM
17:45-18:00 Y. Yamamoto (Nagoya Institute Tech.)
     Action mechanism of anesthetic molecules by interfacial chemical approach
18:00-18:15 T. Tominaga (JSR)
     Structural analysis of JSR polymer materials by using synchrotron radiations
18:15-18:30 H. Kihara (Ritsumeikan Univ.)
     Current status of the full-field imaging microscope at Ritsumeikan Univ. and expectation for new STXM
18:30-18:45 R. Mizutani (Tokai Univ.)
     Three-dimensional structural analysis of brain tissue by microtomography

18:45-19:30   T. Ohigashi (UVSOR)
              Discussions
19:40-21:00   Banquet

UVSOR Workshop on Novel Development for Low-Energy Photoemission Spectroscopy at UVSOR-III

Date: June 21-22, 2012
Place: Seminar room (#201) of main building, Institute for Molecular Science, Okazaki, Japan

June 21th (Thu)

13:00-13:30   Registration

<Session 1, Chair: K. Soda>
13:30-13:40   M. Matsunami (UVSOR)
      Opening remarks
13:40-14:00   M. Adachi (UVSOR)
      Present status of UVSOR-III
14:00-14:25   K. Tsuchiya (KEK-PF)
      Design of variably polarized undulator
14:25-14:45   T. Ito (Nagoya Univ.)
      3D-ARPES for strongly correlated quasi-2D system GdTe$_2$
14:45-15:05   H. Miyazaki (Nagoya Institute Tech.)
      Electronic structure of rare-earth oxide thin films studied by 3D-ARPES
15:05-15:30   T. Hirahara (Univ. Tokyo)
      Spin-polarized surface electronic states of non-magnetic ultrathin films
15:30-15:55   T. Ujihara (Nagoya Univ.)
      Effect of minibands and periodic modulations in semiconductor superlattice structures

15:55-16:25   Coffee break

<Session 2, Chair: M. Matsunami>
16:25-16:50   S. Tanaka (Osaka Univ.)
      Low-energy ARPES of HOPG
16:50-17:15   T. Takeuchi (Nagoya Univ.)
      High-resolution photoemission spectroscopy for thermoelectric-material development
17:15-17:40   K. Ishizaka (Univ. Tokyo)
      Spin-orbit interaction studied by low-energy ARPES
17:40-18:05   R. Yoshida (ISSP)
      Hidden-order transition in URu$_2$Si$_2$ studied by ultrahigh-resolution ARPES
18:05-18:30   K. Shimada (HiSOR)
      Development and perspective for precise analyses of the electronic structure in solids by low-energy synchrotron radiation ARPES

18:30-19:00   Facility tour
19:00-21:00   Banquet

June 22th (Fri)

<Session 3, Chair: S. Kimura>
09:00-09:30   G. Zhang (NSRL)
      Introduction of the ARPES facility and the upgrade program of Hefei Light Source
09:30-09:50   H. J. Im (Hirosaki Univ.)
      Low-energy excitation in A-site ordered perovskite CaCu$_3$Ti$_4$O$_{12}$ studied by hν-dependent ARPES
09:50-10:15   K. Nakayama (Tohoku Univ.)
      High-resolution ARPES study of superconducting gap symmetry in Fe-based superconductors

10:15-10:40   S. Kera (Chiba Univ.)
                   Photoemission spectroscopy for organic semiconductor films: electron-phonon coupling and band gap states

10:40-11:10   Coffee break

<Session 4, Chair: T. Ito>
11:10-11:35   H. Kumigashira (KEK-PF)
                   In-situ synchrotron-radiation photoemission study for surface and interface in strongly correlated oxide heterostructures
11:35-12:00   M. Fujisawa (ISSP)
                   Design of low-photon energy VLS-PGM of BL5U
12:00-12:20   S. Kimura (UVSOR)
                   Discussion
12:20-12:30   **Closing remarks**

UVSOR workshop "Perspectives of the beamline for organic solids at UVSOR"

Date: Sep 25-26, 2012
Place: Seminar room (#304) of UVSOR building, Institute for Molecular Science, Okazaki, Japan

Sep 25th (Tue)

13:30-13:40   **Opening Remarks**

<Session 1, Chair: S. Kera>

13:40-14:05   M. Adachi (UVSOR)
         Present status of UVSOR-III

14:05-14:35   H. Ishii (Chiba Univ.)
         Research of interfacial electronic structures of organic semiconductors by electron spectroscopy

14:35-15:00   Y. Nakayama (Chiba Univ.)
         Valence band structure of organic single crystals challenged by synchrotron radiation photoelectron spectroscopy

15:00-15:25   S. Tanaka (Shimane Univ.)
         Photoelectron spectroscopy of organic thin films under light irradiation

15:25-15:55   Coffee break

<Session 2, Chair: K. K. Okudaira>

15:55-16:20   I. Yamamoto (Saga Univ.)
         Researches on electronic structure of organic thin films at Saga University beamline BL13 in SAGA-LS

16:20-16:50   T. Hosokai (Iwate Univ.)
         A systematic study of correlation between org/metal interface electronic structure and bonding distance by using X-ray standing waves technique and angle resolved photoemission spectroscopy

16:50-17:20   H. Yoshida (Kyoto Univ., PRESTO)
         Depth resolved electronic structure of organic solids with angle resolved X-ray photoemission spectroscopy and multivariate analysis

17:20-17:50   T. Sakurai (Univ. of Tsukuba, PRESTO)
         Investigation of properties at electrode interfaces in organic solar cells using synchrotron-based analytical techniques

17:50-18:30   Break
18:30-   Banquet

Sep 26th (Wed)

<Session 3, Chair: H. Ishii>

9:00-9:30   D. Yoshimura (SAGA Light Source)
         Memories of UVSOR BL8B2 and outline of the soft X-ray beamlines at SAGA-LS

9:30-10:00   K. Mase (Photon Factory)
         Present status and prospects of a high-brilliance VUV/SX beamline BL-13A in PF; expectations for the beamline dedicated for organic solids in UVSOR

10:00-10:30   H. Yamane (UVSOR)
         Present status of high-resolution ARPES system at BL6U for various solids and surfaces

10:30-11:00   T. Ito (Nagoya Univ.)
         VUV Angle-Resolved Photoemission Study of Quasi-One-Dimensional Organic Conductors

11:00-11:25   K. Shimada (HiSOR)
         Studies of surface electronic structures of organic materials at HiSOR

11:25-13:00   Lunch Break

<Session 4, Chair: S. Tanaka>
13:00-13:30   K. Kanai (Tokyo Univ. of Science)
                     Electronic structure of various organic materials probed by synchrotron radiation
13:30-14:00   T. Miyazaki (Ehime Univ.)
                     Photoelectron Spectroscopy of Endohedral Metallofullerenes
14:00-14:25   K. Okudaira (Chiba Univ.)
                     Evaluation of molecular orientation by ARUPS
14:25-14:55   S. Kera (Chiba Univ.)
                     Photoelectron angular distribution from valence band of organic thin films:
                     Reconstruction view of molecular orbitals

14:55-15:20   Discussion: Perspectives at BL2B
15:20-   **Closing Remarks**

UVSOR Symposium 2012

Date: Nov 10-11, 2012
Place: Okazaki Conference Center, Okazaki, Japan

Nov 10th (Sat)

<Session 1, Chair: M. Katoh>
13:00-13:15   M. Katoh (UVSOR)
                    Opening remarks
13:15-13:30   N. Kosugi (IMS)
                    Evaluation of UVSOR and perspective of IMS
13:30-13:50   M. Adachi (UVSOR)
                    Present status of UVSOR-III
13:50-14:20   T. Ohigashi (UVSOR)
                    Perspective for applicative observations by using a scanning transmission X-ray microscopy
14:20-14:40   A. Ito (Tokai Univ.)
                    Biomedical application of soft X-ray scanning microscope

14:40-15:00   Coffee Break

<Session 2, Chair: M. Matsunami>
15:00-15:20   T. Hirahara (Univ. Tokyo)
                    Electronic structure of ultrathin Bi films: influence of the substrate and its implication on topological properties
15:20-15:40   T. Hajiri (Nagoya Univ.)
                    Polarization-dependent angle-resolved photoemission spectroscopy on LiFeAs
15:40-16:00   S. Tanaka (Osaka Univ.)
                    Direct observation of the electron-phonon scattering by using angle-resolved photoelectron spectroscopy
16:00-16:20   S. Kera (Chiba Univ.)
                    Origin of interface state for $\square$-conjugated molecules adsorbed on metal

16:20-16:40   Coffee Break

<Session 3, Chair: E. Shigemasa>
16:40-17:00   Y. Takagi (IMS)
                    The X-ray magnetic circular dichroism measurement at BL4B
17:00-17:20   M. Nagasaka (IMS)
                    Local structures of methanol-water binary liquid studied by soft X-ray absorption spectroscopy
17:20-17:40   H. Iwayama (UVSOR)
                    Dissociation pathways of inner-shell ionized $C_4H_5F_3O_2$ molecules studied by an auger-electron-ion coincidence method

<Poster Session and Banquet, 18:00-21:00>
P01   K. Eguchi (IMS)
        XAS/XMCD measurement of vanadyl pthalocyanine films on Si(111)
P02   T. Tajiri (Hyogo Univ.)
        Development of novel nozzle for molecule spectroscopy by ultrasonic atomization method
P03   K. Soda (Nagoya Univ.)
        Electronic structure of pyrite-type $Ni_{1-x}Cu_xS_2$ (I): CuS_2
P04   Y. Liu (Chiba Univ.)
        Angle-resolved ultraviolet photoelectron spectroscopy investigation of transition-metal phthalocyanines thin films on graphite
P05   M. Sawa (Niigata Univ.)
        Development of a high-resolution magnetic bottle electron spectrometer

Ⅴ. WORKSHOPS

P06   Y. Konosu (Niigata Univ.)
Multi-electron spectroscopy of condensed water molecules

P07   H. Zen (Kyoto Univ.)
Intense and short pulse generation by CHG-FEL utilizing pulse compression

P08   Y. Inaguma (Gakushuin Univ.)
Photoluminescence upon vacuum ultraviolet excitation in $M_3(PO_4)_2$:Pr^{3+} (M = Ca, Sr, and Ba)

P09   Y. Uematsu (Nagoya Univ.)
Performance of new optical klystron at UVSOR and application to CHG

P10   Y. Hida (Nagoya Univ.)
Study of pulsed sextupole magnet system for beam injection at UVSOR

P11   M. Sato (Tohoku Univ.)
Local structure analysis of zeolite synthesized from blast furnace slag

P12   Y. Nakamura (Fukui Univ.)
Development of spectroscopic ellipsometry for UV-VUV region

P13   T. Toyoda (Fukui Univ.)
A Study of visible photoluminescence in boron-doped diamond thin films

P14   D. Itoh (Fukui Univ.)
Band structure of CN_x

P15   K. Fujita (Fukui Univ.)
Ultra-violet photoluminescence spectra from AlGdN by core excitation

P16   K. Hayashi (Gifu Univ.)
Characterization of photoinduced phenomena in amorphous chalcogenide semiconductors

P17   T. Niwa (Nagoya Univ.)
Development of an electron beam bunch length measurement system for the transmission-type polarized electron source

P18   M. Kaneko (Nagoya Univ.)
Angle-resolved photoemission spectroscopy of $Sm_{1-x}Y_xS$

P19   Y. Inaba (Waseda Univ.)
XANES analysis of electronic structure of Mn in $La_{1-x}A_x$MnO3±□ (A=Ca, Ba)

P20   Y. Shingaki (Waseda Univ.)
Local environment analysis of dilute rare earth elements in phosphor materials

P21   H. Miyazaki (Nagoya Institute Tech.)
Electronic structure of half-Heusler type ZrNiSn alloy

P22   H. Miyazaki (Nagoya Institute Tech.)
Electronic structure of K-doped EuO ultrathin films

P23   K. Yoshida (Kyoto Univ.)
Analysis of the electric status of ZnO treated by microwave

P24   S. Kimura (UVSOR)
IR micro-spectroscopic imaging using SR from UVSOR-III

P25   H. Katayanagi (IMS)
Photodissociation dynamics of fullerenes by velocity map imaging with improved mass resolution

P26   Y. Takagi (IMS)
Magnetic property of iron phthalocyanine on the metallic substrates

P27   H. Yamane (IMS)
Weak intermolecular interaction of organic crystalline films revealed by high-precision valence-band dispersion measurement

P28   H. Arai (UVSOR)
Development to solutions in the scanning transmission soft X-ray microscopy at BL4U of UVSOR

P29   T. Shimada (Nagoya Univ.)
High-resolution angle resolved photoemission spectroscopy of $FeSb_2$

P30   Y. Imoto (Fukui Univ.)
Current status of the VUV beamline BL3B (HOTRLU)

Nov 11th (Sun)

<Session 3, Chair: S. Kimura>
9:00-9:30   M. Kitaura (Yamagata Univ.)

	Formation and relaxation of photo-excited states of localized electron systems induced by excitation with vacuum ultraviolet photons
9:30-9:50	T. Nakazato (Osaka Univ.)
	Temperature dependence of rare-earth doped APLF glass photoluminescence
9:50-10:10	R. Ishikawa (NAOJ)
	Development of chromospheric Lyman-alpha spectro-polarimeter (CLASP) with BL7B
10:10-10:30	K. Fukui (Fukui Univ.)
	Current status of the VUV beamline BL3B (HOTRLU)
10:30-10:50	K. Nakagawa (Kobe Univ.)
	Toward a complete measurement of wide-range-absorption spectra of 20 protein amino acids, 5 nuclear bases and 3 dipeptides

10:50-11:20   Coffee Break

<Session 5, Chair: T. Ito>

11:20-11:50	M. Kamada (Saga Univ.)
	Personal review of UVSOR-I generation
11:50-	K. Soda (Nagoya Univ.)
	Discussion and closing remarks

Review of Beamlines and Science at UVSOR

1. Overview

I was asked by the Director General to review the present status and future directions of science using UVSOR from the perspectives of

- international activities
- application to molecular science
- in-house contributions and challenges in the area of molecular science

My comments are based on the recent (2010, 2011) annual reports and a series of nine one-hour sessions with UVSOR researchers and UVSOR users from other departments in IMS and other institutions. I thank all the presenters for the careful work they put into their presentations, which allowed me considerable insight into the present status and future directions. I was particularly struck by the relative youth and enthusiasm of many of the presenters which speaks well for the vitality of UVSOR and IMS.

Here I make selected comments on each presentation / area of research / status of the instrumentation. After that I make some general observations on how these current activities position UVSOR relative to other facilities with strong research programs in molecular science, and where I think there are opportunities for improving international participation and enhancing the relevance of UVSOR research to the overall mission of IMS, which I take to be primarily fundamental research into systems and phenomena where the perspective of the molecular unit is a strong organizing principle.

2. Comments on researches

2.1 Facility and light source research (Masahiro KATOH, Director, UVSOR)

The synchrotron source, after updating to UVSOR-III in early 2012 (this year!), is a very competitive facility relative to all other sub-1GeV SR sources. The most recent upgrade has significantly reduced the emittance and has freed up space for additional insertion devices (total 6). This has provided an opportunity for adding a new, very competitive beamline for science (BL4U, STXM), a number of other beamline and end-station upgrades, and conversion of BL1U into a very versatile platform for advanced light source generation experimentation. The latter is an important aspect of a synchrotron facility as it provides ongoing challenges for the accelerator group, opportunities for collaboration with other accelerator light source facilities, and can lead to large improvements in light source technology, which may be a platform for a future upgrade of UVSOR. At the same time there appear to be too many challenging initiatives under way – free electron laser development, coherent THz systems, fs slicing, and laser Compton gamma ray generation. It was not clear which of these had priority or which had a potential or actual user community. The latter should be an important principle in guiding priorities for further investment and development in this area.

It was noted that some beamlines have challenges with operation in the current top-up mode. The fraction of the time devoted to top-up injection, and thus perturbation of the storage ring is 20% (12 seconds each minute), due to rather short lifetime of the electron beam just after the upgrade to UVSOR-III. The present 12 seconds (12 injections) per minute seem long relative to those at other SR facilities. The number of top-up injections will decrease as the electron beam lifetime and the injection efficiency improve as in UVSOR-II. Efforts should be made to improve the top-up injection procedure, as soon as possible, not only to reduce the fraction of the time, but also to reduce any perturbations of the beam position or size associated with the top-up. This is particularly important for brightness dependent experiments such as STXM.

2.2 Spectroscopy of liquid systems (BL3U: Masanari NAGASAKA, KOSUGI Group, IMS)

The liquid spectroscopy instrumentation developed at UVSOR is better than versions I have seen at the ALS and CLS. This is a very rapidly developing area of SR science with tremendous potential for both fundamental and applied studies. The cluster apparatus on BL3U is also an outstanding piece of equipment. Together with the gas, liquid and solid spectroscopy capabilities at BL3U and other UVSOR beamlines, the ensemble is ideally suited for systematic studies of the evolution of structure (electronic, magnetic and geometric) from isolated molecules/atoms, to the solid state. The session on cluster and liquid spectroscopy at the recent ICESS-12 meeting (St. Malo, France, Sep 2012) was one of the best of that conference in my opinion.

The plans that Nagasaka outlined to extend the methods to *in situ* electrochemistry, liquid-solid interfaces; solid-gas interface and *in situ* chemical and photochemical reactions are very exciting and will be some of the outstanding research from UVSOR in the next few years. This area should be supported fully. There is also very strong synergy between these spectroscopy studies and science with similar goals but with lateral spatial resolution, that will be performed on the BL4U STXM, which should

be operational and open to various classes of users by spring 2013.

2.3 VUV, EUV and X-ray absorption and photoemission spectroscopy of solids and gases (BL2A, BL4B, BL5B, BL6U: Eiji SHIGEMASA, UVSOR)

BL2A (double crystal monochromator) provides the highest energy photons at UVSOR. Despite being non-competitive relative to similar BL at other SR facilities, due to the low critical energy at UVSOR, it operates well and has a small but steady use by a number of Japanese research groups, primarily for materials science using X-ray absorption. It was noted that the publication rate was low which may reflect the non-competitive nature of this beamline. For a low energy ring like UVSOR a better choice to cover the high energy range would be a grating monochromator, which, with suitable multilayer mirror technology, can provide quite high performance up to 3 - 4 keV.

BL5B features an unusually wide photon energy range (6-600 eV) and a very large chamber equipped with a very flexible 6-axis goniometer. It is apparently one of only a few beamlines in Japan that are capable of characterizing large optical elements in a very flexible way. The research carried out on this beamline is primarily of a service character. At other facilities (e.g. ALS BL 6.3.2), there are active research programs in developing coatings and characterizing optics for semiconductor EUV lithography. This could be an area for future research at BL5B.

BL4B, the first soft X-ray beamline at UVSOR with high energy resolution, has produced some high quality molecular and materials science in recent years, based on research by in-house and external users. The newer BL3U undulator line covers a similar energy range and is now the preferred beamline for spectroscopy research in this energy range. However BL4B still has an active research program in magnetic materials (see discussion of the presentation by T. Yokoyama in section 2.7).

BL6U is the most modern and competitive of the beamlines supervised by Shigemasa. Its variable angle, variable line spacing PGM monochromator provides good intensity with outstanding energy resolution. It was noted that the minimum undulator gap that can be achieved at present is 13 mm, whereas the design specified a 10 mm minimum gap. The reason for this should be identified and repaired if possible, since there are some photon energies that cannot be reached due to the out-of-spec minimum gap. The two end stations for BL6U are each internationally competitive. The gas phase Auger electron photoion coincidence (AEPICO) apparatus is ideally suited for studies of molecular photoionization dynamics with high energy electrons, and complements research at other facilities which use the Cold Target Recoil Ion Momentum Spectrometer (ColTRIMS) approach. The MBS-A1 photoemission end station is also very competitive internationally

and has been adapted for two-dimensional electron spectroscopic studies in gas phase. Consistent with its competitive character, there are a number of outstanding international collaborators (Lablanquie, Simon, Piancastelli) using this instrument.

The gas phase examples presented by Shigemasa, along with those in the 2011 UVSOR annual report are excellent examples of modern synchrotron based molecular dynamics and photo-physics science. I particularly admired the studies of ultrafast dissociation in C 1s excited CF_4 (p 53) and the electronic Doppler result in S 2p excited OCS (p 56). BL6U is one of the outstanding examples of molecular science research at UVSOR and should continue to be well supported. Identification of suitable collaborators and independent researchers from the international community should be a target for increasing the international visibility of the molecular science program at UVSOR.

I note that Shigemasa and his group members are now using the SACLA X-ray free electron laser for advanced molecular photophysics studies. This is a very good development for UVSOR. Opportunities of using research at UVSOR to complement SACLA research, possibly resulting in joint publications, should be encouraged.

2.4 X-ray absorption, X-ray emission and angle resolved photoemission of solids (BL3U, BL6U: Hiroyuki YAMANE, KOSUGI Group, IMS)

BL3U is a world class facility for X-ray absorption, X-ray emission and resonant X-ray scattering. This has enabled some exceptional research by UVSOR and outside researchers. The examples of XAS characterization of organic conductors and semiconductors for organic LED, organic electronics, and organic photovoltaic systems were fascinating. I draw particular attention to *in operando* measurements which used the difference of FY_NEXAFS spectra induced by applied potentials or currents to characterize the changes in molecular structure of electronic states (PRL 107 (2011) 147401). This is one of the first *in operando* soft X-ray studies of a device material to my knowledge. It revealed the surprising result that the electronic structure changes are associated with σ states, rather than the π states normally believed to be involved in the conductivity of organic conductors and semiconductors. These results have important implications for the field of single molecule electronic devices, which is a very hot topic and target of development at many research facilities around the world.

The X-ray emission spectrometer has exceptional performance relative to similar facilities at other SR centers. The energy resolution is below 100 meV at 140 eV X-ray energy, which is very competitive. The efficiency of the novel transmission grating spectrometer is probably the highest in the world for soft X-ray spectrometers. It has been used for studies of a number of interesting systems, including

DNA polymers (poly(G-C), poly(A-T)) and N-doped graphene nano flakes (J. Phys. Chem. C 116 (2012) 16251). The higher performance transmission grating which is planned for the XES spectrometer will further improve energy resolution and possibly efficiency. The future plan to apply XES and RIXS techniques to *in operando* studies of molecular devices is really at the cutting edge of international SR science with X-ray emission spectroscopy.

An outstanding program of angle-resolved photoemission from molecular solids and thin films on **BL6U** was also described by Dr. Yamane. The system for these studies is one of the best in the world, achieving < 5 meV overall energy resolution (photon & electron), ability to cool to 13 K, and a 5-axis motion system that allows rather complete band structure studies with the sensitivity needed to track band dispersion in organic systems which are typically much smaller than the dispersion in semiconductor and metal systems. The achievement of these technical capabilities in an instrument constructed at IMS is a tribute to the excellence of the Equipment Development Center which is a real asset for UVSOR and IMS. The quality of the preparation chamber and its ability to allow for preparation of organic thin films in a system also used for semiconductor and other samples was noted. There is strong international participation on BL6U. A number of interesting examples were outlined, including: band alignment at the interface between carbon nanotubes (CNT) and a SiC substrate in CNT rafts prepared surface decomposition of SiC (Maruyama); spin-orbit (Rashba) band splitting in 1-d Pt nanowires (Yeom); nanoscale phase separation in DNA Watson-Crick (G-C) multilayer films (Friedlein); and valence band dispersion in metal phthalocyanines (Yamane). The latter project, a major effort by Dr. Yamane, showed very fascinating temperature dependent dynamics results which gave important insights into intermolecular interactions and how these can be tuned by adding substituents to the phthalocyanine or changing the metal. Since the molecular films which are the focus of these studies are easily damaged by synchrotron radiation, it is essential to be able to prepare very uniform samples which can then be used to circumvent radiation damage by scanning the sample to fresh areas during the measurements. This system is one of the best in the world for ARPES studies of organic solids.

Dr. Yamane identified a number of improvements that could be made to further enhance the performance of this facility. These include a larger analyzer (e.g. D80 VG Scienta) to improve efficiency; a new analysis chamber; and addition of an O_2 dosing system to remove carbon contamination on the BL6U optics. To the extent these will facilitate new molecular science, UVSOR / IMS should seriously consider these requests.

2.5 Scanning Transmission X-ray Microscopy (BL4U: Takuji, OHIGASHI, UVSOR)

BL4U is a new soft X-ray undulator beamline with a dedicated STXM end station. STXM is a relatively new spectromicroscopy technique which has may applications in both fundamental and applied science. The planned science program is very ambitious. Further development of the instrumentation and techniques (cryo spectromicroscopy, cryo-tomography, ptychography) will require substantial effort, and should be staged after reliable basic operation is achieved. The STXM project at UVSOR will have a significant advantage relative to other STXM facilities, as IMS is able to provide on site sample preparation (ultramicrotomy, focused ion beam milling, high end optical microscope with encoders and micromanipulators, etc). BL4U & the STXM end station are part of the Nanotechnology Platform Project in Japan. This is very appropriate and will link the STXM to the on site analytical transmission electron microscope (TEM), which is an excellent complementary research tool. The presence of scanning Raman and IR microscopes (both lab and UVSOR based) provide additional complementary analytical microscopy techniques. Efforts should be made to facilitate multi-technique studies, for example, by developing sharable sample mounting and methods to quickly locate the same spatial regions of samples in the different microscopes.

2.6 Solid State Science (BL1B, BL5U, BL6B, BL7U: Shin-ichi KIMURA, UVSOR)

BL7U and **BL5U**, both dedicated to angle resolved photoemission (ARPES) of surfaces and solids, are the 1st and 2nd most popular beamlines at UVSOR, as judged by usage, ratio of allocated to requested shifts, and numbers of publications in high profile journals. BL7U is among the very best facilities world wide for condensed matter electronic structure studies using low energy photons. Usually researchers turn to beamlines with higher photon energy (>100 eV) if they need additional sampling depth to ensure they are sampling bulk properties. At **BL7U** very low outgoing electron energies are used, as these are also bulk sensitive. The energy resolution of 2 meV (electron and photon combined) is only surpassed by a few other lines in the world. The Apple II insertion device means that the full polarization properties of samples can be explored. A range of outstanding condensed matter science is taking place on BL7U including: detailed studies of Fe-based superconductors; exploration of charge density wave effects at the surface of graphite; investigation of organic conductors. The ongoing development of conventional optical focusing techniques for UV light to achieve sub-micron spot sizes in the 7-9 eV photon energy could lead to some world-unique capabilities which would complement higher photon energy nano-ARPES lines at the ALS (Maestro) and Soleil (Antares). The potential for using such a facility to study laterally heterogeneous surfaces was illustrated with a novel system of electronic phase separation which is suspected to occur in κ-$(Et)_2Cu[N(CN)_2]Br$ on the sub-micron spatial scale. BL7U should invite more international users.

While **BL5U** is a somewhat older ARPES system with lower performance, its higher photon energy range (up to 200 eV) provides a useful complement to BL7U. Planned modifications to improve the performance of BL5U were described, including replacement of the monochromator, which has a resolving power of only 3000, as opposed to the 10,000-50,000 resolving power of BL7U. Although a number of organic materials are being studied with BL7U and 5U, the majority of the science is in the realm of condensed matter physics of semiconductors, metals and correlated electron materials.

BL6B provides light in the IR and THz range. Kimura outlined some exciting instrumentation developments, including his magic mirror which achieves exceptionally large angular collection of bend magnet IR radiation (only exceeded by the mirror array system of the IRENI facility at SRC, Wisconsin), and the recent adoption of a focal plane array detector for far- and mid-IR spectromicroscopy on BL6B. Interesting science using far-IR (THz) to study organic materials at high pressure was presented. However there has been relatively little molecular science using BL6B despite the extensive use of synchrotron IR spectroscopy and spectromicroscopy for molecular science at other SR facilities around the world. Given the activities in organic electronic materials and biosciences at IMS, it would seem there is excellent potential to expand use of BL6B, especially in the mid-IR to visible range where many non-SR scientists are actively using lab based IR spectroscopy and spectromicroscopy. I understand that Assoc. Prof. Furutani (Life and Co-ordination Complex Molecular Science, IMS) is interested in partly-dedicated use of BL6B for bioscience applications. The new program to provide such 'approved program' time (outlined by Kimura at the end of his Friday presentation) seems to be an excellent opportunity to increase molecular science activity at the IR microscope on BL6B. There is also a lot of science which can be advanced using STXM and IR microscopy in a complementary fashion. Development of identical or cross-compatible sample mounting and fiducialization approaches (perhaps linked through the encoded stages of the optical microscope at BL4U STXM) could significantly facilitate that development.

BL1B has capabilities for developing novel coherent THz and THz-VUV experiments using laser slicing with amplitude modulated pulse trains. This is very exciting light source physics with good potential to achieve new physics. Possible molecular science applications of the coherent THz source were outlined in the areas of protein motion and carrier dynamics in Li ion battery and organic Dirac Fermion materials. At present the motivation is clearly exploration of novel instrumentation / light source capabilities. Its impact on molecular science is likely to be limited, at least in the short term.

2.7 Magnetic materials (XAS, XMCD) (BL4B: Toshihiko YOKOYAMA, IMS)

The superconducting magnetic spectroscopy system on **BL4B** is a competitive facility relative to related systems internationally. It has among the highest on-sample magnetic field at SR facilities and has a good degree of flexibility in sample mounting relative to the field and photon polarization such that all aspects of the magnetic properties of samples can be measured. The facility is part of the Nanotechnology Platform Project in Japan, for which funding was recently renewed for a 10 year period. Professor Yokoyama gave overviews of five specific research projects in the surface and thin film magnetism: magnetic properties of Fe islands and nanowires on W(110); Co nanorods on Cu(110)-(2x3)N; γ'FeN/Cu(001); Fe on Si_3N_4/Si(111)-(8x8); VOPc/Si(111). The latter is the only example with a molecular science flavor. In this case, a combination of polarization dependent NEXAFS and V 2p XMCD was used to determine the structure and magnetism. Although there was a significant change in electronic structure and bonding between monolayer and multilayer VOPc, the V 2p XMCD magnetic signature was identical indicating the V 3d character is similar despite the bonding change. All of the examples presented high quality data from very challenging low signal systems. While similar science is being done elsewhere, Professor Yokoyama noted a major advantage of the UVSOR operation was the much lower time pressure which allows for sufficient time to study samples requiring careful *in situ* preparation.

2.8 Photoemission of organic solids (BL8B: Satoshi KERA, Chiba Univ)

BL8B is a public beamline dedicated to ultraviolet photoemission spectroscopy and ARPES of organic solids. The presentation gave a strong motivation for the research of the Chiba group in terms of the need to understand the fundamental principles of molecular assembly in order to control electronic structure and functionality of organic materials for electronics applications. A quantum perspective and the theme of wavefunction spreading was used to interpret recent results on: weak band gap states in fullerene thin films; conduction mechanism and hole-phonon coupling as a limit to charge mobility in pentacene films; band dispersion in rubrene. BL8B is the oldest beamline at UVSOR. Plans to improve the instrumentation (replace the current analyzer with a modern 2D angle-energy electron spectrometer) and move from 8B to 2B were described and motivated by the need for higher performance to enable use of UV-ARPES for momentum space orbital mapping of organic solids. This approach was highlighted by a number of presentations at the recent ICESS12 meeting and is clearly a trend in international science in this area.

2.9a VUV optical properties (BL3B, BL7B: Shin-ichi KIMURA, UVSOR)

BL3B and **BL7B** are dedicated to studies of the

optical properties (reflection, absorbance and luminescence) in the visible – and vacuum UV regions. **BL7B** is an older beamline that has recently been reconfigured to focus on ellipsometry measurements. **BL3B** has recently been moved from BL1B and significantly upgraded to the HOTRLU system which has greatly improved flux (relative to the previous BL1B system), and a smaller spot size by using a Kirkpatrick-Baez focusing system. Research on the UV optical properties of a number of interesting materials was described, including AlN and EBSTO, a layered organic-inorganic system, as well as studies related to calibrating instruments for astrophysics. There is significant international participation and quite high productivity (BL3B & BL7B generated over 20% of all UVSOR publications in the past 5 years), although the publications are rarely in the first rank journals.

2.9b VUV spectroscopy of biological molecules (BL3B, BL7B: Kazumichi NAKAGAWA, Kobe Univ.)

Professor Nakagawa described his program for careful transmission measurements on thin films of the individual amino acids and DNA bases, which are used to generate absolute absorption cross-sections. Results are typically reliable to 5-10%, but often only after a sum-rule normalization correction. The motivation for the work is UV biosensors, and connections to UV damage related to cataracts. However there was no evidence for a direct link to those areas, and the energy range relevant to these issues is only a very small part of the energy range over which the absorption was measured. However, in terms of understanding the fundamental physics and chemistry of radiation damage, such a wide range of spectral studies may be meaningful.

3. General comments about science and future directions for UVSOR

3a. International competitiveness

As outlined in detail above, some beamlines, end-stations and research programs are more internationally competitive than others. Of particular high quality I consider BL3U, BL6U and BL3B.

3b. Relevance to molecular science mission

The liquids, electrochemistry, and chemical / photochemical reaction science, as well as the electronic structure (ARPES, XAS, XES) studies of molecular thin films are areas of the most direct relevance to molecular science. There is a strong tradition of gas phase spectroscopy studies at UVSOR which is very relevant to molecular science. However, I was less impressed by the instrumentation and science in this area, than in other areas. Although not mainstream molecular science, the instrumentation and programs in condensed matter electronic structure (ARPES) are very strong and definitely worth continuing.

3c. Role of in-house contributions / future directions

A key aspect of UVSOR is that a large proportion of the scientific direction, instrumentation development, and beamtime is determined by the in house scientists. This is in strong contrast to most other SR facilities, where it is the science and interests of external researchers that is dominant. I consider the exceptional in-house research programs to be a real strength of UVSOR. The quality of the science on the international scale then strongly depends on the quality of the team leaders, the researchers they attract to their teams, and their international collaborations. IMS is fortunate to have some very talented researchers. Relative to other facilities, the size of the UVSOR staff is very small, yet the output is outstanding, from the perspectives of quality, diversity and quantity. Hiring of at least one additional faculty in IMS or UVSOR, at the professor or associate professor level should be (and, I understand, is) a high priority. While the main goal should be to find a dynamic young or mid-career individual with a passion for synchrotron-based research applied to molecular science, if there are equally good candidates, research in the area of nanoscience would build best on the existing instrumentation and strengths of UVSOR.

November 22, 2012

Adam P. Hitchcock, FRSC
Professor of Chemistry & Chemical Biology
McMaster University
Canada